

**Magnetic Properties of Nanosized Greigite and Magnetite  
and their Application in Environmental Studies**

---

A thesis submitted to attain the degree of  
DOCTOR OF SCIENCES of ETH ZURICH  
(Dr. sc. ETH Zurich)

presented by

**BARBARA LESNIAK**

M. Sc. in Engineering, Gdansk University of Technology  
born on 06.12.1991  
citizen of Poland

accepted on recommendation of

Prof. Dr. Andrew Jackson, examiner

Prof. Emer. Ann Hirt, co-examiner

Prof. Dr. Timothy Eglinton, co-examiner

Prof. Dr. Michael Winklhofer, external-examiner



*Dla moich rodziców, bez których nigdy nie osiągnęłabym niczego.*

To my parents without whom I would never achieve anything.



## **Abstract**

Magnetic nanoparticles are widely studied because of their diverse applications in different research areas. Their presence in natural systems can provide information about environmental change or microbial evolution in environmental studies, but also changes in the Earth's magnetic field in paleomagnetic studies. Natural samples, however, contain many different iron phases, and understanding the source of a magnetic response can be complex. In the studies in this thesis, I have analyzed magnetic properties of pure, synthetic magnetic nanoparticles of greigite and magnetite, which are often found in sedimentary records, and can be characterized by unique magnetic properties. I then used the obtained knowledge for determining the magnetic minerals in sediments from natural environments. The greigite nanoparticles, which were analyzed, are characterized by flake-like morphology, and the magnetite nanoparticles are from magnetotactic bacteria (MTB). Rock magnetic methods and electron magnetic resonance (EMR) spectroscopy were accompanied by other analytical techniques to identify the main magnetic phase, and to define its physical properties with special focus on possible applications in natural environments.

Both the synthetic and natural greigite samples have flake-like shape, and reveal a low-temperature change in their spectral parameters at around 50 K for pure synthetic greigite and around 90 K for the natural sample. This change could originate from the flake-like morphology or be an intrinsic feature of greigite; in the latter case, the feature could serve in the detection of greigite in sedimentary records. The results from this study are then applied to sediments from a core taken from a tailings pond of a former uranium mine in Lower Williams Lake, Canada. EMR spectra together with other magnetic properties show the gradual transformation of greigite at the top of the sediments to pyrite down core. The natural flake-like greigite serves as the precursor for framboidal pyrite.

Magnetite, originating from lab-cultured and natural MTB, is aligned in chains, and this chain-like configuration affects its spectral properties. For this reason, EMR spectroscopy can be a useful method for the detection of intact chains of magnetite in the environment, which in turn can serve as an environmental proxy. In natural environments, this chain-arrangement is often destroyed after the

bacteria die, due to decomposition of organic matter. An analogy for the decomposition of bacteria, which leads to the breakdown of chains, is incremental heating of lab-cultured MTB, which destroys the organic matter. The breakup of the chain arrangement leads to a change in spectral properties, and can be used to calibrate the degree of decomposition.

The results from this experiment are applied to two natural systems. The first system examines how a change in redox conditions as shown in lacustrine sediments from Lake Constance affects the preservation of MTB chains. The highest concentration of MTB chains is found immediately above a sharp change in redox condition, associated with re-oligotrophication. The second application is in marine sediments from the Bengulean Upwelling off the western coast of Namibia. In this study, I show that intact chains of MTB are preserved in marine sediments that are composed of organic and opal ooze.

In conclusion, the collected results from this thesis demonstrate the usefulness of applying EMR in the study of magnetic mineralogy. The spectra provide information on the magnetic state, i.e., paramagnetism or ferromagnetism (*s.l.*), and morphology of the iron phases in a natural system, and possibly interaction between ferromagnetic (*s.l.*), minerals. When used together with other rock magnetic methods, it is possible to obtain a better understanding of the iron minerals in a sediment.

## Zusammenfassung

Magnetische Nanopartikel werden wegen ihren unterschiedlichen Anwendungsmöglichkeiten in verschiedenen Forschungsgebieten breit untersucht. Ihre Anwesenheit kann Informationen über Umweltveränderungen oder die mikrobielle Evolution in Umweltstudien liefern, aber auch Veränderungen des Erdmagnetfelds in paläomagnetischen Untersuchungen können nachgewiesen werden. Natürliche Proben können allerdings viele verschiedene Eisenphasen enthalten und das Verständnis der Ursache der magnetischen Eigenschaften kann vielfältig interpretiert werden. In den Untersuchungen in dieser Dissertation habe ich die magnetischen Eigenschaften von reinen synthetischen Greigit- und Magnetit-Nanopartikeln analysiert, welche sich oft in sedimentären Ablagerungen befinden lassen und sich durch einzigartige Eigenschaften auszeichnen. Die erhaltenen Erkenntnisse wurden genutzt, um die magnetischen Mineralien in Sedimenten aus einem natürlichen Umfeld zu verstehen. Die untersuchten Greigit-Nanopartikel zeichnen sich durch eine flockige Morphologie aus und die Magnetit-Nanopartikel stammen von magnetotaktischen Bakterien (MTB). Gesteinsmagnetische Methoden und Elektronen-Spin-Resonanz (ESR) wurden durch andere analytische Verfahren ergänzt, um die magnetische Hauptphase zu identifizieren und ihre physikalischen Eigenschaften, mit besonderem Fokus auf möglichen Anwendungen in natürlicher Umgebung, zu bestimmen.

Synthetische und natürliche Greigitproben haben eine flockige Form zeigen eine Tieftemperaturänderung bei etwa 50 K bei synthetischem Greigit und bei etwa 90 K bei der natürlichen Probe. Diese Änderung könnte von der flockigen Morphologie herkommen oder eine intrinsische Eigenschaft von Greigit sein; in letzterem Fall könnte diese Eigenschaft zur Detektion von Greigit in Sedimentablagerungen dienen. Die Resultate dieser Untersuchung wurden dann auf Sedimente aus einem Bohrkern aus einem Absetzbecken eines ehemaligen Uranbergwerks in Lower Williams Lake, Kanada, angewandt. EMR-Spektren, zusammen mit anderen magnetischen Eigenschaften, zeigen die graduelle Transformation von Greigit am oberen Ende der Sedimente zu Pyrit weiter unten im Bohrkern. Der natürliche flockige Greigit dient als Vorstufe von framboidischem Pyrit.

Magnetit, von Laborkulturen stammenden oder natürlichen MTB, ist in Reihen ausgerichtet und diese reihenartige Konfiguration beeinflusst seine spektralen Eigenschaften. Aus diesem Grund kann EMR-Spektroskopie eine nützliche Methode sein, um intakte Magnetit-Ketten in der Umwelt zu detektieren, was wiederum als Umweltproxy dienen kann. In natürlichen Umgebungen ist diese Reihenanordnung aufgrund der Zersetzung organischer Materie nach dem Tod des Bakteriums oft zerstört. Eine Analogie für den Zersetzungsprozess des Bakteriums, und somit auch der Ketten, ist die stufenweise Erhitzung von laborkultivierten MTB, was organische Materie zerstört. Das Aufbrechen der Kettenstruktur führt zu einer Änderung der spektralen Eigenschaften und kann genutzt werden, um den Grad der Zersetzung zu kalibrieren.

Die Ergebnisse dieser Laborexperimente werden auf zwei natürliche Systeme angewandt. In einer ersten Anwendung wird gezeigt, wie sich eine Änderung in der Redoxbedingungen im Seesedimenten vom Bodensee der Kettenstruktur der MTB beeinflusst. Die höchste Konzentration der MTB-Ketten entsteht unmittelbar oberhalb einer starken Änderung in der Redoxbedingungen in Verbindung mit einer Wieder-Oligotrophierung. Die zweite Anwendung betrifft marine Sedimente vom Benguelia Tiefenwasseraufstieg vor der Westküste Namibias. In dieser Studie zeige ich, dass intakte MTB in marinen Sedimenten erhalten sind und dass sich diese aus organischem Schlamm und Opalschlamm zusammensetzen.

Die gesammelten Resultate dieser Dissertation zeigen den Nutzen der Anwendung von EMR bei der Untersuchung magnetischer Mineralogie. Die Spektren liefern Informationen über die magnetischen Zustände, beispielsweise Paramagnetismus oder Ferromagnetismus (*s.l.*), und die Morphologie der Eisenphasen in natürlichen Systemen und mögliche Interaktionen zwischen ferromagnetischen Mineralien (*s.l.*). In Kombination mit anderen gesteinsmagnetischen Methoden, ist es möglich ein besseres Verständnis von Eisenmineralien in Sedimenten zu erlangen.



# Table of Contents

<b>Abstract</b> .....	v
<b>Zusammenfassung</b> .....	vii
List of Abbreviations and Units.....	xiii
<b>1. Introduction</b> .....	<b>1</b>
1.1. Background Information .....	1
1.2. Greigite .....	2
1.3. Magnetite.....	3
1.4. Magnetotactic Bacteria (MTB) .....	4
1.5. Motivation of the Work .....	4
1.6. Thesis Outline .....	5
1.7. Author Contributions.....	6
1.8. References .....	8
<b>2. Theory and Methodology</b> .....	<b>11</b>
2.1. Fundamental Concepts of Magnetism.....	11
2.2. Experimental Methods .....	18
2.3. References .....	27
<b>Part I – Greigite</b>	
<b>3. Low-Temperature and Angular Dependence FMR Studies of Greigite (Fe<sub>3</sub>S<sub>4</sub>) Aggregates</b> .	<b>29</b>
3.1. Introduction .....	29
3.2. Material and Methods .....	31
3.3. Results .....	33
3.4. Discussion .....	41
3.5. Conclusions .....	44
3.6. Author Contributions .....	45
3.7. References .....	45
3.8. Appendix .....	47

<b>4. Greigite as a Magnetic Carrier in Sediments from Lower Williams Lake, Canada .....</b>	<b>49</b>
4.1. Introduction .....	49
4.2. Samples and Methods .....	51
4.3. Results .....	55
4.4. Discussion .....	65
4.5. Conclusions .....	69
4.6. Author Contributions .....	69
4.7. References .....	70
4.8. Appendix .....	72

**Part II – Magnetotactic Bacteria**

<b>5. From Magnetotactic Bacteria to Magnetofossils: an Experimental Approach.....</b>	<b>75</b>
5.1. Introduction .....	75
5.2. Samples and Methods .....	78
5.3. Results .....	80
5.4. Discussion .....	89
5.5. Conclusions .....	92
5.6. Author Contributions .....	93
5.7. References .....	93
5.8. Appendix .....	96
<b>6. Ferromagnetic Resonance of Magnetite Biominerals Traces Redox Changes .....</b>	<b>101</b>
6.1. Introduction .....	102
6.2. Materials and Methods .....	103
6.3. Results and Discussion .....	108
6.4. Conclusions .....	114
6.5. Acknowledgments .....	115
6.6. Author Contributions .....	115
6.7. References Cited .....	115
6.8. Appendix .....	120

<b>7. Magnetic Carriers in Sediments Offshore the Namibian Coast and their Relation to Upwelling .....</b>	<b>123</b>
7.1. Introduction .....	123
7.2. Geological Background .....	125
7.3. Materials and Methods .....	127
7.4. Results .....	129
7.5. Discussion .....	139
7.6. Conclusions .....	143
7.7. Author Contributions and Acknowledgements .....	143
7.8. References .....	144
7.9. Appendix .....	147
<b>8. Conclusions and Outlook.....</b>	<b>171</b>
Conclusions .....	171
Outlook .....	172
<b>Acknowledgements .....</b>	<b>175</b>
<b>Curriculum Vitae .....</b>	<b>177</b>



## List of abbreviations and units

$M_S$	Saturation magnetization ( $\text{Am}^2/\text{kg}$ )*	$TEM$	Transmission electron microscopy
$M_R$	Remanent magnetization ( $\text{Am}^2/\text{kg}$ )*	$SEM$	Scanning electron microscopy
$B_C$	Coercivity field (T)*	$XRD$	X-ray diffraction
$B_{CR}$	Remanent coercivity field (T)*	$SP$	Superparamagnetic
$B_{res}$	Resonance field (T)	$SD$	Single-domain
$\text{dB}$	Linewidth (T)	$SSD$	Stable single-domain
$g_{\text{eff}}$	g-factor	$PSD$	Pseudo single-domain
$T_C$	Curie temperature (K)	$MD$	Multi-domain
$T_N$	Néel temperature (K)	$RT$	Room temperature
$T_V$	Verwey transition ( $\sim 120$ K)	$LT$	Low temperature
$MTB$	Magnetotactic Bacteria	$HT$	High temperature
$EMR$	Electron magnetic resonance	$\mu_B$	Bohr magneton
$EPR$	Electron paramagnetic resonance	$\hbar$	Reduced Planck constant
$FMR$	Ferromagnetic resonance	$Eh$	Redox potential

\* In the geomagnetic community  $M_S$  and  $M_R$  are commonly used to represent specific (mass) magnetizations and therefore are presented in  $\text{Am}^2/\text{kg}$ . In the rock magnetism the magnetic field ( $H$ ) is often written as a magnetic induction ( $B$ ) and its value is given in T. It is in this form that those values are presented in this thesis.



# 1. Introduction

## 1.1. BACKGROUND INFORMATION

Magnetic nanoparticles have attracted strong interest in a variety of research areas, due to the wide range of applications in which they are employed. Their ability to respond and to be modifiable by external magnetic fields, has been exploited for data storage, drug delivery, hyperthermia as a treatment of cancer, nanofluids, water treatment in an environmental context, and many others (Ateia et al., 2017; Deatsch and Evans, 2014; Frey and Sun, 2010; Gupta and Gupta, 2005; Sheikholeslami, 2017; Tang and Lo, 2013). In environmental studies, magnetic nanoparticles in nature are of great importance, because they are sensitive to environmental processes, microbial evolution, and changes of the Earth's magnetic field (Faivre et al., 2008; Jiang et al., 2001; Pan et al., 2005; Snowball and Thompson, 1988).

Sedimentary systems are extremely complicated because they are influenced by the source rocks of the sediments, the climate and environment of the depositional area, and geochemical processes at the time of diagenesis and lithification. Not only ferrimagnetic minerals, such as magnetite, greigite, hematite, pyrrhotite, and goethite, can be found in the sedimentary rocks and influence the rock's magnetic properties, but paramagnetic and even diamagnetic minerals may dominate the magnetic signal. The complex relationship between these factors will dictate which ferromagnetic minerals are found in a sediment and whether they are preserved in the sedimentary record. To be able to analyze such systems, and define the magnetic minerals, we must at first understand their basic properties. It is only in this way, that their role in a bigger picture can be evaluated. In this thesis, I investigate the magnetic properties of both synthetic and natural samples of greigite and magnetite nanoparticles. Using the knowledge about the properties, which has been obtained from the pure synthetic sample, I have applied this information in the analysis of natural sedimentary records.

23

In the natural environments, magnetite ( $\text{Fe}_3\text{O}_4$ ) and greigite ( $\text{Fe}_3\text{S}_4$ ) nanoparticles have been found in the sedimentary record. These ferrimagnetic phases are characterised by a strong spontaneous magnetization, and they are sensitive to redox-conditions and environmental changes. Magnetite

27 nanocrystals are of special interest, as they have been shown to be in some cases produced by  
28 magnetotactic bacteria (MTB) within their body cells (Bazylinski et al., 1995). Often these magnetite  
29 crystals, known as magnetosomes, build chains (Blakemore, 1982). Greigite is commonly found in a  
30 form of single-domain (SD) aggregates in the sediments, frequently of nano-size. It is formed often in  
31 anoxic, sulfate-reducing conditions in association with bacterial decomposition of organic matter  
32 (Berner, 1984). A detailed description of greigite, magnetite and MTB is presented below (sections 1.2,  
33 1.3, and 1.3.1, respectively).

34

### 35 **1.2. GREIGITE (Fe<sub>3</sub>S<sub>4</sub>)**

36 Greigite (Fe<sub>3</sub>S<sub>4</sub>) is a ferrimagnetic mineral occurring in terrestrial samples (Roberts et al., 2011). It has  
37 been identified in both lacustrine and marine sediments (Rowan et al., 2009; Snowball and Thompson,  
38 1988). It has been also been found in magnetotactic bacteria (Bazylinski et al., 1995). Greigite has an  
39 inverse spinel structure with ferric iron (Fe<sup>3+</sup>) occupying tetra and octahedral sites and with ferrous iron  
40 (Fe<sup>2+</sup>) in octahedral sites (Chang et al., 2009a), and stoichiometric formula Fe<sup>2+</sup>Fe<sup>3+</sup><sub>2</sub>S<sub>4</sub>. It is a sulphur  
41 isomorphous to ferrimagnetic magnetite (Fe<sub>3</sub>O<sub>4</sub>) (Skinner et al., 1964), and reveals similar structure,  
42 where oxygen atoms in magnetite are substituted with sulphur (Fig.1). The saturation magnetization of  
43 a pure, synthetic greigite sample is  $M_s = 59 \text{ Am}^2/\text{kg}$  (Chang et al., 2008). This value is lower than of  
44 magnetite ( $93.6 \text{ Am}^2/\text{kg}$ ) (Özdemir and Dunlop, 1999) and it could be explained either by the higher  
45 degree of covalence between iron and sulphur in comparison to iron and oxygen, or by increased  
46 delocalization of the 3d electrons in greigite (Roberts et al., 2011). Greigite does not reveal any low  
47 temperature transition (Chang et al., 2009b; Dekkers et al., 2000), and its Curie temperature is not well  
48 defined, because it thermally decomposes into wide range of different heating products at around 350°  
49 C (Chang et al., 2008; Skinner et al., 1964).(Roberts et al., 2011).

50

51

52



### 53 1.3. MAGNETITE ( $\text{Fe}_3\text{O}_4$ )

54 Magnetite ( $\text{Fe}_3\text{O}_4$ ) is one of the most important carriers of remanence in rocks and sediment samples. It  
 55 has been found to form in MTB (Blakemore, 1982). Iron appears in two oxidation states  $\text{Fe}^{2+}$  and  $\text{Fe}^{3+}$   
 56 and its chemical formula can be written as a  $\text{Fe}^{2+}\text{Fe}^{3+}_2\text{O}_4$ . It is characterized by an inverse spinel  
 57 structure with  $\text{Fe}^{2+}$  and  $\text{Fe}^{3+}$  on the octahedral sublattices, and  $\text{Fe}^{3+}$  on tetrahedral sublattices (Fig. 1).  
 58 Magnetite is ferrimagnetic with the saturation magnetization of  $M_s = 480 \text{ kA/m}$  or  $93.6 \text{ Am}^2/\text{kg}$  in its  
 59 pure state, and its Curie temperature,  $T_c = 858\text{K}$  ( $585^\circ\text{C}$ ) (Dunlop and Özdemir, 1997). Magnetite is  
 60 characterized by low temperature transition, known as a Verwey transition at  $T_v = 120 \text{ K}$  (Verwey,  
 61 1939). On cooling through the Verwey transition (at about 120 K), magnetite undergoes a  
 62 crystallographic change from cubic to monoclinic crystal structure, with a marked increase in  
 63 magnetocrystalline anisotropy. Another magnetic transition of magnetite occurs at the isotropic point  
 64 at 135 K, where the first-order cubic magnetocrystalline anisotropy constant  $K_1$  changes sign  
 65 (Muxworthy and McClelland, 2000). The Verwey transition can be used as an unambiguous  
 66 characteristic of magnetite, although that it is only found in multi-domain magnetite, and single domain  
 67 or superparamagnetic magnetite that is dominated by magnetocrystalline, rather than shape anisotropy.

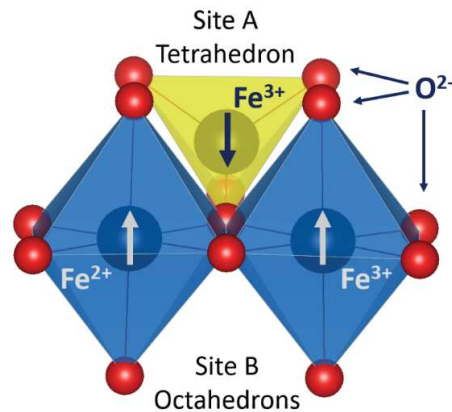


Fig. 1 Crystal structure of  $\text{Fe}_3\text{O}_4$ , with  $\text{Fe}^{2+}$  and  $\text{Fe}^{3+}$  on the octahedral sublattice, and  $\text{Fe}^{3+}$  on tetrahedral sublattice. Red spheres indicate single oxygen atoms. Arrows represent magnetic ordering between Fe atoms. Figure created using Vesta program (Momma and Izumi, 2008). Greigite structure is similar with sulphur atoms substituting oxygen.

### 68 **1.3.1. Magnetotactic Bacteria (MTB)**

69 MTB synthesize nano-sized, membrane-encapsulated ferrimagnetic particles that for many species  
70 align in chains (Bazylinski et al., 1994; Schüler and Frankel, 1999). These particles often have a size  
71 in the range of stable single domain (SSD), which is around 20 nm to 80 nm (Baumgartner et al., 2013;  
72 Butler and Banerjee, 1975; Faivre et al., 2008), and their composition can be magnetite ( $\text{Fe}_3\text{O}_4$ ) or less  
73 commonly greigite ( $\text{Fe}_3\text{S}_4$ ) (Devouard et al., 1998). Magnetosomes are synthesized by a genetically  
74 controlled mineralization process, therefore they have well-defined grain sizes, high crystalline purity  
75 and narrow size and shape distribution. The chain configuration affects the magnetic properties of the  
76 magnetite, which can be used to aid in the detection of MTB (Egli et al., 2010; Gehring et al., 2011;  
77 Moskowitz et al., 1993). The membrane encapsulating the ferromagnetic particles is responsible for  
78 maintaining chain arrangement in MTB and magnetofossils (Schüler and Frankel, 1999), and also helps  
79 to prevent oxidation of magnetosomes. In diagenetic environments, magnetotactic bacteria (MTB) are  
80 an important carrier of the information about the environment, microbial evolution and variations of  
81 Earth's magnetic field (Faivre et al., 2008; Faivre and Schuler, 2008; Hesse, 1994; Kopp and  
82 Kirschvink, 2008; Pan et al., 2005). Their inorganic remains, known as magnetofossils (Kirschvink and  
83 Chang, 1984), have been detected in lakes and marine sediment years after the sedimentation and can  
84 be preserved as a magnetic record within a geological time-frame (Kobayashi et al., 2006; Yan et al.,  
85 2012).

86

### 87 **1.4. MOTIVATION OF THE WORK**

88 The original motivation of the research in this thesis, was to search for MTB in marine sediments in an  
89 upwelling system, the results of which are presented in chapter 7. The project was supported by Swiss  
90 National Sciences Foundation grant no. 200021\_165851.

91

92

93

94 **1.5. THESIS OUTLINE**

95 The thesis covers contributions on the magnetic properties of synthetic crystals of greigite and magnetite  
96 that were obtained from electron spin resonance (ESR) spectroscopy and magnetic methods. The results  
97 were then compared to sediments from natural systems. The thesis can be divided in two main parts:  
98 studies on greigite and studies on magnetite.

99

100 **Part I – Greigite with nanotexture**

101 In **Chapter 3**, I describe the magnetic and spectroscopic properties of synthetic greigite ( $\text{Fe}_3\text{S}_4$ )  
102 aggregates that consist of nanocrystallites, with focus on its low temperature properties. Here, I present  
103 the data from X-ray diffraction, electron microscopy, rock magnetic methods, and ferromagnetic  
104 resonance spectroscopy (FMR).

105

106 **Chapter 4** presents the magnetic and spectroscopic properties of a natural greigite in sediments that  
107 were taken from the tailing pond of a former uranium-mine pond in Canada. The flakes are intergrown  
108 together. Electron microscopy, chemical analysis, rock methods and ESR spectroscopy are used to  
109 analyze the iron minerals in the sediments. Based on the results, I use this information to evaluate the  
110 influence of anthropogenic activity on the formation and preservation of the iron-bearing minerals.

111

112 **Part II – Magnetite in Magnetotactic Bacteria**

113 **Chapter 5** describes the spectroscopic response of the lab-cultured MTB during heat treatment; since  
114 heating serves as a proxy for diagenetic decomposition of the organic matter in the sediments.  
115 Hysteresis loops, first-order reversal curve (FORC) diagrams and FMR spectroscopy are used to  
116 evaluate the changes in magnetic and spectroscopic properties.

117

118 **Chapter 6** is joint work between different working groups that examines the preservation of MTB in  
119 lake sediments, and evaluates the use of magnetic and spectroscopic properties as a geochemical proxy.  
120 Here, I was responsible for the analysis and characterization of the magnetic and spectroscopic data,  
121 with particular emphasis on simulation of the FMR spectra.

122

123 **Chapter 7** uses the results that were obtained in Chapter 5 to identify the presence of MTB that may  
124 be associated with an oceanographic upwelling system. I used rock magnetic methods, ESR  
125 spectroscopy and fluorescence X-ray diffraction in order to characterize the iron minerals in the  
126 sediments offshore the Namibian coast, and their relationship to upwelling system, with special focus  
127 on MTB.

128

129 The final chapter, **Chapter 8** presents a short summary of the main findings in this thesis. In addition,  
130 I present ideas for future research that should be done to answer question that arose from the work that  
131 is presented.

132

### 133 **1.6. AUTHOR CONTRIBUTIONS**

134 Andreas U. Gehring organized the grant and initiated the study. Throughout the studies  
135 Andreas U. Gehring, Michalis Charilaou, and Ann Hirt contributed to the study with their ideas and  
136 supported the analysis and writing process.

137

138 **Chapter 3** „*Low-temperature and angular dependence FMR studies of greigite ( $Fe_3S_4$ ) aggregates*”

139 Jordan M. Rhodes and Janet E. Macdonald from Vanderbilt University (Nashville, USA) synthesized  
140 the sample and performed TEM measurements. Jordan M. Rhodes, Janet E. Macdonald, and Peter  
141 Weidler from Karlsruhe Institute of Technology (Karlsruhe, Germany) performed XRD analysis.

142 Dimitrios Koulialias from ETH Zurich (Zurich, Switzerland) performed part of the low-temperature  
143 PPMS measurements.

144

145 **Chapter 4** „*Greigite as a magnetic carrier in sediments from Lower Williams Lake, Canada*”

146 Kazuhito Mizutani and Susan Glasauer from University of Guelph (Guelph, Canada) collected the  
147 samples, and provided the SEM Fig. 6g, and elemental analysis. These data are part of the master  
148 thesis of Kazuhito Mizutani (Mizutani, 2019). The SEM Fig. 6a-f pictures were taken at the  
149 Scientific Center for Optical and Electron Microscopy, ETH Zurich (Zurich, Switzerland) by Dr.  
150 Luiz Grafulha Morales and Dr. Karsten Kunze. Dimitrios Koulialias from ETH Zurich (Zurich,  
151 Switzerland) performed part of the low-temperature PPMS measurements.

152

153 **Chapter 5** „*From Magnetotactic Bacteria to Magnetofossils: an experimental approach*”

154 The samples were cultured by members of the under Dirk Schüler from University of Bayreuth  
155 (Bayreuth, Germany).

156

157 **Chapter 6** „*Ferromagnetic resonance of magnetite biominerals traces redox changes*”

158 The samples were collected by Thomas M. Blattmann from ETH Zurich (Zurich, Switzerland), and  
159 Martin Wessels from Baden-Württemberg State Institute for the Environment, Survey and Nature  
160 Conservation (Langenargen, Germany). Thomas M. Blattmann, performed geochemical analysis.  
161 Inés García-Rubio from ETH Zurich (Zurich, Switzerland), and Centro Universitario de la Defensa  
162 (Zaragoza, Spain) performed spectroscopic measurements. Dimitrios Koulialias from ETH Zurich  
163 (Zurich, Switzerland) measured magnetic susceptibility. Ann Hirt from ETH Zurich (Zurich,  
164 Switzerland) measured hysteresis and FORC. Thomas M. Blattmann analyzed the non-magnetic  
165 data. Barbara Lesniak analyzed and characterized the magnetic and spectroscopic data, including  
166 simulation of the FMR spectra. All authors contributed to discussion and writing.

167

168 **Chapter 7** „Magnetic carriers in sediments offshore the Namibian coast and their relation to  
169 upwelling”

170 The samples were collected under the Regional Research Graduate Network in Oceanography  
171 (RGNO) 2017. Northern samples were collected by Anastasiia Ignatova from ETH Zurich (Zurich,  
172 Switzerland), and southern by Barbara Leśniak, under supervision of Daniel Montluçon.

173

## 174 1.7. REFERENCES

- 175 Ateia, M., Koch, C., Jelavić, S., Hirt, A., Quinson, J., Yoshimura, C., Johnson, M., 2017. Green and  
176 facile approach for enhancing the inherent magnetic properties of carbon nanotubes for water  
177 treatment applications. *PloS one* 12, e0180636, doi:10.1371/journal.pone.0180636
- 178 Baumgartner, J., Bertinetti, L., Widdrat, M., Hirt, A.M., Faivre, D., 2013. Formation of magnetite  
179 nanoparticles at low temperature: from superparamagnetic to stable single domain particles. *PloS*  
180 *one* 8, e57070
- 181 Bazylinski, D.A., Frankel, R.B., Heywood, B.R., Mann, S., King, J.W., Donaghay, P.L., Hanson, A.K.,  
182 1995. Controlled Biomineralization of Magnetite (Fe (inf3) O (inf4)) and Greigite (Fe (inf3) S  
183 (inf4)) in a Magnetotactic Bacterium. *Appl. Environ. Microbiol.* 61, 3232-3239,  
184 doi:10.1128/AEM.61.9.3232-3239.1995
- 185 Bazylinski, D.A., Garratt-Reed, A.J., Frankel, R.B., 1994. Electron microscopic studies of  
186 magnetosomes in magnetotactic bacteria. *Microscopy research and technique* 27, 389-401,  
187 doi:10.1002/jemt.1070270505
- 188 Berner, R.A., 1984. Sedimentary pyrite formation: an update. *Geochimica et Cosmochimica Acta* 48,  
189 605-615
- 190 Blakemore, R.P., 1982. Magnetotactic bacteria. *Annual Reviews in Microbiology* 36, 217-238,  
191 doi:10.1146/annurev.mi.36.100182.001245
- 192 Butler, R.F., Banerjee, S.K., 1975. Theoretical single-domain grain size range in magnetite and  
193 titanomagnetite. *Journal of Geophysical Research* 80, 4049-4058
- 194 Chang, L., Rainford, B.D., Stewart, J.R., Ritter, C., Roberts, A.P., Tang, Y., Chen, Q., 2009a. Magnetic  
195 structure of greigite (Fe<sub>3</sub>S<sub>4</sub>) probed by neutron powder diffraction and polarized neutron  
196 diffraction. *Journal of Geophysical Research: Solid Earth* 114
- 197 Chang, L., Roberts, A.P., Rowan, C.J., Tang, Y., Pruner, P., Chen, Q., Horng, C.S., 2009b. Low-  
198 temperature magnetic properties of greigite (Fe<sub>3</sub>S<sub>4</sub>). *Geochemistry, Geophysics, Geosystems* 10
- 199 Chang, L., Roberts, A.P., Tang, Y., Rainford, B.D., Muxworthy, A.R., Chen, Q., 2008. Fundamental  
200 magnetic parameters from pure synthetic greigite (Fe<sub>3</sub>S<sub>4</sub>). *Journal of Geophysical Research:*  
201 *Solid Earth* 113
- 202 Deatsch, A.E., Evans, B.A., 2014. Heating efficiency in magnetic nanoparticle hyperthermia. *Journal*  
203 *of magnetism and magnetic materials* 354, 163-172
- 204 Dekkers, M.J., Passier, H.F., Schoonen, M.A., 2000. Magnetic properties of hydrothermally  
205 synthesized greigite (Fe<sub>3</sub>S<sub>4</sub>)—II. High- and low-temperature characteristics. *Geophysical*  
206 *Journal International* 141, 809-819
- 207 Devouard, B., Posfai, M., Hua, X., Bazylinski, D.A., Frankel, R.B., Buseck, P.R., 1998. Magnetite from  
208 magnetotactic bacteria: Size distributions and twinning. *American Mineralogist* 83, 1387-1398
- 209 Dunlop, D.J., Özdemir, Ö., 1997. *Rock Magnetism: Fundamentals and Frontiers*. Cambridge University  
210 Press, Cambridge.
- 211 Egli, R., Chen, A.P., Winklhofer, M., Kodama, K.P., Horng, C.S., 2010. Detection of noninteracting  
212 single domain particles using first-order reversal curve diagrams. *Geochemistry, Geophysics,*  
213 *Geosystems* 11, n/a-n/aQ01Z11, doi:10.1029/2009gc002916

- 214 Faivre, D., Menguy, N., Pósfai, M.I., Schüler, D., 2008. Environmental parameters affect the physical  
215 properties of fast-growing magnetosomes. *American Mineralogist* 93, 463-469
- 216 Faivre, D., Schuler, D., 2008. Magnetotactic bacteria and magnetosomes. *Chemical Reviews* 108, 4875-  
217 4898, doi:10.1021/cr078258w
- 218 Frey, N.A., Sun, S., 2010. Magnetic nanoparticle for information storage applications. *Inorganic*  
219 *Nanoparticles: Synthesis, Application, and Perspective*, 33-68
- 220 Gehring, A.U., Kind, J., Charilaou, M., García-Rubio, I., 2011. The detection of magnetotactic bacteria  
221 and magnetofossils by means of magnetic anisotropy. *Earth and Planetary Science Letters* 309,  
222 113-117
- 223 Gupta, A.K., Gupta, M., 2005. Synthesis and surface engineering of iron oxide nanoparticles for  
224 biomedical applications. *biomaterials* 26, 3995-4021, doi:10.1016/j.biomaterials.2004.10.012
- 225 Hesse, P.P., 1994. Evidence for bacterial palaeoecological origin of mineral magnetic cycles in oxic  
226 and sub-oxic Tasman Sea sediments. *Marine Geology* 117, 1-17
- 227 Jiang, W.-T., Horng, C.-S., Roberts, A.P., Peacor, D.R., 2001. Contradictory magnetic polarities in  
228 sediments and variable timing of neoformation of authigenic greigite. *Earth and Planetary*  
229 *Science Letters* 193, 1-12
- 230 Kirschvink, J.L., Chang, S.-B.R., 1984. Ultrafine-grained magnetite in deep-sea sediments: Possible  
231 bacterial magnetofossils. *Geology* 12, 559-562
- 232 Kobayashi, A., Kirschvink, J.L., Nash, C.Z., Kopp, R.E., Sauer, D.A., Bertani, L.E., Voorhout, W.F.,  
233 Taguchi, T., 2006. Experimental observation of magnetosome chain collapse in magnetotactic  
234 bacteria: Sedimentological, paleomagnetic, and evolutionary implications. *Earth and Planetary*  
235 *Science Letters* 245, 538-550
- 236 Kopp, R.E., Kirschvink, J.L., 2008. The identification and biogeochemical interpretation of fossil  
237 magnetotactic bacteria. *Earth-Science Reviews* 86, 42-61
- 238 Momma, K., Izumi, F., 2008. VESTA: a three-dimensional visualization system for electronic and  
239 structural analysis. *Journal of Applied Crystallography* 41, 653-658
- 240 Moskowitz, B.M., Frankel, R.B., Bazylinski, D.A., 1993. Rock magnetic criteria for the detection of  
241 biogenic magnetite. *Earth and Planetary Science Letters* 120, 283-300
- 242 Muxworthy, A., McClelland, E., 2000. Review of the low-temperature magnetic properties of magnetite  
243 from a rock magnetic perspective. *Geophysical Journal International* 140, 101-114
- 244 Özdemir, Ö., Dunlop, D.J., 1999. Low-temperature properties of a single crystal of magnetite oriented  
245 along principal magnetic axes. *Earth and Planetary Science Letters* 165, 229-239
- 246 Pan, Y., Petersen, N., Winklhofer, M., Davila, A.F., Liu, Q., Frederichs, T., Hanzlik, M., Zhu, R., 2005.  
247 Rock magnetic properties of uncultured magnetotactic bacteria. *Earth and Planetary Science*  
248 *Letters* 237, 311-325
- 249 Roberts, A.P., Chang, L., Rowan, C.J., Horng, C.S., Florindo, F., 2011. Magnetic properties of  
250 sedimentary greigite (Fe<sub>3</sub>S<sub>4</sub>): An update. *Reviews of Geophysics* 49
- 251 Rowan, C.J., Roberts, A.P., Broadbent, T., 2009. Reductive diagenesis, magnetite dissolution, greigite  
252 growth and paleomagnetic smoothing in marine sediments: A new view. *Earth and Planetary*  
253 *Science Letters* 277, 223-235
- 254 Schüler, D., Frankel, R.B., 1999. Bacterial magnetosomes: microbiology, biomineralization and  
255 biotechnological applications. *Applied Microbiology and Biotechnology* 52, 464-473,  
256 doi:10.1007/s002530051547
- 257 Sheikholeslami, M., 2017. Numerical simulation of magnetic nanofluid natural convection in porous  
258 media. *Physics Letters A* 381, 494-503
- 259 Skinner, B.J., Erd, R.C., Grimaldi, F.S., 1964. Greigite, the thio-spinel of iron; a new mineral. *American*  
260 *Mineralogist: Journal of Earth and Planetary Materials* 49, 543-555
- 261 Snowball, I., Thompson, R., 1988. The occurrence of greigite in sediments from Loch Lomond. *Journal*  
262 *of Quaternary Science* 3, 121-125
- 263 Tang, S.C., Lo, I.M., 2013. Magnetic nanoparticles: essential factors for sustainable environmental  
264 applications. *Water research* 47, 2613-2632, doi:10.1016/j.watres.2013.02.039
- 265 Verwey, E., 1939. Electronic conduction of magnetite (Fe<sub>3</sub>O<sub>4</sub>) and its transition point at low  
266 temperatures. *Nature* 144, 327-328
- 267 Yan, L., Zhang, S., Chen, P., Liu, H., Yin, H., Li, H., 2012. Magnetotactic bacteria, magnetosomes and  
268 their application. *Microbiological research* 167, 507-519





## 2. Theoretical Background and Methods

### 2.1. FUNDAMENTAL CONCEPTS OF MAGNETISM

This chapter provides a theoretical overview of the fundamentals of magnetism and experimental methods that have been employed in the studies making up this thesis.

#### 2.1.1. Definitions and units

Magnetism is a physical phenomenon which originates from the elementary particles. Macroscopically a magnetic moment ( $\mu$ ) can be described by a vector perpendicular to surface, which is created by an electric current loop (Eq.2.1, Fig. 2.1)

$$\mu = SI = \pi R^2 I, \quad (2.1)$$

where  $S$  is the surface area closed by electric current loop,  $I$  is an electric current strength (in Amperes) (Fig. 2.1a).



Fig. 2.1 a) Magnetic moment of electric current loop, and b) graphic representation of volume  $V$  containing magnetic moments.

Magnetisation is the density of magnetic moment:

$$\underline{M} = \sum \mu_i / V, \quad (2.2)$$

where  $V$  is the volume containing the moments  $\mu_i$  ( $\text{Am}^2$ ). For a single atom there are three sources of magnetization: spin magnetic moment, orbital magnetic moment and nuclear magnetic moment.

18 **Spin magnetic moment** ( $\mu_S$ ) –arises from the spin of an electron. According to the Fermi-Dirac  
 19 statistics, electrons are fermions, which means that electrons are quantized and have a spin quantum  
 20 number ( $m_s$ ) =  $\pm 1/2$ . The spin magnetic moment can only be determined with respect to a specific  
 21 direction and is antiparallel to the reference direction:

$$22 \quad \mu_S = -2m_s \frac{e\hbar}{2m_e} = -2m_s \mu_B = \pm \mu_B, \quad (2.3)$$

23 where  $e$  is the elementary charge of an electron ( $1.60 \times 10^{-19}$  C),  $\hbar$  is the reduced Plank's constant  
 24 ( $\hbar/2\pi = 1.055 \times 10^{-34}$  J s), and  $m_e$  is an electron's elementary mass ( $9.11 \times 10^{-31}$  kg). The spin moment  
 25 is the fundamental unit of magnetic moment, and is known as the Bohr magneton ( $\mu_B$ ), which has a  
 26 value  $9.27 \times 10^{-24}$  Am<sup>2</sup>.

27 **Orbital magnetic moment** ( $\mu_L$ ) – arises from the motion of the electron about the nucleus of an atom,  
 28 where in a Bohr atomic model the orbit is circular. The orbital magnetic moment can also only be  
 29 described relative to a specific direction, and is antiparallel to this reference direction:

$$30 \quad \mu_L = -m_L \frac{e\hbar}{2m_e} = -m_L \mu_B, \quad (2.4)$$

31 where  $m_L$  is the magnetic quantum number, and can take on an integer value of  $0, \pm 1, \dots, \pm l$ , where  $l$   
 32 is orbital quantum number. Equation 2.2 and 2.3 can be written in a more general form:

$$33 \quad \mu_S = -g_s m_s \mu_B, \quad \mu_L = -g_L m_L \mu_B \quad (2.5)$$

34 where  $g$ , is known as Landé's  $g$ -factor or the spectroscopic splitting factor, and can take on the value  
 35  $g_L = 1$  for orbital motion and  $g_s = 2$  for spin motion.

36 **Nuclear magnetic moment** - some atomic nuclei can have a spin  $I$ , which leads to existence of a nuclear  
 37 magnetic moment. The nuclear magnetic moment is very small, around 2000 times smaller than typical  
 38 magnetic moments (Szewczyk et al., 2017).

$$39 \quad \mu_N = g_N \mu_B I, \quad (2.6)$$

40 where  $\mu_N$  is a nuclear magnetic moment,  $g_N$  is a nuclear  $g$ -factor,  $I$  is the spin of an atomic nucleus.

41 The orbital and spin magnetic moments will generate a magnetic field, which is called the magnetic  
42 flux density  $B$  (T). However, when  $B$  passes through a magnetic material, it will be affected by the  
43 internal magnetic fields of the magnetic body. In this case the magnetic field within the body is referred  
44 as the  $H$ -field,  $H$  (A/m). The relation between magnetic flux density and magnetic field can be described  
45 by equation:

$$46 \qquad \qquad \qquad B = \mu_0(H + M), \qquad \qquad \qquad (2.7)$$

47 where  $\mu_0$  is the permeability in a vacuum, and  $M$  (A/m) is magnetisation.

48 The magnetic response of a material can be described also by magnetic susceptibility ( $\chi$ ), which  
49 measures the ease in which a material will become magnetised in an applied magnetic field:

$$50 \qquad \qquad \qquad M = \chi \cdot H, \qquad \qquad \qquad (2.8)$$

51 Magnetic susceptibility is dimensionless because  $M$  and  $H$  have the same units.

52

### 53 **2.1.2. Classification of magnetic materials**

54 Susceptibility is a physical property of any material and is used to distinguish types of magnetization.

55 There are three types of magnetic behaviour: diamagnetic, paramagnetic and ferromagnetic and a brief  
56 description is given below.

57

#### 58 *2.1.2.1. Diamagnetism*

59 Diamagnetism (DIA) is characteristic for all materials, because it arises from the orbit of electrons.

60 Although, often it may be overwhelmed by stronger type of magnetism, such as paramagnetism, which  
61 may be of hundreds times stronger, or ferromagnetism, which may be of hundred thousands times  
62 stronger, there are materials in which electron spins are coupled so that the total spin magnetic moment  
63 is zero, and their magnetism arises only from an orbital moment (Evans and Heller, 2003) (Fig. 2.2).

64 Langevin's theory of diamagnetism is based on the orbital motion of the electron, known as Larmor  
65 precession, and how this motion is influenced by the change of magnetic field. According to the

66 classical theory of diamagnetism, diamagnetic susceptibility ( $\chi_{dia}$ ) is small, negative, reversible and  
 67 temperature independent.

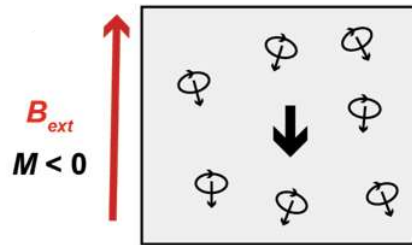


Fig. 2.2 Schematic diagram for a diamagnetic material showing the alignment of net magnetic moments in an applied magnetic field.

### 68 2.1.2.2 Paramagnetism

69 Paramagnetism originates from non-interacting, unpaired electron spins. Although atoms always  
 70 possess a non-zero magnetic moment, in the absence of an external field there is no net magnetic  
 71 moment, because the moments are randomised (Fig. 2.3a). When an external magnetic field is applied,  
 72 the unpaired electrons in the atom align statistically with the external magnetic field, which results an  
 73 induced magnetisation (Fig. 2.3b). Its magnetization disappears when the field is removed. Thermal  
 74 energy prevents the perfect alignment of the magnetic moments in the field, but with decreasing  
 75 temperature thermal energy decreases which leads to an increase in the magnetization. Paramagnetic  
 76 susceptibility ( $\chi_p$ ) is small, positive and reversible. The Curie law describes the magnetic susceptibility  
 77 ( $\chi_p$ ) of a paramagnet in a magnetic field:

$$78 \quad \chi_p = \frac{C}{T-\theta}, \quad (2.9)$$

79 where  $C$  is a Curie constant,  $T$  is temperature, and  $\theta$  is the paramagnetic Curie temperature, i.e., the  
 80 temperature under which the magnetic moments become blocked. For many minerals  $\theta$  is close to 0 K.

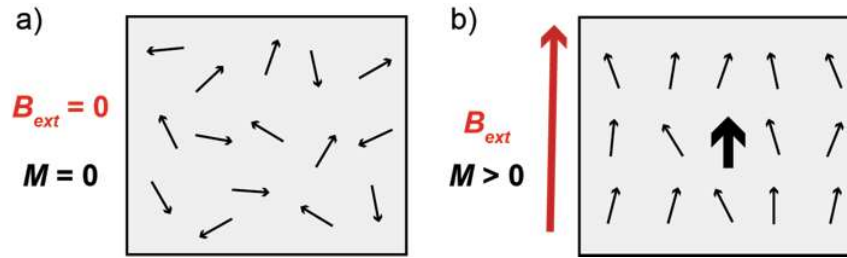


Fig. 2.3 Schematic diagram for a paramagnetic material showing the alignment of net magnetic moments with respect to the applied field; a) in absence of an external field, b) in an applied magnetic field.

### 81 2.1.2.3. Ferromagnetism (*s.l.*)

82 Ferromagnets are characterised by long-range order, magnetic interaction, which helps to keep magnetic  
 83 moments of all unpaired electron spins aligned even after the applied field is removed. This alignment  
 84 leads to a strong spontaneous magnetization below the ferromagnetic Curie temperature ( $T_C$ ). The  
 85 induced magnetization shows a field dependence that is described by a magnetic hysteresis (Fig. 2.4).

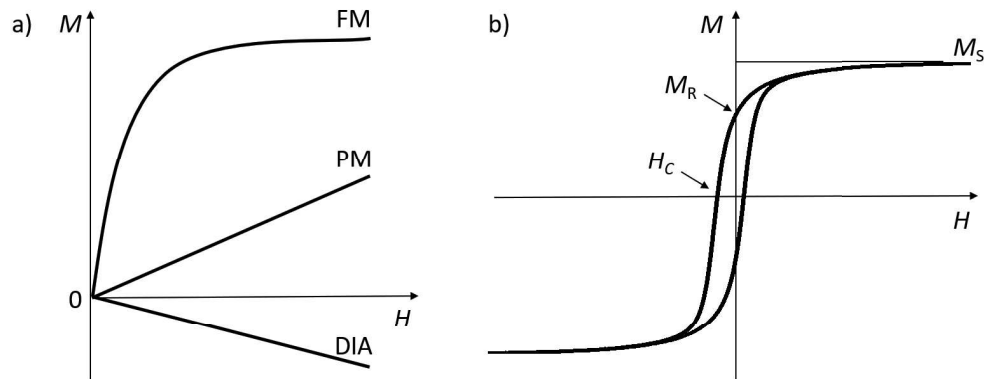


Fig. 2.4 a) Magnetization curves for the different magnetization types: ferromagnetic (FM), paramagnetic (PM), and diamagnetic (DIA). b)  $M(H)$  for a ferromagnetic material showing full hysteresis loop and hysteresis parameters.

86 In a strong magnetic field magnetic moments will be aligned, and this is known as the saturation  
 87 magnetization ( $M_S$ ). When the inducing field is reduced to zero the remaining magnetization ( $M_R$ ) is  
 88 known as the remanent magnetization or remanent saturation magnetization ( $M_{RS}$ ). The field needed to  
 89 bring the induced magnetization to zero is the coercivity or coercive force ( $H_C$ ).

90 There are four subclasses of ferromagnetism (*s.l.*): true ferromagnetism or ferromagnetism (*s.s.*),  
 91 antiferromagnetism, ferrimagnetism, and defect or canted antiferromagnetism (Fig. 2.5d).

92 In **true ferromagnetism (s.s.)** all magnetic moments align parallel to the applied field due to a direct  
 93 exchange of electrons between neighbouring atoms (Fig. 2.5a). Typical ferromagnets are native metals,  
 94 such as iron, nickel, cobalt. Above the Curie temperature ferromagnets behave paramagnetically, and  
 95 the susceptibility is described by the Curie-Weiss law:

$$96 \quad \chi = \frac{C}{T - \theta_{CW}}, \quad (2.10)$$

97 Where,  $\theta_{CW}$  is the Curie-Weiss temperature.

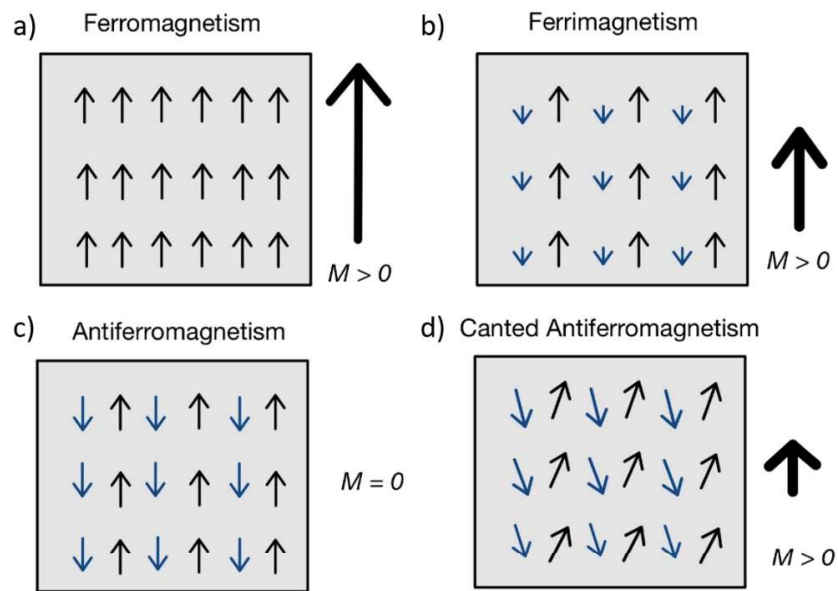


Fig. 2.5 Schematic diagram for a ferromagnetic material showing the alignment of net magnetic moments with respect to the applied field for a) ferromagnet, b) ferrimagnet, c) antiferromagnet and d) canted ferrimagnet.

98 In most ferromagnetic minerals there is not a direct exchange of electrons from the Fe atoms, the  
 99 exchange occurs over neighboring oxygen or sulfur atoms, and this is known as a super-exchange. The  
 100 spin of the iron atoms may be no longer parallel to each other but antiparallel, what leads to sublattices  
 101 with opposite spins moments. **Ferrimagnetism** cover materials in which the different sub-lattices have  
 102 different magnetic moment which leads to a net magnetization (Fig. 2.5b). The temperature dependence  
 103 of ferrimagnetic materials is similar to ferromagnetism (s.s.) and the susceptibility is described by  
 104 Eqn. 2.10. **Antiferromagnetism** covers materials, in which magnetic moments of the sublattices are  
 105 equal in strength, so that antiparallel net magnetization is zero (Fig. 2.5c). As with ferromagnetism

106 (s.s.), the long-range ordering of the moments is observed below a certain temperature, which is known  
 107 as the Neel temperature ( $T_N$ ). In some cases, however, a weak magnetization can arise from lattice  
 108 defects and vacancies or from atomic moments that are slightly canted from perfect antiparallelism  
 109 (spin canting) (Fig. 2.5d).

110

111 **Ferromagnetism and magnetic domains** – For very small ferromagnetic particles the magnetization  
 112 will be the same throughout the entire particle. If the grain exceeds a certain size, the energy that is  
 113 required to keep the magnetic moments of the atoms aligned becomes very large, and the grain forms  
 114 magnetic domains. These smaller areas within the particle have a spontaneous magnetization, but to  
 115 minimize energy, the direction of magnetization between the domains will vary, which results in zero  
 116 net magnetization.

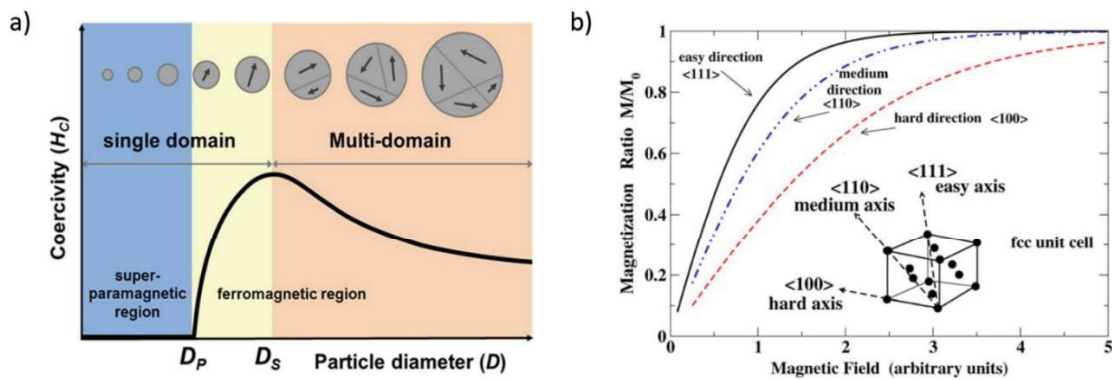


Fig. 2.6 a) Schematic diagram for a magnetic domain state as a function of particle size (after Lee et al. (Lee et al., 2015).

b) Induced magnetization for field along different crystallographic directions for magnetite, adapted from Mulheran (Mulheran, 2008).

117 The formation of a magnetic domain will be dependent on the particle size. The materials, which  
 118 separate into domains are called multi-domain (MD). Smaller particles, which have only one domain  
 119 are called single-domain (SD) (Fig. 2.6a). The state between SD and MD, which shows feature of both  
 120 of them are called pseudo-single domain (PSD) and are commonly characterized by spin vortex  
 121 structure (SV). For very small SD particles, the anisotropy energy that keeps the magnetic moment  
 122 aligned is smaller than the thermal energy. Although they show magnetic saturation, the relaxation time  
 123 of the remanent magnetization is very short. For this reason, they are called superparamagnetic (SP).

124 **Magnetic anisotropy** – magnetic anisotropy is the directional dependency of the magnetization with  
125 respect to the crystallographic structure of a particle or its shape. This means that it is easier to magnetize  
126 a material in some directions with respect to others, i.e., there are easy or hard axes of magnetization.

127 The most common types of magnetic anisotropy are:

- 128 • Magnetocrystalline anisotropy – is an intrinsic feature of a crystal and its caused by crystal-  
129 field effect (spin orbit coupling). An example of this is shown for magnetite in Fig. 2.6b.  
130 Magnetite is a cubic mineral, and its easy axis of magnetization is along the crystallographic  
131 [111] axis, whereas the hard axis of magnetization is along the [100] axis.
- 132 • Shape anisotropy - in materials with high spontaneous magnetization, the easy axis of  
133 magnetization will be related to the shape of the particle. This is because the  $H$ -field within the  
134 grain acts as a demagnetizing field ( $H_d$ ), thus reducing the induced magnetization.  $H_d$  will be  
135 smaller along the long axis of a particle, compared to the short axis. Therefore, the induced  
136 magnetization will be larger along the long axis compared to the short axis.

137

## 138 **2.2. EXPERIMENTAL METHODS**

139 In this paragraph a short description of the instrumentation used for the measurements in this  
140 dissertation is presented.

141

### 142 **2.2.1. Magnetic Methods**

#### 143 *2.2.1.1. Agico MKF 1A Susceptibility Bridge*

144 Magnetic susceptibility ( $\chi$ ) provides information about material's behavior in the magnetic field  
145 (diamagnetism, paramagnetism, ferromagnetism). For sediment samples, it can be used to evaluate the  
146 concentration of magnetic particles. When monitored as a function of temperature,  $\chi$  provides  
147 additional information such as Curie temperature, thermal stability and cations substitution in magnetite  
148 (Dunlop and Özdemir, 2001). The Kappabridge MFK-1 (Agico, Czech Republic) measures bulk  
149 magnetic susceptibility of the samples with a measurement accuracy of  $5 \times 10^{-8}$  (SI) (Pokorny et al.,



150 2011). The instrument is also equipped with a furnace unit, which allows the measurement of  
151 susceptibility at room temperature (Chapter 7). Magnetic susceptibility measurements were performed  
152 at the Laboratory of Natural Magnetism, ETH-Zurich.

153

#### 154 2.2.1.2. *MicroMag vibrating sample magnetometer (VSM)*

155 A Princeton Measurement Corporation (PCM), MicroMag VSM, model 3900, was used to measure  
156 magnetization as a function of magnetic field  $M(H)$ . Magnetization curves provide information on the  
157 dominant type of magnetization, i.e., dia-, para-, and/or ferromagnetism (*s.l.*) (Fig. 2.4a).  $M(H)$  reveals  
158 hysteresis properties, i.e., saturation magnetization ( $M_s$ ), remanence ( $M_R$ ) and coercivity ( $H_C$ , or  $B_C$   
159 when the units are given in terms of the field flux density) (Fig. 2.4b). In the case of ferromagnetic  
160 minerals, hysteresis properties are useful in identifying the composition and grain size. Magnetite with  
161 a particle size in the SD and PSD (or SV) size range will show an open hysteresis loop. SP and MD  
162 particles, however, will have  $M_R = 0$  and  $H_C = 0$ , whereas  $M_s \neq 0$ . The coercivity ( $H_C / H_{CR}$ ) and the  
163 ratio  $M_s / M_R$  can be used to determine the domain state of a material (SD and MD) and to estimate  
164 grain sizes (Dunlop, 2002). Note that  $H_{CR}$  is the remanent coercivity, or the field needed to remove  $M_R$ .  
165 This can be obtained by measuring back-field demagnetization on the PMC MicroMag VSM. A series  
166 of partial  $M(H)$  curves, known as First Order Reversal Curves (FORC) can also be measured on a VSM.  
167 The main information obtained from FORC curve is the coercivity distribution and information on  
168 interaction fields. This coercivity distribution provides insight into the grain size variations and particle  
169 assemblies in geological samples. The FORC data were processed with the FORCinel program of  
170 (Harrison and Feinberg, 2008).  $M(H)$  curves were measured at the Laboratory of Natural Magnetism,  
171 ETH-Zurich.

172

#### 173 2.2.1.3. *MPMS and PMPS (Quantum Design)*

174 The magnetic properties measurement system (MPMS3: XL) and physical properties measurement  
175 system (PPMS: 6000) from Quantum Design were used to measure magnetisation as a function of  
176 magnetic field and temperature. The MPMS measures magnetic moment in AC field, which allows one  
177 to obtain the in-phase and out-of-phase susceptibility as a function of field and temperature. The PPMS

178 measures magnetic moment in DC fields. The measurement sensitivity of both instruments is  $10^{-11}$  Am<sup>2</sup>.  
179 The MPMS was used for hysteresis measurements and measurement of magnetic moment as a function  
180 of temperature with/without applied magnetic field (Chapter 3, Chapter 4). The PPMS performed low-  
181 temperature hysteresis measurements (Chapter 3, Chapter 4). The MPMS measurements were made at  
182 the Laboratory of Solid State Physics, ETH Zurich. The PPMS measurements were made at the  
183 Laboratory of Metal Physics and Technology, ETH Zurich.

184

#### 185 *2.2.1.4. Electron Spin Resonance Spectroscopy (ESR)*

186 Electron spin resonance (ESR) spectroscopy includes electron paramagnetic resonance (EPR) and  
187 ferromagnetic resonance (FMR). In a ESR experiment, a sample is exposed to microwave radiation in  
188 a sweeping magnetic field, where the loss of microwave radiation i.e. absorption by the sample, is  
189 measured by a diode detector. During the measurement, an additional small AC magnetic field (usually  
190 1mT, 100kHz) is applied. The change of the diode voltage, induced by the AC field is measured by  
191 lock-in amplifier (Poole and Farach, 1999). Thus, the ESR spectrum is generally plotted as the first  
192 derivative of the microwave absorption as a function of the external field. In the following the basic  
193 principles of ESR are briefly described.

194

195 The Zeeman effect is the splitting of electron energy levels in an applied magnetic field. In an ESR  
196 experiment the sweeping magnetic field splits the energy levels (Fig.2.7). When a transverse microwave  
197 field is applied, unpaired electrons can absorb microwave energy. If the absorbed energy is equal to the  
198 energy gap then electrons from lower energy states pass to levels with higher energy. This absorption  
199 is visible in ESR spectra. The energy gap between levels is

$$200 \qquad \qquad \qquad \Delta E = g\mu_B H \qquad \qquad \qquad (2.11)$$

201 where  $g$  is the Landé spectroscopic splitting factor.

202

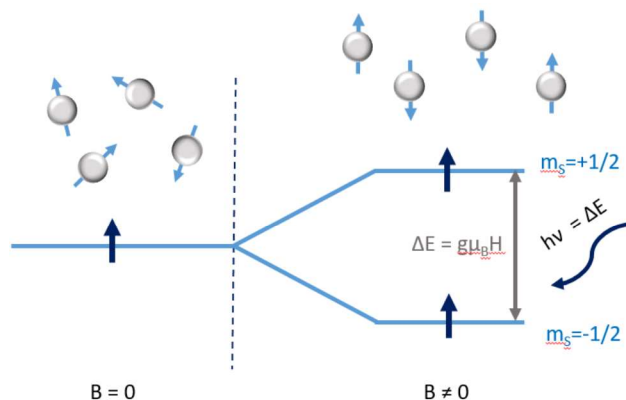


Fig. 2.7 Schematic sketch of the Zeeman Effect ( $B \neq 0$ ).  $\Delta E$  is an energy gap, and  $h\nu$  represents transverse energy, which may be absorbed by the electron from the lower energy state ( $m_s = -1/2$ ). When  $h\nu \geq \Delta E$  then the electron passes to the higher energy level ( $m_s = +1/2$ ).

203 Electron paramagnetic resonance (EPR) spectroscopy is used to detect chemical species with unpaired  
 204 spins (e.g. radicals, paramagnetic cations). Two cases can be considered in EPR. The first case is for  
 205 spin only, where the typical Zeeman splitting is observed for free electrons, such as radicals in organic  
 206 matter or defects in clay minerals, i.e. excess / deficit of electrons at a diamagnetic lattice (Fig. 2.8a)  
 207 (Perry, 1990). Absorption occurs as a narrow signal in the 1<sup>st</sup> derivative of intensity spectrum at  $g = 2$ .

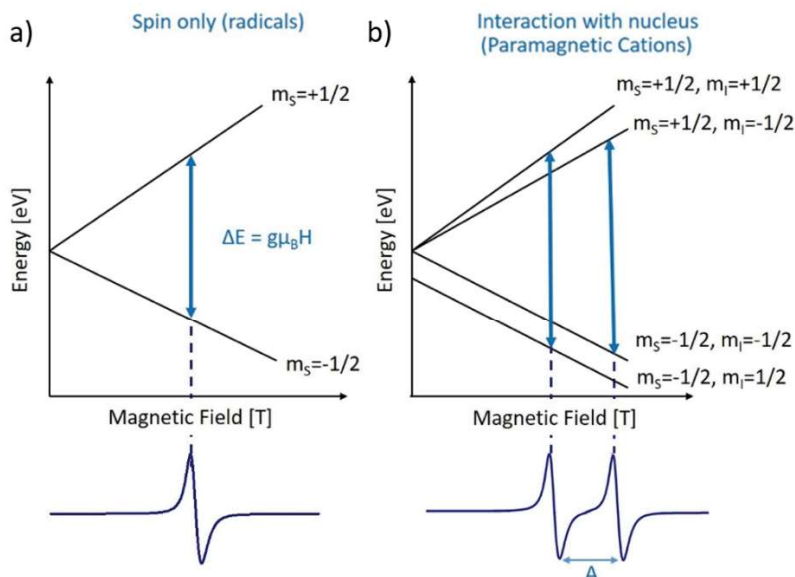


Fig. 2.8 Splitting of the energy level in the magnetic field for: a) the spin-only case, and b) interaction between magnetic moments of electron and nucleus with nuclear spin  $\mu_N = 1/2$  (e.g., Ti, Fe). The lower panel of both figures shows the EPR signal.

208 In the second case the electron magnetic moment  $\mu_e$  interacts with nuclear magnetic moment  $\mu_N$ , causing  
 209 separation of the energy levels, known as hyperfine splitting (Fig. 2.8b). This interaction generates  
 210 multiple spectral features and the distance between these denotes the hyperfine splitting constant ( $A$ ).  
 211 The number of the splitting lines is determined by the nucleus spin, e.g.,  $Mn^{2+}$  and  $^{55}Mn$  have a nuclear  
 212 magnetic moment of  $\mu_N = 5/2$  and the EPR spectrum consist of the sextet of lines centered at  $g = 2$ .  $A$   
 213 provides information about the chemical coordination of the paramagnetic species (Perry, 1990).

214

215 Ferromagnetic resonance (FMR) spectroscopy is used for minerals with magnetic moments that show  
 216 long-range ordering. For FMR the same spectrometer can be used as that used for EPR. The application  
 217 of an external magnetic field ( $H_{ext}$  or  $B_{ext}$ ) causes the magnetization ( $M$ ) to precess around the direction  
 218 of the effective field ( $H_{eff}$  or  $B_{eff}$ ), known as Larmor precession. The precession is damped over the time  
 219 and the total magnetic moment aligns with  $H_{ext}$ . The sample is irradiated with a transverse microwave  
 220 field (mw) with constant frequency (Fig.2.7a). If the microwave frequency coincides with the Larmor  
 221 frequency, the resonance condition is fulfilled and microwave absorption is observed. The resonance  
 222 condition is

$$223 \quad \omega = \gamma H_{eff}, \quad (2.12)$$

$$224 \quad \hbar\omega = g\mu_B H_{eff}, \quad (2.13)$$

225 where  $\omega$  is the Larmor frequency,  $\gamma$  is the gyromagnetic ratio,  $g$  is the Landé spectroscopic splitting  
 226 factor, and  $H_{eff}$  is the effective magnetic field in the sample, which consist of both external and internal  
 227 fields.

228

229 Examples of a FMR spectra are shown in Fig. 2.9 for a chain of MTB and for particles without chain-  
 230 arrangement. Two magnetic anisotropies need to be considered when analysing MTB: 1) the  
 231 magnetocrystalline anisotropy of magnetite ( $H_{cub}$ ), which is an internal feature of the mineral; and 2)  
 232 the uniaxial shape anisotropy ( $H_{uni}$ ) originating from the chain itself (Dunin-Borkowski et al., 1998).  
 233 The latter is often the factor that is indicative for the presence of chains of magnetofossils. The chain of  
 234 magnetic nanoparticles is characterized by two maxima (Fig. 2.9a), the low-field maximum originates

235 from chains aligned parallel to the magnetic field, and the high field maximum indicates chains  
 236 perpendicular to the magnetic field. Such a FMR signal can be decomposed into different contributions.  
 237 Note that the minimum is larger in magnitude than the maximum due to overlapping minima from  
 238 different contributions. In reality, FMR signals of samples containing MTB are often more complex,  
 239 because the chains' arrangement is randomly distributed. Fig. 2.9b shows a schematic sketch  
 240 representing clusters of magnetic nanoparticles, without uniaxial shape anisotropy. The signal is  
 241 characterized by a distinct maximum and minimum, which have this same magnitude (so-called  
 242 isotropic and/or symmetric signal).

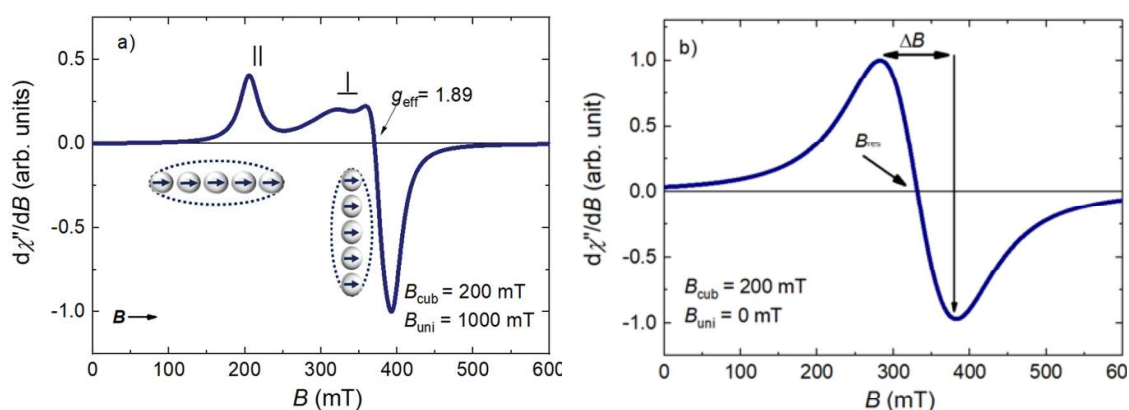


Fig. 2.9 Schematic sketch representing the FMR signal of a) chains of MTB characterised by high  $B_{uni}$ , and b) a cluster of particles, with random arrangement. Note on Fig. 2.9a the low-field peak represents a feature of the chains aligned parallel (||) to the magnetic field, whereas the second peak indicates chains aligned perpendicular ( $\perp$ ) to the field.

The accuracy of the X-band ESR spectrometer is dependent on the applied frequency and field. The accuracy of the frequency is  $10^{-8}$  Hz and an estimate of the field's accuracy is presented in Fig. 2.10, as determined measuring the offset in field for a sample at the center of the cavity center compared to a sample shifted of 5cm from the cavity center. The FMR measurements were performed at Electron Paramagnetic Resonance research group, Laboratory of Physical Chemistry ETH Zurich.

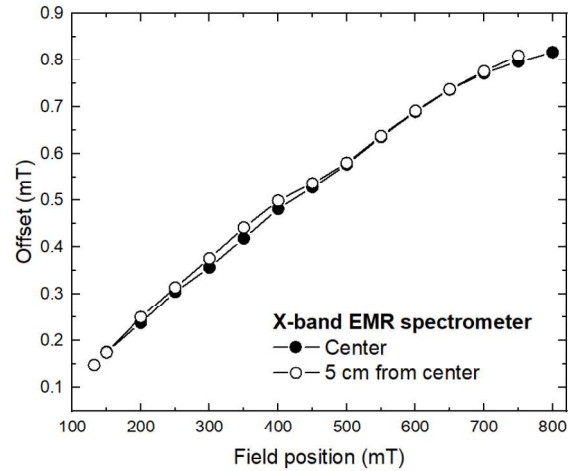


Fig. 2.10 The offset of the magnetic field measured at selected applied fields, defined by the program. Measurement by was made by Vidmantas Kalendra in October, 2014.

### 243 2.2.1.5. Numerical Analysis

244 The simulation of FMR signals is a major part in the analysis of the FMR spectra in this thesis. This  
 245 spectral analysis is based on the simulation program by Charilaou et al. (Charilaou et al., 2011). The  
 246 simulation program allows the theoretical calculation of the FMR spectra, which can be later compared  
 247 to the experimental results, and subsequently used for the extraction of the physical parameters. The  
 248 simulation process is based on three main steps, which are shortly described below. The full description  
 249 of the simulation program with all the relevant equations can be found in the Charilaou (Charilaou,  
 250 2017; Charilaou et al., 2011).

251

252 The first step is the calculation of the total energy density of the MTB chain. The main components are  
 253 specified below:

- 254 • Zeeman energy ( $F_z$ ), which represents the energy of a magnetized body influenced by an  
 255 external magnetic field ( $H_0$ ).
- 256 • Magnetocrystalline anisotropy energy ( $F_{\text{crist}}$ ), which arises from the spin-orbit lattice coupling.  
 257 Due to the interaction between orbital and the spin motion, the spins prefer to align along some  
 258 crystallographic direction (easy axis).
- 259 • Magnetostatic self-energy ( $F_{\text{self}}$ ), which originates from the elongation (shape) of the particles.

260 • Dipole-dipole interaction ( $F_{dip}$ ), which describes interaction between particles in the chain.

261 Considering all the above, the total energy density of a chain formed by  $n$  particles is:

$$262 \quad F = F(n) = F_{dip} + \sum_i^n (F_Z + F_{self} + F_{cryst}), \quad (2.14)$$

263 The second step is to calculate the resonance field ( $H_{res}$ ) for each field orientation. Previously obtained,  
264 the total energy density of the chain can be used to calculate the effective field ( $H_{eff}$ ) inside the material.

$$265 \quad \vec{H}_{eff} = \left(\frac{1}{4\pi}\right) \partial_{\vec{m}} F, \quad (2.15)$$

266 Using this effective field, we may calculate the Landau-Lifshitz-Gilbert (LLG) equation of motion,  
267 which describes the magnetization dynamics.

$$268 \quad \partial_t \vec{M} = -\gamma (\vec{M} \times \vec{H}_{eff}) + \frac{G}{(\gamma M^2)} (\vec{M} \times \partial_t \vec{M}), \quad (2.16)$$

269 where  $G$  is a Gilbert damping parameter,  $\gamma$  is the gyromagnetic ration, and  $\partial_t \vec{M}$  is the time derivative of  
270 the magnetization vector. The resonance equation can be obtained from the LGG equation, by  
271 calculating angle dependent  $H_{res}(\theta, \varphi)$  at the fixed frequency  $\omega$  using the resonance equation, which is:

$$272 \quad \frac{\omega}{\gamma} = H_{eff}, \quad (2.17)$$

273 The angular dependence of the ferromagnetic resonance frequency  $\omega$ , can be expressed in the form of  
274 second derivatives of the free energy.

$$275 \quad \left(\frac{\omega}{\gamma}\right)^2 = \frac{1}{M^2} \left[ \partial_{\theta\theta} F \left( \frac{\partial_{\varphi\varphi} F}{\sin^2 \theta} + \frac{\cos \theta}{\sin \theta} \partial_{\theta} F \right) - \left( \frac{\partial_{\theta\varphi} F}{\sin \theta} - \frac{\cos \theta}{\sin \theta} \frac{\partial_{\varphi} F}{\sin \theta} \right)^2 \right], \quad (2.18)$$

276 The free energy equations consider the magnetization described in the coordinate system. The solution  
277 of the resonance equation is found for each set of polar and azimuthal values, for  $|H_0| = H_{res}$ , where  
278  $H_0$  is the intensity of the external field.

279

280 When the resonance field is defined, one can calculate the FMR signal for a specific ensemble of MTB,  
281 which is the third step in the process. Here, the specific system parameters are taken into account, which  
282 are described using two anisotropy fields; the uniaxial field ( $H_{uni}$ ) and the cubic anisotropy fields ( $H_{cub}$ ).  
283  $H_{cub}$  is defined by the crystal symmetry.  $H_{uni}$  originates from the dipole-dipole interaction, which  
284 depends on the particle's elongation, number of the particles, distances between particles, and the  
285 strength of the interaction.

**2.2.2. Non-magnetic methods***2.2.2.1. Powder X-ray diffraction (XRD)*

X-ray Powder Diffraction (XRD) characterizes mineralogical composition of minerals in geological materials (cf., Chapter 3). XRD provides information about crystal structure and lattice constants, and to obtain detailed information about the atomic structure, an additional Rietveld analysis can be executed. One limitation of XRD is that about 2 wt.% concentration is needed for a phase to be detected.

292

*2.2.2.2. Electron Microscopy*

Electron Microscopy analysis provides information on: 1) the morphology of minerals and their surfaces, 2) particle shape and size, 3) coexistence of different phases and their arrangement, and 4) chemical composition of the mineral with elemental distribution through the scanned area. The concentration of ferromagnetic minerals in geological samples is often extremely low; therefore, subjecting the sample to magnetic extraction beforehand enhances the chance to image these particles. Scanning Electron Microscopy (SEM) and Transmission Electron Microscopy (TEM) operate in the different resolution ranges (Chapter 3, Chapter 4)

301

*2.2.2.3. Fluorescence X-ray (XRF)*

XRF allows the analysis of the major and trace elements in the rock/ sediment samples. It was used to analyse selected sediment samples from marine system (Chapter 7). The elements analysis was performed based on the elemental function as an environmental proxy obtained from Croudance and Rothwell (Croudace and Rothwell, 2015). The XRF analysis was performed at the Soil Chemistry Laboratory ETH Zurich.

308

309

310

311



312 **2.3. REFERENCES**

- 313 Charilaou, M., 2017. Ferromagnetic resonance of biogenic nanoparticle-chains. *Journal of Applied*  
314 *Physics* 122, 063903
- 315 Charilaou, M., Winklhofer, M., Gehring, A.U., 2011. Simulation of ferromagnetic resonance spectra of  
316 linear chains of magnetite nanocrystals. *Journal of Applied Physics* 109093903,  
317 doi:10.1063/1.3581103
- 318 Croudace, I.W., Rothwell, R.G., 2015. *Micro-XRF Studies of Sediment Cores: Applications of a non-*  
319 *destructive tool for the environmental sciences.* Springer.
- 320 Dunin-Borkowski, R.E., McCartney, M.R., Frankel, R.B., Bazylinski, D.A., Pósfai, M., Buseck, P.R.,  
321 1998. Magnetic microstructure of magnetotactic bacteria by electron holography. *Science* 282,  
322 1868-1870, doi:10.1126/science.282.5395.1868
- 323 Dunlop, D.J., 2002. Theory and application of the Day plot (Mrs/Ms versus Hcr/Hc) 1. Theoretical  
324 curves and tests using titanomagnetite data. *Journal of Geophysical Research: Solid Earth*  
325 1072056, doi:10.1029/2001jb000486
- 326 Dunlop, D.J., Özdemir, Ö., 2001. *Rock magnetism: fundamentals and frontiers.* Cambridge university  
327 press.
- 328 Evans, M., Heller, F., 2003. *Environmental magnetism: principles and applications of enviromagnetics.*  
329 Elsevier.
- 330 Harrison, R.J., Feinberg, J.M.F., 2008. An improved algorithm for calculating first-order reversal curve  
331 distributions using locally weighted regression smoothing. *Geochemistry, Geophys. Geosystems*  
332 9, n/a-n/aQ05016, doi:10.1029/2008GC001987
- 333 Lee, J.S., Cha, J.M., Yoon, H.Y., Lee, J.-K., Kim, Y.K., 2015. Magnetic multi-granule nanoclusters: A  
334 model system that exhibits universal size effect of magnetic coercivity. *Scientific reports* 5, 1-7
- 335 Mulheran, P., 2008. *Handbook of Metal Physics.*
- 336 Perry, D.L., 1990. *Instrumental surface analysis of geologic materials.* Wiley-VCH.
- 337 Pokorny, J., Pokorny, P., Suza, P., Hrouda, F., 2011. A multi-function kappabridge for high precision  
338 measurement of the ams and the variations of magnetic susceptibility with field, temperature and  
339 frequency.
- 340 Poole, C.P.J., Farach, H.A., 1999. *Handbook of Electron Spin Resonance.* Springer Science & Business  
341 Media.
- 342 Szewczyk, A., Szymczak, H., Puźniak, R., Wiśniewski, A., 2017. *Magnetyzm i nadprzewodnictwo.*  
343 *Wydawnictwo Naukowe PWN.*

344

345

346

347

348

349

350

351



### 3. Low-Temperature and Angular Dependence FMR Studies of

#### Greigite (Fe<sub>3</sub>S<sub>4</sub>) Aggregates

*Some of the presented data are published in Scientific Reports as “Polycrystalline texture causes magnetic instability in greigite” (B. Lesniak, D. Koulialias, M. Charilaou, P.G. Weidler, J. M. Rhodes, J. E. Macdonald & A.U. Gehring, 2021), (Lesniak et al., 2021).*

#### **Abstract**

Greigite is an iron sulphide that is found in sulfate-reducing environments and it has been shown to be a faithful recorder of the Earth’s magnetic field and an indicator for environmental conditions. It is often found in natural sediments in the form of aggregated crystals. In order to better understand its magnetic properties, we performed ferromagnetic resonance (FMR) spectroscopy at low temperature and as a function of angular position of aggregates of single domain crystals. These results are supported by room temperature X-ray diffraction (XRD), transmission electron microscope (TEM), and rock magnetic measurements. The XRD and TEM analysis demonstrate that the sample is a pure greigite and consists of aggregates of nanocrystallites that form larger flakes. The rock magnetic methods show interacting single-domain (SD) behaviour similar to what has been reported for other synthetic and natural samples of greigite. The spectroscopic studies demonstrate that there is a notable change in spectral properties below 50 K, which can arise from magnetostatic interactions and/or possible change in anisotropy energies. This behaviour has not been reported previously for greigite, and may be an intrinsic feature of greigite; alternatively, it may suggest that crystal morphology influences the magnetic properties of greigite.

#### **3.1. INTRODUCTION**

Greigite (Fe<sub>3</sub>S<sub>4</sub>) is an iron sulphide mineral that is commonly found in lacustrine and marine sediments (Rowan et al., 2009; Snowball and Thompson, 1988). It is of interest to the paleomagnetic community

27 because it has been shown to be a reliable recorder of the Earth's magnetic field (Jiang et al., 2001;  
28 Sagnotti et al., 2005; Sagnotti and Winkler, 1999). Its presence is also of interest in environmental  
29 studies, as it provides information about redox conditions. It is frequently formed as a precursor of  
30 pyrite in sulfate-reducing environments (Hunger and Benning, 2007), but has also been found in  
31 magnetotactic bacteria (Bazylinski et al., 1995).

32 Greigite has an inverse spinel structure with ferric iron in both tetrahedral and octahedral sites and  
33 ferrous iron in octahedral sites (Chang et al., 2009a); therefore it is a sulphur analogue to magnetite  
34 ( $\text{Fe}_3\text{O}_4$ ) (Skinner et al., 1964). It is characterised by co-linear ferrimagnetism with antiferromagnetic  
35 coupling between iron in octahedral and tetrahedral sites (Chang et al., 2009a). The saturation  
36 magnetisation,  $M_s$ , of greigite is  $59 \text{ Am}^2/\text{kg}$  for pure synthetic crystals (Chang et al., 2008); however  
37 this value is higher than previously reported in the literature due to mixtures with residual phases  
38 (Dekkers and Schoonen, 1996; He et al., 2006). In any case, it is lower than the  $M_s$  of magnetite ( $93.6$   
39  $\text{Am}^2/\text{kg}$ ), and this difference can be explained by the higher degree of covalence between iron and  
40 sulphur in comparison to iron and oxygen, or by increased delocalisation of the 3d electrons in greigite  
41 (Chang et al., 2009a). The other studies have shown that synthetic greigite is characterised most likely  
42 by easy axis of  $\langle 111 \rangle$ , similarly to magnetite (Li et al., 2014), and that the magnetocrystalline  
43 anisotropy constant is around two times larger than the one obtained for magnetite (Winklhofer et al.,  
44 2014).

45 A number of studies have reported on the magnetic behaviour of greigite since its discovery in Miocene  
46 lake sediments by Skinner et al. (1964, Giovanoli, 1979; Reynolds et al., 1994; Rowan and Roberts,  
47 2005; Sagnotti and Winkler, 1999; Skinner et al., 1964). A thorough review of the magnetic properties  
48 of greigite at room temperature and low temperature is provided in Roberts et al. (2011), in which the  
49 authors reviewed properties that were obtained from synthetic cubo-octahedral crystals and sedimentary  
50 greigite. Chang et al. (2012) carried out the first ferromagnetic resonance (FMR) experiments at room  
51 temperature on pure, crystalline, synthetic greigite with pseudo-single domain/multi-domain (PSD/MD)  
52 particle size (Chang et al., 2007), and aggregates of single domain (SD) greigite samples from Italy  
53 (van Dongen et al., 2007). The FMR spectra at X-band of the sample with good crystallinity, which was

54 measured in fields between 10 mT and 600 mT, have a single absorption line with  $\Delta B_{PP}$  in between 155  
55 mT and 173 mT, and high  $g_{\text{eff}}$  values between 2.9 and 3.1 ( $B_{\text{res}}$  between 214.4 mT to 227.8 mT), which  
56 was attributed to their MD size. Sedimentary greigite has a slightly more complicated absorption with  
57 a  $g_{\text{eff}}$  value of 2.02 ( $B_{\text{res}} = 332.4$  mT) and  $\Delta B_{PP}$  of 93 mT. At present, no low-temperature FMR studies  
58 have been performed on greigite. Such information could reveal potential changes in the anisotropy  
59 properties and/ or interactions with temperature.

60 In the present study, we report on FMR spectra of SD greigite at low temperature together with  
61 information from X-ray diffraction (XRD), transmission electron microscopy (TEM), and rock  
62 magnetic studies on aggregates of greigite. The sample consist of aggregates of greigite crystallites that  
63 form larger flakes on the scale of a few hundred nm. Often natural greigite is found in aggregates of  
64 crystallites (cf. Roberts et al., 2011), but flakes have also been reported by Snowball and Thompson  
65 (1988). Our results are compared with previous studies on synthetic greigite in order to gain insight into  
66 the influence of morphology and grain size on the magnetic properties of greigite aggregates.

67

### 68 **3.2. MATERIAL AND METHODS**

69 The greigite sample was synthesized through phase-controlled colloidal synthesis by the group at  
70 Vanderbilt University, by heating a mixture of organosulfur precursor dibenzyl disulphide and  $\text{FeCl}_2$ ,  
71 using the method described in Rhodes et al. (2017). The crystal structure and purity were controlled  
72 with transmission electron microscopy (TEM) and X-ray diffraction analysis (Rhodes et al., 2017).  
73 Additional XRD fits were used to define the lattice parameters, mean coherence length (MCL) and the  
74 stress/strain parameter  $\varepsilon_0 = \Delta d/d$ , where  $\Delta d$  is the mean deviation of the lattice spacing  $d$ . For the minor  
75 phase magnetite, lattice- and shape-parameters were fixed and adjusted to meet the observed data by P.  
76 Weidler from the Chemistry of Oxydic and Organic Interfaces Group, Karlsruhe Institute of  
77 Technology, Germany.

78

---

79 The room temperature magnetic characterization was made with a vibrating sample magnetometer  
80 (Princeton Measurement Corporation 3900 MicroMag). Magnetisation was measured as a function of  
81 field between  $\pm 1$  T with a variable sample interval: 0.5 mT steps between  $\pm 100$  mT, 2 mT steps from  $\pm$   
82 100 to  $\pm 200$  mT, and 5 mT steps for fields between  $\pm 200$  and 1000 mT with an averaging time of  
83 200 ms. In addition, first order reversal curves (FORC) were obtained, using 160 FORCs with a  
84 measurement interval of 1.87 mT and averaging time of 100 ms (Pike et al., 1999). The FORC  
85 measurements were processed using FORCinel 3.06 program (Harrison and Feinberg, 2008). The VSM  
86 measurements were performed at the Laboratory of Natural Magnetism, ETH Zurich. Magnetisation  
87 was also measured as a function of temperature between 300 K and 10 K using a SQUID magnetometer  
88 (Quantum Design MPMS XL) in sweeping mode at the Laboratory for Solid State Physics, ETH Zurich.  
89 The cooling/ warming rates were 5 K/min between room temperature to 50 K, and 0.25 K/min between  
90 50 K and 10 K. The induced magnetization was measured both in cooling from 300 K to 10 K and then  
91 rewarming back to 300 K in a series of fields 10 mT, 50 mT, 100 mT, and 1 T. In addition, the  
92 magnetization as a function of field was measured using a Physical Property Measurement System  
93 susceptometer (Quantum Design PPMS Model 6000) in sweeping mode at the Laboratory of Metal  
94 Physics and Technology, ETH Zurich. Hysteresis loops were obtained at 17 temperature steps between  
95 10 and 300 K, with measurement interval of 1 mT steps between  $\pm 150$  mT, and 10 mT steps for fields  
96 between  $\pm 150$  and 3000 mT with an averaging time of 1 s. Due to settlement problems in the  
97 susceptometer at temperatures below 90K, some measurement points were erroneous and thus excluded  
98 from the results. Fig. A1 elaborates the origin of the settlement problems.

99

100 Ferromagnetic resonance (FMR) spectroscopy was used to evaluate anisotropy properties of the sample.  
101 The magnetic parameters that are commonly extracted from these measurements include the g-factor  
102 ( $g_{\text{eff}}$ ), which measures the energy splitting of degenerate states in the magnetic field, the resonance field  
103 ( $B_{\text{res}}$ ), which is the field at the maximum absorption, and the line-width ( $\delta B$ ), which is a peak-to-peak  
104 linewidth of the resonance spectrum. The asymmetry of the spectra, or negative skewness of the  
105 absorption, can be defined by the parameter  $A$ , as defined by Weiss et al. (2004). The measured net

---

106 absorption signal is a superposition of all resonance events, i.e., the measured spectrum is the sum of  
107 the spectra originating from particles in all orientations. The absorption of microwave radiation is  
108 generally plotted as the first derivative spectrum of intensity. The X-band Bruker ElexSys E500  
109 spectrometer was used to record spectra in fields between 5 mT and 600 mT with frequencies at ~9.86  
110 GHz and ~9.39 GHz at the Electron Paramagnetic Resonance Group, Laboratory of Physical Chemistry  
111 ETH Zurich. The spectrometer is equipped with temperature controllers and a helium gas-flow cryostat  
112 from Oxford Instruments in order to record FMR spectra at variable temperatures. Furthermore, the  
113 FMR signal was monitored at different angles, using every 20° between 0° and 360° at room  
114 temperature and every 45° between 0° and 180° at 10 K. For this set of measurements, the absorption  
115 was at first measured between 0 – 650 mT and then returned to 0 mT with remeasuring of the subsequent  
116 absorption for a set angle. Between each measurement, the absorption was remeasured at the initial  
117 position of 0°.

118

### 119 **3.3. RESULTS**

#### 120 **Structural and Morphological properties**

121 XRD analysis indicates that the greigite sample is characterised by high-purity and is free of any  
122 secondary phases (Fig. 1a), which is confirmed by the Rietveld refinement of the XRD pattern (Rhodes  
123 et al., 2017). The sample has an inverse spinel structure with the space group of Fd-3m and the lattice  
124 constant of 9.8506 +/- 0.0015 Å, which is slightly lower than 9.872 Å found by Chang et al. (2007). Its  
125 mean coherence length (MCL) is 19 +/- 2nm and stress/strain parameter  $\epsilon_0 = 2 \times 10^{-5}$ . The TEM analysis  
126 of the sample reveals inhomogeneous, irregular flake-like morphologies in a relatively broad size range  
127 that is generally > 100 nm (Fig. 1b). Flakes tend to overlap to form aggregates. The bigger flakes seem  
128 to have uneven structure within the grains, creating chequered pattern.

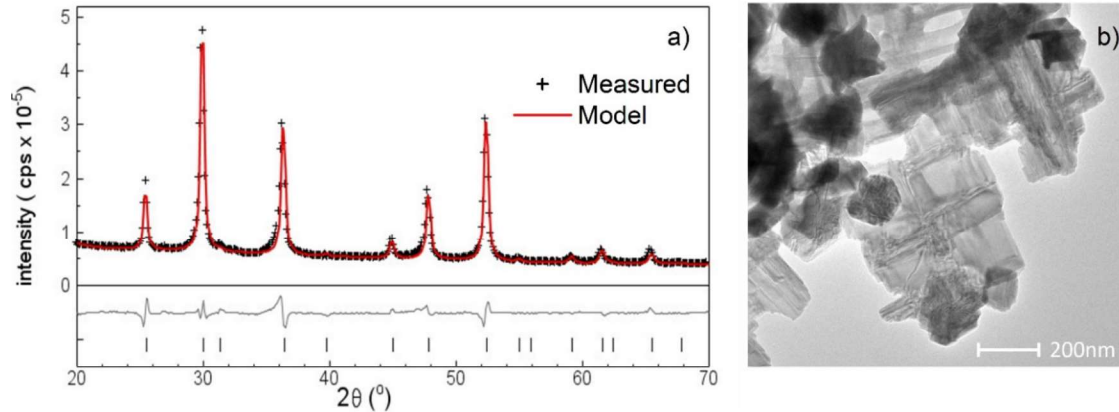


Fig.1. The a) X-ray diffraction pattern of the greigite's sample with measured data points (+), with model pattern for greigite (red line), and the b) TEM picture of the sample illustrating the flake-like morphology of the aggregates. The grey line below the diffractogram represents the difference between measurement and model. Data collected and analysed by P. Weidler from Karlsruhe Institute of Technology, Germany. Reproduced from Lesniak et al. (2021).

### 129 **Rock magnetic properties**

130 The rock magnetic properties at room temperature are defined from magnetic hysteresis and FORC  
 131 measurements. The magnetization approaches saturation in fields above 300 mT, but is not completely  
 132 saturated at 1 T, where  $M_{IT} = 32.70 \text{ Am}^2/\text{kg}$ . Remanent magnetization is  $M_R = 17.67 \text{ Am}^2/\text{kg}$  and  
 133 coercivity is  $B_c = 41.2 \text{ mT}$ , which gives  $M_R / M_{IT} = 0.54$  and  $B_{cr} / B_c = 1.33$  (Fig. 2). Both  $M_{IT}$  and  $B_c$   
 134 are less than the values reported for pure greigite by Chang et al. (2008). The ratios, however, are within  
 135 the range of the expected values for single-domain (SD) greigite (Roberts, 1995). Note that the high  
 136 magnetization ratio indicates that magnetocrystalline anisotropy is dominant.

137

138



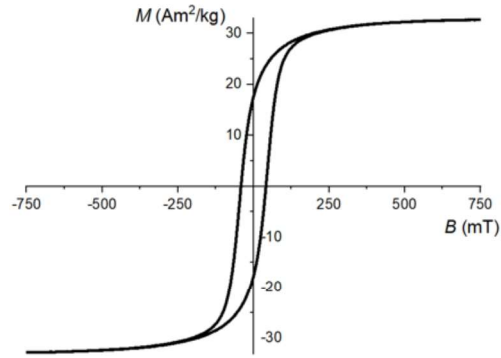


Fig.2 Room temperature hysteresis loop of the greigite's sample with  $M_{IT} = 32.70 \text{ Am}^2/\text{kg}$ ,  $M_R = 17.67 \text{ Am}^2/\text{kg}$ , and  $B_C = 41.2 \text{ mT}$ . Reproduced from Lesniak et al. (2021).

139 The FORC diagram has an oval density distribution with a large vertical spread that is offset towards  
 140 the negative interaction field, which is characteristic of interacting single domain (SD) particles of  
 141 greigite (Fig. 3a) (Roberts et al., 2014). The negative feature marked with a blue colour in the negative  
 142 interaction area of the diagram (around  $-30 B_u$ ) is an inherent manifestation of SD behaviour (Newell,  
 143 2005) and occurs in experimentally determined FORC diagrams. The horizontal coercivity distribution  
 144 of the coercivity presents clear Gaussian-like shape with maximum at around 49 mT (Fig. 3b). The  
 145 small feature visible in the FORC diagram and in the horizontal coercivity profile at around 0 mT is  
 146 within the noise level of the measurement.

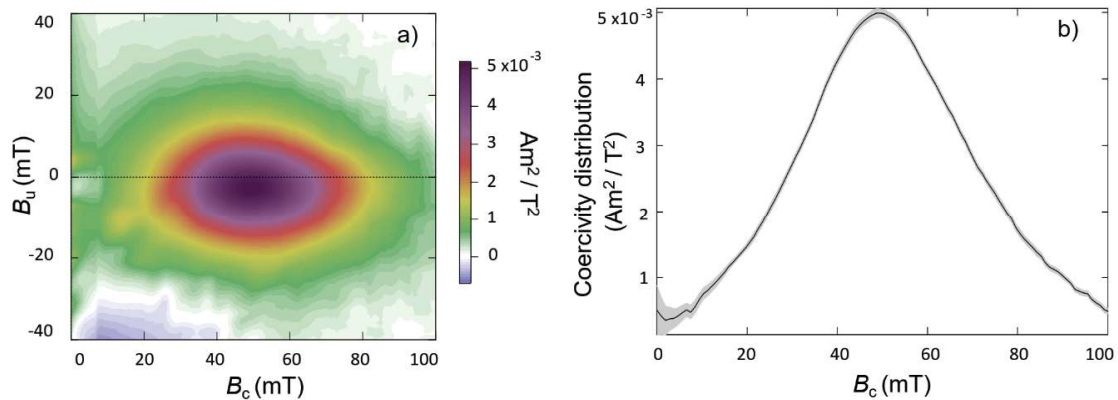


Fig.3 a) FORC diagram of the greigite's sample and b) horizontal coercivity profile. FORC is characterised by presence of interacting SD particles. The horizontal profile shows a broad- $B_C$  feature with the centre at around 49 mT, where the grey line is an error bar. Fig. 3a is reproduced from Lesniak et al. (2021).

147 **Low temperature hysteresis properties**

148 In addition to room temperature hysteresis properties, the low temperature hysteresis was measured  
 149 between 300 K and 10 K (Fig. 4). The magnetization was measured in fields up to 3 T, but is not  
 150 saturated in the highest field. A progressive increase in coercivity, saturation magnetisation and  
 151 remanent magnetisation at 3 T is observed with decreasing temperature (Fig. 4a, b).  $M_{3T}$  raises  
 152 continuously from 35.23 Am<sup>2</sup>/kg at room temperature to 38.05 Am<sup>2</sup>/kg at 15 K, which is an increase of  
 153 8 %. The remanent magnetisation increases from the RT value 17.79 Am<sup>2</sup>/kg to 20.39 Am<sup>2</sup>/kg at 30 K,  
 154 with a decrease to 19.93 Am<sup>2</sup>/kg at 15 K.  $M_r/M_{3T}$  ratio varies slightly upon cooling and remains > 0.5.  
 155 Coercivity shows the largest change, where it almost doubles from  $B_C = 41.58$  mT at RT to  $B_C = 73.29$   
 156 mT at 15 K (Fig. 4c). The monotonic steady increase in all three hysteresis parameters to 15 K does not  
 157 reveal the presence of a low temperature transition, similar to what has been previously reported (Chang  
 158 et al., 2009b; Dekkers et al., 2000).

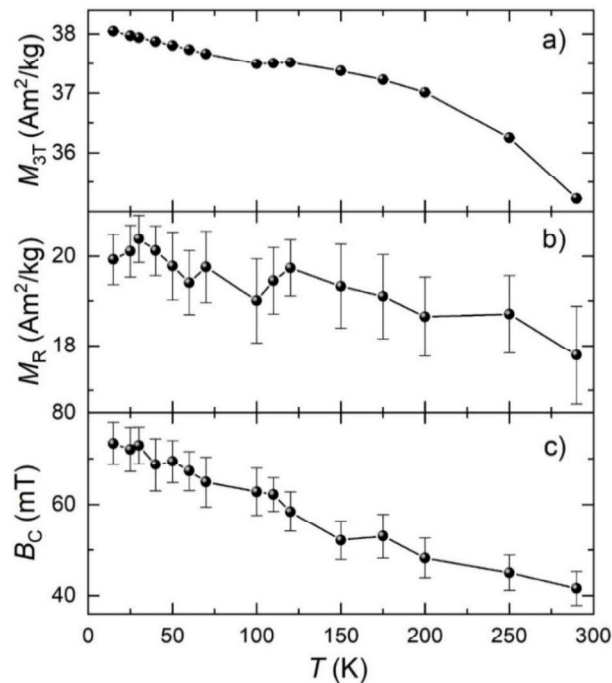


Fig.4 a) Magnetisation at 3T, b) remanent magnetisation, and c) coercivity as a function of temperature. The small variations in the values are minor in comparison to their magnitude. For saturation magnetisation ( $M_{3T}$ ) the error bars are within the size of the point.

**159 Induced magnetisation as a function of temperature**

160 The sample was subjected to the magnetic field of 10 mT, 100 mT, 500 mT and 1T in order to measure  
161 an induced magnetisation as a function of magnetic field (Fig. 5). The cooling and warming curves with  
162 the applied DC field of 10 mT display a low-temperature divergence between the curves. Cooling of  
163 the sample at 10 mT (Fig. 5a) reveals a slight decrease of the magnetisation down to 10 K. During  
164 warming, however, the sample acquires magnetisation continuously back to room temperature. The  
165 peak susceptibility in cooling is at 295 K. The same behaviour is observed for the sample when  
166 measured at 50 mT, with a shift in the maximum when cooling to 198 K (Fig. 5a inset). The sample  
167 was then cooled and rewarmed in a field of 100 mT, where the two curves diverge only at higher  
168 temperatures (Fig. 5b). Peak susceptibility while cooling is around 167 K followed by sharp drop of the  
169 susceptibility at higher temperature and a slower drop at lower temperature. With an applied field of  
170 500 mT the magnetization is close to saturation and the warming and cooling curves are identical with  
171 the peak susceptibility at 18 K (Fig. 5c).

172

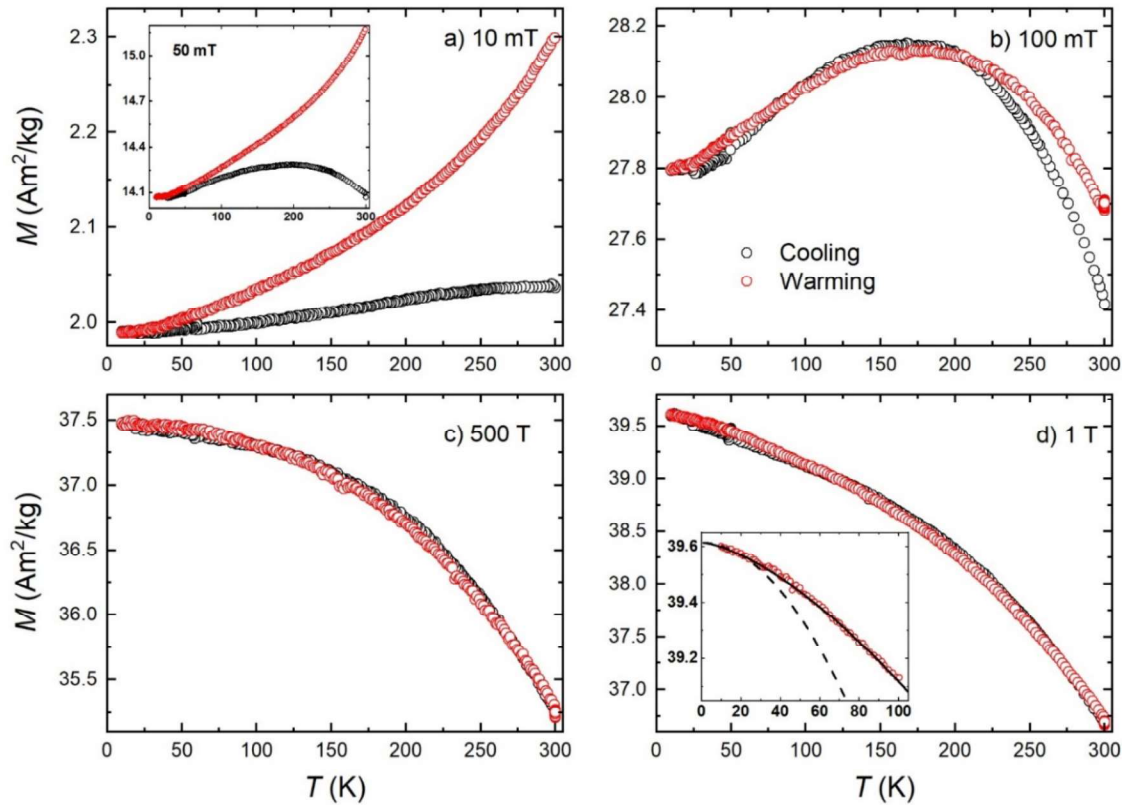


Fig.5 The magnetisation behaviour as a function of the temperature a) 10 mT, b) 100 mT, c) 500 mT, and d) 1 T, where (○) and (●) represent cooling and warming curve, respectively. Inset in Fig.5a represents the magnetisation behaviour in 50 mT. Inset in Fig. 5d shows low-temperature Bloch fit, with  $T_C > 1000$  K (solid line) and  $T_C = 650$  K (dashed line). Defined measurement error for all curves is close to zero. For cooling, the curve maxima are at 295 K, 198 K, 167 K, 18 K, and 10 K for 10 mT, 50 mT, 100 mT, 500 mT, and 1 T, respectively. Fig. 5 a, b, d are reproduced from Lesniak et al. (2021).

173 Applying a 1 T field shows a slight increase in the induced magnetization (Fig. 5d), compared to using  
 174 an applied field of 500 mT, with the peak at 10 K. The change in magnetization from 10 K to 300 K is  
 175 7.4 %, which is similar to the change of 7.1 % reported by Chang et al. (Chang et al., 2008), who  
 176 attributed it to an increase in thermal fluctuations. At the highest applied fields, where the magnetization  
 177 is close to saturation, the induced magnetisation follows Bloch's law, which predicts  $M(T) = M_0 (1 -$   
 178  $(T/T_C)^{3/2})$ , where  $M_0$  is the magnetization at  $T = 0$  and  $T_C$  is the Curie temperature (Bloch, 1930). The fit  
 179 that is shown in Fig. 5d uses a  $T_C$  to give the best fit, but this predicts  $T_C > 1000$  K, which is not realistic.  
 180 Estimated  $T_C$  of greigite is  $> 650$  K (Roberts et al., 2011), and if it is used as a lower limit then the fit  
 181 follows the Bloch-law only in the very low temperature range, and starts to diverge at around 20 K (Fig.

182 5d inset). The low-temperature behaviour of the magnetisation following Bloch law was previously  
183 shown by Chang et al. (2008).

184

### 185 **Temperature dependent FMR**

186 The FMR spectra were measured as a function of temperature to identify low temperature changes in  
187 anisotropy of the sample. At room temperature the absorption spectrum is characterized by a single  
188 asymmetric line with  $A = 0.84$ ,  $B_{\text{res}} = 247.6$  mT,  $g_{\text{eff}} = 2.85$ , and  $dB = 155$  mT (Fig. 6a). These values  
189 are between values shown for synthetic cubo-octahedral crystals, and those reported for the natural  
190 sample in Chang et al., (2008). With cooling the derivative of the absorption spectra shifts continuously  
191 to the slightly lower field and becomes broader (Fig. 6 b-e). Below 50K there is a larger shift in the  
192 absorption spectra, and the high peak in the derivative slowly moves outside the measurement range,  
193 which influences  $dB$  at low temperatures.  $B_{\text{res}}$ ,  $g_{\text{eff}}$  and  $dB$  are shown as a function of the temperature  
194 (Fig.6e - g).  $B_{\text{res}}$  shows a gradual decrease to 50 K and a slightly larger drop between 140 K and 110 K.  
195 This is followed by sharp drop of  $B_{\text{res}}$  observed around 50 K, which corresponds to a doubling of  $g_{\text{eff}}$  at  
196 10 K, compared to above 50 K. A similar trend is seen in  $dB$  with small variations observed at higher  
197 temperatures.

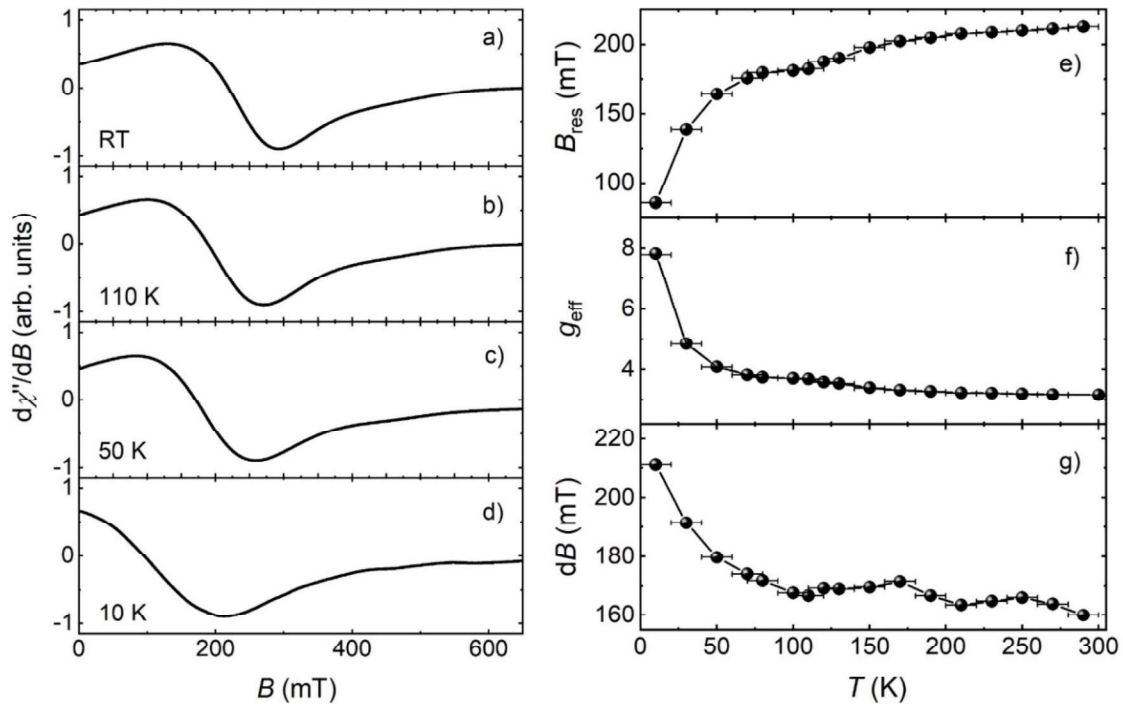


Fig.6 The left panel represents the selected spectra of the low temperature FMR profile at a) RT, b) 110 K, c) 50 K and d) 10 K. The right panel shows the e) resonance field, f)  $g_{eff}$  and g) line-width  $dB$  as a function of temperature. In (g) the value of  $dB$  at 10 K is most likely larger than presented, due to the fact that maximum of the peak lies outside the measurement range.

Fig. 6e, g are reproduced from Lesniak et al. (2021).

### 198 Angular dependence of FMR

199 The angular dependence of FMR was measured to determine whether greigite exhibits spatial  
 200 anisotropy (Fig. 7). At room temperature, the 1<sup>st</sup> scan at the new position is characterised by zero/low  
 201 absorption at the starting field (Fig. 7a) that is related to the initial magnetization of the sample. For this  
 202 reason, the 1<sup>st</sup> scans differ up to around 200 mT, before the magnetization is close to saturation. Once  
 203 the magnetization is close to saturation then the absorption spectrum is repeatable. We found that the  
 204 2<sup>nd</sup> scan is the same for each angular position, which indicates that there is no spatial anisotropy at room  
 205 temperature. This would be expected for randomly-oriented minerals with cubic crystallographic  
 206 structure. The experiment was repeated at 10 K, and in this case there is a difference in the magnitude  
 207 of the absorption as a function of angle (Fig. 7b). The highest absorption is found for the starting  
 208 position, and becomes weaker with each successive angle. Each spectrum crosses each of the other  
 209 spectra at around 145 mT, which is also the field at which 1<sup>st</sup> and 2<sup>nd</sup> scans at the same angle become

210 similar (Fig. A2a). We repeated this experiment at 10 K on a second sample, but did not see a difference  
 211 in the magnitude of the absorption as a function of angle. In this case the 2<sup>nd</sup> absorption spectra were  
 212 independent of the angle (Fig. A2b)

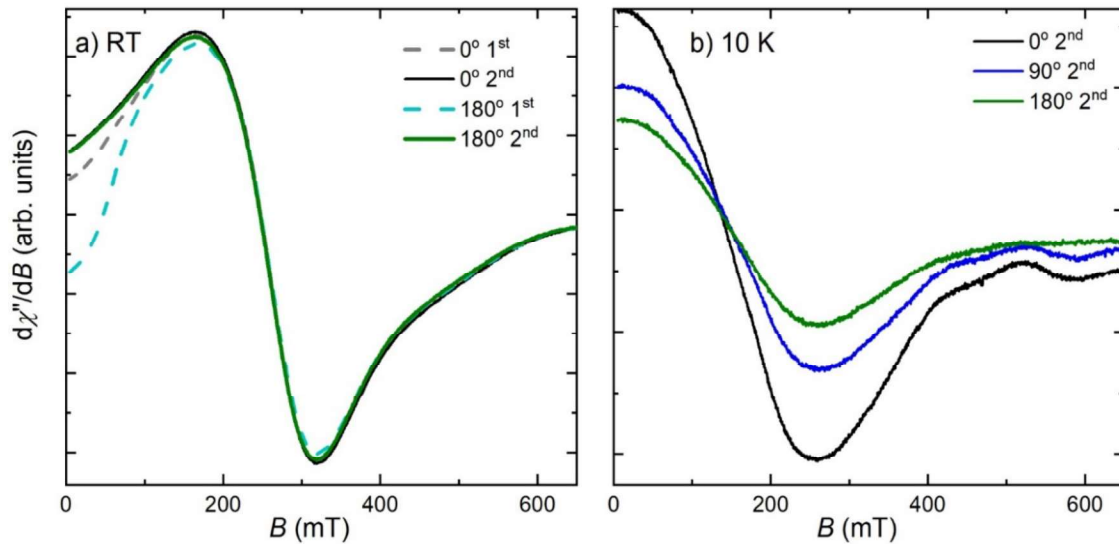


Fig. 7 Rotational FMR analysis of the sample at a) room temperature (RT), and b) 10 K. The sample was measured two times at each angle different angle (1<sup>st</sup> and 2<sup>nd</sup>). Each higher angle measurements were preceded by measurement at 0 deg. Reproduced from Lesniak et al. (2021).

### 213 3.4. DISCUSSION

214 The greigite was produced, using the synthesis method outlined in Rhodes et al. (2017). It is  
 215 characterised by aggregates of crystallites of 19 nm size that undergo most likely an epitaxial growth to  
 216 form flakes that area generally larger than 100 nm (Fig. 1). This type of morphology has been previously  
 217 reported by Hu et al. (1998). Furthermore, the rather low stress/strain parameter of  $\epsilon_0 = 2 \times 10^{-5}$  indicates  
 218 that the crystallites do not originate from mechanical processes, but rather chemical growth which led  
 219 to growth into flakes. A study by Paoletta et al (2011) on greigite flakes with nanocrystalline structure  
 220 shows the flakes of greigite formed from the intergrown nanocrystallites, which are distributed in  
 221 different directions with regard to crystallographic axes. We suggest similar behavior in our sample.

222 The hysteresis parameters together with FORC analysis reveal the clear dominance of interacting SD  
 223 particles, typical for natural greigite (Roberts et al., 2011; Roberts et al., 2014) (Fig. 3). Chang et al.

224 (2007) reported that greigite approaches saturation by 300 mT, but is not saturated at 5 T. This is the  
225 case in our sample, and this lack of saturation may be related to the antiferromagnetic coupling between  
226 Fe in the octahedral and tetrahedral sites.  $M_{IT} = 32.70 \text{ Am}^2/\text{kg}$  is smaller than the theoretical value of  
227  $59 \text{ Am}^2/\text{kg}$  estimated by Chang et al. (2008) or  $M_s$  in greigite particles of similar in size at ca. 44  
228  $\text{Am}^2/\text{kg}$  (Lyubutin et al., 2013) (Fig. 2). As argued by Chang et al. (2009a) such a difference may  
229 originate from the sample's impurities and small grain size. In our sample, the first one can be excluded  
230 due to the high purity defined by XRD (Fig. 1). The grain size, however, is much smaller than observed  
231 by Chang et al. (2008), and that could be the reason of such a difference in  $M_s$ . Additionally, possible  
232 presence of vacancies in lattice structure may decrease  $M_s$  (Chang et al., 2009b), and this presence of  
233 vacancies could possibly be related to the morphology of the aggregates. The change in magnetization  
234 parameters while cooling were obtained from hysteresis loops, and show similar behaviour to what has  
235 been reported previously (cf., Chang et al. 2009) with a gradual increase of  $B_C$  and  $M_R / M_s$  with  
236 decreasing temperature (Fig. 4), where hysteresis broadening was associated to progressive blocking of  
237 fine magnetic particles.

238 Near-saturation magnetisation as a function of temperature  $M(T)$  does not follow Bloch-like behaviour  
239 (Bloch, 1930), unless greigite would be characterised by high  $T_C > 1000 \text{ K}$ . (Fig. 5d). A fit using an  
240 estimated value of  $T_C = 650 \text{ K}$  can only fit low-temperature values up to 20 K. Chang et al. (2008)  
241 discussed the accuracy of the Bloch-law in the very low temperature range, and attributed the small  
242 increase in the induced magnetization decreasing with temperature to an increase in thermal  
243 fluctuations. What has not been considered in this discussion is the role of interactions, which is  
244 documented by the spread in the FORC density plots in relation to interaction fields (Fig. 3a). Further  
245 evidence for an interacting system of particles is seen by the shift in peak susceptibility (or induced  
246 magnetization) to lower temperature with increasing applied field (Fig. 5). This behaviour has been  
247 noted for aggregates of weakly interacting nanoparticles (El-Hilo et al., 1992). The role of interactions  
248 on the magnetization behaviour at low temperature is also supported by data on natural samples, which  
249 have shown FORC density plots similar to our sample (Chapter 4).



---

250 Comparing the FMR spectral parameters at room temperature from this study to those reported for  
251 synthetic PSD/MD cubo-octahedral crystals of Chang et al. (2008) shows some difference. In general,  
252 they are similar, with  $B_{res}$ , and consequently  $g_{eff}$ , slightly increased/ decreased, respectively, in the  
253 direction that was seen for the natural sample, which was analysed by Chang et al. (2012). The exception  
254 is the  $A$  value, which is similar to the value obtained for the natural sample by Chang et al. (2012).  
255 This suggests that the morphology of the crystal or aggregates and/or the particle size are affecting the  
256 spectral parameters. Moreover, Chang et al. (2012) suggested that rather large  $g_{eff}$  observed in their  
257 sample is an feature of MD size grain, and that SD particles reveal  $g_{eff}$  of around 2. We observe  
258  $g_{eff} = 2.85$  for our SD sample, which is a similar value to those observed for PSD/MD particles (2.95  
259 – 3.13). Therefore, we claim that high  $g_{eff}$  in greigite is not dependent on the particle size, but rather on  
260 the magnetostatic interactions, as previously shown by Valstyn et al. (1962) and Kopp et al. (2006).

261 The FMR spectra show a change at low temperature. Cooling from room temperature to 50 K leads to  
262 a continuous shift of the absorption to slightly lower fields and broader signals (Fig. 7). Below 50 K the  
263 shift and broadening become larger, which is reflected in the change of  $B_{res}$ ,  $g_{eff}$  and  $\delta B$  (Fig 6 e-g).  
264 This abrupt change in the spectral parameters can be explained by the influence of the sample's  
265 morphology or by variation of the total anisotropy properties, i.e. alternation of magnetocrystalline  
266 or/and shape anisotropy. However, it was previously shown that spectra broadening and shift in  $g_{eff}$  to  
267 higher values may be caused by the magnetostatic interactions (Kopp et al., 2006; Valstyn et al., 1962).  
268 This explanation is compatible with the shift in peak susceptibility (Fig. 5) and FORC diagram (Fig. 2),  
269 which defines a strongly interacting system. Thus magnetostatic interactions arising from the sample's  
270 morphology, in particular the nanocrystalline structure, may be responsible for the broadening and shift.  
271 What we cannot explain, however, is the abrupt change in the spectroscopic parameters below 50 K.  
272 As FMR is sensitive to the anisotropy properties, we suggest that there is an additional change of the  
273 total anisotropy properties, and it may originate from the nanocrystallite flake morphology, or it may  
274 be an intrinsic feature of greigite. Interestingly, Chang et al. (2008) showed that the Mössbauer spectra  
275 of the PSD/MD greigite crystals below 50 K lose the quadrupole doublet observed at room temperature,  
276 which they associated to the presence of SP particles, but we have no evidence for a significant SP

277 population of crystallites that undergoes blocking below 50 K. A ceasing of electron hopping between  
278 sublattices may occur at lower temperatures, as observed for magnetite, and this could possibly  
279 influence the FMR response (Gehring et al., 2011; Kronmüller and Walz, 1980). Further research,  
280 however, would be needed to resolve this issue.

281 The FMR spectra show no indication for spatial anisotropy as seen in Fig. 7. After the magnetization is  
282 saturated by ca. 200 mT, the FMR spectra show no angular dependency. The fact that a difference was  
283 observed with each position in the first scan is related to remagnetizing the sample in each new position.  
284 The rotational dependence at 10 K, could not be repeated. It does suggest, however, that in the first  
285 sample the magnetic moments were not fully aligned with the direction of the applied field. At present  
286 this would also require further research to understand if there is an angular dependency of the anisotropy  
287 constant at very low temperature.

288

### 289 **3.5. CONCLUSION**

290 The structural, morphological, magnetic and spectroscopies studies were performed to study the  
291 properties of aggregates of flake-like greigite. The XRD and TEM show that the greigite flakes are  
292 formed by the epitaxially intergrowth of nano-size crystallites. The magnetic properties are  
293 characterized by single domain behaviour in an interacting system, similar to what has been reported in  
294 earlier studies. The spectroscopic studies show that there is a marked change in spectral properties  
295 below 50K, which indicates magnetostatic interaction and possible change in anisotropy energies. This  
296 behaviour has not been reported previously for greigite, and may be an intrinsic feature arising from  
297 greigite or from the flake-like morphology. Further work is needed to better understand how the  
298 anisotropy energy is changing at low temperature and if the change is related to sample morphology or  
299 is typical in all greigite.

300

301

---

**302 3.6. AUTHOR CONTRIBUTIONS**

303 Jordan M. Rhodes and Janet E. Macdonald from Vanderbilt University (Nashville, USA) synthesized  
304 the sample and performed TEM measurements. Jordan M. Rhodes, Janet E. Macdonald, and Peter  
305 Weidler from Karlsruhe Institute of Technology (Karlsruhe, Germany) performed XRD analysis.  
306 Dimitrios Koulialias from ETH Zurich (Zurich, Switzerland) performed part of the low-temperature  
307 PPMS measurements.

308

**309 3.7. REFERENCES**

- 310 Bazylinski, D.A., Frankel, R.B., Heywood, B.R., Mann, S., King, J.W., Donaghay, P.L., Hanson, A.K.,  
311 1995. Controlled Biomineralization of Magnetite (Fe (inf3) O (inf4)) and Greigite (Fe (inf3) S  
312 (inf4)) in a Magnetotactic Bacterium. *Appl. Environ. Microbiol.* 61, 3232-3239,  
313 doi:10.1128/AEM.61.9.3232-3239.1995
- 314 Bloch, F., 1930. Zur theorie des ferromagnetismus. *Zeitschrift fur Physik* 61, 206-219
- 315 Chang, L., Rainford, B.D., Stewart, J.R., Ritter, C., Roberts, A.P., Tang, Y., Chen, Q., 2009a. Magnetic  
316 structure of greigite (Fe<sub>3</sub>S<sub>4</sub>) probed by neutron powder diffraction and polarized neutron  
317 diffraction. *Journal of Geophysical Research: Solid Earth* 114
- 318 Chang, L., Roberts, A.P., Muxworthy, A.R., Tang, Y., Chen, Q., Rowan, C.J., Liu, Q., Pruner, P., 2007.  
319 Magnetic characteristics of synthetic pseudo-single-domain and multi-domain greigite (Fe<sub>3</sub>S<sub>4</sub>).  
320 *Geophysical Research Letters* 34
- 321 Chang, L., Roberts, A.P., Rowan, C.J., Tang, Y., Pruner, P., Chen, Q., Horng, C.S., 2009b. Low-  
322 temperature magnetic properties of greigite (Fe<sub>3</sub>S<sub>4</sub>). *Geochemistry, Geophysics, Geosystems* 10
- 323 Chang, L., Roberts, A.P., Tang, Y., Rainford, B.D., Muxworthy, A.R., Chen, Q., 2008. Fundamental  
324 magnetic parameters from pure synthetic greigite (Fe<sub>3</sub>S<sub>4</sub>). *Journal of Geophysical Research:*  
325 *Solid Earth* 113
- 326 Chang, L., Winklhofer, M., Roberts, A.P., Dekkers, M.J., Horng, C.S., Hu, L., Chen, Q., 2012.  
327 Ferromagnetic resonance characterization of greigite (Fe<sub>3</sub>S<sub>4</sub>), monoclinic pyrrhotite (Fe<sub>7</sub>S<sub>8</sub>),  
328 and non-interacting titanomagnetite (Fe<sub>3-x</sub>Ti<sub>x</sub>O<sub>4</sub>). *Geochemistry, Geophysics, Geosystems* 13
- 329 Dekkers, M.J., Passier, H.F., Schoonen, M.A., 2000. Magnetic properties of hydrothermally  
330 synthesized greigite (Fe<sub>3</sub>S<sub>4</sub>)—II. High- and low-temperature characteristics. *Geophysical*  
331 *Journal International* 141, 809-819
- 332 Dekkers, M.J., Schoonen, M.A., 1996. Magnetic properties of hydrothermally synthesized greigite  
333 (Fe<sub>3</sub>S<sub>4</sub>)—I. Rock magnetic parameters at room temperature. *Geophysical Journal International*  
334 126, 360-368
- 335 El-Hilo, M., O'grady, K., Chantrell, R., 1992. Susceptibility phenomena in a fine particle system: II.  
336 Field dependence of the peak. *Journal of Magnetism and Magnetic Materials* 114, 307-313
- 337 Gehring, A.U., Fischer, H., Charilaou, M., Garcia-Rubio, I., 2011. Magnetic anisotropy and Verwey  
338 transition of magnetosome chains in *Magnetospirillum gryphiswaldense*. *Geophysical Journal*  
339 *International* 187, 1215-1221
- 340 Giovanoli, F., 1979. A comparison of the magnetization of detrital and chemical sediments from Lake  
341 Zurich. *Geophysical Research Letters* 6, 233-235
- 342 Harrison, R.J., Feinberg, J.M., 2008. FORCinel: An improved algorithm for calculating first-order  
343 reversal curve distributions using locally weighted regression smoothing. *Geochemistry,*  
344 *Geophysics, Geosystems* 9

- 345 He, Z., Yu, S.H., Zhou, X., Li, X., Qu, J., 2006. Magnetic-field-induced phase-selective synthesis of  
346 ferrosulfide microrods by a hydrothermal process: Microstructure control and magnetic  
347 properties. *Advanced Functional Materials* 16, 1105-1111
- 348 Hu, S., Appel, E., Hoffmann, V., Schmahl, W.W., Wang, S., 1998. Gyromagnetic remanence acquired  
349 by greigite (Fe<sub>3</sub>S<sub>4</sub>) during static three-axis alternating field demagnetization. *Geophysical*  
350 *Journal International* 134, 831-842
- 351 Hunger, S., Benning, L.G., 2007. Greigite: a true intermediate on the polysulfide pathway to pyrite.  
352 *Geochemical Transactions* 8, 1, doi:10.1186/1467-4866-8-1
- 353 Jiang, W.-T., Horng, C.-S., Roberts, A.P., Peacor, D.R., 2001. Contradictory magnetic polarities in  
354 sediments and variable timing of neoformation of authigenic greigite. *Earth and Planetary*  
355 *Science Letters* 193, 1-12
- 356 Kopp, R.E., Nash, C.Z., Kobayashi, A., Weiss, B.P., Bazylinski, D.A., Kirschvink, J.L., 2006.  
357 Ferromagnetic resonance spectroscopy for assessment of magnetic anisotropy and magnetostatic  
358 interactions: A case study of mutant magnetotactic bacteria. *Journal of Geophysical Research:*  
359 *Solid Earth* 111
- 360 Kronmüller, H., Walz, F., 1980. Magnetic after-effects in Fe<sub>3</sub>O<sub>4</sub> and vacancy-doped magnetite.  
361 *Philosophical Magazine B* 42, 433-452
- 362 Lesniak, B., Koulialias, D., Charilaou, M., Weidler, P.G., Rhodes, J.M., Macdonald, J.E., Gehring,  
363 A.U., 2021. Polycrystalline texture causes magnetic instability in greigite. *Scientific Reports* 11,  
364 3024, doi:10.1038/s41598-020-80801-4
- 365 Li, G., Zhang, B., Yu, F., Novakova, A.A., Krivenkov, M.S., Kiseleva, T.Y., Chang, L., Rao, J.,  
366 Polyakov, A.O., Blake, G.R., 2014. High-purity Fe<sub>3</sub>S<sub>4</sub> greigite microcrystals for magnetic and  
367 electrochemical performance. *Chemistry of Materials* 26, 5821-5829
- 368 Lyubutin, I., Starchikov, S., Lin, C.-R., Lu, S.-Z., Shaikh, M.O., Funtov, K., Dmitrieva, T.,  
369 Ovchinnikov, S., Edelman, I., Ivantsov, R., 2013. Magnetic, structural, and electronic properties  
370 of iron sulfide Fe<sub>3</sub>S<sub>4</sub> nanoparticles synthesized by the polyol mediated process. *Journal of*  
371 *Nanoparticle Research* 15, 1397
- 372 Newell, A.J., 2005. A high-precision model of first-order reversal curve (FORC) functions for single-  
373 domain ferromagnets with uniaxial anisotropy. *Geochemistry, Geophysics, Geosystems* 6
- 374 Paoella, A., George, C., Povia, M., Zhang, Y., Krahn, R., Gich, M., Genovese, A., Falqui, A.,  
375 Longobardi, M., Guardia, P., 2011. Charge transport and electrochemical properties of colloidal  
376 greigite (Fe<sub>3</sub>S<sub>4</sub>) nanoplatelets. *Chemistry of Materials* 23, 3762-3768
- 377 Pike, C.R., Roberts, A.P., Verosub, K.L., 1999. Characterizing interactions in fine magnetic particle  
378 systems using first order reversal curves. *Journal of Applied Physics* 85, 6660-6667
- 379 Reynolds, R.L., Tuttle, M.L., Rice, C.A., Fishman, N.S., Karachewski, J.A., Sherman, D.M., 1994.  
380 Magnetization and geochemistry of greigite-bearing Cretaceous strata, North Slope Basin,  
381 Alaska. *American Journal of Science* 294, 485-528
- 382 Rhodes, J.M., Jones, C.A., Thal, L.B., Macdonald, J.E., 2017. Phase-controlled colloidal syntheses of  
383 iron sulfide nanocrystals via sulfur precursor reactivity and direct pyrite precipitation. *Chemistry*  
384 *of Materials* 29, 8521-8530
- 385 Roberts, A.P., 1995. Magnetic properties of sedimentary greigite (Fe<sub>3</sub>S<sub>4</sub>). *Earth and Planetary Science*  
386 *Letters* 134, 227-236
- 387 Roberts, A.P., Chang, L., Rowan, C.J., Horng, C.S., Florindo, F., 2011. Magnetic properties of  
388 sedimentary greigite (Fe<sub>3</sub>S<sub>4</sub>): An update. *Reviews of Geophysics* 49
- 389 Roberts, A.P., Heslop, D., Zhao, X., Pike, C.R., 2014. Understanding fine magnetic particle systems  
390 through use of first-order reversal curve diagrams. *Reviews of Geophysics* 52, 557-602
- 391 Rowan, C.J., Roberts, A.P., 2005. Tectonic and geochronological implications of variably timed  
392 magnetizations carried by authigenic greigite in marine sediments from New Zealand. *Geology*  
393 33, 553-556
- 394 Rowan, C.J., Roberts, A.P., Broadbent, T., 2009. Reductive diagenesis, magnetite dissolution, greigite  
395 growth and paleomagnetic smoothing in marine sediments: A new view. *Earth and Planetary*  
396 *Science Letters* 277, 223-235
- 397 Sagnotti, L., Roberts, A.P., Weaver, R., Verosub, K.L., Florindo, F., Pike, C.R., Clayton, T., Wilson,  
398 G.S., 2005. Apparent magnetic polarity reversals due to remagnetization resulting from late  
399 diagenetic growth of greigite from siderite. *Geophysical Journal International* 160, 89-100

- 400 Sagnotti, L., Winkler, A., 1999. Rock magnetism and palaeomagnetism of greigite-bearing mudstones  
 401 in the Italian peninsula. *Earth and Planetary Science Letters* 165, 67-80  
 402 Skinner, B.J., Erd, R.C., Grimaldi, F.S., 1964. Greigite, the thio-spinel of iron; a new mineral. *American*  
 403 *Mineralogist: Journal of Earth and Planetary Materials* 49, 543-555  
 404 Snowball, I., Thompson, R., 1988. The occurrence of greigite in sediments from Loch Lomond. *Journal*  
 405 *of Quaternary Science* 3, 121-125  
 406 Snowball, I.F., 1991. Magnetic hysteresis properties of greigite (Fe<sub>3</sub>S<sub>4</sub>) and a new occurrence in  
 407 Holocene sediments from Swedish Lapland. *Physics of the Earth and Planetary Interiors* 68, 32-  
 408 40  
 409 Valstyn, E., Hanton, J., Morrish, A., 1962. Ferromagnetic resonance of single-domain particles.  
 410 *Physical Review* 128, 2078  
 411 van Dongen, B.E., Roberts, A.P., Schouten, S., Jiang, W.-T., Florindo, F., Pancost, R.D., 2007.  
 412 Formation of iron sulfide nodules during anaerobic oxidation of methane. *Geochimica et*  
 413 *Cosmochimica Acta* 71, 5155-5167  
 414 Weiss, B.P., Kim, S.S., Kirschvink, J.L., Kopp, R.E., Sankaran, M., Kobayashi, A., Komeili, A., 2004.  
 415 Ferromagnetic resonance and low-temperature magnetic tests for biogenic magnetite. *Earth and*  
 416 *Planetary Science Letters* 224, 73-89  
 417 Winklhofer, M., Chang, L., Eder, S.H., 2014. On the magnetocrystalline anisotropy of greigite (Fe<sub>3</sub>S<sub>4</sub>).  
 418 *Geochemistry, Geophysics, Geosystems* 15, 1558-1579

419

420

421

422

423

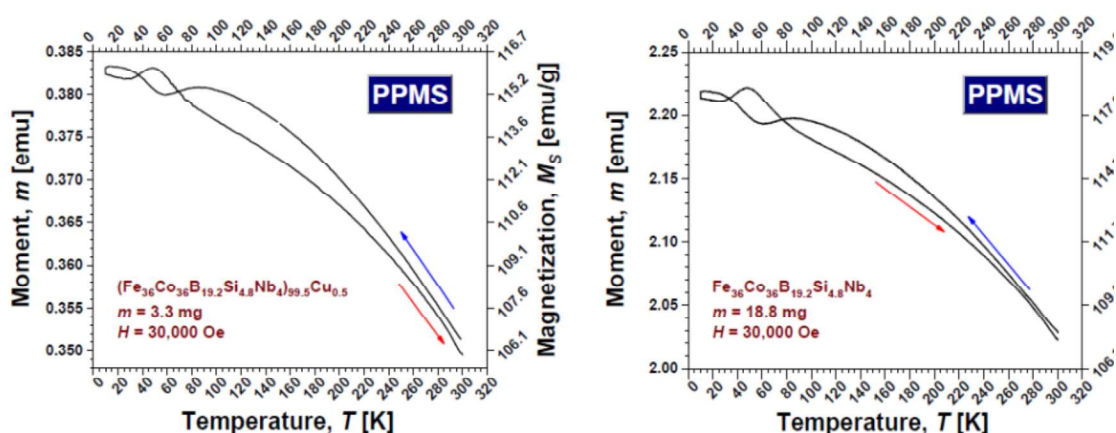
424 **3.7. APPENDIX**

Fig. A1 Thermomagnetic curves for two different compounds showing low-temperature anomaly of PPMS. Deviations are observed at approx. 90 K, 55 K and below 20 K for cooling curves and at approx. 25 K, 50 K, and 75 K while heating.

Measurements and plots were made by Dr. Mihai Stoica from ETH Zurich.

425

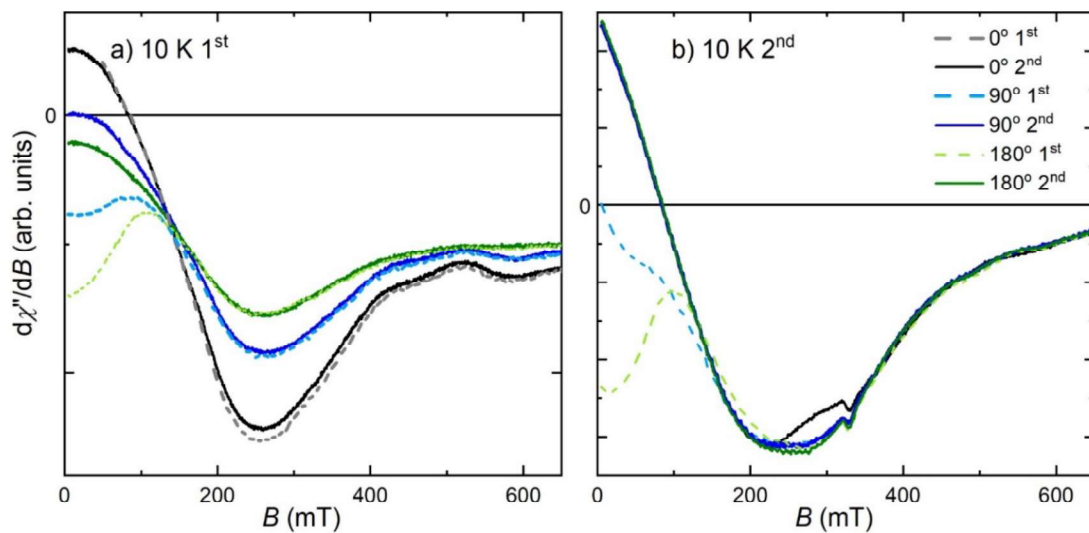


Fig. A2 Rotational FMR analysis of the samples at 10 K a) 1<sup>st</sup> sample and b) 2<sup>nd</sup> sample. The samples were measured two times at each angle different angle (1<sup>st</sup> and 2<sup>nd</sup>). Each higher angle measurements were preceded by measurement at 0 deg. The 1<sup>st</sup> and 2<sup>nd</sup> scan of the 0 position are overlapping due to cooling in the position.

426

---

## 4. Greigite as a Magnetic Carrier in Sediments from Lower Williams Lake, Canada

### Abstract

Anthropogenic activity can strongly influence an environment even after cessation of this activity, particularly in the case of ore mining. Changes in iron mineralogy has been demonstrated to be a good indicator of processes related to both contamination by mining practices or subsequent remediation. Rock magnetic methods, electron spin resonance spectroscopy (ESR), scanning electron microscope (SEM) and inductively coupled plasma atomic emission spectroscopy (ICP-AES) are used to identify the iron minerals in a sediment core that was taken in a tailing pond, which has undergone remediation, at the former uranium mining site in Elliot Lake, Canada. The core consists of a layer of organic sediments overlying the tailings. The organic sediments are characterized by higher magnetic susceptibility, which decreases in the tailings. The main ferromagnetic (*s.l.*) carrier in the sediment is greigite, which is found as intergrown flakes that are accompanied by pyrite framboids. The change of the magnetic and geochemical properties down the core indicates that the greigite is replaced progressively by pyrite framboids. This study demonstrates the process by which this replacement occurs as part of the evolution of environmental conditions associated with the remediation in this former tailing pond.

### 4.1. INTRODUCTION

Greigite ( $\text{Fe}_3\text{S}_4$ ) is a ferrimagnetic mineral, which can be found in lacustrine and marine sedimentary records (Rowan et al., 2009; Snowball and Thompson, 1988), and has been shown to record the ancient geomagnetic field (Jiang et al., 2001; Roberts et al., 1996). In natural sediments greigite usually occurs in single domain (SD) state (Roberts et al., 2011), but may be also found in a superparamagnetic (SP) state (Rowan and Roberts, 2006), and occasionally in multi-domain (MD) form (Hoffmann, 1992; Roberts et al., 2006). It is also an important indicator of past environmental conditions as it only forms

26 in a narrow stability field of redox potential Eh, which defines how likely is that the redox reaction will  
27 occur, and in a pH range of 5.9 to 7.4, if there is enough reactive iron available to react with sulfide  
28 during pyritization (Kao et al., 2004). Greigite is an intermediate phase along the pathway from  
29 mackinawite (FeS) to pyrite (Hunger and Benning, 2007). Its preservation is dependent on terrigenous  
30 sediments to dilute organic carbon supply and reactive iron to exhaust sulfide, which is supplied by  
31 anaerobic decomposition of organic matter, so that pyritization is arrested (Roberts et al., 2011).  
32 Therefore the presence of greigite provides information about the biogeochemical cycle of Fe, S, and C  
33 in anoxic sediments (Rowan and Roberts, 2006; Snowball, 1991). It has been noted that this  
34 biogeochemical cycle plays also a role in the mobility of radioactive elements, such as U, in near-surface  
35 environments (Livens et al., 2004).

36 The role of greigite as a precursor to pyrite (FeS<sub>2</sub>) during early diagenetic sedimentary sulfate reduction  
37 is described in several studies (Berner, 1984; Pósfai et al., 1998). Pyrite is a one of the most common  
38 natural sulphides, found in a wide variety of geological materials from sedimentary deposits to  
39 hydrothermal veins and as a constituent of metamorphic rocks (Large et al., 2007; Raiswell and Berner,  
40 1985; Raiswell and Canfield, 1998; Schoonen, 2004). It is paramagnetic and it often occurs in the form  
41 of spherical aggregates, so called framboids (Sweeney and Kaplan, 1973; Wilkin et al., 1996). It has  
42 been suggested that framboids form as a result of magnetic interactions between greigite crystals, which  
43 later converts to pyrite, while preserving the morphology (Wilkin and Barnes, 1997).

44 One noted site where framboidal pyrite is found is the tailing-basin of Lower Williams Lake in Canada  
45 (Paktunc and Davé, 2002). The lake consists of tailings from U-milling that was undertaken in the late  
46 1950's thru early 1960's. The area was left open until 1976-1977, which allowed for oxidation of the  
47 upper 10 to 20 cm, before the tailings were covered by a layer of limestone to neutralize acidity,  
48 followed by a layer of glacial sand and till over the central and eastern part of the tailing basin. This  
49 area was then vegetated as part of the remediation, and the area has since gradually turned into a natural  
50 marsh. In the western area, the pond has not been covered and an organic-rich sediment has been  
51 deposited over the tailings. For this reason, the former tailing pond of Lower Williams Lake represents  
52 a transition zone between terrestrial and aquatic habitats, and provides a unique environment for



53 dynamic evolution of iron minerals in an anoxic environment. Paktunc and Davé (2002) have described  
54 hydrogeology and mineralogy at the site, and postulated that the framboidal pyrite formed through  
55 amorphous FeS and greigite.

56 In this study, we investigate the change in iron mineralogy of a sediment core that was taken in the  
57 marsh at Lower Williams Lake (Canada). Rock magnetic methods, electron spin resonance  
58 spectroscopy (ESR), scanning electron microscope (SEM) and inductively coupled plasma atomic  
59 emission spectroscopy (ICP-AES) are used to identify the iron minerals in the sediments. This  
60 information is applied to expand our understanding of the role that anthropogenic activity plays in the  
61 formation and preservation of iron-bearing minerals in an anoxic environment, particularly the role of  
62 greigite in the formation of pyrite

63

## 64 **4.2. SAMPLES AND METHODS**

### 65 **Study site and sampling**

66 The sediment core was collected by K. Mizutani from the area that marks the shallow transition from  
67 the water diversion ditch to the area of dense marsh vegetation (Fig.1) (Paktunc and Davé, 2002). The  
68 sediment profile can be separated into two parts: an organic-sediment; and the tailings (Fig. 2a). The  
69 organic-sediment is characterized by the organic-rich black sediments that make up the upper ca. 25 cm  
70 of the cores, followed by a transition to the gray-color tailing sediments with low organic-content.

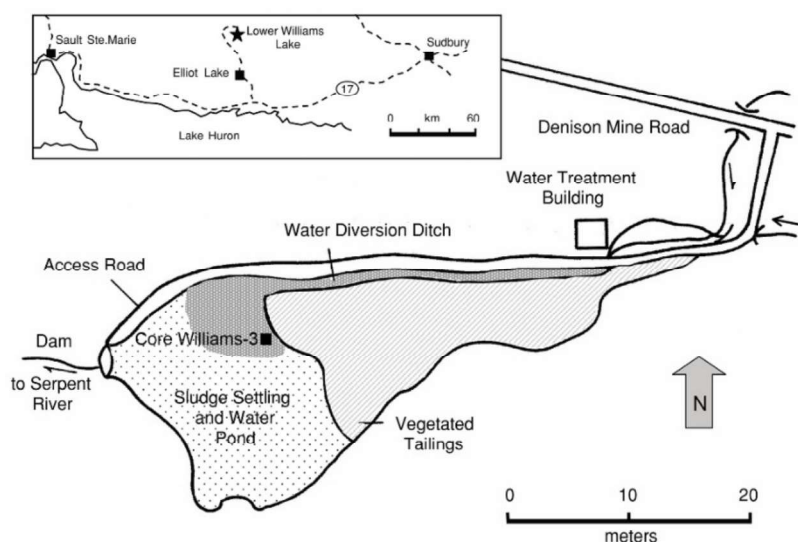


Fig. 1 Map showing the Lower Williams Lake tailings basin with marked sample's position (Core Williams-3) adapted from Paktunc and Davé (Paktunc and Davé, 2002) by Kazuhito Mizutani (pers. comm. 2020).

71 The core was collected and the sampling process was described by K. Mizutani in his master's thesis,  
 72 the University of Guelph (Mizutani, 2019). A short summary is given on the sampling procedure.  
 73 Mizutani describes how a plastic PVC tube with 8 cm diameter and 60 cm length was pressed into the  
 74 sediment by hand, and then sealed with rubber stoppers after it was removed. After transport the  
 75 sediment was kept frozen and sampled two days after collection at the School of Environmental  
 76 Sciences, University of Guelph, Canada by slicing into 3 to 5 cm segments in a frozen state. The  
 77 segments were further sliced in two separate pieces and freeze-dried. Afterwards the sediment was  
 78 passed through a 177  $\mu\text{m}$  (80 mesh) sieve to remove any coarser grains. The sieved, dried sediment was  
 79 then stored in glass vials with a polymer cap. Samples for this study were provided by K. Mizutani and  
 80 S. Glasauer (University of Guelph),,

81

## 82 **Sedimentary Sulphur and Iron**

83 Elemental analysis was made by Mizutani on 0.5 g of sediment in a teflon sample holder that was placed  
 84 in a fume hood (Mizutani, 2019). A NIST 2711A Montana II soil was used for calibration. Samples  
 85 were treated with a combination of trace-metal grade reagents, including 3 ml of concentrated

---

86 hydrochloric acid and 9 ml of 70% nitric acid. Samples were subjected to a pre-digestion period of  
87 about 12 hours with stirring, due to the gas-releasing reactions between the reagents and organic  
88 components in the soil. Afterwards, the sealed samples were placed in an oven for 12 hours at 120°C,  
89 and then filtered and diluted to 50 ml for analysis. A small percentage of the minerals, such as quartz,  
90 were not fully dissolved by the reagents. The total elemental abundances of Na, Mg, Al, P, S, K, Ca,  
91 Mn, Fe, As, Sr, Ba, Pb, Th and U were defined using the ICP-AES analysis by K. Mizutani at the  
92 University of Guelph (Mizutani, 2019). The samples were provided by K. Mizutani and S. Glasauer  
93 (University of Guelph).

94

#### 95 **Structural and Morphological analysis**

96 The magnetically separated grains were coated with Pt and their grain size, shapes and compositions  
97 were determined via scanning electron microscopy using a field emission gun Zeiss Merlin SEM at the  
98 Scientific Centre for Optical and Electron Microscopy (ScopeM) of ETH Zürich by Dr. Luiz Grafalha  
99 Morales and Dr. Karsten Kunze. Secondary and backscattered electron images, together with EDS semi-  
100 quantitative analysis, were acquired using accelerating voltages of 10 and 15 kV and beam currents of  
101 around 2 nA.

102

#### 103 **Magnetic analysis**

104 A MFK-1 Kappabridge (Agico, Czech Republic) was used to measure bulk magnetic susceptibility of  
105 the samples with an applied AC field of 200 A/m with frequency 976 Hz. The kappabridge is  
106 characterized by high sensitivity and a measurement accuracy of  $5 \times 10^{-8}$  (SI) (Pokorny et al., 2011). A  
107 Princeton Measurement Corporation (PCM), MicroMag VSM, model 3900, was used to measure  
108 magnetization as a function of field between  $\pm 1$  T with a variable sample interval with 0.5 mT steps  
109 between  $\pm 100$  mT, 2 mT steps from  $\pm 100$  to  $\pm 200$  mT, and 5 mT steps for fields between  $\pm 200$  and  
110 1000 mT with an averaging time of 300 ms. Additionally, FORC analysis was performed (Pike et al.,  
111 1999), using 170 FORCs with a measurement interval of 1.75 mT and averaging time of 100 ms. The

---

112 obtained FORC results were analyzed using the FORCinel 3.06 program (Harrison and Feinberg, 2008).  
113 The magnetic susceptibility and VSM measurements were made at room temperature at the Laboratory  
114 of Natural Magnetism, ETH Zurich.

115 Magnetic characterization was accompanied by magnetization experiments between 300 and 10 K using  
116 a SQUID magnetometer (MPMS XL: Quantum Design) in sweeping mode at the Laboratory for Solid  
117 State Physics, ETH Zurich. The cooling/ warming rates were 5 K/min between room temperature to 50  
118 K, and 0.25 K/min between 50 K and 10 K. The remanence behavior in the temperature range between  
119 300 K and 10 K was measured after acquisition of a saturation isothermal remanent magnetization  
120 (SIRM) in a 3 T field at 300 K followed by oscillating demagnetization to remove any small remanent  
121 field in the magnet. The SIRM was monitored both in cooling from 300 K to 10 K and then rewarming  
122 back to 300 K. In a second experiment induced magnetization was measured during cooling and  
123 rewarming in a series of fields 10 mT, 50 mT and 1 T for field-cooling (FC) with the induced  
124 magnetization being measured both during cooling and warming. In addition, the magnetization as a  
125 function of field was measured at 17 temperature steps between 10 and 300 K. The measurement was  
126 made using Physical Property Measurement System (PPMS: Quantum Design) in sweeping mode at  
127 the Laboratory of Metal Physics and Technology, ETH Zurich. The measurement interval was 1 mT  
128 steps between  $\pm 150$  mT, and 10 mT steps for fields between  $\pm 150$  and 3000 mT with an averaging  
129 time of 1 s.

130 ESR spectroscopy was used to detect paramagnetic response originating from uncoupled spins as  
131 electron paramagnetic resonance (EPR) or magnetic phases and their anisotropy properties as  
132 ferromagnetic resonance (FMR). The magnetic parameters that are often extracted from these  
133 measurements include the  $g$ -factor, which measures the energy splitting of degenerate states in the  
134 magnetic field, the  $B_{\text{res}}$ , which is the field at the maximum absorption, and the line-width  $\Delta B$ , which is  
135 a peak-to-peak linewidth of the resonance spectrum. The measured net signal is a superposition of all  
136 resonance events, i.e., the measured spectrum is the sum of the spectra originating from particles in all  
137 orientations. The absorption of microwave radiation is generally plotted as the first derivative spectrum  
138 of intensity. The X-band Bruker ElexSys E500 spectrometer was used to record spectra with frequencies

139 either at around 9.86 GHz or 9.39 GHz, depending on the dewar in use, at the lab of the Electron  
140 Paramagnetic Resonance research group, ETH Zurich. The spectrometer is equipped with temperature  
141 controllers and helium gas-flow cryostat from Oxford Instruments. The ESR spectra were recorded at  
142 variable temperatures.

143

### 144 **4.3. RESULTS**

#### 145 **Sediment Profile**

##### 146 *Chemical and magnetic data of the sediment core*

147 The iron content of the uppermost layer has the highest concentration of 145.8 mg/g, and steadily  
148 decreases to ca. 31 mg/g by 17.5cm (Fig. 2b). Within the tailings the iron content varies between 24.2  
149 mg/g to 56.8 mg/g. The concentration of calcium increase gradually in first 15 cm, reaching a  
150 concentration of 125.9 mg/g and then decreases abruptly with the concentration remaining around 1.7  
151 mg/g to 6.4 mg/g within the tailings (Fig. 2b). In contrast, the sulphur concentration is lowest in the top-  
152 most sediment layer and linearly increases down to a depth of 10 - 15 cm where the concentration is  
153 23.8 mg/g. It decreases in the layer below to 14.8 mg/g and slowly increases through the tailing  
154 sediments to a concentration of 25.9 mg/g (Fig.2c).

155

156 Total organic carbon (TOC) follows a trend similar to iron with highest concentration in the uppermost  
157 sediment followed by a gradual decrease at 20 – 25 cm depth; it remains low in the tailing sediments  
158 (Fig. 2d). Total inorganic carbon (TIC), which is associated with carbonate minerals, such as calcite  
159 and siderite, shows an increase at 10 - 15 cm depth, followed to an abrupt decrease in below (Fig. 2d).  
160 The chemical analysis and carbon analysis results are taken from Master's thesis of K. Mizutani  
161 (Mizutani, 2019).

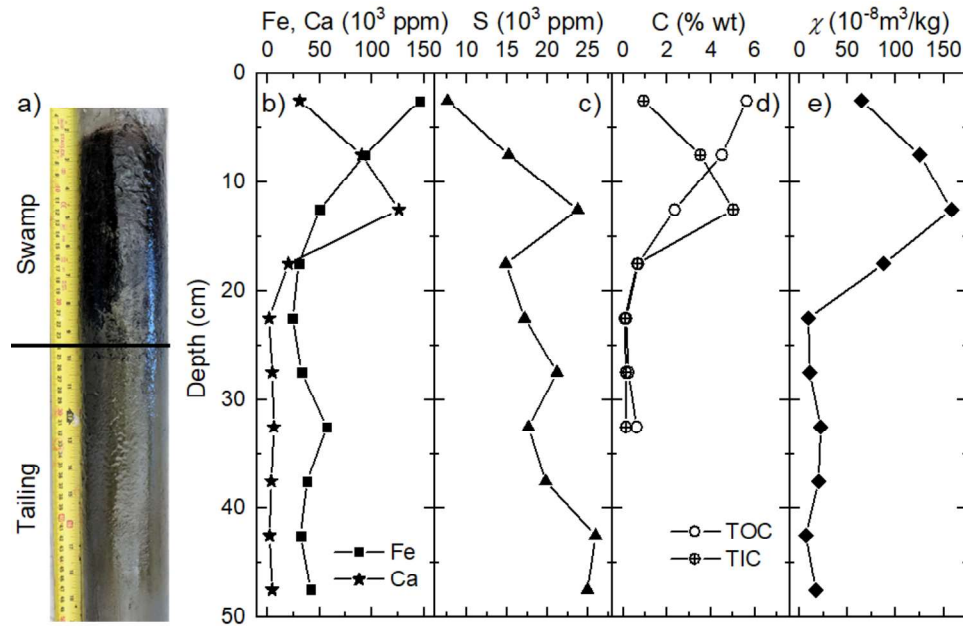


Fig. 2 a) Sediment's profile with separation for organic sediment and tailing segments, depth profile representing b) iron and calcium concentrations, c) sulphur concentration, d) total organic carbon, total inorganic carbon, and e) magnetic susceptibility. Note chemical analysis is available in the Master thesis of K. Mizutani (Mizutani, 2019).

### 162 **Magnetic susceptibility and magnetic hysteresis**

163 The magnetic mass susceptibility ( $\chi$ ) of the samples from the core varies between  $6.43$  and  $158 \times 10^{-8}$   
 164  $\text{m}^3/\text{kg}$  with maximum at  $12.5$  cm (Fig. 2e). Overall  $\chi$  is high in the organic sediments, compared to the  
 165 tailings, in which  $\chi$  remains relatively constant with values between  $6.4 \times 10^{-8} \text{ m}^3/\text{kg}$  and  $21.9 \times 10^{-8}$   
 166  $\text{m}^3/\text{kg}$ .

167 Magnetization as a function of magnetic field was measured for all samples from the core (Fig.3, A1),  
 168 and all samples are characterized by an open hysteresis loop with a variable paramagnetic contribution  
 169 (Fig. A1). The clearest magnetic hysteresis is observed for samples from  $5$ - $10$  cm,  $10$ - $15$  cm, and  
 170  $15$ - $20$  cm. The sample from the depth  $15$ - $20$  has the smallest paramagnetic contribution, with the  
 171 ferromagnetic contribution (*s.l.*) making up  $79\%$  of the total magnetization, which indicates that the  
 172 highest ferromagnetic concentration (*s.l.*) (Table A1; Fig. 2e).

173 Saturation ( $M_s$ ) and remanent ( $M_R$ ) magnetizations follow the same trend as magnetic susceptibility as  
 174 a function of depth, i.e. the highest values are observed in the organic-rich sediments. Maximum  $M_s$   
 175 and  $M_R$  are observed for depth  $10$ - $15$  cm and are  $194.78 \times 10^{-3} \text{ Am}^2/\text{kg}$  and  $87.90 \times 10^{-3} \text{ Am}^2/\text{kg}$ ,

176 respectively. Both of these parameters are distinctly smaller in samples from the tailings. The coercivity  
 177 of the magnetically strongest sample is  $B_C = 32.54$  mT and is similar to samples from depths 5–10 cm,  
 178 15–20 cm, and 20–25 cm. Interestingly, the highest coercivity is observed for sample 40–45 cm. The  
 179 sample from the depth 25–30 cm shows wasp-waisting, which indicates the presence of two  
 180 ferromagnetic (*s.l.*) minerals with strongly contrasting coercivities. The magnetization ratio ( $M_R / M_S$ )  
 181 is relatively high and the coercivity ratio ( $B_{CR} / B_C$ ) is relatively low in the organic sediments, which is  
 182 indicative of ferromagnetic (*s.l.*) minerals with fine grain size (Table A1). Both these parameters are  
 183 more variable in the tailing sediments, which suggests a broader composition and/or grain size range  
 184 for the ferromagnetic (*s.l.*) minerals.

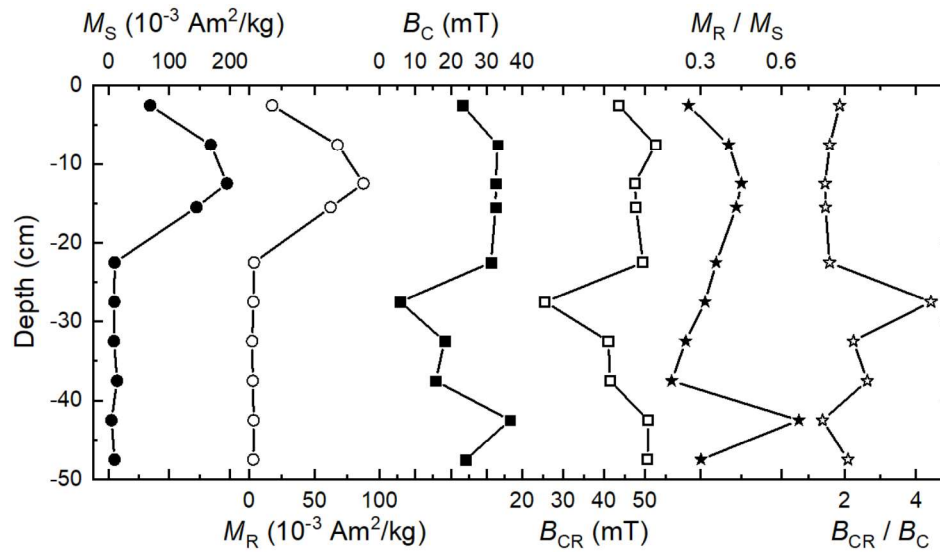


Fig. 3 The hysteric parameters as a function of profile's depth, from the left: saturation magnetization (●), remanent magnetization (○), coercivity (■), remanent coercivity (□), remanence ratio (★) and coercivity ratio (☆).

#### 185 *ESR spectroscopy*

186 The ESR signal of samples from the sediment core change as a function of depth, which would be  
 187 expected from the change in  $\chi$  (Fig.4, Fig. A2). The upper most sample, characterized by relatively low  
 188 susceptibility, differs from the lower sediments, and in terms of its complexity, is most similar to the  
 189 sample from 20–25 cm, which is the transition to the tailings. The samples from the middle 5 cm to 20  
 190 cm are characterized by a broader and symmetric shape in the spectrum, which is due to the dominant

191 ferrimagnetic phase. Secondary paramagnetic signals, due to  $\text{Mn}^{2+}$  and  $\text{Fe}^{3+}$ , are indicated by the  
 192 multiple, sharp lines in the middle of absorption spectrum and characteristic features below 200 mT,  
 193 respectively (Meads and Malden, 1975). The spectra from the tailing part are characterized by similar  
 194 features, which can be ascribed to paramagnetic phases (Fig. A2).

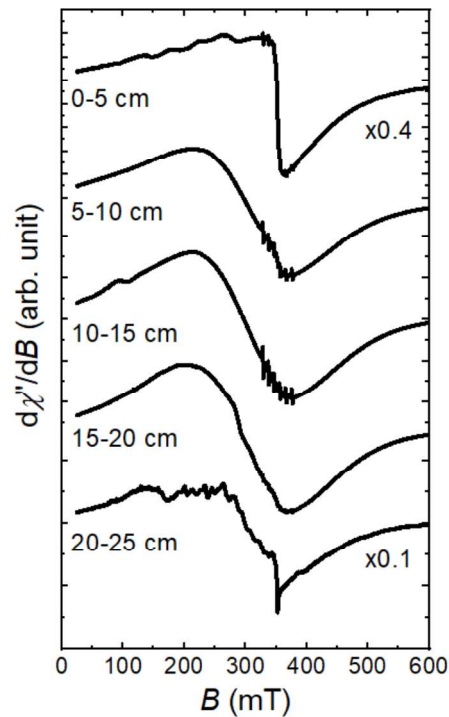


Fig. 4 ESR spectroscopy of the selected samples of the core from the depth 0-5 cm, 5-10 cm, 10-15 cm, 15-20 cm, 20-25 cm. Note the intensity fractions of the samples 0-5 cm and 20-25 cm, showed as a “x0.4” and “x0.1”, respectively. The intensity fractions represent the signal intensity in comparison to the strongest samples. (See Fig. A2 for all samples from the tailing section of core).

#### 195 **Sediment with high ferromagnetic (*s.l.*) concentration (15 – 20 cm depth)**

196 Further detailed analysis was carried out on the layer with the highest susceptibility in order to  
 197 identify the iron minerals in this section.

#### 198 ***SEM analysis***

199 SEM reveals presence of iron-sulphide framboids settled in the cauliflower-like structure (Fig. 6a, b),  
 200 made up of an iron-sulphide phase that still retains a flake-like morphology (Fig. 6b). Both the  
 201 framboids and the cauliflower-like structure are iron and sulphur rich (Fig. 6c, d), but the sulphur



202 content is visibly higher in the framboids. (Fig. 6e, f). The framboids are most-likely pyrite, which is  
203 commonly found in the sediments of Lake Williams (Paktunc and Davé, 2002). The cauliflower  
204 structure is made up of flakes of an iron sulphide phase, similar to what we show in Chapter 3, what  
205 could indicate greigite. In addition, in the sediments are also present microspheres that are characterized  
206 by high iron and oxygen composition (Fig. 6g). These particles may be magnetite or maghemite, with  
207 small sulphur content.

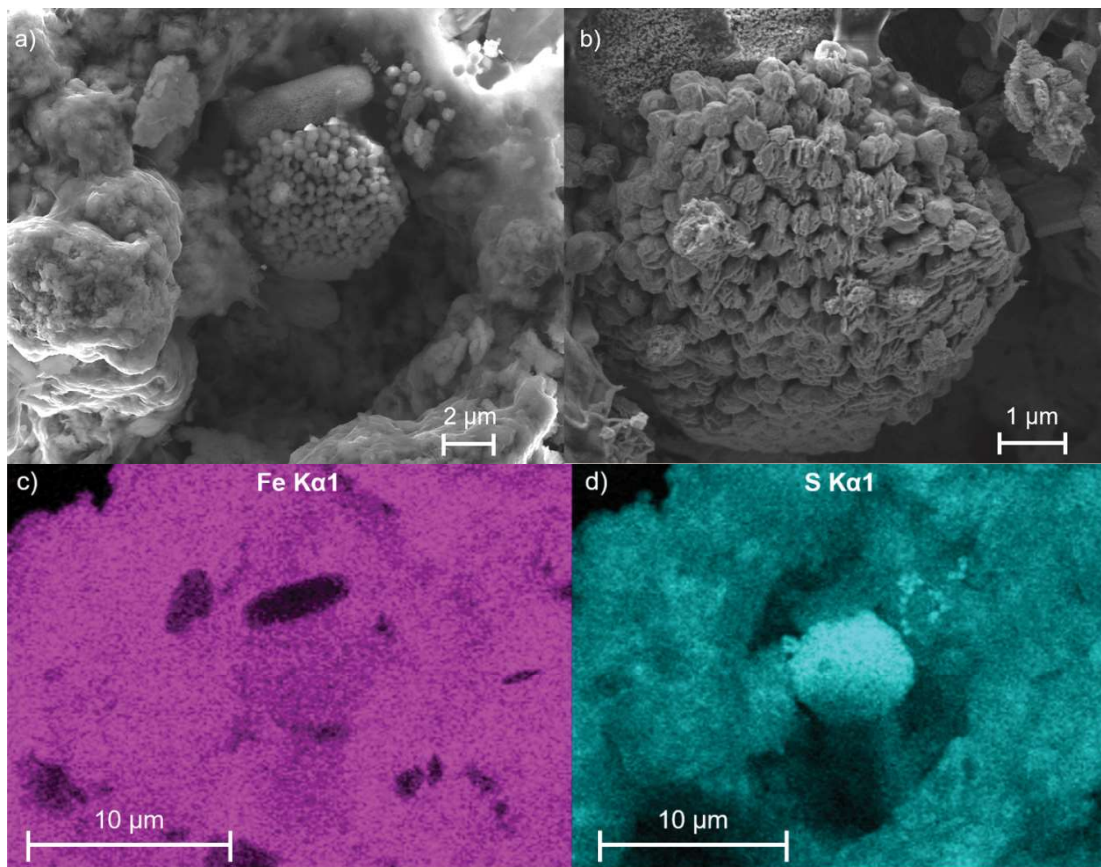


Fig. 6 Continued overleaf.

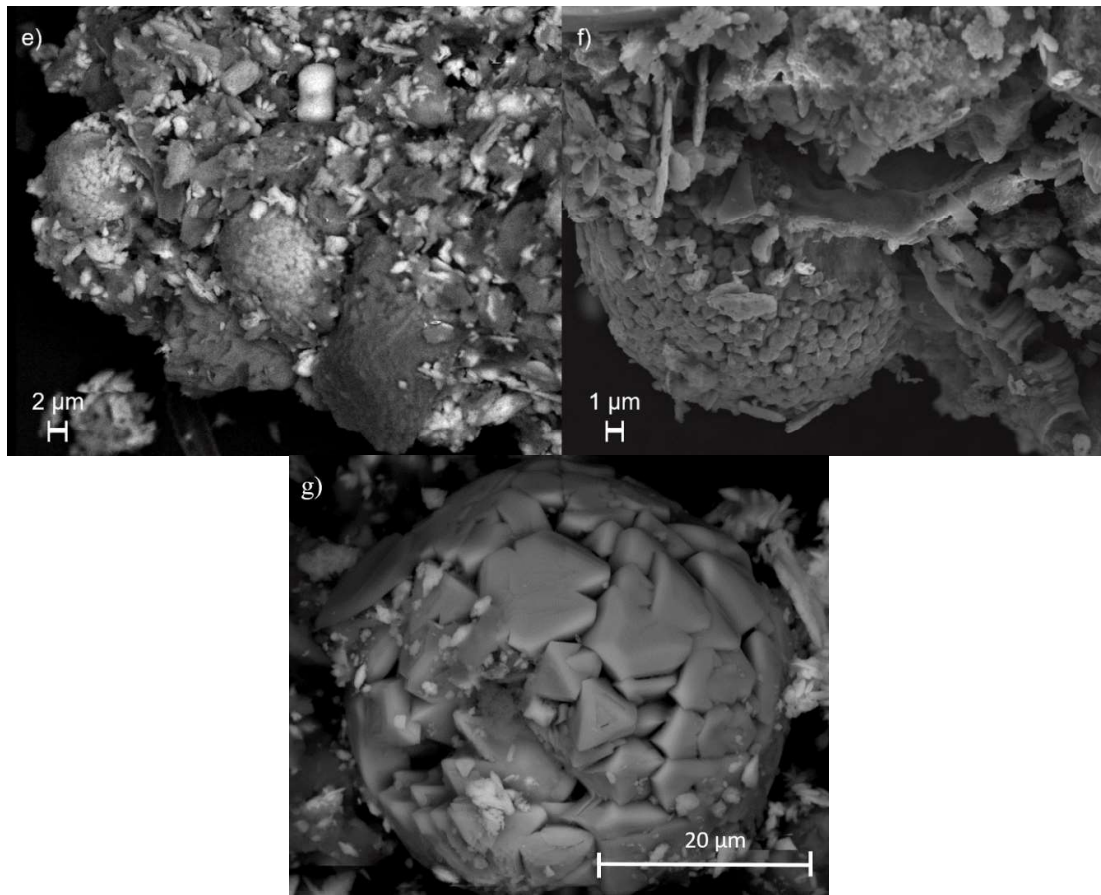


Fig. 6 SEM pictures of the sample from 15-20 cm depth representing a) framboid settled in the cauliflower-like structure, b) flake-like structure of the framboid, c) chemical distribution of iron, d) chemical distribution of sulphur, e) further example of framboids embedded in flakes, f) framboid and flake-like morphology under higher magnification. SEM Fig. 6a-f were performed by Dr. Luiz Grafulha Morales and Dr. Karsten Kunze from ScopeM, ETH Zurich, the SEM Fig. 6g is reproduced from the Master thesis of K. Mizutani (2019).

## 208 *Magnetic properties*

209 The magnetic properties are derived from room temperature analysis, which includes magnetic  
 210 hysteresis (Figs.3, A1) and a FORC measurements (Figs.A1, 7). The FORC analysis shows a typical  
 211 FORC diagram of an aggregate of SD particles, accompanied by the presence of secondary multi-  
 212 domain (MD) phase and/or superparamagnetic contribution (Fig.7) (Roberts et al., 2011; Roberts et al.,  
 213 2014). The peak of the FORC distribution, represented as the patch of maximum density is displaced  
 214 below the  $B_u = 0$ . Such a displacement indicates a positive mean field (Roberts et al., 2014). The blue-  
 215 colored feature marked in  $B_u < 0$  is an inherent manifestation of SD behavior (Newell, 2005) as has been

216 previously observed in experimentally determined FORC diagrams, and in the Chapter 3 for synthetic  
 217 greigite. The horizontal distribution of the coercivity presents clear Gaussian-like shape with maximum  
 218 at around 40 mT and small maximum at around 0 mT. That indicates presence of a dominant SD phase  
 219 with minor MD and/or SP contribution, respectively.

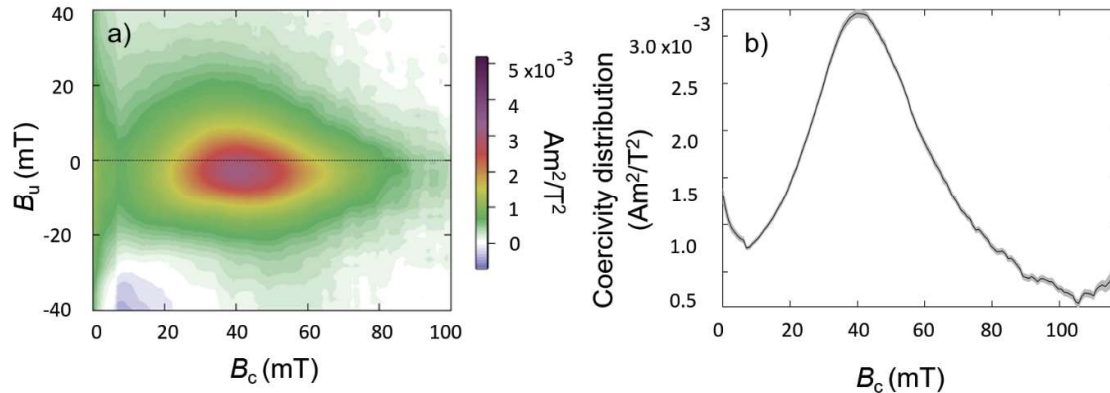


Fig. 7. For sample from 15-20 cm depth; a) FORC distribution that is typical for an aggregate of SD greigite and secondary MD phase, b) the coercivity spectrum, at  $B_u = 0$  mT, showing a maximum coercivity around 40 mT. In b) the gray shaded area defines the error envelope.

220 In addition to the room temperature hysteresis, a series of hysteresis measurements were made on this  
 221 sample between 300 K and 10 K. A summary of the hysteresis parameters is shown in Fig. 8. There is  
 222 a gradual increase in the saturation magnetization with decreasing temperature (Fig 8a), similar to what  
 223 was observed for synthetic greigite (Chapter 3) and sedimentary greigite from Taiwan with a small  
 224 amount of SP grain sizes that block with decreasing temperature (Roberts et al., 2011). Note, however,  
 225 that the increase becomes stronger below 40 K. Remanent magnetization shows a more irregular  
 226 increase, which is partly related to temperature stabilisation problems of the susceptometer (Fig. 8b).  
 227 Coercivity also shows a gradual increase with decreasing temperature, which supports the blocking of  
 228 SP particles. Note that both  $M_R$  and  $B_c$  show a stronger increase at the lowest temperatures (Fig. 8c).

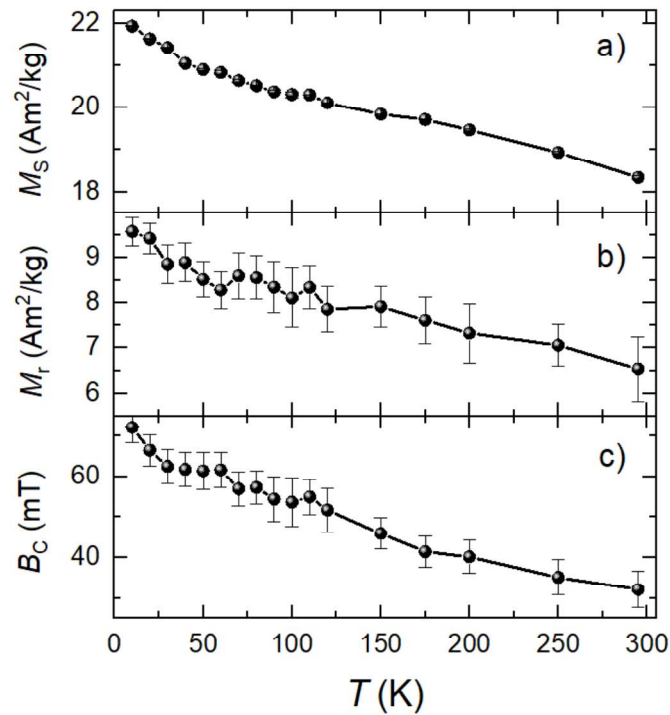


Fig.8. Change in hysteresis parameters as a function of temperature of the sample from 15-20 cm depth a) saturation magnetization, b) remanent magnetization, and c) coercivity. All of parameters slightly increase with the cooling, which is the result of decreasing thermal excitation. The error bars represent standard deviation for definition of the  $M_S$ ,  $M_R$ ,  $B_C$ , while for  $M_S$  errors are within the size of the point.

## 229 *Magnetisation as a function of temperature*

230 The cooling of SIRM shows a rapid decrease in the remanent magnetization that was acquired at 300  
 231 K, which suggests a high concentration of particles that unblock immediately below room temperature  
 232 (Fig. 9) (Roberts, 1995) or possible Morin transition indicating hematite (Morin, 1950). The  
 233 magnetization remains low but shows an increase at 118 K, which indicates the presence of magnetite  
 234 that passes through the Verwey transition. There is a marked drop in the remanent magnetization at 35  
 235 K, which suggest the magnetic blocking of an iron phase.

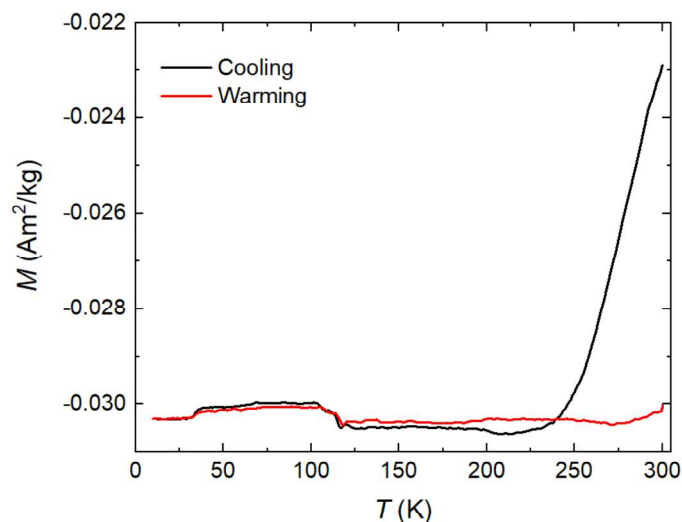


Fig. 9. Cooling and rewarming of SIRM as a function of temperature of the sample from 15-20 cm depth. Note demagnetization of finer SP particle in the cooling, Verwey transition at 118 K and magnetic blocking of a phase at 35 K. The error bars are within the size of the lines.

236 An induced magnetization was measured as a function of temperature in three applied fields, 10 mT,  
 237 50 mT and 1 T, to help further identify the ferromagnetic (*s.l.*) phases in the sample (Fig. 10). The  
 238 cooling and warming curves with the applied DC field of 10 mT represents low-temperature divergence  
 239 between cooling and warming curve (Fig. 10a), previously observed for synthetic greigite (Chapter 3).  
 240 The warming curve increases continuously back to room temperature. The small inflection of the curve  
 241 around 118 K represents the Verwey transition ( $T_v$ ), confirming the presence of MD magnetite. The  
 242 magnetization measured at 50 mT reveals similar changes as observed for 10 mT with the stronger  
 243 bending of the cooling curve (Fig. 10b). Here, the divergence between cooling and warming is shifted  
 244 to higher temperatures. For both measurements the small bending of the curve at around 35 K is  
 245 observed and it could originate from the paramagnetic contribution (PM). The magnetization as a  
 246 function of temperature measured at 1 T shows that the magnetization is the same for the cooling and  
 247 subsequent warming curve, indicating that the magnetization blocking, respectively unblocking  
 248 phenomena with the change in thermal activation of finer particles (Fig. 10c). The drop in  
 249 magnetization from low temperature to room temperature is 10.36 % and is similar in magnitude as has  
 250 been reported by Chang et al. (2008), who attributed it to increased thermal fluctuations. The induced

251 magnetization at lower applied fields is more sensitive in distinguishing magnetic transitions, because  
 252 the magnetization is not saturated.

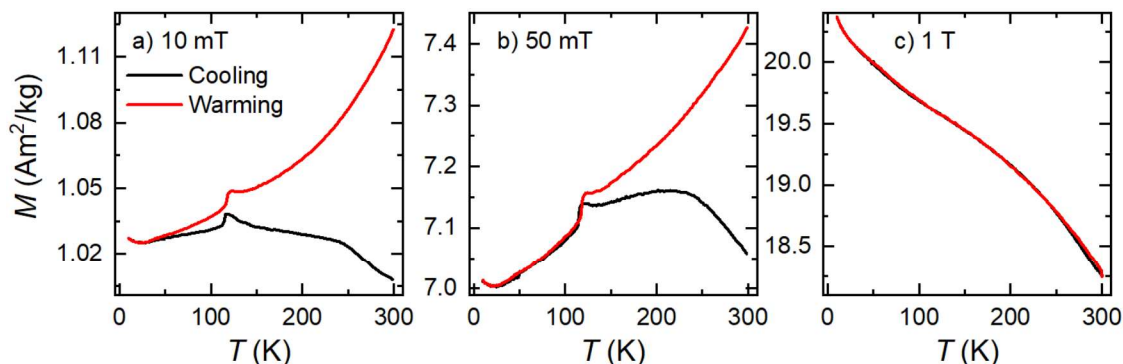


Fig. 10. The magnetization as a function of temperature with applied field of the sample from 15-20 cm depth a) field of 10 mT, b) field of 50 mT, and c) field of 1 T recorded for both during cooling down to 10K (black line) and warming back to room temperature (red line). The error bars are within the size of the lines.

### 253 *ESR spectroscopy at low temperature*

254 The ESR spectra were measured as a function of temperature to help further identify magnetic phases  
 255 in the sample. The peak in the ESR spectra continuously shifts to the lower fields and becomes broader  
 256 when cooling down (Fig. 11a). The resonance field ( $B_{\text{res}}$ ) decreases continuous down to approximately  
 257 90 K and subsequently shows sharp decline at lower temperature. This decrease is accompanied by a  
 258 corresponding increase in g-factor ( $g_{\text{eff}}$ ), which becomes much more pronounced below 90 K. The line-  
 259 width ( $\delta B$ ) increases similar to  $g_{\text{eff}}$ . All three parameters reveal strong dependence on temperature with  
 260 visible change below 90 K. Additionally,  $\delta B$  shows maximum at 30 K.

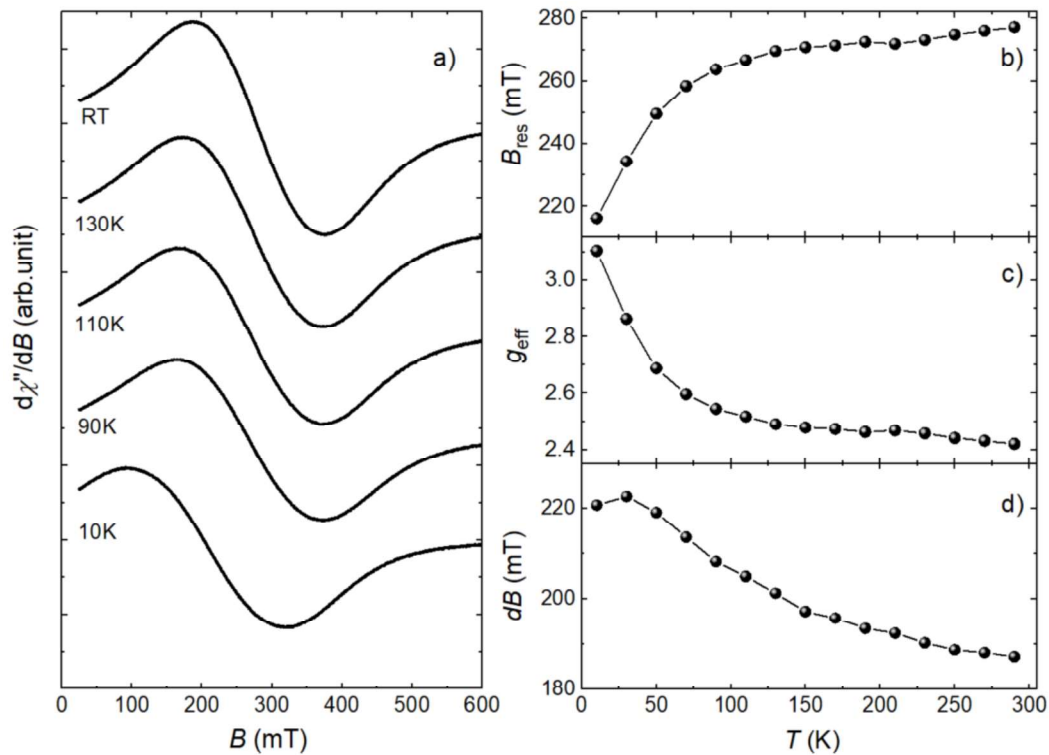


Fig. 11 The left panel represents the chosen spectra of the low temperature FMR profile of RT, 130K, 110K, 90K measured from sample from 15-20 cm depth e) 10K. While cooling the spectral shift towards lower fields. The right panel shows the b) resonance field, c)  $g_{eff}$  and d) line-width as a function of temperature.

#### 261 4.4. DISCUSSION

##### 262 Chemical and magnetic data of the sediment profile

263 Wilkins and Barnes (1997) and Hunger and Benning (2007) have postulated that framboidal pyrite  
 264 forms from nucleation and growth a monosulfide that reacts to form greigite, which is eventually  
 265 replaced by pyrite. At the remediated tailing pond at Lower Williams Lake, Canda, Paktunc and Davé  
 266 (2002) found that framboidal pyrite formed rapidly at the redox front from oxygen-bearing to hydrogen  
 267 sulphide –bearing fluids in the tailings. The presence of pyrite framboids together with greigite in  
 268 sediments from the interface with the tailing, suggests that greigite was part of the chemical pathway  
 269 leading to framboidal pyrite. As noted above greigite is only stable in slightly oxidizing condition in a  
 270 narrow stability field of Eh and in a pH range of 5.9 to 7.4.

271

272 The sediments from the core in this study show that the iron content decreases with depth (Fig. 2b),  
273 whereas the sulphur content increases through the organic sediments and remains high through the  
274 tailings (Fig.2c) (Mizutani, 2019). The maximum in the magnetic susceptibility ( $\chi$ ) is observed in the  
275 organic layer and corresponds to maximum sulfur content (Fig. 2d), but also a peak in TIC and Ca (Fig.  
276 2c). The minimum susceptibility is observed in the tailing sediments, which could be explained by the  
277 loss of a ferrimagnetic phase with the replacement by paramagnetic iron phases, such as pyrite. All  
278 samples are characterized by open hysteresis loops, indicating the presence of ferromagnetic (*s.l.*)  
279 minerals in all samples (Figs. 3, A1, Table A1). The samples from the organic sediments have the  
280 highest ferromagnetic (*s.l.*) concentration as seen from  $M_s$  (Table A2). The high magnetization ratios  
281 ( $M_R / M_s$ ) for the sediments between 5 and 25 cm depth is indicative of greigite as the main  
282 ferromagnetic (*s.l.*) phase in these organic-rich sediments. Samples from the tailings show more variety  
283 in terms of their hysteresis parameters, but ( $M_R / M_s$ ) is  $< 0.4$ , except for the sample at 40 - 45 cm, which  
284 has a high coercivity (0.66). This high ratio suggests the presence of an antiferromagnetic mineral, such  
285 as goethite, which has been identified in the tailings by Paktunc and Davé (2002). The ESR signal of  
286 the sediment profile changes accordingly to the  $\chi$ , where the samples characterized by the highest  $\chi$   
287 (5-10 cm, 10-15 cm, 15-20 cm) have a relatively broad and simple spectrum, which can be ascribed to  
288 a single ferromagnetic (*s.l.*) phase. The uppermost sample, and samples from the tailing are  
289 characterized by rather complex signal (Fig.4) that can represent the superposition of the iron-  
290 hydroxides, superparamagnetic particles (SP), and/or large particles of magnetite. The sharp 6-lines  
291 indicate the presence of manganese.

292 In summary, a ferromagnetic (*s.l.*) phase, whose magnetic properties are consistent with greigite is  
293 found in the organic rich sediments between 5 cm to 25 cm depth. The tailings show more variety with  
294 a higher contribution of paramagnetic phases to the induced magnetization (Table A1) and indication  
295 for different paramagnetic and ferromagnetic (*s.l.*) minerals. The variety of ferromagnetic (*s.l.*) minerals  
296 in the tailing is most likely related to the rocks which were mined.

297

298



---

**299 Chemical and magnetic data of the sample with the highest ferromagnetic (*s.l.*) concentration**

300 In order to better understand the ferrimagnetic mineral in the organic-rich sediment, a more detailed  
301 examination of the structural, magnetic and spectroscopic properties was made. Scanning Electron  
302 Microscopy (SEM) reveals presence of the cauliflower structure commonly formed by flakes (Fig. 6a,  
303 e, f). The flake structure was previously observed for synthetic greigite (Cao et al., 2009; Herbert Jr et  
304 al., 1998), but also in greigite that was identified in lacustrine sediments from Lake Lomond, Scotland  
305 (Snowball and Thompson, 1988).

306 The presence of greigite is also supported by the magnetic and spectroscopic data. The FORC analysis  
307 of the magnetically strongest sample reveals clear dominance of interacting SD particles, typical for  
308 single domain (SD) aggregates of greigite (Roberts et al., 2011; Roberts et al., 2014) (Fig.7). SIRM  
309 cooling and warming curves show rapid unblocking of SP greigite, which blocking volume is 17 nm  
310 (Roberts et al., 2011) (Fig. 9). The ESR spectra as a function of temperature show a continuous shift of  
311 the resonance signal to the slightly lower fields and it's broadening with cooling down (Fig. 8a), which  
312 was found in synthetic greigite (Chapter 3). The resonance field ( $B_{res}$ ), the corresponding g-factor ( $g_{eff}$ )  
313 and the line-width ( $\delta B$ ) reveal rather sharp change with cooling below 90 K, which is in contrast to the  
314 change around 50 K found in the synthetic sample (Chapter 3). The difference may reflect difference  
315 in structure, size, interactions, and impurities from additional iron phases.

316 The greigite is accompanied by the pyrite framboids (Fig. 6a, b, e, f), which is supported by the decrease  
317 in susceptibility. The pyrite starts as smaller framboids that eventually replace the greigite, and this is  
318 supported by remains of greigite flakes on the framboids. These results support Paktunc and Davé's  
319 (2002) idea that the pyrite framboids form from a greigite precursor.

320 In addition to the sulfide phases, SEM analysis also shows micro-sized spherules in the sediments high  
321 iron and oxygen composition, indicative of an iron oxide (Fig. 6f, g) (Mizutani, 2019). The presence of  
322 a Verwey transition, which is seen from the measurement of remanent and induced magnetization at  
323 low temperature (Figs. 9 and 10), confirms the presence of magnetite. Because these spherules resemble  
324 what has been seen for magnetite that forms as a by-product of combustion of fossil fuels (Horng et

---

325 al., 2009 pers. comm. Beata Górká-Kostruba; Locke and Bertine, 1986) their presence suggests that  
326 they come from atmospheric deposition. In addition to these phases, the increase in induced  
327 magnetization and the decrease in the remanent magnetization that occurs below 35 K, suggest magnetic  
328 ordering of another Fe phase. This could be an iron oxide, but is more likely siderite, which has a Néel  
329 temperature of 38 K (Jacobs, 1963). The presence of siderite is supported by the work of Paktunc and  
330 Davé (2002), who found that the groundwater at the site is saturated in siderite, and calcian siderite in  
331 the tailings, and confirmed by K. Mizutani (2019).

332

### 333 **Chemical pathway**

334 In summary, the sediments from the Lake Williams contain greigite, particularly in the organic-rich  
335 sediment, and it is characterized by flake structure coexisting with pyrite framboids. Although pyrite  
336 has been reported in the tailings, we demonstrate that it is already forming in the organic sediment. It is  
337 well known that greigite is formed along pathway in a reaction between mackinawite and excess sulfur  
338 to form pyrite (Hunger and Benning, 2007). This reaction process proceeds via sulfur addition or iron  
339 loss (Wilkin and Barnes, 1997). In this study, the constant decrease in iron together with increase in  
340 sulfur (Fig.1b, c) lead to an increase in magnetic susceptibility from top down to 12.5 cm, which can be  
341 associated with transformation of non / weakly magnetic mackinawite to ferrimagnetic greigite.  
342 Magnetic properties of mackinawite are not well known because it is metastable. The further decrease  
343 of  $\chi$  with depth can be associated with the further transformation of ferrimagnetic greigite to  
344 paramagnetic pyrite. The framboidal structure of pyrite replaces the cauliflower-like greigite to keep its  
345 morphology, thus acting as a template for the mineral-chemical transition between the two sulfur  
346 phases. We have also demonstrated that the greigite consists of an aggregate of greigite flakes. Such a  
347 texture was previously observed for synthetic SD greigite flakes by Snowball and Thompson (1988).  
348 The observed broadening of the ESR spectra, which is observed below 90 K, suggests a change in  
349 anisotropy contributions. At present it is not clear if this feature would be found in all types greigite or  
350 if it may arise from the sheet-like morphology of the aggregated flakes. These results confirm previously  
351 defined characteristic features of greigite (Chapter 3), which can be used to detect nano-sized,

---

352 polycrystalline greigite in natural environments. Moreover, Paktunc and Davé concluded that the  
353 remediation of the former tailing pond in the vegetated area can be considered a success (Paktunc and  
354 Davé, 2002), because the part of the pond that was covered with glacial sand and gravel and  
355 subsequently vegetated area, has created reducing conditions that together with microbial degradation  
356 of organic material led to an increase in alkalinity. This counters the previous oxidation, hence acidity,  
357 in the tailings. We demonstrate that the reducing conditions are also found in the adjacent pond  
358 sediments that were not covered by glacial sand and gravel.

359

#### 360 **4.5. CONCLUSION**

361 A core from a former tailing pond at Lower Lake Williams, Ontario, consists of an organic-rich  
362 sediment overlying the tailings. Greigite, which forms of intergrown flakes, is found in the organic  
363 sediments, whereas paramagnetic iron minerals dominate the tailings. Within the organic-rich  
364 sediments there is an increase in susceptibility and  $M_s$ , which indicates the formation of greigite with a  
365 peak in its concentration between 15 to 20 cm. The concentration, however decreases at the bottommost  
366 part of this layer. This change in the magnetic properties can be explained by the replacement of the  
367 greigite by pyrite in the form of framboids; the pyrite framboids are the dominant phase in the tailing.  
368 The results from this study results indicate that the process of pyritization of greigite into pyrite  
369 framboids is observed under a change in redox conditions. Moreover, this study elucidates the evolution  
370 of environmental condition associated with the rehabilitating process in a former tailings pond.

371

#### 372 **4.6. AUTHOR CONTRIBUTIONS**

373 Kazuhito Mizutani and Susan Glasauer from University of Guelph (Guelph, Canada) collected the  
374 samples, and provided the SEM Fig. 6g, and elemental analysis. These data are part of the master thesis  
375 of Kazuhito Mizutani (Mizutani, 2019). The SEM Fig. 6a-f pictures were taken at the Scientific Center  
376 for Optical and Electron Microscopy, ETH Zurich (Zurich, Switzerland) by Dr. Luiz Grafulha Morales  
377 and Dr. Karsten Kunze. Dimitrios Koulialias from ETH Zurich (Zurich, Switzerland) performed part of  
378 the low-temperature PPMS measurements.

379 **4.7. REFERENCES**

- 380 Berner, R.A., 1984. Sedimentary pyrite formation: an update. *Geochimica et Cosmochimica Acta* 48,  
381 605-615
- 382 Cao, F., Hu, W., Zhou, L., Shi, W., Song, S., Lei, Y., Wang, S., Zhang, H., 2009. 3D Fe<sub>3</sub>S<sub>4</sub> flower-  
383 like microspheres: high-yield synthesis via a biomolecule-assisted solution approach, their  
384 electrical, magnetic and electrochemical hydrogen storage properties. *Dalton Transactions*, 9246-  
385 9252
- 386 Chang, L., Roberts, A.P., Tang, Y., Rainford, B.D., Muxworthy, A.R., Chen, Q., 2008. Fundamental  
387 magnetic parameters from pure synthetic greigite (Fe<sub>3</sub>S<sub>4</sub>). *Journal of Geophysical Research:*  
388 *Solid Earth* 113
- 389 Harrison, R.J., Feinberg, J.M., 2008. FORCinel: An improved algorithm for calculating first-order  
390 reversal curve distributions using locally weighted regression smoothing. *Geochemistry,*  
391 *Geophysics, Geosystems* 9
- 392 Herbert Jr, R.B., Benner, S.G., Pratt, A.R., Blowes, D.W., 1998. Surface chemistry and morphology of  
393 poorly crystalline iron sulfides precipitated in media containing sulfate-reducing bacteria.  
394 *Chemical Geology* 144, 87-97
- 395 Hoffmann, V., 1992. Greigite (Fe<sub>3</sub>S<sub>4</sub>): magnetic properties and first domain observations. *Physics of*  
396 *the Earth and Planetary Interiors* 70, 288-301
- 397 Horng, C.-S., Huh, C.-A., Chen, K.-H., Huang, P.-R., Hsiung, K.-H., Lin, H.-L., 2009. Air pollution  
398 history elucidated from anthropogenic spherules and their magnetic signatures in marine  
399 sediments offshore of Southwestern Taiwan. *Journal of Marine Systems* 76, 468-478
- 400 Hunger, S., Benning, L.G., 2007. Greigite: a true intermediate on the polysulfide pathway to pyrite.  
401 *Geochemical Transactions* 8, 1, doi:10.1186/1467-4866-8-1
- 402 Jacobs, I., 1963. Metamagnetism of siderite (FeCO<sub>3</sub>). *Journal of Applied Physics* 34, 1106-1107
- 403 Jiang, W.-T., Horng, C.-S., Roberts, A.P., Peacor, D.R., 2001. Contradictory magnetic polarities in  
404 sediments and variable timing of neof ormation of authigenic greigite. *Earth and Planetary*  
405 *Science Letters* 193, 1-12
- 406 Kao, S.-J., Horng, C.-S., Roberts, A.P., Liu, K.-K., 2004. Carbon–sulfur–iron relationships in  
407 sedimentary rocks from southwestern Taiwan: influence of geochemical environment on greigite  
408 and pyrrhotite formation. *Chemical Geology* 203, 153-168
- 409 Large, R.R., Maslennikov, V.V., Robert, F.o., Danyushevsky, L.V., Chang, Z., 2007. Multistage  
410 sedimentary and metamorphic origin of pyrite and gold in the giant Sukhoi Log deposit, Lena  
411 gold province, Russia. *Economic Geology* 102, 1233-1267
- 412 Livens, F.R., Jones, M.J., Hynes, A.J., Charnock, J.M., Mosselmans, J.F.W., Hennig, C., Steele, H.,  
413 Collison, D., Vaughan, D.J., Patrick, R.A., 2004. X-ray absorption spectroscopy studies of  
414 reactions of technetium, uranium and neptunium with mackinawite. *Journal of Environmental*  
415 *Radioactivity* 74, 211-219, doi:10.1016/j.jenvrad.2004.01.012
- 416 Locke, G., Bertine, K., 1986. Magnetite in sediments as an indicator of coal combustion. *Applied*  
417 *Geochemistry* 1, 345-356
- 418 Meads, R., Malden, P., 1975. Electron spin resonance in natural kaolinites containing Fe<sup>3+</sup> and other  
419 transition metal ions. *Clay Minerals* 10, 313-345
- 420 Mizutani, K., 2019. Biogeochemical Influence on the Mobility of Uranium in the Marsh Soil of the  
421 Lower Williams Lake, Elliot Lake.
- 422 Morin, F., 1950. Magnetic susceptibility of  $\alpha$  Fe<sub>2</sub>O<sub>3</sub> and  $\alpha$  Fe<sub>2</sub>O<sub>3</sub> with added titanium. *Physical*  
423 *Review* 78, 819
- 424 Newell, A.J., 2005. A high-precision model of first-order reversal curve (FORC) functions for single-  
425 domain ferromagnets with uniaxial anisotropy. *Geochemistry, Geophysics, Geosystems* 6
- 426 Paktunc, A.D., Davé, N.K., 2002. Formation of secondary pyrite and carbonate minerals in the Lower  
427 Williams Lake tailings basin, Elliot Lake, Ontario, Canada. *American Mineralogist* 87, 593-602
- 428 Pike, C.R., Roberts, A.P., Verosub, K.L., 1999. Characterizing interactions in fine magnetic particle  
429 systems using first order reversal curves. *Journal of Applied Physics* 85, 6660-6667
- 430 Pokorny, J., Pokorny, P., Suza, P., Hrouda, F., 2011. A multi-function kappabridge for high precision  
431 measurement of the ams and the variations of magnetic susceptibility with field, temperature and  
432 frequency.

- 433 Pósfai, M., Buseck, P.R., Bazylinski, D.A., Frankel, R.B., 1998. Reaction sequence of iron sulfide  
434 minerals in bacteria and their use as biomarkers. *Science* 280, 880-883
- 435 Raiswell, R., Berner, R.A., 1985. Pyrite formation in euxinic and semi-euxinic sediments. *American*  
436 *Journal of Science* 285, 710-724
- 437 Raiswell, R., Canfield, D.E., 1998. Sources of iron for pyrite formation in marine sediments. *American*  
438 *Journal of Science* 298, 219-245
- 439 Roberts, A.P., 1995. Magnetic properties of sedimentary greigite (Fe<sub>3</sub>S<sub>4</sub>). *Earth and Planetary Science*  
440 *Letters* 134, 227-236
- 441 Roberts, A.P., Chang, L., Rowan, C.J., Horng, C.S., Florindo, F., 2011. Magnetic properties of  
442 sedimentary greigite (Fe<sub>3</sub>S<sub>4</sub>): An update. *Reviews of Geophysics* 49
- 443 Roberts, A.P., Heslop, D., Zhao, X., Pike, C.R., 2014. Understanding fine magnetic particle systems  
444 through use of first-order reversal curve diagrams. *Reviews of Geophysics* 52, 557-602
- 445 Roberts, A.P., Liu, Q., Rowan, C.J., Chang, L., Carvallo, C., Torrent, J., Horng, C.S., 2006.  
446 Characterization of hematite ( $\alpha$ -Fe<sub>2</sub>O<sub>3</sub>), goethite ( $\alpha$ -FeOOH), greigite (Fe<sub>3</sub>S<sub>4</sub>), and pyrrhotite  
447 (Fe<sub>7</sub>S<sub>8</sub>) using first-order reversal curve diagrams. *Journal of Geophysical Research: Solid Earth*  
448 111
- 449 Roberts, A.P., Reynolds, R.L., Verosub, K.L., Adam, D.P., 1996. Environmental magnetic implications  
450 of greigite (Fe<sub>3</sub>S<sub>4</sub>) formation in a 3 my lake sediment record from Butte Valley, northern  
451 California. *Geophysical Research Letters* 23, 2859-2862
- 452 Rowan, C.J., Roberts, A.P., 2006. Magnetite dissolution, diachronous greigite formation, and secondary  
453 magnetizations from pyrite oxidation: Unravelling complex magnetizations in Neogene marine  
454 sediments from New Zealand. *Earth and Planetary Science Letters* 241, 119-137
- 455 Rowan, C.J., Roberts, A.P., Broadbent, T., 2009. Reductive diagenesis, magnetite dissolution, greigite  
456 growth and paleomagnetic smoothing in marine sediments: A new view. *Earth and Planetary*  
457 *Science Letters* 277, 223-235
- 458 Schoonen, M.A., 2004. Mechanisms of sedimentary pyrite formation. SPECIAL PAPERS-  
459 GEOLOGICAL SOCIETY OF AMERICA, 117-134
- 460 Snowball, I., Thompson, R., 1988. The occurrence of greigite in sediments from Loch Lomond. *Journal*  
461 *of Quaternary Science* 3, 121-125
- 462 Snowball, I.F., 1991. Magnetic hysteresis properties of greigite (Fe<sub>3</sub>S<sub>4</sub>) and a new occurrence in  
463 Holocene sediments from Swedish Lapland. *Physics of the Earth and Planetary Interiors* 68, 32-  
464 40
- 465 Sweeney, R., Kaplan, I., 1973. Pyrite framboid formation; laboratory synthesis and marine sediments.  
466 *Economic Geology* 68, 618-634
- 467 Wilkin, R., Barnes, H., 1997. Formation processes of framboidal pyrite. *Geochimica et Cosmochimica*  
468 *Acta* 61, 323-339
- 469 Wilkin, R., Barnes, H., Brantley, S., 1996. The size distribution of framboidal pyrite in modern  
470 sediments: an indicator of redox conditions. *Geochimica et Cosmochimica Acta* 60, 3897-3912
- 471
- 472
- 473
- 474
- 475
- 476
- 477
- 478
- 479
- 480
- 481
- 482
- 483
- 484
- 485

## 486 4.8. APPENDIX

No.	Depth	Hysteresis parameters						Percentage of FM phase
		$M_S$	$M_R$	$B_C$	$B_{CR}$	$B_{CR} / B_C$	$M_R / M_S$	%
units	cm	$\cdot 10^{-3}$ Am <sup>2</sup> /kg	$\cdot 10^{-3}$ Am <sup>2</sup> /kg	mT	mT			
1	0-5	68.55	17.55	23.30	43.50	1.87	0.26	30.98
2	5-10	168.08	67.91	33.08	52.57	1.59	0.40	60.11
3	10-15	194.78	87.90	32.54	47.50	1.46	0.45	72.73
4	15-20	144.83	62.58	32.49	47.77	1.47	0.43	79.00
5	20-25	10.22	3.65	31.22	49.46	1.58	0.36	73.83
6	25-30	9.98	3.16	5.78	25.53	4.42	0.32	38.20
7	30-35	9.23	2.26	18.23	41.02	2.25	0.25	20.60
8	35-40	14.31	2.75	15.71	41.47	2.64	0.19	32.87
9	40-45	5.09	3.38	36.51	50.71	1.39	0.66	56.29
10	45-50	10.22	3.08	24.11	50.62	2.10	0.30	41.79

Table A1. The hysteretic parameters obtained for the depth profile at room temperature and Percentage of ferromagnetic

(s.l.) (FM) phase calculated from  $M_S/M_{750}$ 

487

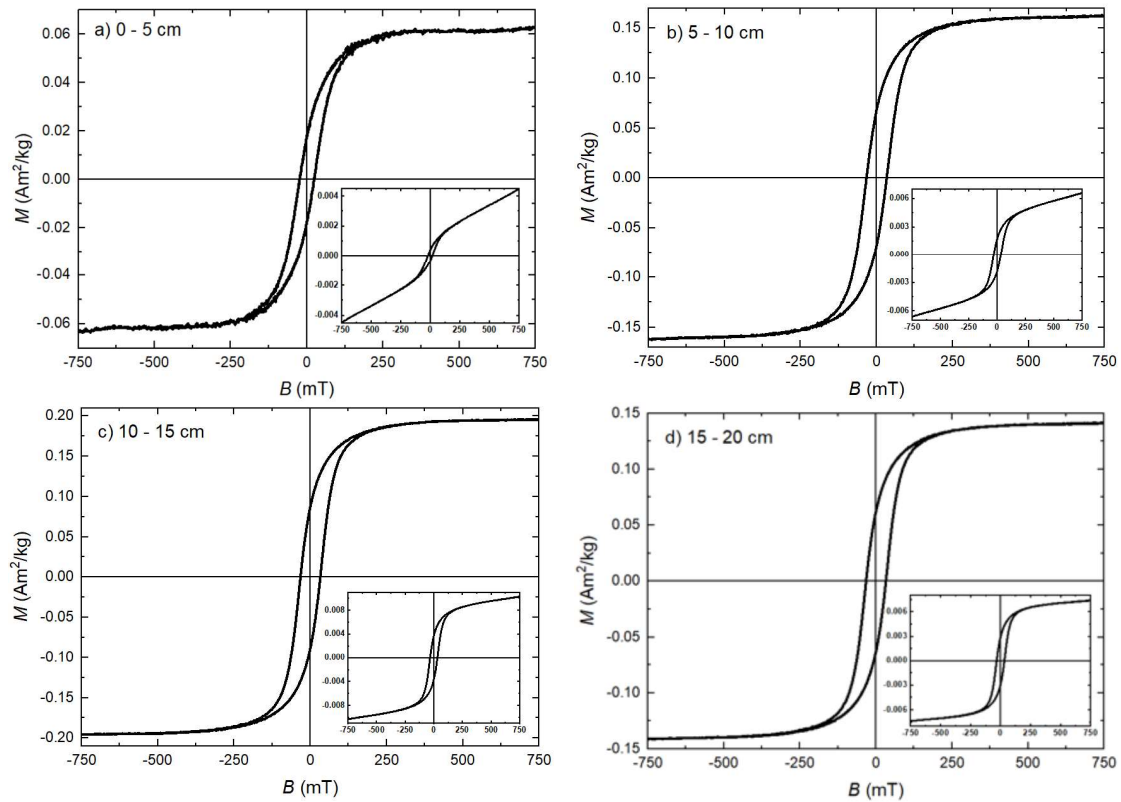


Fig. A1 Continued overleaf.

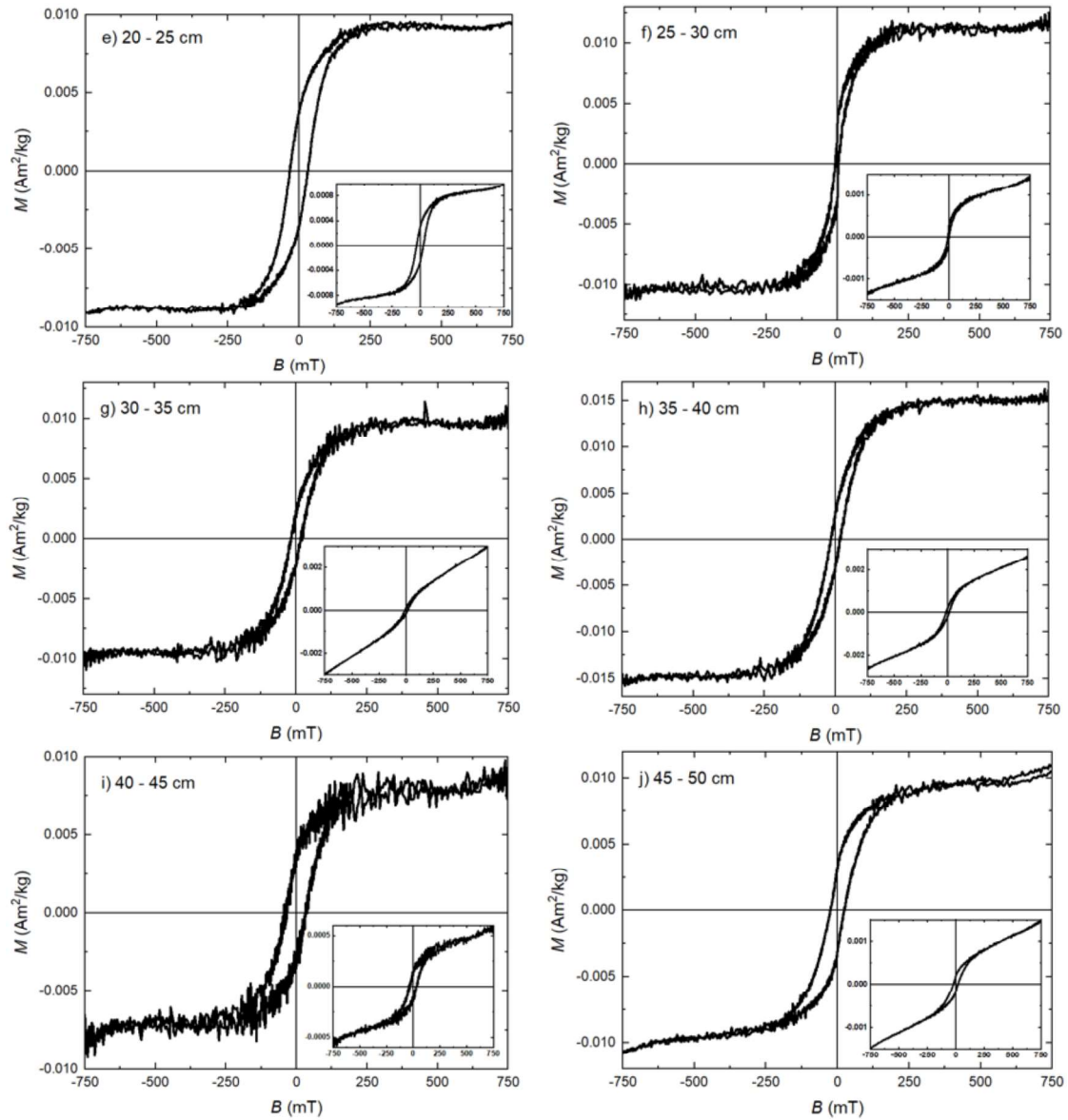


Fig. A1 The hysteresis loop obtained at room temperature for the depth profile after the paramagnetic slope correction. The insets show the slope before the paramagnetic correction.

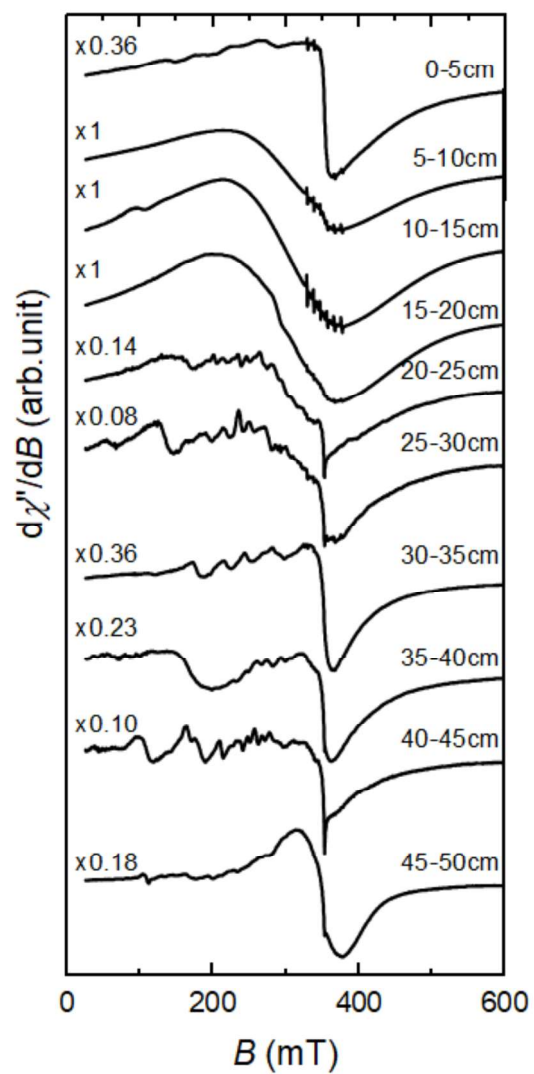


Fig. A2 The ESR spectra obtained for whole depth profile. Please note the intensity fraction of the signals, shown as a „x 0.XX”. The intensity fractions represent the how intense is the signal in comparison to the strongest samples, marked as “x 1”.



## 1 5. From Magnetotactic Bacteria to Magnetofossils: An Experimental

### 2 Approach

#### 3 **Abstract**

4 Magnetofossils, the fossil remains of magnetotactic bacteria (MTB) in sediments, provide information  
5 about past environmental conditions. Different rock magnetic tests have been developed in order to  
6 identify their presence. Many species of MTB build chains, but when their organic matter decays after  
7 their death and deposition, any chain arrangement can be destroyed. Hysteresis loops, first-order  
8 reversal curve (FORC) diagrams and ferromagnetic resonance (FMR) spectroscopy are used to analyze  
9 the magnetic response of the lab-cultured MTB during heat treatment, which imitates the diagenetic  
10 decomposition of the organic matter. For the analysis, wild-type bacteria and a mutant strain are used,  
11 which synthesize particles either in chains or aggregates, respectively. The FORC diagrams reveal the  
12 presence of a central ridge for wild-type bacteria and a vortex-like structure for mutants. After heating,  
13 both samples show a similar distribution with a decrease in the coercivity that arises from particle  
14 interaction. The FMR spectra for wild-type bacteria reveal a high uniaxial shape anisotropy,  
15 characteristic of chain arrangement, while for mutants we observe lower shape anisotropy, but also  
16 indications of small chains. With heating, both signals become symmetric with rather low uniaxiality,  
17 which indicates chain decomposition. Further heating leads to oxidation of the particles. We  
18 demonstrate how our experimental approach can be used to determine the presence of magnetofossils  
19 in natural systems in which the organic material has decomposed, and how it can aid in distinguishing  
20 MTB remains from diagenetic particles within the geological record.

21

#### 22 **5.1. INTRODUCTION**

23 Magnetotactic bacteria (MTB) are an important carrier of information about the environment, microbial  
24 evolution and variations of Earth's magnetic field (Faivre et al., 2008; Faivre and Schuler, 2008; Hesse,  
25 1994; Kopp and Kirschvink, 2008; Pan et al., 2005). Their inorganic remains, known as magnetofossils

26 (Kirschvink and Chang, 1984), can be detected in lakes/marine sediments years after sedimentation and  
27 can be preserved as a magnetic signal within the geological record (Kobayashi et al., 2006; Yan et al.,  
28 2012). MTB synthesize nano-sized, membrane-encapsulated ferrimagnetic particles that for many  
29 species align in chains (Bazylinski et al., 1994; Schüler and Frankel, 1999). Magnetosomes are  
30 synthesized by genetically controlled mineralization and are characterized by well-defined grain size,  
31 high crystalline purity, and narrow size and shape distribution. They often have a size in the range of  
32 stable single domain (SSD) (Pan et al., 2005), and are composed of magnetite ( $\text{Fe}_3\text{O}_4$ ) or less commonly  
33 greigite ( $\text{Fe}_3\text{S}_4$ ) (Devouard et al., 1998). The organic matter encapsulating these nanoparticles, for species  
34 that form chains of magnetosomes, helps to maintain their alignment (Schüler and Frankel, 1999). When  
35 the bacteria die, the organic matter eventually decays, which can lead to chain disintegration into clumps  
36 (Kobayashi et al., 2006).

37 For any environmental or paleomagnetic study, it is important to understand which magnetic minerals  
38 are present in geological materials. Although many techniques have been developed in rock magnetism  
39 for this purpose, it is more difficult to attribute the source of a ferromagnetic (*s.l.*) mineral to bacterially  
40 produced magnetosomes. In natural systems, MTB and their magnetofossils are generally identified by  
41 microscopy and magnetic methods. Electron microscopy is the best method of identification and allows  
42 for a detailed characterisation of the magnetosomes' morphology (Bazylinski et al., 1994; Mann et al.,  
43 1987). In practice, however, it is often difficult to find MTB or magnetosomes, which can be unevenly  
44 distributed in sediments or have very low concentration. For this reason, different magnetic tests have  
45 been proposed for defining their properties. These include: 1) narrow size and shape distribution of the  
46 ferromagnetic (*s.l.*) particles; and 2) in the case of chains of magnetosomes, pronounced uniaxial  
47 anisotropy ( $B_{\text{uni}}$ ), which arises from the particle alignment (Kopp and Kirschvink, 2008). Chain  
48 configuration gives a distinct magnetic signature of MTB (Egli et al., 2010; Gehring et al., 2011;  
49 Moskowitz et al., 1993), which is why many tests concentrate on this aspect. Magnetic methods are  
50 sensitive to the presence of ferrimagnetic phases, thus these phases will dominate the magnetic  
51 properties in a bulk sediment. The standard approach to identify chains in bulk sediments is the  
52 Moskowitz test (Moskowitz et al., 1993). This test analyses the changes in magnetic remanence

53 properties of magnetite, while warming through the Verwey transition after zero-field cooling and field  
54 cooling, respectively. In the case of MTB, the ratio of the difference in remanent magnetization ( $M$ )  
55 above and below the Verwey transition for the field-cooled  $M$  relative to the zero-field-cooled  $M$   
56 ( $\delta_{FC}/\delta_{ZFC}$ ) is defined as  $\delta_{FC,ZFC} = (M_{FC,ZFC}(80K) - M_{FC,ZFC}(150K)) / M_{FC,ZFC}(80K)$ , where  
57  $M(T)$  is the moment measured at temperature  $T$  following either FC or ZFC treatment. If chains of MTB  
58 are present,  $(\delta_{FC}/\delta_{ZFC}) > 2.0$ . The Moskowitz test, however, does not take into account the presence  
59 of the oxidised chains or possibility that chains are mixed with particles of detrital origin (Kopp and  
60 Kirschvink, 2008; Weiss et al., 2004a). Chang et al. (2013) proposed an alternative method based on  
61 the low temperature measurements that allows to detect magnetofossils. The method, referred as a  
62 dipole-spring mechanism, is less sensitive to the oxidation of magnetite and therefore allows to detect  
63 even oxidised chains. The dipole-spring mechanism restores the room temperature remanence after  
64 cooling and consequent warming through the Verwey transition, however, it only allows to identify  
65 intact magnetosomes. Another possibility for defining the presence of magnetofossils is by using the  
66 hysteresis or remanence properties (Lascu et al., 2010). Among the different methods, first order  
67 reversal curves (FORCs) are commonly used to identify chain arrangement, as they are sensitive to  
68 interactions (Pike et al., 1999) and variations in domain state (Roberts et al., 2000). The analysis of  
69 sediments with abundant magnetofossils reveals a characteristic elongated central ridge along the  
70 coercivity axis (Chen et al., 2007; Egli et al., 2010). A central ridge, however, can arise from any  
71 particles that have high shape anisotropy such as elongated magnetic particles in volcanic rock (Chang  
72 et al., 2014). Ferromagnetic resonance spectroscopy (FMR) has also been proposed as a good method  
73 for identifying chains of magnetosomes (Fischer et al., 2008; Kopp and Kirschvink, 2008; Kopp et al.,  
74 2006; Weiss et al., 2004a). FMR reveals characteristic spectral features, which are caused by the  
75 difference in magnetisation parallel and perpendicular to the axes of assemblies of magnetosomes.  
76 However, as chains in sediments are randomly orientated, less-pronounced traits can be found, when  
77 magnetosomes are preserved in different configurations (Kopp and Kirschvink, 2008), and/or  
78 accompanied by diagenetic particles (Gehring et al., 2011; Kind et al., 2011). In this case, the magnetic  
79 contributions are much harder to deconvolve. Although many studies use multiple methods to

80 characterise magnetofossils, some ambiguity often remains. This is especially the case, if the chain  
81 structure is no longer preserved.

82 In this study, we perform heating experiments on laboratory grown and genetically modified bacteria  
83 to simulate the decomposition of uniaxial anisotropy with the disruption of the chain configuration. The  
84 thermal decomposition allows us to observed stepwise changes in the decomposition process. FMR  
85 spectroscopy, hysteresis loops and analysis of FORCs are used to characterize any change in the  
86 magnetic properties. For comparison reasons, we apply the same experimental measurements on both  
87 cultured wild-type magnetotactic bacteria and mutant *M. gryphiswaldense* (Schüler, 2008), which  
88 synthesize magnetosomes either in chains or aggregates, respectively. This approach will provide a  
89 means to evaluate the degradation of magnetosome chains in natural systems.

90

## 91 5.2. SAMPLES AND METHODS

92 Two types of MTB were cultured in the laboratory at the University of Bayreuth. The wild type MTB  
93 (WT) produces chains of magnetite particles, which are similar to species that are found in nature  
94 (Fig. 1a). The mutant MTB ( $\Delta$ mamJ) has had the  $\Delta$ mamJ gene removed, which suppresses the formation  
95 of chains, and leads to aggregates of magnetosomes (Fig. 1b) (Scheffel et al., 2006; Scheffel and Schüler,  
96 2007). The magnetite particles are enveloped by lipid biomembrane in both types of bacteria. The  
97 bacteria were stored in a freezer at  $-18^{\circ}\text{C}$ , and subsequently freeze-dried prior the analysis.

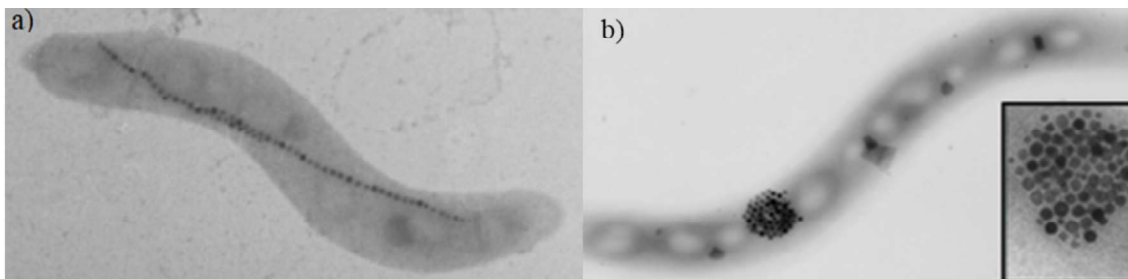


Fig.1 Transmission electron micrograph (TEM) of the a) chain assembly in the wild type bacteria b) particles agglomerate in clumps in the mutant MTB. Figures reproduced from Fig. 5 and Fig. 6 from Schüler (2008). No scale was presented by the authors.

---

98 A Princeton Measurement Corporation (PCM), MicroMag VSM, model 3900 at the Laboratory of  
99 Natural Magnetism, ETH Zurich, was used to obtain hysteresis loops and FORC. For the hysteresis  
100 loops, the magnetization was measured as a function of field between  $\pm 1$  T with a variable sample  
101 interval of 0.5 mT steps between  $\pm 100$  mT, 2 mT steps from  $\pm 100$  to  $\pm 200$  mT, and 5 mT steps for  
102 fields between  $\pm 200$  and 1000 mT. An averaging time of 500 ms was used for all the intervals.  
103 Saturation magnetization ( $M_s$ ) and the coercivity ( $B_c$ ) are defined from the loop. We measured the first  
104 order reversal curves (FORC) before heating and after heating the samples up to 320°C. A series of 130  
105 curves were measured using a 1.93 mT sampling interval and 200 mT averaging time. The FORC data  
106 were processed with the FORCinel program of Harrison and Feinberg (Harrison and Feinberg, 2008),  
107 using the VariFORC option with a smoothing factor of 3 for the central ridge, 4 for the vertical peak  
108 and 7 for the background. Note that the magnetization of the samples was normalised by total weight,  
109 which includes both magnetite particles and organic matter. Ferromagnetic resonance spectroscopy  
110 (FMR) was used to evaluate anisotropy fields associated with the magnetosomes in their different  
111 configurations (Bickford Jr, 1950; Vonsovskii, 1966). The freeze-dried MTB were mounted with  
112 paraffin in glass tube. The magnetic parameters that are commonly obtained from these measurements  
113 include the  $g$ -factor, which measures the energy splitting of degenerate states in the magnetic field, the  
114  $B_{res}$ , which is the field at the maximum absorption, and the line-width  $\delta B$ , which is a peak-to-peak  
115 linewidth of the resonance spectrum. The measured net signal is a superposition of all resonance events,  
116 i.e., the measured spectrum is the sum of the spectra originating from particles in all orientations. The  
117 absorption of microwave radiation is generally plotted as the first derivative spectrum of intensity. The  
118 X-band Bruker ElexSys E500 spectrometer was used to record spectra with frequency at around 9.17  
119 GHz at the Electron Paramagnetic Resonance research group, Laboratory of Physical Chemistry, ETH  
120 Zurich. The spectrometer is equipped with temperature controllers and heating apparatus from Oxford  
121 Instruments. The FMR spectra were recorded at room temperature and during heating in a nitrogen  
122 atmosphere, in order to prevent oxidation. The FMR spectra were further processed using a simulation  
123 program from Charilaou et al. (2011) in order to define the contributions of different components of  
124 magnetization. Two magnetic anisotropies were considered (Dunin-Borkowski et al., 1998): 1) the  
125 magnetocrystalline anisotropy of magnetite ( $B_{cub}$ ), which is an internal feature of the mineral; and 2)

126 the uniaxial shape anisotropy ( $B_{uni}$ ) originating from the chain itself. The latter is often the factor that is  
 127 used as an indication for the presence of chain magnetofossils. For the simulation the thermally induced  
 128 changes in magnetocrystalline anisotropy ( $B_{cub}$ ) were taken into account. In order to quantify the change  
 129 in strength of the FMR absorption spectra, the absolute areas under the signal were calculated as a  
 130 function of the temperature (Fig.5). The absolute areas are defined by:

$$A = \int_{x_1}^{x_n} |[f(x) - f(x_0)]| dx$$

### 132 5.3. RESULTS

#### 133 Magnetic Hysteresis

134 Hysteresis loops were measured at room temperature for WT and  $\Delta mamJ$  before and after heat treatment  
 135 (HT) (Fig. 2). Before HT, the loops are open and the magnetization reaches saturation by 150 mT  
 136 (Table 1). WT is characterised by remanent magnetisation of  $M_R = 0.345 \text{ Am}^2/\text{kg}$  and coercivity of  $B_C$   
 137  $= 16.9 \text{ mT}$  (Fig. 2a, Table 1). The coercivity of  $\Delta mamJ$  is almost three times lower ( $B_C = 6.2 \text{ mT}$ ) than  
 138 of the wild-type bacteria, and  $M_R = 0.165 \text{ Am}^2/\text{kg}$  (Fig. 2b, Table 1). The remanence and coercivity  
 139 ratios ( $M_R / M_S$  and  $B_{CR} / B_C$ ) for WT are typical for non-interacting single-domain (SD) magnetite, but  
 140  $M_R / M_S$  is lower for  $\Delta mamJ$ , which can be due to dipolar interactions (Dunlop, 2002) (Table 1).

Parameter	WT			$\Delta mamJ$	
	Before HT	After 320°C	After 5 days	Before HT	After 320°C
$M_S$ ( $\text{Am}^2/\text{kg}$ )	0.831	0.275	0.260	0.817	0.316
$M_R$ ( $\text{Am}^2/\text{kg}$ )	0.345	0.063	0.058	0.165	0.050
$M_R / M_S$	0.415	0.229	0.223	0.202	0.158
$B_C$ (mT)	16.907	5.887	5.379	6.230	3.013
$B_{CR}$ (mT)	22.935	14.139	13.286	15.381	9.330
$B_{CR} / B_C$	1.357	2.400	2.470	2.469	3.100

Table 1. Hysteresis parameters of the wild-type and mutant MTB before and after HT. The samples are normalized by total weight which includes organic matter.

141 After heating up to 320°C, samples were again measured at room temperature and hysteretic parameters  
 142 of both samples decrease markedly (Fig. 2c, d, Table 1). The saturation magnetisation reduces for both  
 143 samples by more than 2.5 times. Interestingly, the coercivity of the post-HT WT decreases to a value

144 similar to the unheated  $\Delta$ mamJ (Table 1). We repeated the hysteresis loop for WT five days after heating  
 145 and the hysteretic parameters decrease slightly further with time (Table 1, Fig. A1).

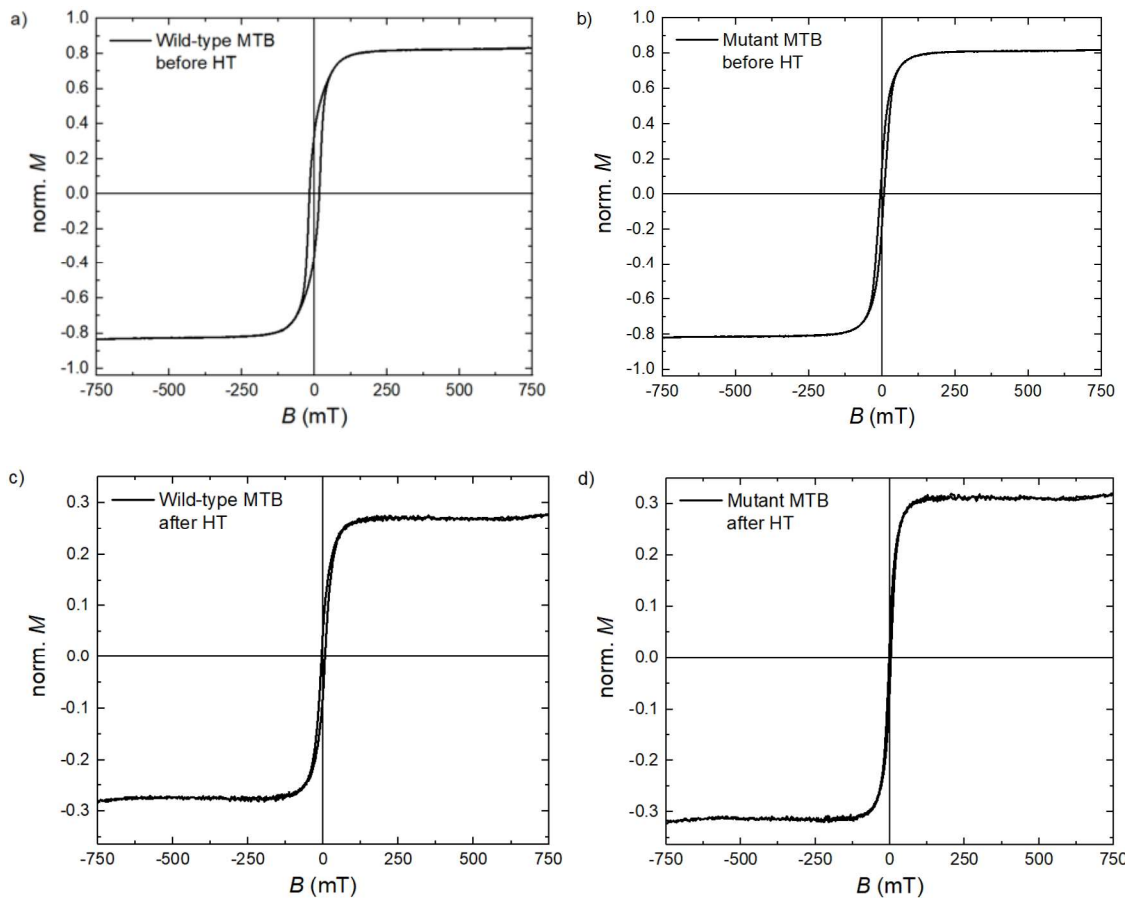


Fig.2. Magnetization as a function of applied field for the WT a) before heating and c) after heating to 320°C; and for  $\Delta$ mamJ, b) before heating and d) after heating. The loops have been corrected for paramagnetic slope. Samples are normalized by total weight which includes organic matter.

146 In the FORC analysis (Fig. 3), the coercivity distribution of WT shows an elongated central ridge that  
 147 extends from ca. 15 mT to 40 mT, and a narrow range of interaction fields (Fig. 3a). This type of FORC  
 148 diagram is typical for chains of non-interacting single domain magnetic particles that would be expected  
 149 for chains of magnetosomes. The coercivity distribution shows the elongation along the horizontal axis,  
 150 observed for weakly-interacting SD particles, typical for MTB in chains (Katzmann et al., 2013). There  
 151 is a small positive flux at zero coercivity, which is accompanied by a negative interaction field (Fig.  
 152 3a), and this feature is also visible in the reversible part of the magnetisation as a maximum

153 accompanied by a small shoulder in the negative reverse peak by the peak field (Fig. A2a). For  
154 magnetite dominated by shape anisotropy, the reversible contribution for non-interacting SD particles  
155 should be 50% of the irreversible magnetisation (Kumari et al., 2014); here, however, it is slightly  
156 lower.  $\Delta m_m J$  shows butterfly-like type FORC distribution that is characteristic of vortex-like magnetic  
157 structures as shown by Dumas et al. (Dumas et al., 2007a; Dumas et al., 2007b; Roberts et al., 2019)  
158 (Fig. 3b). The butterfly-like coercivity distribution together with an elongated central ridge along the  
159  $B_c$ -axis, similar to the signal obtained for wild-type bacteria, suggest that the sample contains chain-  
160 like structures in addition to aggregates of particles (Katzmann et al., 2013), but it is also typical for  
161 cluster-like particles distribution of nanodots (Dumas et al., 2007a; Dumas et al., 2007b). The  
162 reversible/irreversible parts of the magnetization reveal an additional contribution at zero coercivity  
163 that suggest an additional superparamagnetic contribution to the magnetization (Fig. A2d). After  
164 heating, the coercivity distribution of WT shifts to the lower fields and resembles results observed for  
165 magnetofossils (Heslop et al., 2014) (Fig. 3c).



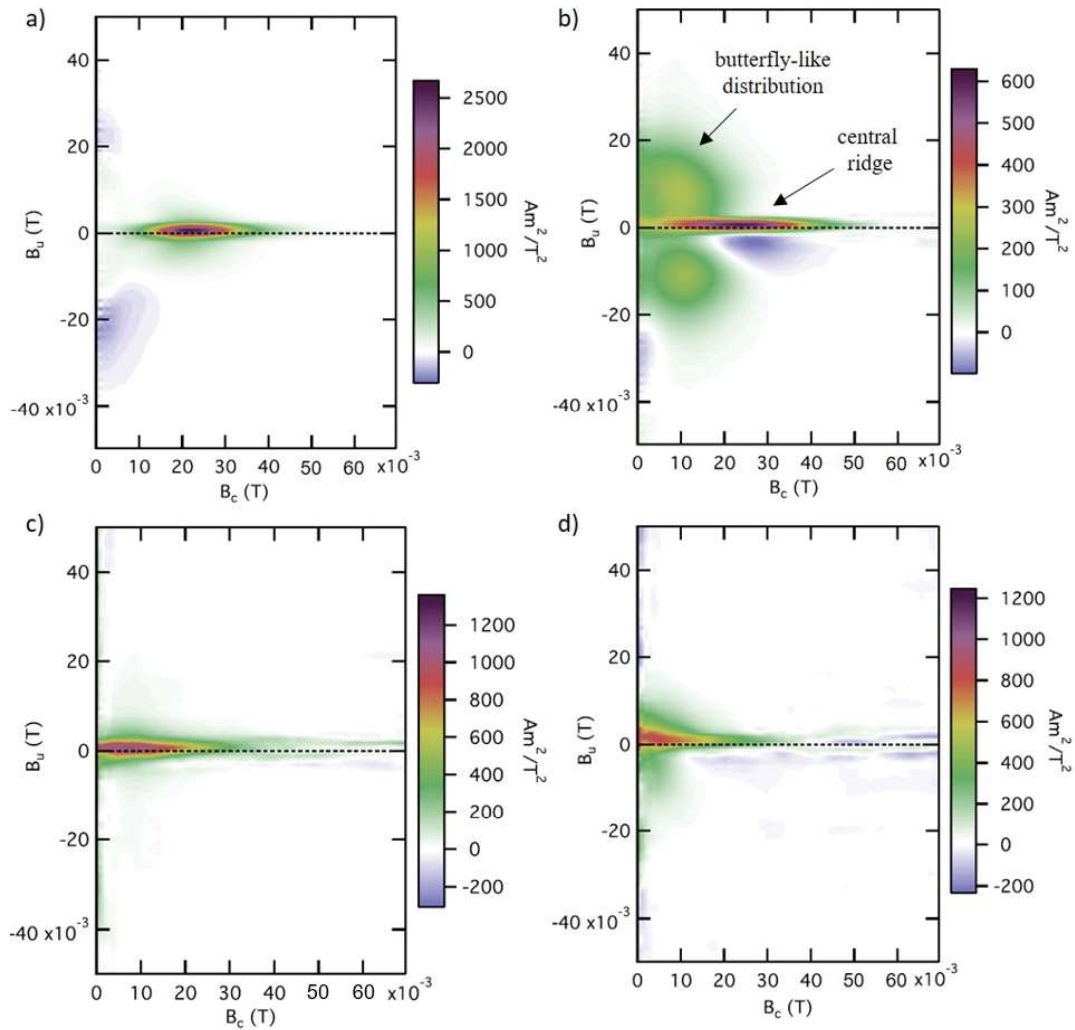


Fig.3 FORC spectra before heat treatment (HT) for a) WT showing elongated central ridge, b)  $\Delta amJ$  characterised by butterfly-like distribution with indications of central ridge; and after HT for c) WT, and d)  $\Delta amJ$ . Both samples WT and  $\Delta amJ$  after HT show distribution coercivity shifted to lower fields.

166 The coercivity distribution of the heated sample changes only slightly after 5 days (Fig. A1b), which  
 167 may suggest some oxidation of the magnetosomes over time. After heating, the mutant MTB is  
 168 characterised by a simple elongated central ridge with lower coercivity (Fig. 3d), similar to the post-HT  
 169 WT with notably broader spread at zero coercivity (Fig. 3c). The presence of a weak high-coercivity  
 170 contribution is observed. Interestingly, for all spectra, the peak of the FORC distribution, i.e. the patch  
 171 of maximum coercivity, is displaced above  $B_u = 0$ . Such a displacement indicates a negative mean field  
 172 (Roberts et al., 2014) (Fig. 3).

---

**173 Ferromagnetic Resonance (FMR) spectroscopy**

174 The FMR spectra were measured at a series of increasing temperatures between room temperature and  
175 500 °C and selected temperature spectra are shown in Fig. 4 (Fig. A3 presents all FMR spectra). The  
176 room temperature spectrum was remeasured after heating to 500 °C to check for any alteration in the  
177 sample. The FMR signal from WT, at room temperature shows the characteristic traits of chain  
178 arrangement, with a spectrum that consists of two low-field peaks with maxima at around 200 mT and  
179 293 mT, and a high-field peak at 378 mT (Fig. 4a). With increasing temperature, the peaks move closer  
180 to each other and entire spectrum becomes narrower (Fig. A3b-m). At 300°C the signal reduces to a  
181 single or isotropic spectrum i.e., the absorption is a Lorentzian distribution, the  $d\chi''/dB$  shows the  
182 characteristic positive/negative curve. Further heating causes a steady decrease of amplitude of the  
183 single peak until it vanishes completely. The decrease in amplitude is accompanied by formation of the  
184 sharp narrow signal at around 350 mT ( $g \approx 2.02$ ), which represents a free electron radical in organic  
185 matter (Perry, 1990). The room temperature spectrum after HT shows only a very minor presence of  
186 the magnetic phase in addition to the radical in the organic matter (Fig. 4a, Fig. A3n). It is thus entirely  
187 different from the room temperature spectrum before HT.

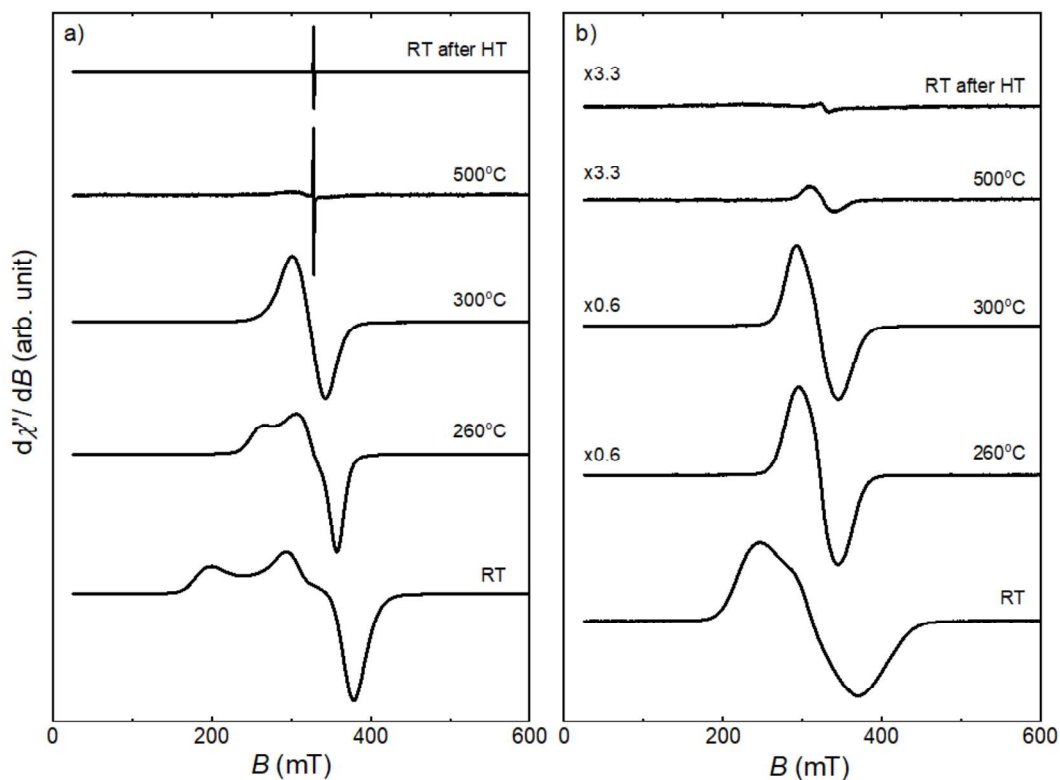


Fig.4 Selected FMR spectra during heat treatment experiment of the a) WT, and b)  $\Delta$ mamJ. Note that the amplitude of the spectra for  $\Delta$ mamJ becomes extremely weak with heating and is scaled by a factor x. The scaled-up RT spectra after heating are shown in Appendix Fig.A3n, ac.

188 The room temperature FMR spectrum from  $\Delta$ mamJ is more symmetric than the spectrum observed for  
 189 WT (Fig. 4b), as previously reported (Ghaisari et al., 2017). The signal is relatively broad with clearly  
 190 defined single-maximum at 247 mT and minimum at 369 mT. The maximum is accompanied by small  
 191 shoulder around 290 mT, which could represent the presence of SP particles, or isolated particles (Kopp  
 192 et al., 2006) and is expected for particles without clear chain-arrangement. With heating, the signal  
 193 becomes narrower and more isotropic (Fig. A3 o-ab). The shoulder accompanying the maximum peak  
 194 initially becomes more pronounced, and subsequently reduces by 300°C when the signal becomes  
 195 isotropic. By 300°C the spectrum from  $\Delta$ mamJ and WT are similar. With further heating amplitude of  
 196 the spectrum diminishes, although there is still a weak isotropic signal at 500 °C. The room temperature  
 197 spectrum after HT reveals the presence of a minor magnetic phase with a small radical contribution  
 198 (Fig. 4b, Fig. A3).

199 The change in absolute area under the FMR absorption spectra during the heat treatment is shown in  
 200 Fig. 5. Both WT and  $\Delta\text{mamJ}$  show a temperature range in which the area remains relatively unchanged,  
 201 followed by a monotonic decline in area up to 500 °C. After returning to room temperature the area  
 202 under the spectra remains negligible.

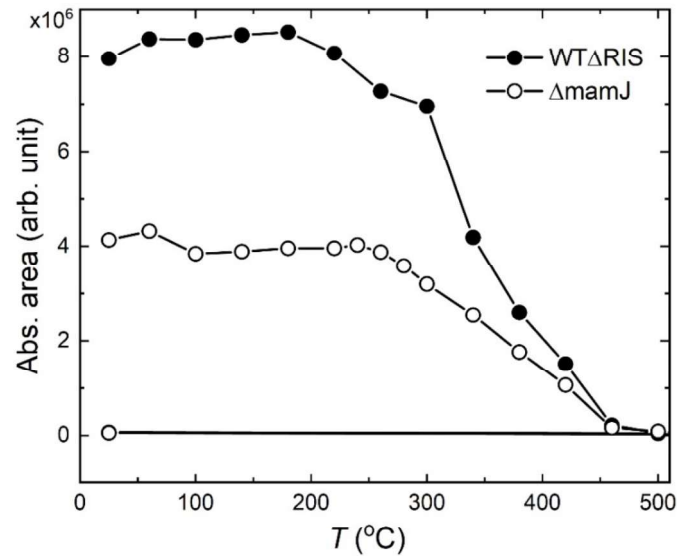


Fig.5 Absolute area under the spectrum as a function of temperature for the a) WT and b)  $\Delta\text{mamJ}$  indicating clear decrease at higher temperatures (around 260-300°C). At 500°C signals of both samples nearly disappear.

### 203 Simulation of the FMR signal

204 As the MTB chains are characterised by a high uniaxial field ( $B_{\text{uni}}$ ), the change of  $B_{\text{uni}}$  may be used to  
 205 quantify the decomposition of the chain to an aggregate of single magnetosomes. To test how the  
 206 heating experiment influences  $B_{\text{uni}}$ , we compare the spectra with simulations for MTB. Fig. 6 shows the  
 207 experimental spectra for WT and  $\Delta\text{mamJ}$  at room temperature and 300°C, and simulated heating steps  
 208 for all spectra are shown in Appendix Fig. A3. The room temperature spectrum of WT can be fit using  
 209  $B_{\text{uni}} = 94$  mT, a uniaxial anisotropy field, which is an indicative of the presence of chain-arrangement  
 210 (Charilaou et al., 2011) (Fig. 6a). The shoulder, which appears for the second maximum, may be an  
 211 indication of strong cubic anisotropy superimposed on the contribution from uniaxiality (Charilaou et  
 212 al., 2011). The spectrum obtained at 300°C can be fit with a much smaller  $B_{\text{uni}}$  of 30 mT.

213 The room temperature spectrum for  $\Delta\text{mamJ}$  can be fitted with  $B_{\text{uni}} = 58$  mT, which is lower than of WT  
 214 (Fig. 6b), and is to be expected due to the lack of a chain structure. This field, however, may be slightly  
 215 higher than for fully clustered, therefore suggesting the small presence of self-assembled chain  
 216 fragments. The uniaxial field at 300°C is this same as for WT, i.e., 30 mT.

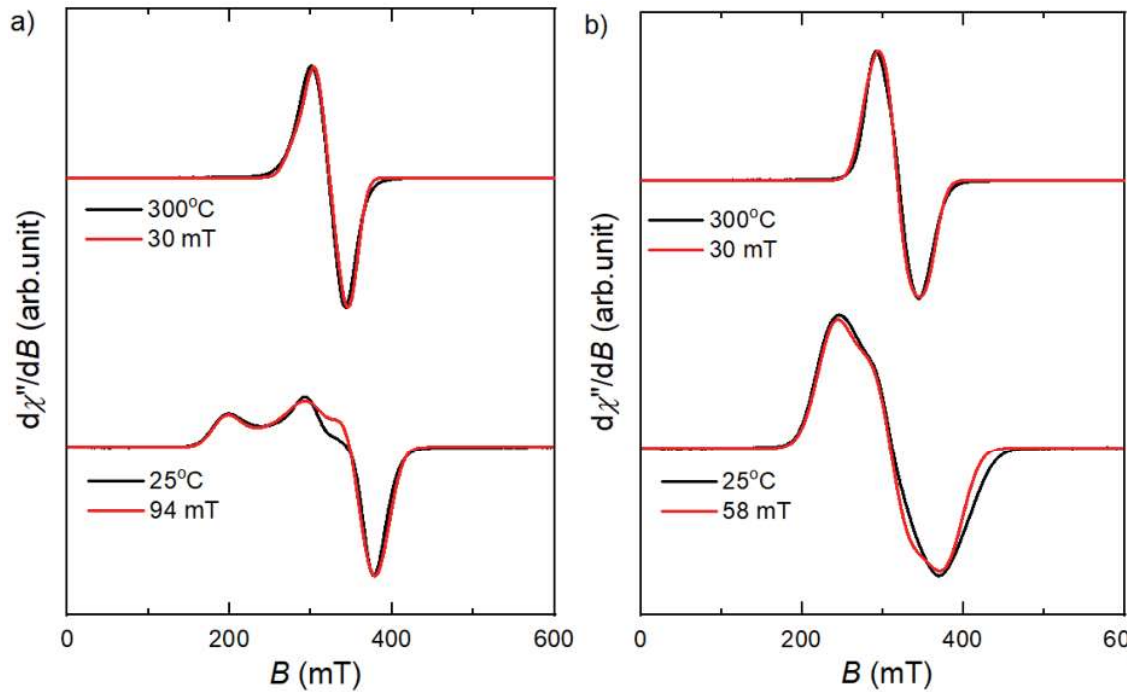


Fig. 6 Simulation of the FMR spectra after heating to 300°C (upper panel) and before at RT (bottom panel) for a) for WT, and b)  $\Delta\text{mamJ}$ . The black line represents the experimental signal. The red line shows the simulated signal. Parameters used by the simulations are shown in the Table A1.

217 Figure 7 shows the change in the uniaxial field as a function of temperature defined from the simulation.  
 218 Both samples are characterised by a similar trend, with a gradual decrease in  $B_{\text{uni}}$  followed by plateau  
 219 in the uniaxial field. The gradual decrease ends at around 260°C – 300°C. At higher temperatures, the  
 220 uniaxial field is around 30 mT and is relatively constant, with small changes from around 400°C up.  
 221 The uniaxial field for  $\Delta\text{mamJ}$ , shows a further drop in  $B_{\text{uni}}$  between 400° C and 500° C.

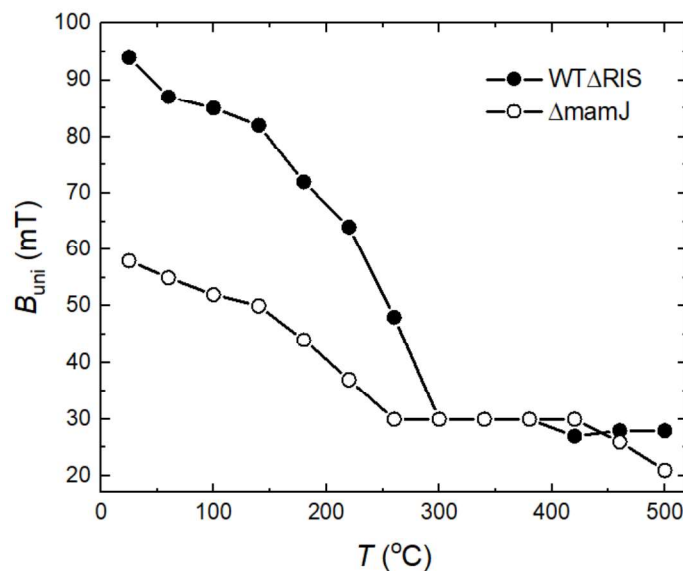


Fig. 7 Uniaxial field ( $B_{uni}$ ) as a function of temperature for a) for WT, and b)  $\Delta mamJ$ , as determined by fitting using the simulation program of Charilaou et al. (Charilaou et al., 2011). For both samples uniaxial field decrease with temperature until it reaches value of 30mT at 260 - 300°C. Further heating causes small changes from around 420 °C.

## 222 FMR of wild-type bacteria during heating cycles

223 In order to separate the reversible and irreversible changes that are happening during heating, an  
 224 additional FMR experiment was performed on WT. In this experiment the spectrum of the sample was  
 225 measured first at room temperature, and then, when the sample was heated incrementally to a target  
 226 temperature. The sample was cooled back down to room temperature and remeasured, before heating  
 227 to the next higher increment. Fig.8 shows spectra from selected temperature steps where the largest  
 228 changes in the spectra are observed. As has been seen above, increasing temperature causes a gradual  
 229 narrowing of the spectrum until it becomes relatively symmetric at around 300-320°C. Interestingly,  
 230 cooling back to room temperature shows a more complicated behaviour. The room temperature spectra  
 231 are essentially the same up to 180° C, i.e. the signal narrowing at high temperature is reversible.  
 232 However, after heating to 220° C, the room temperature spectrum becomes isotropic. The spectrum at  
 233 260°C recovers the traits of chain arrangement., but the subsequent room temperature spectrum is again  
 234 isotropic. Further heat cycling leads to a change to an isotropic spectrum when measured at high  
 235 temperature. However, above 300°C when both high-temperature and room-temperature spectra

236 become isotropic, there are major differences observed in their shapes. The room temperature spectra  
 237 are 1) visibly broader, 2) shifted to the lower field values, and 3) characterised by a much broader  
 238 minimum.

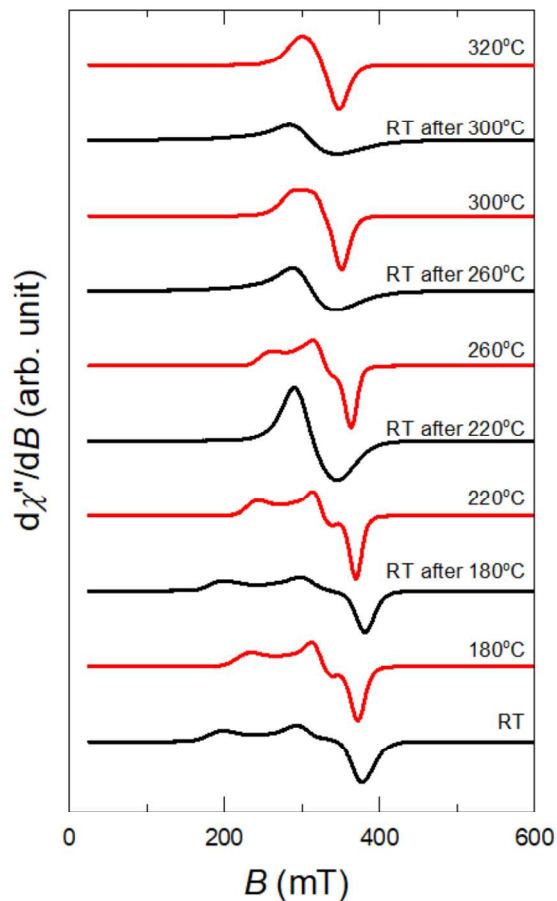


Fig.8 Selected FMR spectra for WT comparing the spectrum at a specific temperatures and after cooling back down to room temperature. The red lines represent the spectra at higher temperature, whereas the black lines show the corresponding spectra at room temperature after the heating. The high temperature spectra seem to maintain chain features longer than following room temperature spectra.

#### 239 5.4. DISCUSSION

240 Hysteresis loops, FORC diagrams, and FMR spectrum of WT at room temperature all indicate that the  
 241 magnetite particles are in the range of stable single domains arranged in chain configurations. The  
 242 hysteresis and FORC results are similar to those reported by Katzmann et al. (2013) on similar  
 243 laboratory strains of bacteria (Fig. 2a, 3a). Although it was not possible to make transmission electron

244 microscope (TEM) images on these samples, previous work has demonstrated that wild type bacteria  
245 have an average particle size of around 35 nm, and a range of sizes between ca. 5 and 70 nm diameter  
246 (Katzmann et al., 2013). An expression of the finer superparamagnetic particles is seen in the reversible  
247 component of the hysteresis loop and the FMR spectrum (Fig. A3a). These finer crystals are found at  
248 the end of the chains (Pan et al., 2005). The two low-field maxima in the FMR spectrum and pronounced  
249 high-field maximum (Fig. 4a, 6a) are typical for a dominant uniaxial anisotropy and arise from the chain  
250 configuration (Charilaou et al., 2011).

251

252 Suppression of  $\Delta\text{mamJ}$  leads to a mutant strain of bacteria that produces magnetosomes of the same  
253 size, morphology and number as the wild-type strain, but a configuration of magnetosomes in a compact  
254 three-dimensional cluster (Scheffel et al., 2006), although short chains or rings have also been reported  
255 (Katzmann et al., 2013). Katzmann et al. (Katzmann et al., 2013) found that the particle size distribution  
256 of magnetosomes for  $\Delta\text{mamJ}$  was between  $< 5$  nm and 50 nm, and the average size was smaller than in  
257 the wild-type bacteria. Clustering leads to a decrease in  $B_c$  in comparison to the chain configuration  
258 (Fig. 2b, Table 1). The FORC diagram shows a butterfly structure, which was also reported by  
259 Katzmann et al. (Katzmann et al., 2013) (Fig. 3b). This type of FORC response is typical for arrays of  
260 single domain Fe-nanodots (Dumas et al., 2007a; Dumas et al., 2007b), which undergo nucleation and  
261 annihilation of vortex structures during hysteresis. The presence of a central ridge, on the other hand  
262 suggests that some shorter chains may be also present within the bacteria. The reversible contribution  
263 around  $B_c = 0$  also detects a contribution from superparamagnetic magnetosomes (Fig A2d). The FMR  
264 spectrum for  $\Delta\text{mamJ}$  shows a weaker resonance and a lower contribution from the uniaxial anisotropy  
265 field (Fig. 4b, 6b) as shown previously by Ghaisari et al. (2017). The narrower spectrum that can arise  
266 from a cluster of single-domain particles with a superparamagnetic contribution. In this case, a cubic  
267 (or magnetocrystalline) anisotropy is dominant.

268

269 The FMR spectra that were measured at temperatures above room temperature show a gradual loss in  
270 the component arising from uniaxial anisotropy at higher temperature. In the case of WT the chain



---

271 structure changes gradually up to 300°C, where its FMR becomes isotropic, indicating that the chain  
272 structure has been destroyed due to degradation of organic material (Fig. 4a, 5a, 7a). This change is  
273 manifested by a strong decrease in the uniaxial anisotropy field with heating (Fig. 6a). At higher  
274 temperatures the spectrum strength decreases. This loss of a resonance absorption at 500°C suggests  
275 that the magnetite may have partially oxidised to hematite (Fig. 4a). The degradation of the chain is  
276 also reflected by the hysteresis loop and FORC diagram, where there is a decrease in the coercivity  
277 spectra that arises from particle interaction (Fig. 2c, 3c). The FMR spectra that were measured after  
278 stepwise heating and returning to room temperature indicate that the organic structure was already  
279 weakening by 220° C, but that with an increase of temperature the magnetosomes would self-assemble  
280 into a chain-like structure (Fig. 8). The reversible unfolding of the protein structure is only an  
281 intermediate state during heating, and above certain temperatures an irreversible denaturation takes  
282 place (Mallamace et al., 2016). However, it needs to be taken into account that the protein structure  
283 could be already strongly damaged by freeze-drying and its behaviour caused by higher temperatures  
284 cannot be easily predicted. Therefore, further work, which would allow us to observe the behaviour of  
285 the bacterial structure while heating, needs to be done.

286

287 The structure of  $\Delta$ mamJ deteriorates at a slightly lower temperature, around 260° C where the FMR  
288 signal becomes isotropic (Fig. 4b, 5b, 7b), due to the degradation of the organic matter. The decrease  
289 of uniaxial field is observed for  $\Delta$ mamJ, however it is much less pronounced than for WT. This decrease  
290 may originate from destruction of the few chain fragments or rings found in the sample and from  
291 tightening of the cluster, which leads to more inter-particle interaction and a decrease in  
292 coercivity. At temperatures above 260°C, the FMR spectra of  $\Delta$ mamJ resembles that of WT,  
293 characterised by the loss of the resonance absorption indicating magnetite oxidation. The degradation  
294 of the organic matter in the cluster structure is also mirrored by the hysteresis loop and FORC diagram  
295 (Fig. 2d, 3d), where the vortex-like magnetic structure is removed and simple elongated central ridge  
296 with lower coercivity similar to post-HT WT is observed. Surprisingly, the  $\Delta$ mamJ undergoes a further  
297 change above 400° C (Fig. 7b). This change may be due to a further tightening of the cluster.

298

---

299 The magnetic responses of WT and  $\Delta$ mamJ are different, but the decomposition process undergoes the  
300 same steps, i.e., the destruction of the particle arrangement and following oxidation process. At the end  
301 of the former, the magnetic response of the WT and  $\Delta$ mamJ become alike. From simulation of the FMR  
302 spectra, three ranges of the uniaxial fields can be determined. The first range indicates the presence of  
303 the chains and chain fragments and is characterised by  $B_{\text{uni}}$  above 58 mT, as this is the highest value  
304 obtained for  $\Delta$ mamJ, which contains a small chain contribution. The second range is a mixture of the  
305 dominant cluster-like structure with small chain contribution and is identified by uniaxiality of between  
306 58 mT and 30 mT. For the natural systems, this range may be also indicative of the single particles with  
307 shape anisotropy. The final range, indicates cluster-like structure with no indications of the chain  
308 arrangement and with  $B_{\text{uni}}$  of around 30 mT, as previously defined for nonaligned particles by Kind et  
309 al. (Kind et al., 2011). Therefore, the FMR analysis allows a clear distinction between chain-presence  
310 and fully-clustered structure, with consideration of the intermediate state. Together with additional  
311 rock-magnetic and geochemical analysis, our approach is useful in determining the presence of  
312 magnetofossils in natural systems during decomposition process of the organic matter. The ability to  
313 identify the presence of magnetofossils is important in understanding past environmental conditions, as  
314 MTB are often found close to the anoxic-oxic transition zone in aquatic system. Thus, their presence  
315 provides information on redox conditions (Bazylinski et al., 1988; Pan et al., 2005), which is crucial  
316 when examining environments in the geologic record. For example, Abrajevitch et al. (2011, 2013) use  
317 rock magnetic properties to infer that the provenance of magnetite in Triassic-age cherts is due to MTB.  
318 Additional information from FMR spectroscopy could help in evaluating if chains of magnetite are  
319 retained, as suggested by the authors. Furthermore, FMR spectroscopy could be an interesting method  
320 to use on extraterrestrial materials, where the presence of magnetofossils is being proposed (Thomas-  
321 Keprta et al., 2000; Weiss et al., 2004b).

322

## 323 **5.5. CONCLUSIONS**

324 In diagenetic environments redox conditions lead to the decomposition of organic matter responsible  
325 for maintaining the chain arrangement in MTB and their fossil remains. Such a decomposition results

326 in disappearance of the characteristic trait of MTB and makes it nearly impossible to define if the  
327 remnant particles originate from MTB. In this study, we examine how progressive decomposition of  
328 the organic matter affects the magnetic properties of bacteria. FMR indicates two clear stages: 1) the  
329 decomposition of the organic matter leading to the breakdown of the chain arrangement; and the 2)  
330 possible oxidation of the magnetite particles. The uniaxial shape anisotropy decreases strongly while  
331 heating and  $B_{uni}$  changes gradually from  $> 58$  mT when in a chain- arrangement to around 30 mT when  
332 the particles are clustered. Therefore,  $B_{uni}$  may be used as a measure of the degree of chain  
333 decomposition in nature. Our results show the value of using FMR spectroscopy together with other  
334 rock magnetic methods for tracking the fate of magnetofossils in the geologic record.

335

## 336 5.6. AUTHOR CONTRIBUTIONS

337

338 The samples were cultured by members of the group of Dirk Schüler from University of Bayreuth  
339 (Bayreuth, Germany).

340

## 341 5.7. REFERENCES

- 342 Abrajewitch, A., Hori, R.S., Kodama, K., 2011. Magnetization carriers and remagnetization of bedded  
343 chert. *Earth and Planetary Science Letters* 305, 135-142
- 344 Abrajewitch, A., Hori, R.S., Kodama, K., 2013. Rock magnetic record of the Triassic-Jurassic transition  
345 in pelagic bedded chert of the Inuyama section, Japan. *Geology* 41, 803-806
- 346 Bazylinski, D.A., Frankel, R.B., Jannasch, H.W., 1988. Anaerobic magnetite production by a marine,  
347 magnetotactic bacterium. *Nature* 334, 518-519
- 348 Bazylinski, D.A., Garratt-Reed, A.J., Frankel, R.B., 1994. Electron microscopic studies of  
349 magnetosomes in magnetotactic bacteria. *Microscopy Research and Technique* 27, 389-401,  
350 doi:10.1002/jemt.1070270505
- 351 Bickford Jr, L., 1950. Ferromagnetic resonance absorption in magnetite single crystals. *Physical*  
352 *Review* 78, 449
- 353 Chang, L., Roberts, A.P., Winklhofer, M., Heslop, D., Dekkers, M.J., Krijgsman, W., Fitz Gerald, J.D.,  
354 Smith, P., 2014. Magnetic detection and characterization of biogenic magnetic minerals: A  
355 comparison of ferromagnetic resonance and first-order reversal curve diagrams. *Journal of*  
356 *Geophysical Research: Solid Earth* 119, 6136-6158
- 357 Chang, L., Winklhofer, M., Roberts, A.P., Heslop, D., Florindo, F., Dekkers, M.J., Krijgsman, W.,  
358 Kodama, K., Yamamoto, Y., 2013. Low-temperature magnetic properties of pelagic carbonates:  
359 Oxidation of biogenic magnetite and identification of magnetosome chains. *Journal of*  
360 *Geophysical Research: Solid Earth* 118, 6049-6065
- 361 Charilaou, M., Winklhofer, M., Gehring, A.U., 2011. Simulation of ferromagnetic resonance spectra of  
362 linear chains of magnetite nanocrystals. *Journal of Applied Physics* 109093903,  
363 doi:10.1063/1.3581103

- 364 Chen, A.P., Egli, R., Moskowitz, B.M., 2007. First-order reversal curve (FORC) diagrams of natural  
365 and cultured biogenic magnetic particles. *Journal of Geophysical Research: Solid Earth*  
366 112B08S90, doi:10.1029/2006JB004575
- 367 Devouard, B., Posfai, M., Hua, X., Bazylinski, D.A., Frankel, R.B., Buseck, P.R., 1998. Magnetite from  
368 magnetotactic bacteria: Size distributions and twinning. *American Mineralogist* 83, 1387-1398
- 369 Dumas, R.K., Li, C.-P., Roshchin, I.V., Schuller, I.K., Liu, K., 2007a. Magnetic fingerprints of sub-100  
370 nm Fe dots. *Physical Review B* 75, 134405, doi:10.1103/PhysRevB.75.134405
- 371 Dumas, R.K., Liu, K., Li, C.-P., Roshchin, I.V., Schuller, I.K., 2007b. Temperature induced single  
372 domain-vortex state transition in sub-100 nm Fe nanodots. *Applied Physics Letters* 91, 202501,  
373 doi:10.1063/1.2807276
- 374 Dunin-Borkowski, R.E., McCartney, M.R., Frankel, R.B., Bazylinski, D.A., Pósfai, M., Buseck, P.R.,  
375 1998. Magnetic microstructure of magnetotactic bacteria by electron holography. *Science* 282,  
376 1868-1870, doi:10.1126/science.282.5395.1868
- 377 Dunlop, D.J., 2002. Theory and application of the Day plot (Mrs/Ms versus Hcr/Hc) 1. Theoretical  
378 curves and tests using titanomagnetite data. *Journal of Geophysical Research: Solid Earth*  
379 1072056, doi:10.1029/2001jb000486
- 380 Egli, R., Chen, A.P., Winklhofer, M., Kodama, K.P., Horng, C.S., 2010. Detection of noninteracting  
381 single domain particles using first-order reversal curve diagrams. *Geochemistry, Geophysics,*  
382 *Geosystems* 11, n/a-n/aQ01Z11, doi:10.1029/2009gc002916
- 383 Faivre, D., Menguy, N., Pósfai, M.I., Schüler, D., 2008. Environmental parameters affect the physical  
384 properties of fast-growing magnetosomes. *American Mineralogist* 93, 463-469
- 385 Faivre, D., Schuler, D., 2008. Magnetotactic bacteria and magnetosomes. *Chemical Reviews* 108, 4875-  
386 4898, doi:10.1021/cr078258w
- 387 Fischer, H., Mastrogiacomo, G., Löffler, J.F., Warthmann, R.J., Weidler, P.G., Gehring, A.U., 2008.  
388 Ferromagnetic resonance and magnetic characteristics of intact magnetosome chains in  
389 *Magnetospirillum gryphiswaldense*. *Earth and Planetary Science Letters* 270, 200-208
- 390 Gehring, A.U., Kind, J., Charilaou, M., García-Rubio, I., 2011. The detection of magnetotactic bacteria  
391 and magnetofossils by means of magnetic anisotropy. *Earth and Planetary Science Letters* 309,  
392 113-117
- 393 Ghaisari, S., Winklhofer, M., Strauch, P., Klumpp, S., Faivre, D., 2017. Magnetosome organization in  
394 magnetotactic bacteria unraveled by ferromagnetic resonance spectroscopy. *Biophysical Journal*  
395 113, 637-644
- 396 Harrison, R.J., Feinberg, J.M.F., 2008. An improved algorithm for calculating first-order reversal curve  
397 distributions using locally weighted regression smoothing. *Geochemistry, Geophys. Geosystems*  
398 9, n/a-n/aQ05016, doi:10.1029/2008GC001987
- 399 Heslop, D., Roberts, A.P., Chang, L., 2014. Characterizing magnetofossils from first-order reversal  
400 curve (FORC) central ridge signatures. *Geochemistry, Geophysics, Geosystems* 15, 2170-2179
- 401 Hesse, P.P., 1994. Evidence for bacterial palaeoecological origin of mineral magnetic cycles in oxic  
402 and sub-oxic Tasman Sea sediments. *Marine Geology* 117, 1-17
- 403 Katzmann, E., Eibauer, M., Lin, W., Pan, Y., Plitzko, J., Schüler, D., 2013. Analysis of magnetosome  
404 chains in magnetotactic bacteria by magnetic measurements and automated image analysis of  
405 electron micrographs. *Applied and Environmental Microbiology* 79, 7755-7762,  
406 doi:10.1128/AEM.02143-13
- 407 Kind, J., Gehring, A.U., Winklhofer, M., Hirt, A.M., 2011. Combined use of magnetometry and  
408 spectroscopy for identifying magnetofossils in sediments. *Geochemistry, Geophysics,*  
409 *Geosystems* 12
- 410 Kirschvink, J.L., Chang, S.-B.R., 1984. Ultrafine-grained magnetite in deep-sea sediments: Possible  
411 bacterial magnetofossils. *Geology* 12, 559-562
- 412 Kobayashi, A., Kirschvink, J.L., Nash, C.Z., Kopp, R.E., Sauer, D.A., Bertani, L.E., Voorhout, W.F.,  
413 Taguchi, T., 2006. Experimental observation of magnetosome chain collapse in magnetotactic  
414 bacteria: Sedimentological, paleomagnetic, and evolutionary implications. *Earth and Planetary*  
415 *Science Letters* 245, 538-550
- 416 Kopp, R.E., Kirschvink, J.L., 2008. The identification and biogeochemical interpretation of fossil  
417 magnetotactic bacteria. *Earth-Science Reviews* 86, 42-61

- 418 Kopp, R.E., Nash, C.Z., Kobayashi, A., Weiss, B.P., Bazylinski, D.A., Kirschvink, J.L., 2006.  
419 Ferromagnetic resonance spectroscopy for assessment of magnetic anisotropy and magnetostatic  
420 interactions: A case study of mutant magnetotactic bacteria. *Journal of Geophysical Research: Solid Earth* 111  
421  
422 Kumari, M., Widdrat, M., Tompa, É., Uebe, R., Schüler, D., Pósfai, M., Faivre, D., Hirt, A.M., 2014.  
423 Distinguishing magnetic particle size of iron oxide nanoparticles with first-order reversal curves.  
424 *Journal of Applied Physics* 116, 124304  
425 Lascu, I., Banerjee, S.K., Berquó, T.S., 2010. Quantifying the concentration of ferrimagnetic particles  
426 in sediments using rock magnetic methods. *Geochemistry, Geophysics, Geosystems* 11Q08Z19,  
427 doi:10.1029/2010GC003182  
428 Mallamace, F., Corsaro, C., Mallamace, D., Vasi, S., Vasi, C., Baglioni, P., Buldyrev, S.V., Chen, S.-  
429 H., Stanley, H.E., 2016. Energy landscape in protein folding and unfolding. *Proceedings of the National Academy of Sciences* 113, 3159-3163, doi:10.1073/pnas.1524864113  
430  
431 Mann, S., Sparks, N., Blakemore, R., 1987. Ultrastructure and characterization of anisotropic magnetic  
432 inclusions in magnetotactic bacteria. *Proceedings of the Royal society of London. Series B. Biological sciences* 231, 469-476  
433  
434 Moskowitz, B.M., Frankel, R.B., Bazylinski, D.A., 1993. Rock magnetic criteria for the detection of  
435 biogenic magnetite. *Earth and Planetary Science Letters* 120, 283-300  
436 Pan, Y., Petersen, N., Winklhofer, M., Davila, A.F., Liu, Q., Frederichs, T., Hanzlik, M., Zhu, R., 2005.  
437 Rock magnetic properties of uncultured magnetotactic bacteria. *Earth and Planetary Science Letters* 237, 311-325  
438  
439 Perry, D.L., 1990. *Instrumental Surface Analysis of Geologic Materials*. Wiley-VHC, New York.  
440 Pike, C.R., Roberts, A.P., Verosub, K.L., 1999. Characterizing interactions in fine magnetic particle  
441 systems using first order reversal curves. *Journal of Applied Physics* 85, 6660-6667  
442 Roberts, A.P., Heslop, D., Zhao, X., Pike, C.R., 2014. Understanding fine magnetic particle systems  
443 through use of first-order reversal curve diagrams. *Reviews of Geophysics* 52, 557-602  
444 Roberts, A.P., Hu, P., Harrison, R.J., Heslop, D., Muxworthy, A.R., Oda, H., Sato, T., Tauxe, L., Zhao, X., 2019. Domain state diagnosis in rock magnetism: Evaluation of potential alternatives to the Day diagram. *Journal of Geophysical Research: Solid Earth* 124, 5286-5314  
445  
446 Roberts, A.P., Pike, C.R., Verosub, K.L., 2000. First-order reversal curve diagrams: A new tool for  
447 characterizing the magnetic properties of natural samples. *Journal of Geophysical Research: Solid Earth* 105, 28461-28475  
448  
449 Scheffel, A., Gruska, M., Faivre, D., Linaroudis, A., Plitzko, J.M., Schüler, D., 2006. An acidic protein  
450 aligns magnetosomes along a filamentous structure in magnetotactic bacteria. *Nature* 440, 110-  
451 114, doi:10.1038/nature04382  
452  
453 Scheffel, A., Schüler, D., 2007. The acidic repetitive domain of the *Magnetospirillum gryphiswaldense*  
454 MamJ protein displays hypervariability but is not required for magnetosome chain assembly.  
455 *Journal of Bacteriology* 189, 6437-6446  
456 Schüler, D., 2008. Genetics and cell biology of magnetosome formation in magnetotactic bacteria.  
457 *FEMS Microbiology Reviews* 32, 654-672, doi:10.1111/j.1574-6976.2008.00116.x  
458 Schüler, D., Frankel, R.B., 1999. Bacterial magnetosomes: microbiology, biomineralization and  
459 biotechnological applications. *Applied Microbiology and Biotechnology* 52, 464-473,  
460 doi:10.1007/s002530051547  
461 Thomas-Keprta, K.L., Bazylinski, D.A., Kirschvink, J.L., Clemett, S.J., McKay, D.S., Wentworth, S.J.,  
462 Vali, H., Gibson Jr, E.K., Romanek, C.S., 2000. Elongated prismatic magnetite crystals in  
463 ALH84001 carbonate globules: Potential Martian magnetofossils. *Geochimica et Cosmochimica Acta* 64, 4049-4081, doi:10.1016/s0016-7037(00)00481-6  
464  
465 Vonsovskii, S.V.e., 1966. *Ferromagnetic Resonance: the Phenomenon of Resonant Absorption of a High-Frequency Magnetic Field in Ferromagnetic Substances*. Pergamon.  
466  
467 Weiss, B.P., Kim, S.S., Kirschvink, J.L., Kopp, R.E., Sankaran, M., Kobayashi, A., Komeili, A., 2004a.  
468 Ferromagnetic resonance and low-temperature magnetic tests for biogenic magnetite. *Earth and Planetary Science Letters* 224, 73-89  
469  
470 Weiss, B.P., Kim, S.S., Kirschvink, J.L., Kopp, R.E., Sankaran, M., Kobayashi, A., Komeili, A., 2004b.  
471 Magnetic tests for magnetosome chains in Martian meteorite ALH84001. *Proceedings of the National Academy of Sciences* 101, 8281-8284, doi:10.1073/pnas.0402292101  
472

473 Yan, L., Zhang, S., Chen, P., Liu, H., Yin, H., Li, H., 2012. Magnetotactic bacteria, magnetosomes and  
 474 their application. Microbiological Research 167, 507-519

475

476 **5.8. APPENDIX**

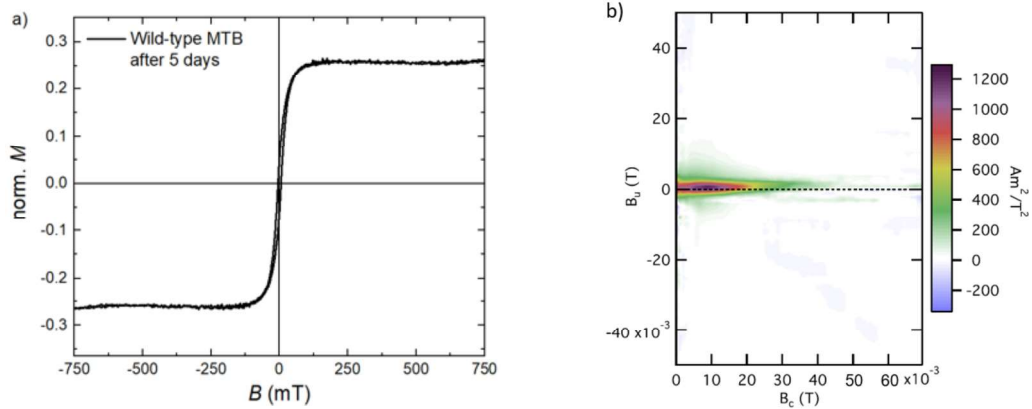


Fig. A1 The magnetisation as a function of magnetic field and corresponding coercivity distribution of the wild-bacteria 5 days after heating procedure. The loop has been corrected for paramagnetic slope. The sample is normalized by total weight which includes organic matter.

477

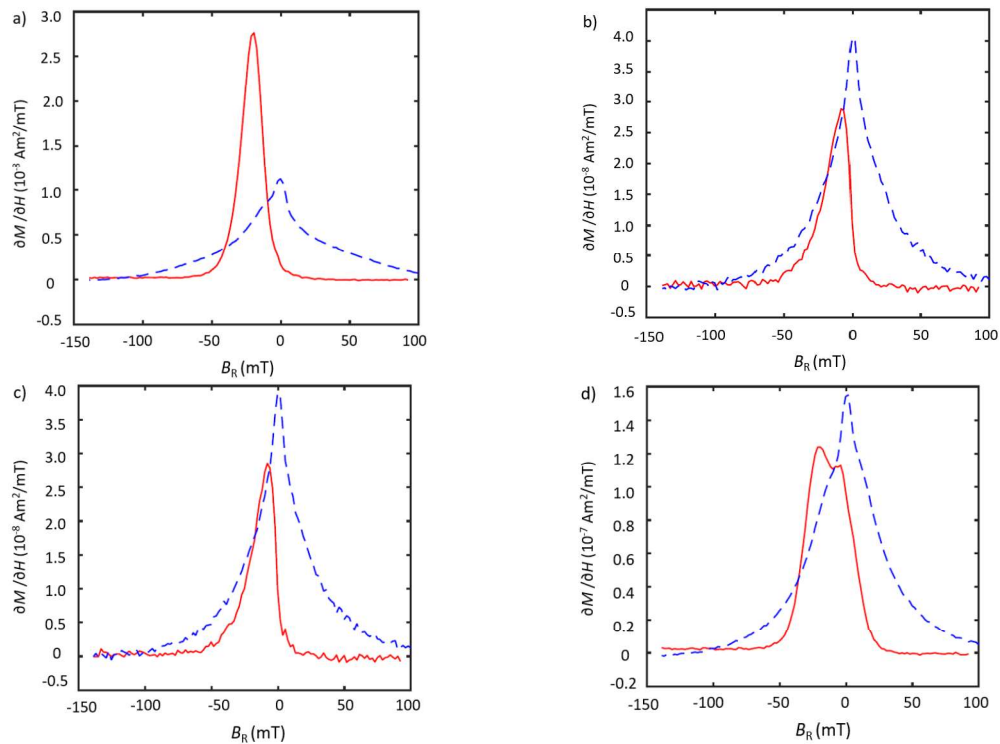


Fig. A2 Continued overlaid.

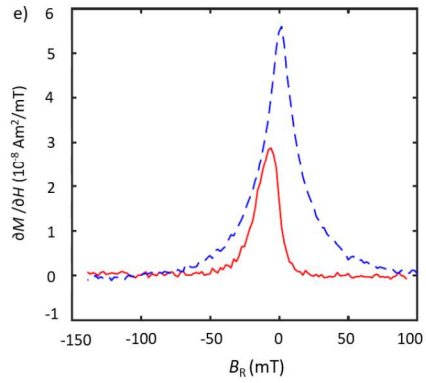


Fig. A2 The irreversible (red solid line) and reversible (blue dashed line) part of magnetisation of WT a) before heating, b) after heating to 320°C, c) 5 days after heating; and  $\Delta m_{\text{M}}/J$  d) before heating and e) after heating. The samples are normalized by total weight which includes organic matter.

478

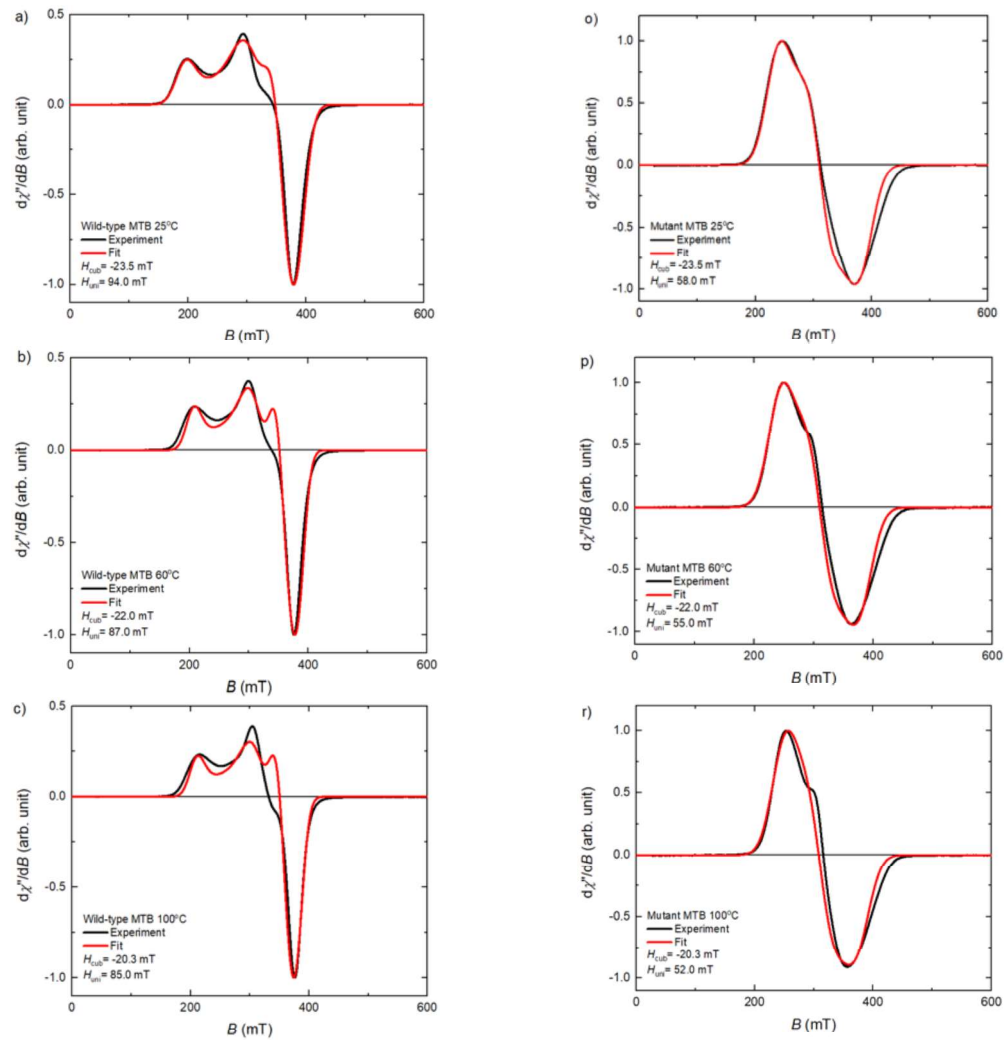


Fig. A3 Continued overleaf.

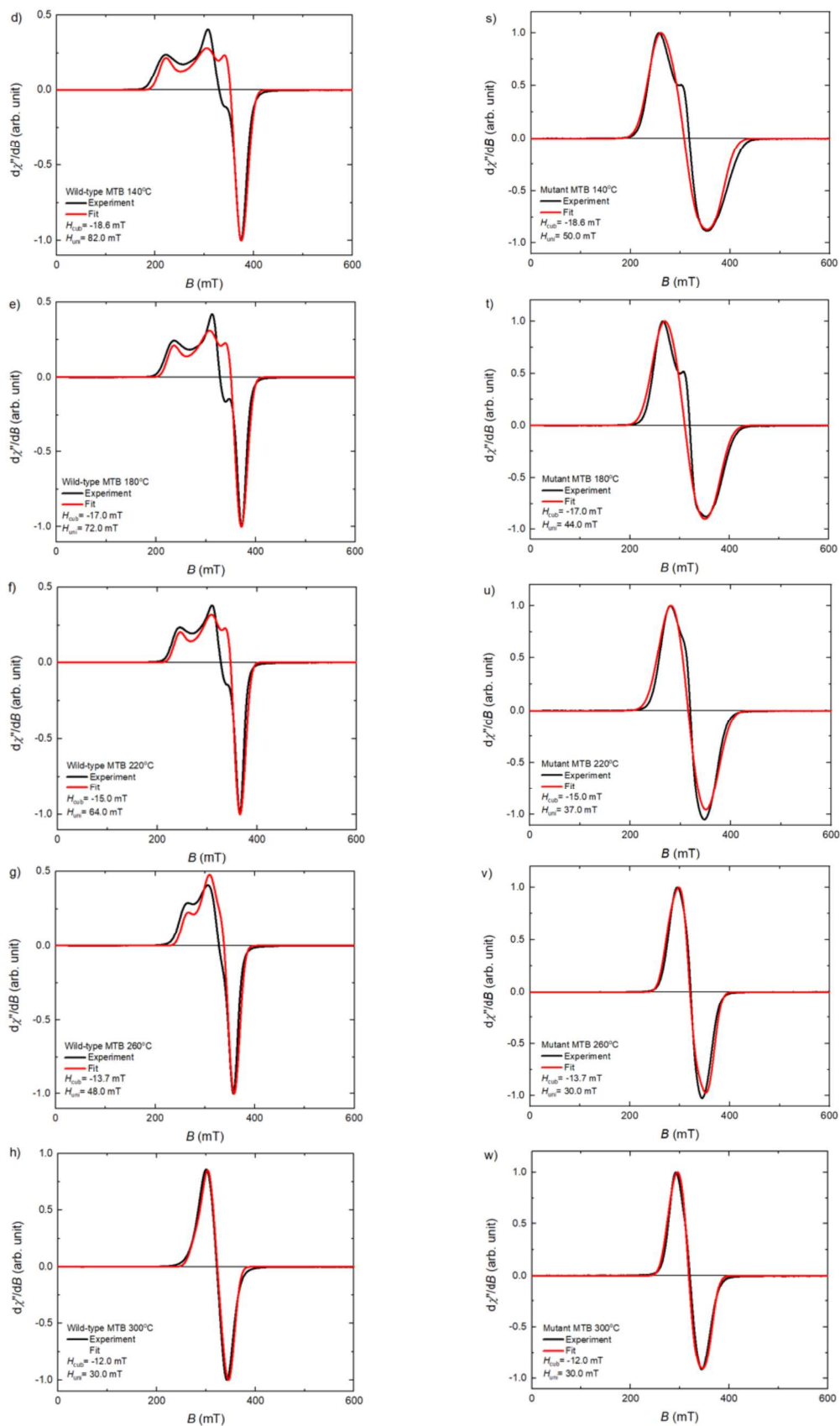


Fig. A3 Continued overleaf.



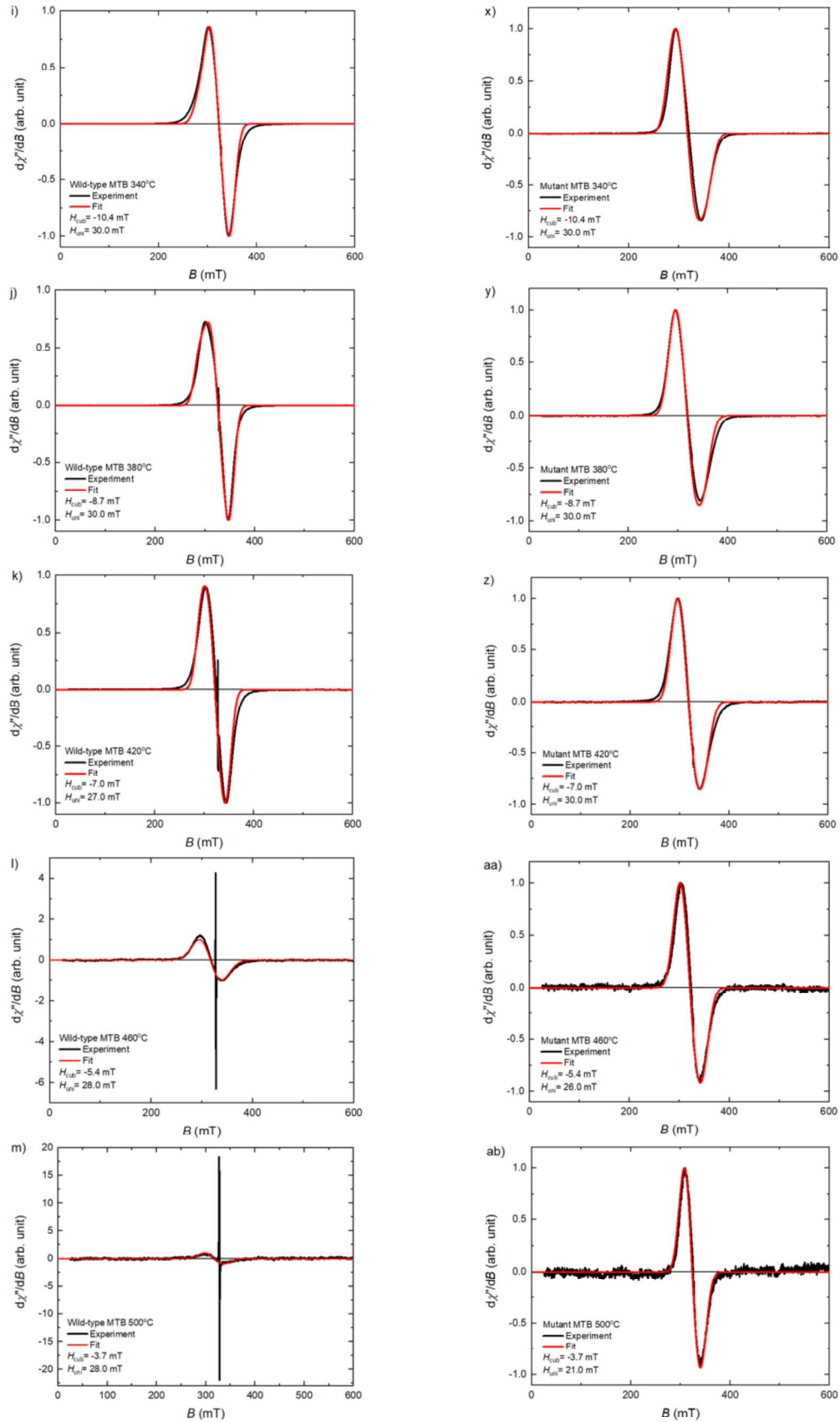


Fig. A3 Continued overleaf.

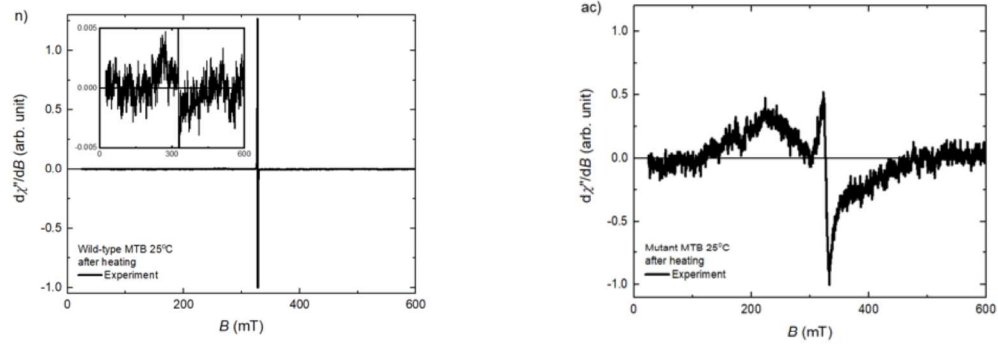


Fig. A3 The FMR spectra with the simulations for WT (left panel, a) to n) and  $\Delta$ mamJ (right panel). The temperature increases in (a) – (m) and in (o) – (ab), while (n) and (ac) are from room temperature after heating. The inset of the Fig. 2n) shows the absorption with omitted radical's signal.

479

480

481

MTB	$T$ (°C)	$B_{uni}$ (mT)	$B_{cub}$ (mT)	$g$ -value	$dB$ (mT)	DC	DW
Frequency = 9.17 GHz							
WT	25	94	-23.5	2.06	16	50	30
	60	87	-22.0	2.04	12	50	30
	100	85	-20.3	2.04	12	50	30
	140	82	-18.6	2.02	12	50	30
	180	72	-17.0	2.01	11	50	30
	220	64	-15.0	2.01	10	50	30
	260	48	-13.7	2.01	10	50	30
	300	30	-12.0	2.04	11	50	26
	340	30	-10.4	2.04	11	50	21
	380	30	-8.7	2.00	10	40	23
	420	27	-7.0	2.00	10	35	21
460	28	-5.4	2.00	18	35	15	
500	28	-3.7	2.00	15	35	15	
Frequency = 9.17 GHz							
$\Delta$ mamJ	25	58	-23.5	2.00	21	27	27
	60	55	-22.0	2.00	21	27	26
	100	52	-20.3	2.00	21	27	25
	140	50	-18.6	2.00	21	27	24
	180	44	-17.0	2.00	21	27	24
	220	37	-15.0	2.00	21	29	24
	260	30	-13.7	2.00	13	34	25
	300	30	-12.0	2.00	13	34	21
	340	30	-10.4	1.98	13	27	21
	380	30	-8.7	1.97	13	26	21
	420	30	-7.0	1.97	13	25	21
460	26	-5.4	1.97	13	25	22	
500	21	-3.7	1.97	11	25	22	

Table A1 Parameters used for simulating the FMR spectra using the program by Charilaou et al. (Charilaou et al., 2011).

The DC and DW are the distribution centre and distribution width, respectively.

482

---

## 6. Ferromagnetic Resonance of Magnetite Biominerals Traces Redox Changes

*Published in EPSL and reproduced with agreement of Thomas M. Blattmann (Blattmann et al., 2020).*

Thomas M. Blattmann<sup>1,2\*</sup>, Barbara Lesniak<sup>3</sup>, Inés García-Rubio<sup>4,5</sup>, Michalis Charilaou<sup>6</sup>, Martin Wessels<sup>7</sup>, Timothy I. Eglinton<sup>2</sup>, and Andreas U. Gehring<sup>3\*</sup>

1) *Biogeochemistry Research Center, JAMSTEC, 237-0061 Yokosuka, Japan*

2) *Geological Institute, ETH Zurich, 8092 Zurich, Switzerland*

3) *Institute of Geophysics, ETH Zurich, 8092 Zurich, Switzerland*

4) *Laboratory of Physical Chemistry, ETH Zurich, 8093 Zurich, Switzerland*

5) *Centro Universitario de la Defensa, 50090 Zaragoza, Spain*

6) *Department of Physics, University of Louisiana at Lafayette, Lafayette, LA 70504, USA*

7) *Institut für Seenforschung, Landesanstalt für Umwelt, Messungen und Naturschutz Baden-Württemberg, 88085 Langenargen, Germany*

### **Abstract**

Redox variations govern a multitude of key geochemical and microbiological processes within lacustrine and marine systems, yet the interpretation of these geological archives can be limited because redox-sensitive microorganisms leave behind sparse fossil evidence. Here, we assess a biologically controlled magnetic proxy through investigation of a well-constrained sedimentary record covering a perturbation of redox-conditions driven by a complete trophic cycle in Lake Constance. Ferromagnetic resonance spectroscopy of sediments reveals strong uniaxial anisotropy, indicative of single-domain magnetite particles in intact or fragmentary chain arrangements, which are an unambiguous trait of magnetotactic bacteria (MTB) and their magnetofossil remains. We show that biogenic magnetite formed intra-cellularly in MTB faithfully records changing redox-conditions at or close to the sediment water-interface. Biogenic magnetite within sedimentary records points to the proliferation of MTB parallel to a decline in water column dissolved oxygen and the formation of sulfidic surface sediments in Lake Constance associated with an episode of eutrophication (1955 – 1991). We conclude that

30 magnetofossils may serve as a sensitive geological proxy to reconstruct dynamic redox-changes along  
31 the sediment-water interface and bottom waters.

32

### 33 **6.1. INTRODUCTION**

34 Understanding the impact of redox dynamics within aquatic systems is important for reconstructing  
35 biogeochemical processes in marine and lacustrine sedimentary records. Changing redox conditions can  
36 drive faunal changes, which in turn critically affect fossil assemblages and molecular (biomarker)  
37 signatures preserved in the geological record (Gambacorta et al., 2016). Redox-sensitive  
38 microorganisms such as magnetotactic bacteria (MTB), which are present in freshwater and marine  
39 settings, are of special interest because they may play an appreciable role in the cycling of iron in aquatic  
40 systems (Chen et al., 2014) and can leave evidence of their existence in sediments in the form of  
41 magnetofossils (Hesse, 1994; Kind et al., 2012; Kodama et al., 2013; Kopp and Kirschvink, 2008;  
42 Roberts et al., 2012). These intracellularly produced ferrimagnetic nanoparticles, generally composed  
43 of magnetite ( $\text{Fe}^{2+}\text{Fe}^{3+}_2\text{O}_4$ ), denoted magnetosomes, are characterized by genetically-determined, well-  
44 defined sizes (typically 35-120 nm) with narrow shape distributions in the single-domain (SD) magnetic  
45 state (Bazylinski et al., 1988; Devouard et al., 1998). Magnetosomes are aligned in chains along a  
46 cytoskeletal filament that stabilizes their arrangement and prevents clumping (Kopp et al., 2006;  
47 Scheffel et al., 2006). This linear arrangement generates a magnetic dipole that is used by MTB as a  
48 compass to navigate along Earth's magnetic field (i.e., magnetotaxis) toward favored habitats around  
49 the oxic-anoxic transition zone (OATZ) (e.g., Spormann and Wolfe, 1984). MTB and their remains have  
50 been reported from Quaternary deposits (Kind et al., 2012; Kodama et al., 2013), but magnetofossil  
51 evidence extends back to the Cretaceous (Kopp and Kirschvink, 2008), with genes associated with  
52 magnetosome formation originating in the Archean (Lin et al., 2017). Paleomagnetic studies are  
53 increasingly considering and seeking to extract paleoenvironmental information (e.g., nutrient  
54 availability, dissolved iron availability, oxygen concentrations) from magnetofossils embedded within  
55 a complex matrix of magnetic minerals in sedimentary records (Larrasoana et al., 2003; Passier et al.,  
56 2001; Roberts et al., 2011; Roberts et al., 2012; Savian et al., 2014; Suk, 2016). Given the OATZ habitat  
57 of MTB and the stability of magnetosomes, magnetofossils may serve as ideal redox-sensitive proxies

---

58 in geological archives as postulated previously (Chang et al., 2018; Hawthorne and McKenzie, 1993;  
59 Larrasoña et al., 2014). In recent years, ferromagnetic resonance (FMR) spectroscopy has been  
60 established as a powerful tool to quantitatively analyze the magnetic traits of cultured MTB (Charilaou,  
61 2017; Kopp et al., 2006), and this in turn opened the door to detect MTB and magnetofossils in  
62 geological samples (Gehring et al., 2011a). Moreover, the FMR spectral response allows the essential  
63 discrimination between biogenic and detrital magnetite characterized by SD and multi-domain,  
64 respectively (e.g., Gehring et al., 2009; Griscom, 1980), paving the way for magnetofossil identification  
65 in sedimentary records and extracting environmental changes.

66

67 Here, we present the FMR spectral evolution yielded from a historically chronicled redox perturbation  
68 recorded in a sediment core from Lake Constance spanning the mid-19<sup>th</sup> to early 21<sup>st</sup> Century as a  
69 testbed to decipher the response of MTB. The rise and fall of MTB as witnessed by their magnetofossil  
70 legacy in sediments is proposed as a proxy for past water column and sediment-water interface redox  
71 changes.

72

## 73 **6.2. MATERIALS AND METHODS**

### 74 **6.2.1. Study Site and Sampling**

75 Lake Constance, bordering Switzerland, Austria, and Germany, is the second largest peri-alpine lake in  
76 Central Europe and includes a shelf, margin, and abyssal plain similar to ocean basin bathymetry  
77 (IGKB, 2016; Müller, 1966b; Wessels, 1998a). The study site (47.5997 °N 9.3581 °E) on the southern  
78 slope of the lake at a water depth of 100 m and sedimentation rate of 1-2 mm/y, is a reference locality  
79 for monitoring of lacustrine primary productivity (Blattmann et al., 2019; Fuentes et al., 2013; IGKB,  
80 2009; Wessels et al., 1999) and is representative of environmental changes since the Late Glacial period  
81 (Wessels, 1998b). For this study, a ~1 m gravity core (BO12-111) was retrieved in December 2012,  
82 extruded, split in sections based on color (Fig. 1) and transferred to polyethylene bags. Each sample  
83 was homogenized, frozen at -20°C, and freeze-dried prior to analysis.

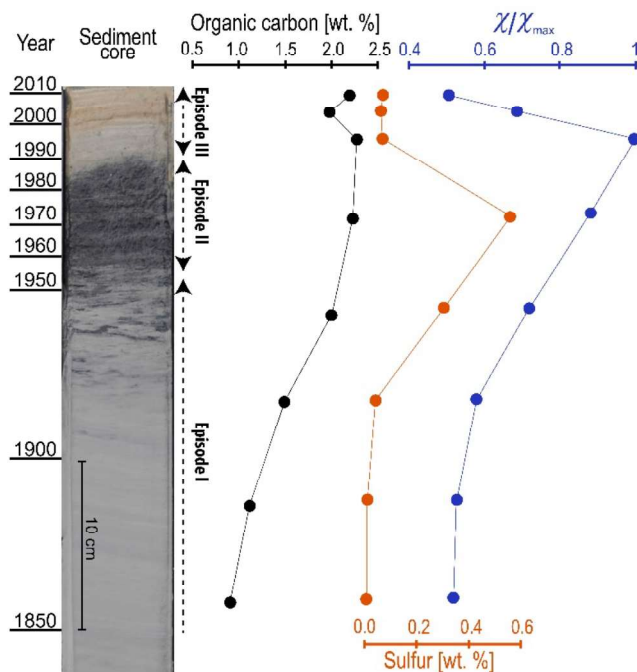


Figure 1. Lake Constance sediment profile with chronology, organic carbon content, total sulfur content, and normalized magnetic susceptibility.

#### 84 6.2.2. Sedimentary Sulfur and Organic Carbon

85 Carbon and sulfur contents were determined using an elemental analyzer (including an acidification  
 86 module and furnace) coupled to an infrared detector (Analytik Jena multiEA 4000). Total inorganic  
 87 carbon content was quantified using an acidification module by applying 15-20% orthophosphoric acid  
 88 onto the sample material under gentle heating and measuring evolved CO<sub>2</sub> until the reaction was  
 89 complete. Total carbon and sulfur were measured by combustion at 1450°C under O<sub>2</sub> flow. The  
 90 instrument was calibrated using calcium carbonate and calcium sulfate dihydrate standards for carbon  
 91 and sulfur, respectively. Total organic carbon (TOC) was determined by difference between total carbon  
 92 and total inorganic carbon.

93

#### 94 6.2.3. Ferromagnetic resonance spectroscopy

95 FMR spectroscopy is used for the characterization of magnetic materials, specifically for the  
 96 measurement of the magnetocrystalline and the uniaxial magnetic anisotropy fields (e.g., Vonsovskii,  
 97 1966). In recent years, it has been successfully applied to quantitatively analyze the magnetic properties

98 of cultured MTB (Charilaou et al., 2011a; 2015) and to detect magnetofossils in sedimentary deposits  
99 (Gehring et al., 2011a; Kind et al., 2012; Kopp et al., 2006; Roberts et al., 2011). In the following we  
100 summarize the basic FMR principles to justify the concept of spectral analysis in our study. In an FMR  
101 experiment, the sample is subjected to a DC external magnetic field and an orthogonal microwave field.  
102 The DC field drives the magnetic moment of the sample to a precession around the field axis at a  
103 frequency that increases linearly with the strength of the external field, i.e., the Larmor frequency,  $\omega_L =$   
104  $g\mu_B B_{\text{eff}}/\hbar$ , where  $\hbar$  is the reduced Planck constant,  $g$  is the Landé spectroscopic splitting factor,  $\mu_B$  is  
105 the Bohr magneton, and  $B_{\text{eff}}$  is the effective magnetic field in the sample, consisting of both internal  
106 (exchange and anisotropy) and external fields (DC field and microwave field). Once the precession  
107 frequency matches that of the incident microwave radiation, i.e.,  $\omega_L = \omega_{\text{mw}}$ , resonance occurs and the  
108 sample absorbs microwave radiation as the magnetic moments precess at maximum amplitude. In a  
109 FMR spectrum, the resonance event is recorded as the absorption of microwaves that results in a  
110 resonance field, as a function of the external magnetic field. When the resonance condition is fulfilled,  
111 the absorption exhibits a maximum, and the FMR spectrum for a simple isotropic system has the shape  
112 of a distribution function, e.g., a Lorentzian or a Gaussian profile, centered at a resonance field denoted  
113  $B_{\text{eff}}$ . Figure 2A shows a FMR spectrum of an isotropic system with  $g = 2.05$ . In a system with magnetic  
114 anisotropy, i.e., SD magnetite particles and chain assemblies, there is an easy axis and a hard axis. The  
115 FMR spectrum is shifted along the field axis depending on the uniaxial internal field. When measured  
116 along the easy axis, the resonance field will be lower than that of the isotropic system, and when the  
117 measurement is along the hard axis the resonance field will be higher than that of the isotropic system  
118 (Fig. 2B). Hence, with FMR spectroscopy we obtain quantitative information about the internal fields  
119 of the sample.

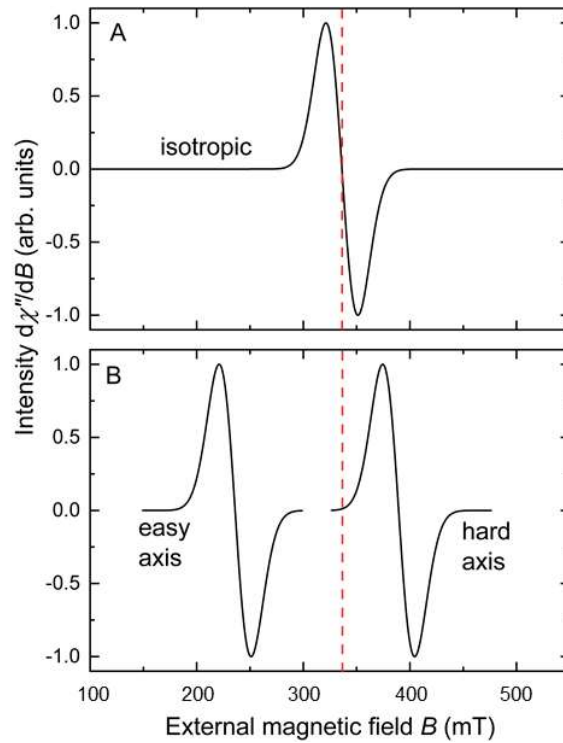


Figure 2. First derivative absorption FMR spectra of (A) an isotropic system with  $g = 2.05$  and (B) of a uniaxial system along its easy and hard axis. The vertical dashed line shows the resonance field of the isotropic system. The anisotropy shifts the spectra along the field axis, i.e., to lower field for the easy axis and to higher fields for the hard axis. Along the easy axis, the anisotropy field is parallel to the external field and contributes to the precession, and therefore a smaller external field is needed to achieve resonance. Contrarily, along the hard axis, the external field needs to compensate for the anisotropy field, which is off-axis to the external field.

120 In contrast to the spectra of oriented magnetic dipoles like those shown in Figure 2B (Charilaou et al.,  
 121 2014), magnetosomes chains are generally randomly distributed within sediments, and therefore all  
 122 resonance events are recorded at once and convoluted in the spectrum. A statistical treatment of the  
 123 FMR, as described by Charilaou et al. (2011a) quantifies the components of the FMR spectrum and  
 124 determines the magnetic properties of chains. Figures 3A and 3B show the convoluted FMR spectrum  
 125 of a uniaxial and a cubic system, respectively. The spectra are spread around the isotropic resonance  
 126 field and their shapes are due to the distribution of resonance fields in the sample. In MTB, the FMR  
 127 spectrum in Figure 3C is a convolution of resonance fields combining both uniaxial and cubic  
 128 symmetries. This spectrum corresponds to a system with MTB that have exactly the same magnetic  
 129 properties, i.e., uniaxial anisotropy field ( $B_{uni}$ ) and cubic anisotropy field ( $B_{cub}$ ). In sedimentary samples



130 that consist of multiple MTB species with different corresponding magnetofossils in varying states of  
 131 preservation, the spectral response becomes more complex.

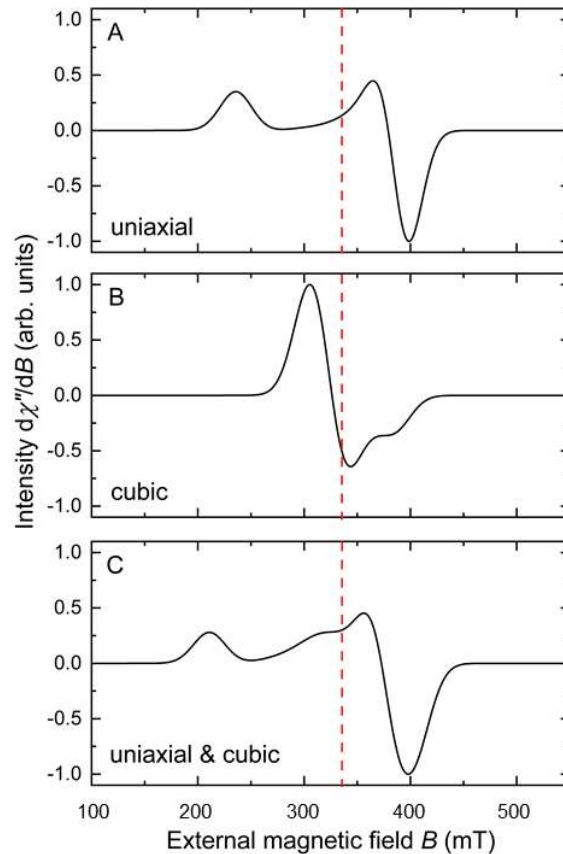


Figure 3. Convolved FMR spectra of (A) a purely uniaxial system, (B) a purely cubic system, and (C) a combined uniaxial and cubic system, corresponding to the spectrum of an ensemble of MTB.

132 In this study, the FMR spectra of the sediment samples were recorded on a X-band Bruker E500 EPR  
 133 spectrometer working at a frequency of 9.81 GHz, 0.06 mW power, 0.1 mT modulation amplitude, and  
 134 a modulation frequency of 100 kHz. The spectra were simulated with the algorithm by Charilaou et al.  
 135 (2011a). Using FMR spectra, contributions from paramagnetic species (mostly  $\text{Mn}^{2+}$ ) are quantified and  
 136 prior to spectral simulation, the paramagnetic signal at  $g \approx 2$  was removed as proposed by Maloof et al.  
 137 (2007). The FMR spectroscopy was complemented by mass magnetic susceptibility ( $\chi$ ) measurements  
 138 on an AGICO MFK1 Kappabridge and by first order reversal curve (FORC) analysis (Pike et al., 1999)  
 139 of the sample with the highest  $\chi$  using a MicroMag 3900 vibrating sample magnetometer and the  
 140 FORClab code for the data processing (Winklhofer and Zimanyi, 2006).

---

## 141 **6.3. RESULTS AND DISCUSSION**

### 142 **6.3.1. Sediment Description and Chronology**

143 Depth intervals from the uppermost 32 cm of the gravity core were investigated, which encompasses  
144 the last 160 years and spans a complete cycle of eutrophication and re-oligotrophication (Müller, 1997).  
145 The chronology of these sediments is subdivided into three episodes (Fig. 1), with deposition ages  
146 constrained by the present-day sedimentation rate of 1.9 mm/yr (Blattmann et al., 2019). Episode I  
147 (1850-1955 AD), corresponding to 21 cm of deposition, is characterized by monotonous bluish-gray  
148 clayey silt with dark striations representing a shoaling of the oxidation front upon continued burial  
149 (Hummel, 1923). Sediments darken continuously upward in the core toward episode II, which reflects  
150 encroaching eutrophic conditions due to increasing anthropogenic phosphorous inputs into the lake  
151 (Müller, 1997; Wessels et al., 1999). In episode II (1955-1991 AD), dark sediment with a pungent  
152 sulfidic odor marks the deposition of iron sulfide-bearing sediments during the most eutrophic stage  
153 (Müller, 1966a, b; Wagner, 1971). These sulfidic, dark clayey silts abruptly transition toward the core  
154 top into bluish-gray finely laminated and fluffy light brown clayey silts of episode III (1991-2012 AD).  
155 The brownish hue of the most recent deposits (uppermost 2 cm) is indicative of a ferric phase and points  
156 to oxic conditions. Hummel (1923) also described such a hue for sediments that are now bluish-gray.

157

### 158 **6.3.2. Biogeochemistry of Sediments and Water Column**

159 Extensive water column and surface sediment monitoring of Lake Constance over the past century  
160 offers a real-time geological window to link sedimentary total organic carbon (TOC) and total sulfur  
161 (TS) contents. In our profile (Fig. 1), TOC content ranges between 0.8 and 2.4 wt% and generally  
162 increases toward the present. The TS content varies between 0.01 and 0.6 wt%. In the later part of  
163 episode I, TS increases to a maximum in episode II. Such change is indicative of a shift from oxic or  
164 post-oxic to prevailing anoxic conditions (Berner, 1981). For the TOC content, the effect of  
165 eutrophication is obscured due to early diagenetic processes that resulted in the attenuation of organic  
166 matter degradation during burial (Blattmann et al., 2019; Müller, 1997). Beginning in the mid-19<sup>th</sup>  
167 Century, the TS trend and historical accounts (Hoppe-Seyler, 1895) are consistent with an absence of  
168 sulfides, and that massive sulfide formation began in the 1950s (Lehn, 1976; Wagner, 1971). Moreover,

169 increased TS correlates with the overall nutrient state of Lake Constance. The latter is gauged by water  
170 column dissolved phosphorous content that peaked in 1979 (Müller, 1997; Wessels et al., 1999),  
171 manifesting itself in the sulfidic sediments of episode II. During peak eutrophication, algal biomass  
172 increased approximately five-fold (Kümmerlin, 1998). This is consistent with observed dissolved  
173 oxygen contents in deep waters (which began in the 1890s) that reveal increasingly frequent and intense  
174 late-summer decreases into the 1950s due to enhanced settling and decay of organic matter (Elster and  
175 Einsele, 1937; Grim, 1955; Hoppe-Seyler, 1895; Lehn, 1976; Muckle, 1967; Rhodes et al., 2017;  
176 Wagner and Kruse, 1995). Oxygen replenishment in deep waters is driven by seasonal water column  
177 mixing and the influx of subducted riverine water masses, especially from the Alpine Rhine (Fink et al.,  
178 2016; Rhodes et al., 2017) and from littoral areas and bays. Compared to the 6.5 to 10 mm oxygen  
179 penetration depth into the sediment during the oligotrophic state (IGKB, 2009; Melton et al., 2014;  
180 Rahalkar et al., 2009), heightened organic matter burial and oxygen consumption by remineralization  
181 led to shoaling of the OATZ with reported oxygen penetration depths of < 2 mm, virtually reaching the  
182 sediment-water interface (Frenzel et al., 1990; Müller, 1966a; Wagner, 1967). In concert with  
183 eutrophication, bacterial biomass increased approximately tenfold and has contributed critically to  
184 dissolved oxygen consumption (Deufel, 1967, 1972). MTB are reported from other anthropogenically  
185 perturbed perialpine lakes, such as the lakes Chiemsee, Greifensee or Soppensee (e.g., Hawthorne &  
186 McKenzie, 1993; Spring et al., 2000; Kind et al. 2012), raising the possibility of their presence in Lake  
187 Constance.

188

### 189 6.3.3. Sediment Magnetic Properties

190 The magnetic susceptibility  $\chi$  varies between 9.44 and  $18.87 \times 10^{-8}$  SI with a relative maximum ( $\chi/\chi_{\max}$   
191 = 1) at the earliest part of episode III coinciding with re-oligotrophication and re-establishment of pre-  
192 eutrophic oxygenated conditions in the water column (Fig. 1). Such an enhanced  $\chi$  has been observed  
193 in several locations throughout the lake (Wessels, 1995). During episode III,  $\chi$  declines continuously  
194 and reassumes pre-eutrophic levels (Fig. 1). The variation in  $\chi$  is also mirrored in the FMR response,

195 i.e. the strongest signal due to the highest ferromagnetic (*s.l.*) content corresponds with the highest,  
 196 relative  $\chi$  (i.e., with  $\chi/\chi_{\max} = 1$ ).

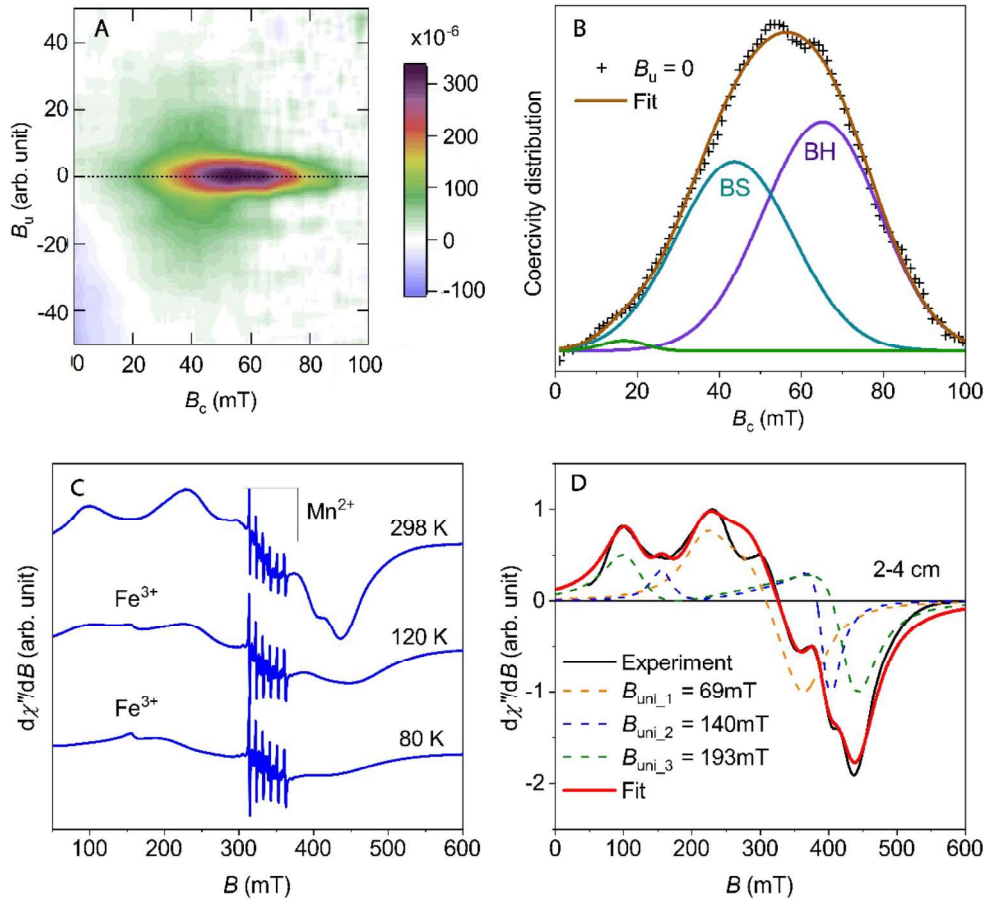


Figure 4. FORC curve of the sample with the highest  $\chi$  (A), deconvolution of  $B_c$  profile along  $B_u = 0$  with the two major Gaussian components denoted B(S) and B(H) and a minor one (B), corresponding FMR spectra superimposed by a  $\text{Mn}^{2+}$  signal at room and low-temperature (C), simulation of the experimental FMR spectrum obtained from the sample at room temperature as superposition of three components with different uniaxial fields (dashed lines) using the model of Charilaou et al. (2011a), the  $\text{Mn}^{2+}$  is omitted for clarity (D).

197 The FMR spectrum at room temperature obtained from the layer with  $\chi/\chi_{\max} = 1$  (Fig. 4D) revealed  
 198 broad ferrimagnetic features upon which a six-line signal typical for structure-bound  $\text{Mn}^{2+}$  in carbonates  
 199 is superimposed (Fig. 4C). The low-temperature behavior of FMR spectra shows characteristic  
 200 broadening associated with the Verwey transition diagnostic for magnetite, and indicates negligible  
 201 contributions of greigite ( $\text{Fe}_3\text{S}_4$ ) as another possible ferrimagnetic phase in MTB since the latter does  
 202 not feature a magnetic transition at low temperatures (Chen et al., 2014; Gehring et al., 2011b). Using

203 the method of Charilaou et al. (2011a), the relatively complex FMR spectrum can be simulated with the  
204 magnetocrystalline anisotropy field  $B_{\text{cub}} = -23.5$  mT for magnetite at room temperature and multiple  
205 uniaxial field  $B_{\text{uni}}$  components (Fig. 4D). The strongest uniaxial anisotropy with  $B_{\text{uni}} = 193$  mT is similar  
206 to that of a wild-type MTB with multiple magnetosome chains (Abraçado et al., 2014). The slightly  
207 lower  $B_{\text{uni}} = 140$  mT is comparable to values for single chains of laboratory-cultured MTB species  
208 (Charilaou et al., 2011b; Ghaisari et al., 2017). Given this, the two spectral components can be attributed  
209 to intact magnetosome chains. The origin of the third one ( $B_{\text{uni}} \approx 60$  mT) is less specific, but could be  
210 due to disintegrated chains that vary from chain fragments to SD magnetite particles (Charilaou et al.  
211 2011; Faivre et al. 2010). The detection of MTB by the pronounced  $B_{\text{uni}}$  is supported by a central ridge  
212 of the coercivity ( $B_c$ ) in the FORC diagram (Fig. 4A) that is a diagnostic feature for magnetic particle  
213 arrangements found in MTB (Egli et al., 2010; Roberts et al., 2012). Following Egli (2004), the central  
214 ridge can be deconvoluted into a bacterial soft (BS) component with 40-45 mT modal coercivity, a  
215 bacterial hard (BH) component 60-70 mT (Fig. 4B). A third minor component stems most likely from  
216 isolated magnetosomes (Fischer et al. 2008). Independent of microscopic evidence (e.g., Snowball,  
217 1994; Chen et al., 2014), the high magnetic anisotropy obtained from FMR and the FORC data provides  
218 clear evidence for a chain arrangement of SD magnetite formed by MTB (e.g., Egli, 2004; Fischer et  
219 al., 2008; Faivre et al., 2010; Charilaou et al., 2011b).

220

221 Superimposed upon the FMR spectra throughout the profile are also  $\text{Mn}^{2+}$  signals and for the weaker  
222 spectra obtained from samples at  $>15$  cm depth, a  $\text{Fe}^{3+}$  signal most likely associated with clay minerals  
223 becomes relatively pronounced (Meads and Malden, 1975). The FMR simulation after removal of the  
224  $\text{Mn}^{2+}$  signal reveals that the spectra from episodes II and III have superimposed signals with high  $B_{\text{uni}}$   
225 that are characteristic of intact magnetosome chains and of signals with  $B_{\text{uni}} < 100$  mT that are attributed  
226 to chain fragments and/or isolated magnetite particles (Fig. 4D, 5, and A1). In the latter case, the spectral  
227 contribution with  $B_{\text{uni}} = 0$  mT can be attributed either to isolated, superparamagnetic or SD magnetite  
228 particles with nearly equidimensional shapes that were most likely formed by MTB species such as  
229 *Magnetospirillum gryphiswaldense* (Scheffel et al., 2006). The deconvoluted FMR spectra of the top of  
230 episode I (11-15 cm) also reveal a mixture of magnetite in chains with  $B_{\text{uni}} = 178$  mT and SD magnetite

231 particles with no specific arrangement, i.e.  $B_{\text{uni}} < 100$  mT (Fig. 5 and A1). In contrast, there is no spectral  
 232 evidence for magnetite in chains in the lower part of episode I (Fig. 5).

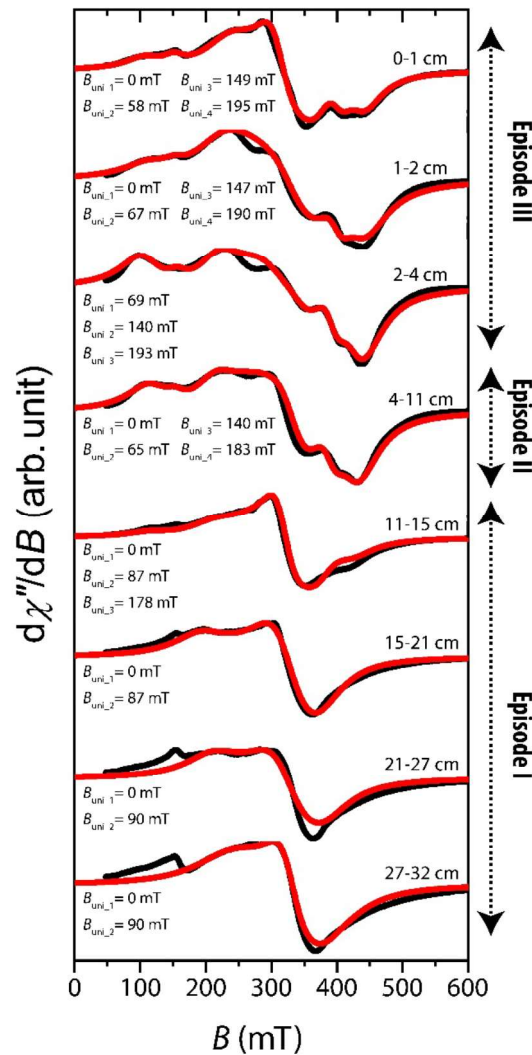


Figure 5. FMR spectra of the sediment core at room temperature and their simulation with  $B_{\text{cub}} = -235$  mT for magnetite.

233 In a MTB growth experiment, it has been shown that the shape of a FMR spectrum continuously  
 234 changes during the formation of the magnetosome chains (Faivre et al., 2010) and that this formation  
 235 can quantitatively be described by means of  $B_{\text{uni}}$  (Charilaou et al. 2011b). With this in mind the decrease  
 236 in  $B_{\text{uni}}$  can then be taken to infer the reverse process, i.e., the breakdown of magnetite chains in a natural  
 237 environment, as documented in the sediment record (Fig. 5; A1).

238

239

---

#### 240 6.3.4. Productivity and preservation of magnetofossils

241 Iron in mixed valence states is needed to form magnetite and it has previously been suggested that the  
242 iron activity within a depositional environment is a critical factor in MTB growth (Roberts et al., 2011).  
243 In Lake Constance, high organic matter fluxes to the sediment floor in the course of eutrophication  
244 leads to the shoaling of the OATZ toward the sediment-water interface and elevates the dissolved iron  
245 concentrations released to the lower water column (Müller, 1997; Roßknecht, 1998). In our profile, such  
246 conditions are indicated by the simultaneous increase in TOC and content of SD magnetic particles  
247 throughout episode II (Fig. 1). The sediments of this episode are characterized by the high relative  
248 content of magnetite as indicated by  $\chi/\chi_{\max}$ , and by uniaxial anisotropy fields that suggest different  
249 arrangements of the ferrimagnetic particles, and this in turn points to variable preservation states of the  
250 magnetofossils between chains and dispersed magnetosomes (Fig. 5). The historically chronicled zenith  
251 in eutrophication with a peak in dissolved phosphorous in 1979 (Müller, 1997) precedes the maximum  
252 in relative  $\chi$ , i.e., the peak in MTB productivity (Fig. 1). This maximum occurs at the onset of re-  
253 oligotrophication, which is characterized by a sharp redox gradient near the sediment-water interface  
254 with sulfidic deposits and well-oxygenated waters only millimeters apart (transition from episode II to  
255 III). Such an environment is ideal for the growth of microaerophilic MTB (e.g., Scheffel et al., 2006).  
256 Moreover, the maximum in MTB production, indicated by high  $\chi/\chi_{\max}$ , goes along with a high degree  
257 of the preservation of magnetosomes in chains as inferred from the FMR spectra (Figs. 1 and 5). Over  
258 the course of re-oligotrophication, a downwards retreat of the OATZ, away from the sediment-water  
259 interface, leads to a decrease in magnetosome content indicated by a decrease of  $\chi/\chi_{\max}$  to a level similar  
260 to that yielded from the sediments deposited before the maximum eutrophication during episode II.  
261 Therefore, the highest abundance of magnetofossils coincides with re-oxygenation, which is also  
262 similarly recorded in a marine environment case study (Passier et al., 2001).

263

264 The above link between magnetic and environmental information provides insight into the production  
265 and preservation of MTB in sedimentary deposits. The comparison of FMR spectra obtained from the  
266 Lake Constance sediment profile shows that magnetofossils, i.e., chain fragments and clumped or  
267 dispersed SD magnetite particles, are preserved. This relatively short diagenetic history of less than 150

---

268 years illustrates that the preservation of intact MTB chains in geological systems is limited.  
269 Nevertheless, the preservation of the magnetosomes can be used to constrain MTB productivity  
270 provided the magnetosomes are not affected by dissolution or mixing in the sediments with detrital  
271 magnetite. In our profile, these general conditions are met by the course of the magnetite content over  
272 time and the absence of multi-domain magnetic particles. With this in mind, our sediment core clearly  
273 indicates that the variations in magnetosome abundance, i.e. MTB productivity, records redox-changes  
274 in a depositional environment.

275

#### 276 **6.4. CONCLUSIONS**

277 Quantitative FMR spectroscopy of a sediment core recording a trophic cycle in Lake Constance shows  
278 that the magnetic content consists of SD magnetite particles originating from MTB, where they were  
279 formed as intracellular chains. The intact magnetosome chains break apart during diagenesis and are  
280 preserved as magnetofossils. Decadal-scale variations in magnetofossil content reflect MTB activity  
281 during the trophic cycle. With the return of an oligotrophic state, the redox gradient along the sediment-  
282 water interface steepened owing to replenishing deep-water oxygen diffusing into near-surface sulfidic  
283 sediments. Capitalizing on this redox gradient, MTB thrive. Under establishment of these oligotrophic  
284 conditions and upon continued sedimentary burial, the OATZ horizon deepened, leading to the rapid  
285 demise of the MTB. This, in turn, leads to the sedimentary magnetic properties reassuming pre-  
286 perturbation, background characteristics. With this in mind, preserved magnetosome assemblies and  
287 their concentration as inferred from FMR spectra in combination with  $\chi/\chi_{\max}$  can shed light on past  
288 microbiological activity in response to redox-changes in a depositional environment. Finally, MTB and  
289 their fossil remains are ideal carriers of paleomagnetic information, and therefore, in a  
290 magnetostratigraphic context, magnetofossils have great potential to constrain time-resolved  
291 microbiological response to redox-changes in geological systems.



---

## 292 6.5. ACKNOWLEDGMENTS

293 The authors thank Dimitrios Koulialias, Andrew Roberts, and anonymous reviewers for their critical  
294 comments on the manuscript and Michael Plötze (ClayLab ETH Zürich) for providing laboratory  
295 support for elemental analysis. The project was supported by Swiss National Sciences Foundation grant  
296 no. 200021\_165851 and ETH research grant ETH-41 14-1. T.M. Blattmann acknowledges funding from  
297 JAMSTEC and JSPS KAKENHI Grant (19K23475) and I. García-Rubio acknowledges funding from  
298 grants MINECO (CTQ2015-64486-R) and Gobierno de Aragón (E35\_17R) and Fondo Social Europeo-  
299 *“Construyendo Europa desde Aragón”*.

300

## 301 6.6. AUTHOR CONTRIBUTIONS

302 The samples were collected by Thomas M. Blattmann from ETH Zurich (Zurich, Switzerland), and  
303 Martin Wessels from Baden-Württemberg State Institute for the Environment, Survey and Nature  
304 Conservation (Langenargen, Germany). Thomas M. Blattmann, performed geochemical analysis. Inés  
305 García-Rubio from ETH Zurich (Zurich, Switzerland), and Centro Universitario de la Defensa  
306 (Zaragoza, Spain) performed spectroscopic measurements. Dimitrios Koulialias from ETH Zurich  
307 (Zurich, Switzerland) measured magnetic susceptibility. Ann Hirt from ETH Zurich (Zurich,  
308 Switzerland) measured hysteresis and FORC. Thomas M. Blattmann analyzed the non-magnetic data.  
309 Barbara Lesniak analyzed and characterized the magnetic and spectroscopic data, including simulation  
310 of the FMR spectra. All authors contributed to discussion and writing.

311

## 312 6.7. REFERENCES CITED

- 313 Abraçado, L., G., Wajnberg, E., Esquivel, D., M. S., Keim, C., N., Silva, K., T., Moreira, E., T. S., Lins,  
314 U., and Farina, M., 2014, Ferromagnetic resonance of intact cells and isolated crystals from  
315 cultured and uncultured magnetite-producing magnetotactic bacteria: *Physical Biology*, v. 11,  
316 no. 3, p. 036006.
- 317 Bazylinski, D. A., Frankel, R. B., and Jannasch, H. W., 1988, Anaerobic magnetite production by a  
318 marine, magnetotactic bacterium: *Nature*, v. 334, no. 6182, p. 518-519.
- 319 Berner, R. A., 1981, A new geochemical classification of sedimentary environments: *Journal of*  
320 *Sedimentary Research*, v. 51, no. 2, p. 359-365.
- 321 Blattmann, T.M., Lesniak, B., García-Rubio, I., Charilaou, M., Wessels, M., Eglinton, T.I., Gehring,  
322 A.U., 2020. Ferromagnetic resonance of magnetite biominerals traces redox changes. *Earth and*  
323 *Planetary Science Letters* 545, 116400

- 324 Blattmann, T. M., Wessels, M., McIntyre, C. P., and Eglinton, T. I., 2019, Petrogenic organic carbon  
325 retention in terrestrial basins: A case study from perialpine Lake Constance: *Chemical Geology*,  
326 v. 503, p. 52-60.
- 327 Chang, L., Harrison, R. J., Zeng, F., Berndt, T. A., Roberts, A. P., Heslop, D., and Zhao, X., 2018,  
328 Coupled microbial bloom and oxygenation decline recorded by magnetofossils during the  
329 Palaeocene–Eocene Thermal Maximum: *Nature Communications*, v. 9, no. 1, p. 4007.
- 330 Charilaou, M., Winklhofer, M., and Gehring, A. U., 2011a, Simulation of ferromagnetic resonance  
331 spectra of linear chains of magnetite nanocrystals: *Journal of Applied Physics*, v. 109, no. 9, p.  
332 093903.
- 333 Charilaou, M., Sahu, K. K., Faivre, D., Fischer, A., García-Rubio, I., and Gehring, A. U., 2011b,  
334 Evolution of magnetic anisotropy and thermal stability during nanocrystal-chain growth:  
335 *Applied Physics Letters*, v. 99, no. 18, p. 182504.
- 336 Charilaou, M., Kind, J., García-Rubio, I., Schüler, D., and Gehring, A. U., 2014, Magnetic anisotropy  
337 of non-interacting collinear nanocrystal-chains: *Applied Physics Letters*, v. 104, no. 11, p.  
338 112406.
- 339 Charilaou, M., Rahn-Lee, L., Kind, J., García-Rubio, I., Komeili, A., and Gehring, A. U., 2015,  
340 Anisotropy of bullet-shaped magnetite nanoparticles in the magnetotactic bacteria  
341 *Desulfovibrio magneticus* sp. strain RS-1: *Biophysical Journal*, v. 108, no. 5, p. 1268-1274.
- 342 Charilaou, M., 2017, Ferromagnetic resonance of biogenic nanoparticle-chains: *Journal of Applied*  
343 *Physics*, v. 122, no. 6, p. 063903.
- 344 Chen, A. P., Berounsky, V. M., Chan, M. K., Blackford, M. G., Cady, C., Moskowitz, B. M., Kraal, P.,  
345 Lima, E. A., Kopp, R. E., Lumpkin, G. R., Weiss, B. P., Hesse, P., and Vella, N. G. F., 2014,  
346 Magnetic properties of uncultivated magnetotactic bacteria and their contribution to a stratified  
347 estuary iron cycle: *Nature Communications*, v. 5, p. 4797.
- 348 Deufel, J., 1967, Hydrobakteriologische Untersuchungen im Bodensee I. Über die Vertikalverteilung  
349 der Bakterien im Pelagial: *Internationale Revue der gesamten Hydrobiologie und*  
350 *Hydrographie*, v. 52, no. 4, p. 617-626.
- 351 -, 1972, Hydrobakteriologische Untersuchungen im Bodensee III. Progressive Zunahme der  
352 planktonabhängigen Bakterienproduktion als Zeichen der Eutrophierung: *Internationale Revue*  
353 *der gesamten Hydrobiologie und Hydrographie*, v. 57, no. 1, p. 153-156.
- 354 Devouard, B., Pósfai, M., Hua, X., Bazylinski, D. A., Frankel, R. B., and Buseck, P. R., 1998, Magnetite  
355 from magnetotactic bacteria: Size distributions and twinning, *American Mineralogist*, Volume  
356 83, p. 1387.
- 357 Egli, R., 2004, Characterization of individual rock magnetic components by analysis of remanence  
358 curves. 3. Bacterial magnetite and natural processes in lakes: *Physics and Chemistry of the*  
359 *Earth, Parts A/B/C*, v. 29, no. 13, p. 869-884.
- 360 Egli, R., Chen, A. P., Winklhofer, M., Kodama, K. P., and Horng, C.-S., 2010, Detection of  
361 noninteracting single domain particles using first-order reversal curve diagrams: *Geochemistry,*  
362 *Geophysics, Geosystems*, v. 11, no. 1, p. n/a-n/a.
- 363 Elster, H.-J., and Einsele, W., 1937, Beiträge zur Hydrographie des Bodensees [Obersee]: *Internationale*  
364 *Revue der gesamten Hydrobiologie und Hydrographie*, v. 35, no. 1-6, p. 522-585.
- 365 Faivre, D., Fischer, A., Garcia-Rubio, I., Mastrogiacomo, G., and Gehring, A. U., 2010, Development  
366 of cellular magnetic dipoles in magnetotactic bacteria: *Biophysical Journal*, v. 99, no. 4, p.  
367 1268-1273.
- 368 Fink, G., Wessels, M., and Wüest, A., 2016, Flood frequency matters: Why climate change degrades  
369 deep-water quality of peri-alpine lakes: *Journal of Hydrology*, v. 540, p. 457-468.
- 370 Fischer, H., Mastrogiacomo, G., Löffler, J. F., Warthmann, R. J., Weidler, P. G., and Gehring, A. U.,  
371 2008, Ferromagnetic resonance and magnetic characteristics of intact magnetosome chains in  
372 *Magnetospirillum gryphiswaldense*: *Earth and Planetary Science Letters*, v. 270, no. 3, p. 200-  
373 208.
- 374 Frenzel, P., Thebrath, B., and Conrad, R., 1990, Oxidation of methane in the oxic surface layer of a deep  
375 lake sediment (Lake Constance): *FEMS Microbiology Letters*, v. 73, no. 2, p. 149-158.
- 376 Fuentes, N., Güde, H., Wessels, M., and Straile, D., 2013, Allochthonous contribution to seasonal and  
377 spatial variability of organic matter sedimentation in a deep oligotrophic lake (Lake Constance):  
378 *Limnologica*, v. 43, no. 2, p. 122-130.

- 379 Gambacorta, G., Bersezio, R., Weissert, H., and Erba, E., 2016, Onset and demise of Cretaceous oceanic  
380 anoxic events: The coupling of surface and bottom oceanic processes in two pelagic basins of  
381 the western Tethys: *Paleoceanography*, v. 31, no. 6, p. 732-757.
- 382 Gehring, A. U., Fischer, H., Louvel, M., Kunze, K., and Weidler, P. G., 2009, High temperature stability  
383 of natural maghemite: a magnetic and spectroscopic study: *Geophysical Journal International*,  
384 v. 179, no. 3, p. 1361-1371.
- 385 Gehring, A. U., Kind, J., Charilaou, M., and García-Rubio, I., 2011a, The detection of magnetotactic  
386 bacteria and magnetofossils by means of magnetic anisotropy: *Earth and Planetary Science  
387 Letters*, v. 309, no. 1, p. 113-117.
- 388 Gehring, A. U., Fischer, H., Charilaou, M., and García-Rubio, I., 2011b, Magnetic anisotropy and  
389 Verwey transition of magnetosome chains in *Magnetospirillum gryphiswaldense*: *Geophysical  
390 Journal International*, v. 187, no. 3, p. 1215-1221.
- 391 Ghaisari, S., Winklhofer, M., Strauch, P., Klumpp, S., and Faivre, D., 2017, Magnetosome Organization  
392 in Magnetotactic Bacteria Unraveled by Ferromagnetic Resonance Spectroscopy: *Biophysical  
393 Journal*, v. 113, no. 3, p. 637-644.
- 394 Grim, J., 1955, Die chemischen und planktologischen Veränderungen des Bodensee-Obersees in den  
395 letzten 30 Jahren: *Archiv für Hydrobiologie*, v. 22, no. 3-4, p. 310-322.
- 396 Griscom, D. L., 1980, Ferromagnetic resonance of fine grained precipitates in glass: A thumbnail  
397 review: *Journal of Non-Crystalline Solids*, v. 42, no. 1, p. 287-296.
- 398 Hawthorne, T. B., and McKenzie, J. A., 1993, Biogenic magnetite: authigenesis and diagenesis with  
399 changing redox conditions in Lake Greifen, Switzerland, *in* Aïssaoui, D. M., McNeill, D. F.,  
400 and Hurley, N. F., eds., *Applications of paleomagnetism to sedimentary geology*, Volume 49,  
401 SEPM.
- 402 Hesse, P. P., 1994, Evidence for bacterial palaeoecological origin of mineral magnetic cycles in oxic  
403 and sub-oxic Tasman Sea sediments: *Marine Geology*, v. 117, no. 1, p. 1-17.
- 404 Hoppe-Seyler, F., 1895, Über die Verteilung absorbierter Gase im Wasser des Bodensees und ihre  
405 Beziehung zu den in ihm lebenden Tieren und Pflanzen: *Schriften des Vereins für Geschichte  
406 des Bodensees und seiner Umgebung*, v. 24, p. 29-48.
- 407 Hummel, K., 1923, Über Sedimentbildung im Bodensee: *Geologisches Archiv von Ernst Kraus:  
408 Zeitschrift für gesamte Geologie und deren Nachbargebiete*, v. 2, p. 35-45.
- 409 IGKB, 2009, Bodensee-Untersuchung-Seeboden, v. 56, p. 107.
- 410 -, 2016, Tiefenschärfe - Hochauflösende Vermessung des Bodensees, v. 61, p. 109.
- 411 Kind, J., van Raden, U. J., García-Rubio, I., and Gehring, A. U., 2012, Rock magnetic techniques  
412 complemented by ferromagnetic resonance spectroscopy to analyse a sediment record:  
413 *Geophysical Journal International*, v. 191, no. 1, p. 51-63.
- 414 Kodama, K. P., Moeller, R. E., Bazylinski, D. A., Kopp, R. E., and Chen, A. P., 2013, The mineral  
415 magnetic record of magnetofossils in recent lake sediments of Lake Ely, PA: *Global and  
416 Planetary Change*, v. 110, p. 350-363.
- 417 Kopp, R. E., Weiss, B. P., Maloof, A. C., Vali, H., Nash, C. Z., and Kirschvink, J. L., 2006, Chains,  
418 clumps, and strings: Magnetofossil taphonomy with ferromagnetic resonance spectroscopy:  
419 *Earth and Planetary Science Letters*, v. 247, no. 1, p. 10-25.
- 420 Kopp, R. E., and Kirschvink, J. L., 2008, The identification and biogeochemical interpretation of fossil  
421 magnetotactic bacteria: *Earth-Science Reviews*, v. 86, no. 1, p. 42-61.
- 422 Kümmerlin, R. E., 1998, Taxonomical response of the phytoplankton community of Upper Lake  
423 Constance (Bodensee-Obersee) to eutrophication and re-oligotrophication, *in* Bäuerle, E., and  
424 Gaedke, U., eds., *Lake Constance Characterization of an ecosystem in transition*: Stuttgart, p.  
425 109-117.
- 426 Larrasoña, J., Liu, Q., Hu, P., Roberts, A., Mata, P., Civis, J., Sierro, F., and Pérez-Asensio, J., 2014,  
427 Paleomagnetic and paleoenvironmental implications of magnetofossil occurrences in late  
428 Miocene marine sediments from the Guadalquivir Basin, SW Spain: *Frontiers in Microbiology*,  
429 v. 5, no. 71.
- 430 Larrasoña, J. C., Roberts, A. P., Stoner, J. S., Richter, C., and Wehausen, R., 2003, A new proxy for  
431 bottom-water ventilation in the eastern Mediterranean based on diagenetically controlled  
432 magnetic properties of sapropel-bearing sediments: *Palaeogeography, Palaeoclimatology,  
433 Palaeoecology*, v. 190, p. 221-242.

- 434 Lehn, H., 1976, Veränderungen im Sauerstoffhaushalt des Bodensees, *in* Müller, P., ed., Verhandlungen  
435 der Gesellschaft für Ökologie Wien 1975: 5. Jahresversammlung vom 22. bis 24. September  
436 1975 in Wien: Dordrecht, Springer Netherlands, p. 121-128.
- 437 Lin, W., Paterson, G. A., Zhu, Q., Wang, Y., Kopylova, E., Li, Y., Knight, R., Bazylinski, D. A., Zhu,  
438 R., Kirschvink, J. L., and Pan, Y., 2017, Origin of microbial biomineralization and magnetotaxis  
439 during the Archean: *Proceedings of the National Academy of Sciences*, v. 114, no. 9, p. 2171-  
440 2176.
- 441 Maloof, A. C., Kopp, R. E., Grotzinger, J. P., Fike, D. A., Bosak, T., Vali, H., Poussart, P. M., Weiss, B.  
442 P., and Kirschvink, J. L., 2007, Sedimentary iron cycling and the origin and preservation of  
443 magnetization in platform carbonate muds, Andros Island, Bahamas: *Earth and Planetary  
444 Science Letters*, v. 259, no. 3, p. 581-598.
- 445 Meads, R. E., and Malden, P. J., 1975, Electron spin resonance in natural kaolinites containing Fe<sup>3+</sup>  
446 and other transition metal ions: *Clay Minerals*, v. 10, no. 5, p. 313-345.
- 447 Melton, E. D., Stief, P., Behrens, S., Kappler, A., and Schmidt, C., 2014, High spatial resolution of  
448 distribution and interconnections between Fe- and N-redox processes in profundal lake  
449 sediments: *Environmental Microbiology*, v. 16, no. 10, p. 3287-3303.
- 450 Muckle, R., 1967, Die Sauerstoffschichtung im tiefen Hypolimnion des Bodensee-Obersees 1963/64  
451 mit Berücksichtigung einiger Untersuchungsergebnisse aus früheren Jahren: *IGKB*, v. 3, p. 20.
- 452 Müller, G., 1966a, Die Verteilung von Eisenmonosulfid (FeS.nH<sub>2</sub>O) und organischer Substanz in den  
453 Bodensedimenten des Bodensees - ein Beitrag zur Frage der Eutrophierung des Bodensees: *Gas  
454 und Wasserfach*, v. 107, no. 14, p. 364-368.
- 455 -, 1966b, Die Sedimentbildung im Bodensee: *Naturwissenschaften*, v. 53, no. 10, p. 237-247.
- 456 -, 1997, Chronologie des anthropogenen Phosphor-Eintrags in den Bodensee und seine Auswirkung auf  
457 das Sedimentationsgeschehen, *in* Matschullat, J., Tobschall, H.-J., and Voigt, H.-J., eds.,  
458 *Geochemie und Umwelt: Relevante Prozesse in Atmo-, Pedo- und Hydrosphäre*: Berlin,  
459 Heidelberg, Springer Berlin Heidelberg, p. 317-342.
- 460 Passier, H. F., de Lange, G. J., and Dekkers, M. J., 2001, Magnetic properties and geochemistry of the  
461 active oxidation front and the youngest sapropel in the eastern Mediterranean Sea: *Geophysical  
462 Journal International*, v. 145, no. 3, p. 604-614.
- 463 Pike, C. R., Roberts, A. P., and Verosub, K. L., 1999, Characterizing interactions in fine magnetic  
464 particle systems using first order reversal curves: *Journal of Applied Physics*, v. 85, no. 9, p.  
465 6660-6667.
- 466 Rahalkar, M., Deutzmann, J., Schink, B., and Bussmann, I., 2009, Abundance and Activity of  
467 Methanotrophic Bacteria in Littoral and Profundal Sediments of Lake Constance (Germany):  
468 *Applied and Environmental Microbiology*, v. 75, no. 1, p. 119.
- 469 Rhodes, J., Hetzenauer, H., Frassl, M. A., Rothhaupt, K.-O., and Rinke, K., 2017, Long-term  
470 development of hypolimnetic oxygen depletion rates in the large Lake Constance: *Ambio*, v.  
471 46, no. 5, p. 554-565.
- 472 Roberts, A. P., Florindo, F., Villa, G., Chang, L., Jovane, L., Bohaty, S. M., Larrasoña, J. C., Heslop,  
473 D., and Fitz Gerald, J. D., 2011, Magnetotactic bacterial abundance in pelagic marine  
474 environments is limited by organic carbon flux and availability of dissolved iron: *Earth and  
475 Planetary Science Letters*, v. 310, no. 3, p. 441-452.
- 476 Roberts, A. P., Chang, L., Heslop, D., Florindo, F., and Larrasoña, J. C., 2012, Searching for single  
477 domain magnetite in the "pseudo-single-domain" sedimentary haystack: Implications of  
478 biogenic magnetite preservation for sediment magnetism and relative paleointensity  
479 determinations: *Journal of Geophysical Research: Solid Earth*, v. 117, no. B8.
- 480 Roßknecht, H., 1998, Langjährige Entwicklung chemischer Parameter im Bodensee-Obersee: *IGKB*, v.  
481 48, p. 143.
- 482 Savian, J. F., Jovane, L., Frontalini, F., Trindade, R. I. F., Coccioni, R., Bohaty, S. M., Wilson, P. A.,  
483 Florindo, F., Roberts, A. P., Catanzariti, R., and Iacoviello, F., 2014, Enhanced primary  
484 productivity and magnetotactic bacterial production in response to middle Eocene warming in  
485 the Neo-Tethys Ocean: *Palaeogeography, Palaeoclimatology, Palaeoecology*, v. 414, p. 32-45.
- 486 Scheffel, A., Gruska, M., Faivre, D., Linaroudis, A., Pletzko, J. M., and Schüler, D., 2006, An acidic  
487 protein aligns magnetosomes along a filamentous structure in magnetotactic bacteria: *Nature*,  
488 v. 440, p. 110.

- 489 Snowball, I. F., 1994, Bacterial magnetite and the magnetic properties of sediments in a Swedish lake:  
490 Earth and Planetary Science Letters, v. 126, no. 1, p. 129-142.
- 491 Spormann, A. M., and Wolfe, R. S., 1984, Chemotactic, magnetotactic and tactile behaviour in a  
492 magnetic spirillum: FEMS Microbiology Letters, v. 22, no. 3, p. 171-177.
- 493 Spring, S., Schulze, R., Overmann, J., and Schleifer, K.-H., 2000, Identification and characterization of  
494 ecologically significant prokaryotes in the sediment of freshwater lakes: molecular and  
495 cultivation studies: FEMS Microbiology Reviews, v. 24, no. 5, p. 573-590.
- 496 Suk, D., 2016, Environmental conditions for the presence of magnetofossils in the Last Glacial  
497 Maximum inferred from magnetic parameters of sediments from the Ulleung Basin, East Sea:  
498 Marine Geology, v. 372, p. 53-65.
- 499 Vonsovskii, S. V., 1966, Magnetic resonance in ferromagnetics, *in* Vonsovskii, S. V., ed., Ferromagnetic  
500 resonance: The phenomenon of resonant absorption of a high-frequency magnetic field in  
501 ferromagnetic substances, Pergamon, p. 1-11.
- 502 Wagner, G., 1967, Beiträge zum Sauerstoff-, Stickstoff- und Phosphorhaushalt des Bodensees: Archiv  
503 für Hydrobiologie, v. 63, no. 1, p. 86-103.
- 504 -, 1971, FeS-Konkretionen im Bodensee: Internationale Revue der gesamten Hydrobiologie und  
505 Hydrographie, v. 56, no. 2, p. 265-272.
- 506 Wagner, G., and Kruse, H. J., 1995, Analysis of the near-bottom oxygen minimum in Upper Lake  
507 Constance via statistical approach: Limnologica, v. 25, no. 1, p. 11-20.
- 508 Wessels, M., 1995, Bodensee-Sedimente als Abbild von Umweltänderungen im Spät- und Postglazial:  
509 Göttingen Arbeiten zur Geologie und Paläontologie, v. 66, p. 105.
- 510 -, 1998a, Geological history of the Lake Constance area, *in* Bäuerle, E., and Gaedke, U., eds., Lake  
511 Constance - Characterization of an ecosystem in transition: Stuttgart, p. 1-12.
- 512 -, 1998b, Natural environmental changes indicated by Late Glacial and Holocene sediments from Lake  
513 Constance, Germany: Palaeogeography, Palaeoclimatology, Palaeoecology, v. 140, no. 1, p.  
514 421-432.
- 515 Wessels, M., Mohaupt, K., Kümmerlin, R., and Lenhard, A., 1999, Reconstructing past eutrophication  
516 trends from diatoms and biogenic silica in the sediment and the pelagic zone of Lake Constance,  
517 Germany: Journal of Paleolimnology, v. 21, no. 2, p. 171-192.
- 518 Winklhofer, M., and Zimanyi, G. T., 2006, Extracting the intrinsic switching field distribution in  
519 perpendicular media: A comparative analysis: Journal of Applied Physics, v. 99, no. 8, p.  
520 08E710.
- 521
- 522
- 523
- 524
- 525
- 526
- 527
- 528
- 529
- 530
- 531
- 532
- 533
- 534

## 535 6.7. APPENDIX

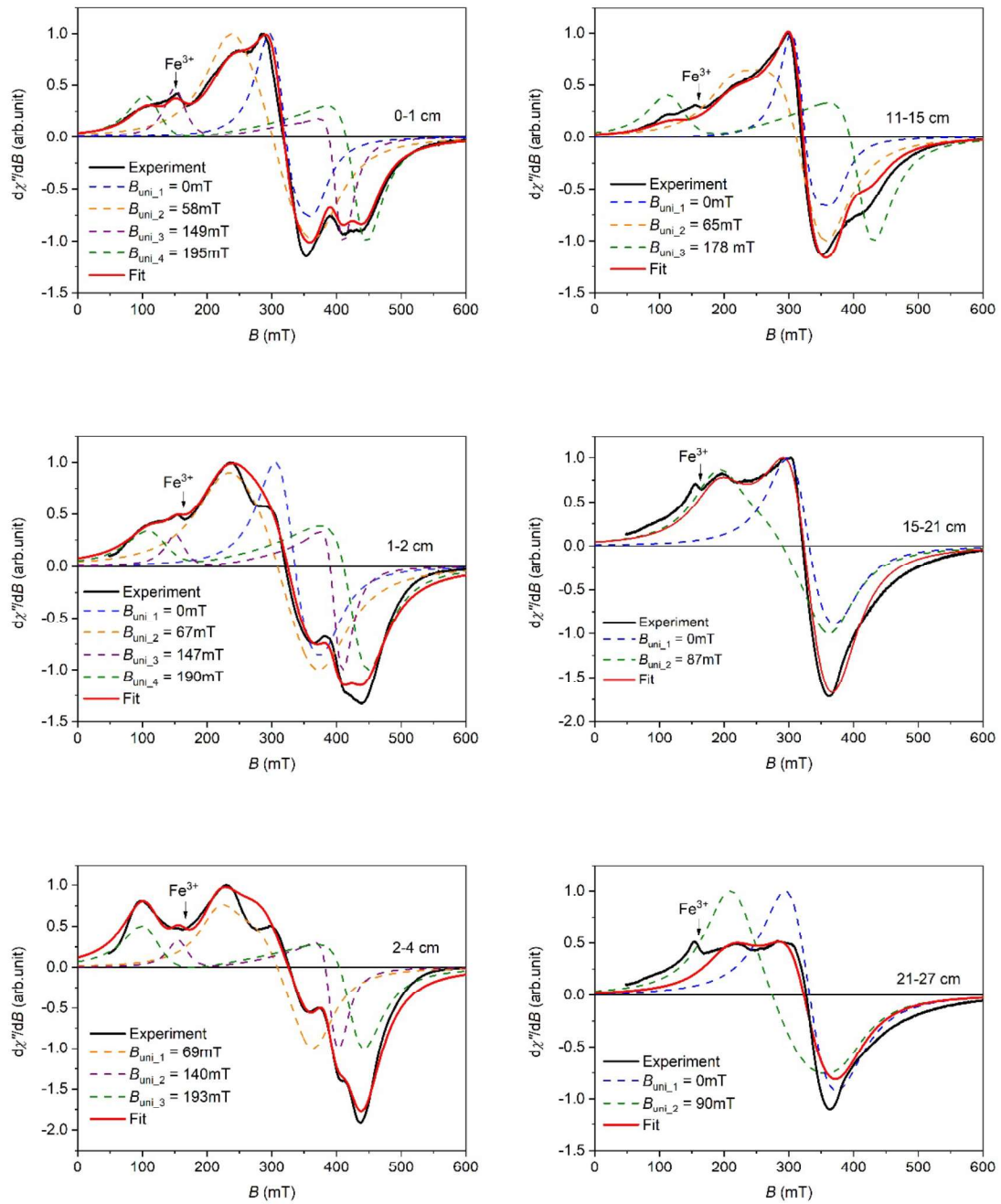


Fig. A1 Continued overleaf.

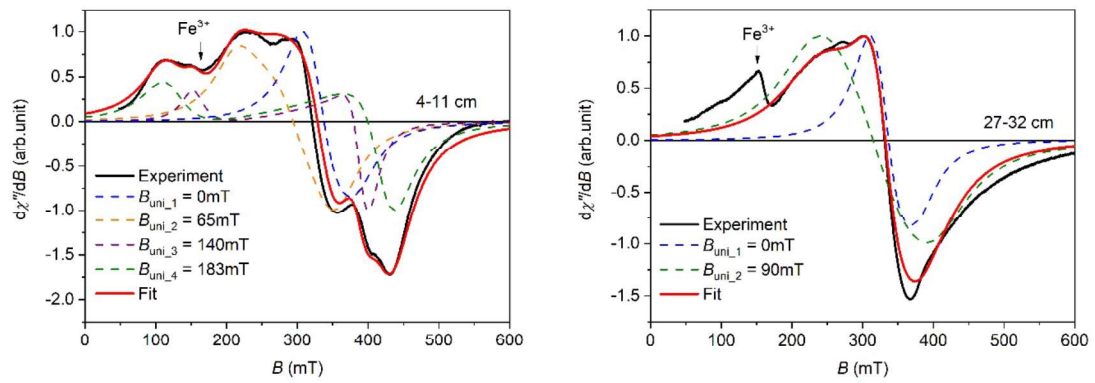


Fig. A1 Normalized FMR spectra at room temperature and their simulations using the model by Charilaou et al. (2011) with  $B_{\text{cub}} = -235$  mT and different Bu components.

536

537

538

539

540

541

542

543

544

545

546

547

548

549

550

551

552

553

554





---

## 1 7. Magnetic Carriers in Sediments Offshore the Namibian Coast and 2 their Relation to Upwelling

### 3 **Abstract**

4 The Benguela upwelling system is one of the strongest in the world and is associated with high  
5 productivity. Earlier studies have shown the occurrence of magnetotactic bacteria (MTB) in the water  
6 column and sediments near Walvis Bay, Namibia. We expand on these earlier studies to examine the  
7 presence of MTB that may be associated with separate upwelling cells along the Namibian coast. Rock  
8 magnetic methods, electron spin resonance (ESR) spectroscopy and fluorescence X-ray diffraction were  
9 used to identify the Fe-bearing minerals in the sediments offshore the Namibian coast, and their  
10 relationship to areas both within upwellings and outside the cells. Paramagnetic minerals are the  
11 dominant iron phases, but there is also the small presence of magnetite. ESR spectra show that the  
12 ferromagnetic (*s.l.*) minerals have a notable uniaxial shape anisotropy, characteristic of chain  
13 arrangement produced by MTB. This contribution is mostly seen, when the paramagnetic contribution  
14 is low and the sediment is mostly made up of organic and opal ooze. Our results confirm the presence  
15 of weak ferrimagnetic signal arising from MTB in the uppermost sediments, which for most sampling  
16 sites is covered by strong terrigenous influx originating from rivers and aeolian transport. ESR  
17 spectroscopy is a useful method to delineate the presence of MTB in the upwelling ecosystem, and we  
18 demonstrate their potential for identifying magnetofossils in marine sediments.

19

### 20 **7.1. INTRODUCTION**

21 Mineral magnetic studies of marine sediments are useful for investigating diagenetic processes (Karlin,  
22 1990; Mohamed et al., 2011; Roberts and Turner, 1993; Shi et al., 2017), and for reconstructing the  
23 course of climatic change, and for near-shore pollution monitoring (Blanchet et al., 2009; Evans and  
24 Heller, 2003; Larrasoana et al., 2015; Perez-Cruz and Urrutia-Fucugauchi, 2009; Scoullos et al., 1979;  
25 Wollin et al., 1971). Change in environmental conditions can be tracked by temporal and spatial  
26 variations in magnetic properties and geochemical properties of sediments over the area of interest.  
27 Magnetic and geochemical properties are dependent on the history of the sedimentary regime. The

---

28 potential sources of magnetic minerals in marine systems are more complex and extended than in other  
29 environmental systems (Thompson and Oldfield, 1986), and include detrital and wind-blown sediments,  
30 diagenetic alteration of original minerals, and biogenic minerals, including magnetotactic bacteria  
31 (MTB). In pelagic marine environments, iron and organic carbon play an important role in the  
32 production and preservation of MTB and their magnetosomes (Roberts et al., 2011). Roberts et al.,  
33 (2011) illustrated that the abundance of MTB can be linked to an increase in aeolian dust flux, which  
34 leads to iron fertilization and an increase in organic carbon export to the sea floor. Therefore, the  
35 presence of MTB will be strongly dependent on the biogeochemistry of the sedimentary environment.

36

37 In the Earth's oceans, the most biologically productive marine ecosystems are upwelling regions  
38 (Capone and Hutchins, 2013; Sowell et al., 2011). In these systems, the wind along the coast causes  
39 offshore movement of surface water (Huyer, 1983), which results in upwelling of cold, highly CO<sub>2</sub>  
40 concentrated, nutrient-rich water to the illuminated zone, where photosynthesis occurs (Calvert and  
41 Price, 1971). Nutrients and CO<sub>2</sub> concentrations are essential for photosynthesis, and their rise results in  
42 increased primary production (Marlow et al., 2000; Pauly and Christensen, 1995). The strongest  
43 upwelling zone in the world is around Lüderitz, Namibia and is part of the Benguela upwelling  
44 ecosystem (Bakun and Weeks, 2004; Des Combes and Abelmann, 2007; Santana-Casiano et al., 2009).  
45 The upwelling system is not evenly distributed along the coast, but it is rather separated in cells, which  
46 have different upwelling strengths (Lutjeharms and Meeuwis, 1987; Lutjeharms and Stockton, 1987).

47

48 An earlier study in this area by Petermann and Bleil (1993) found indication of MTB in the water  
49 column, as well as pelagic and hemipelagic sediments in several profiles along the Namibian coast. A  
50 later work by Hilgenfeldt (2000) examined cores from off the coast of Walvis Bay, to make a high-  
51 resolution rock magnetic study of the upper 20 cm of sediments. He demonstrated that single domain  
52 (SD) magnetite is present in the very top of the sediment, but that its concentration and particle size  
53 decrease gradually until it is no longer found at the depth of 10 cm, below which only coarse-grained  
54 hematite is found. Electron microscopy proves that the magnetite is due to bacterially produced  
55 magnetosomes, which undergo reductive dissolution with depth.

---

56 In this study, we also examine surface sediment samples along the Namibian coast in SW Africa to  
57 investigate the spatial distribution of MTB with respect to separate upwelling cells within the Bengula  
58 ecosystem. Whereas Hilgenfeldt (2000) used cores that were taken around a latitude of 23°S and at  
59 water depths between 600 and 1984 m, we focus on sediments that are taken along the coast of Namibia  
60 at shallower water depths for most sites. In addition, four cores were taken along a profile within the  
61 Lüderitz cell from different water depths. Rock magnetic methods, electron spin resonance  
62 spectroscopy, and fluorescence X-ray diffraction are used to identify the iron minerals in the sediments.  
63 This information should expand our understanding of the role that upwellings play in the concentration  
64 of iron-producing bacteria and their preservation from the coastal shelf to the continental slope.

65

## 66 7.2. GEOLOGICAL BACKGROUND

67 The continental margin along the Namibian coast (Fig.1) can be divided into a northern and southern  
68 section at latitude 18°40'S, due to differences in the margin morphology (Bremner, 1981). The northern  
69 Kunene shelf is narrow and shallow, and consists mostly of terrigenous sediments from the Kunene  
70 River. The southern Walvis shelf is wider and deeper, and consists of predominantly biogenic sediment.  
71 Sediments from the inner region of the Walvis shelf consist of diatomaceous organic-rich muds (Calvert  
72 and Price, 1971), indicating high productivity in the region (Bremner and Willis, 1993). The  
73 diatomaceous mud is characterised by a high content of diamagnetic opal and negligible terrestrial clay  
74 content (Bremner and Willis, 1993). Aeolian dust from the Namib desert together with input from rivers  
75 (e.g. Kunene river, Orange river) is considered to be the source of iron in the Benguela current system  
76 (Boyd and Ellwood, 2010; Bremner and Willis, 1993; Fryberger et al., 1979; Roberts et al., 2011).

77

78 The primary source of terrigenous material in the marine sediments is from aeolian transport of dust  
79 from the Namib desert (Fryberger et al., 1979). The Namib desert can be divided in two parts, the  
80 Skeleton Coast to the north of Walvis Bay and the Namib Sand Sea to the south (Logan, 1960). The  
81 sand of the entire region is rich in silicates (quartz, feldspar) and pyroxene (Garzanti et al., 2014). Note  
82 that the silicate mineral quartz is diamagnetic, whereas the iron-bearing silicates, e.g., pyroxene and  
83 amphibole, are paramagnetic (Dunlop and Özdemir, 1997).

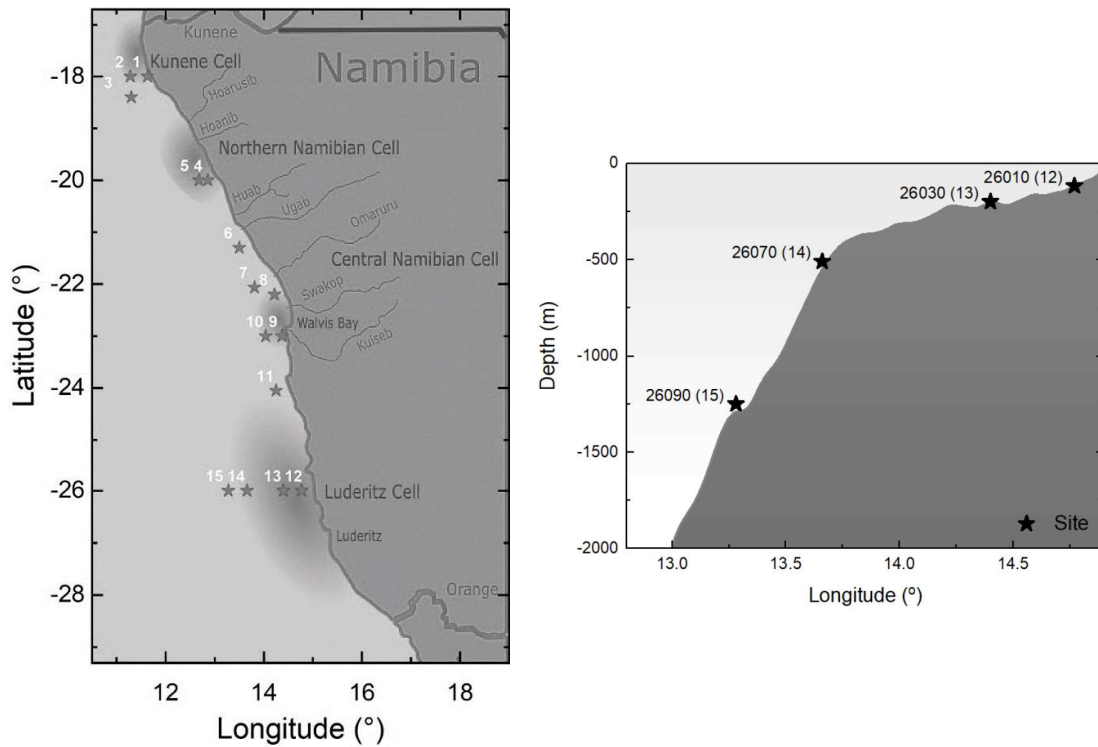


Fig. 1 a) Map of upwelling cells along the Namibian coast, indicating the sites where samples have been collected (red stars). The most important perennial (thick lines) and ephemeral rivers (thin lines) are shown (Strohbach, 2008). The shading along the coast indicate the separate upwelling cells (Lutjeharms and Meeuwis, 1987). The northern border of Namibia is partially the Kunene River, whereas the southern border of Namibia is the Orange river. The numbers 1-15 refer to samples according to the Table 1. b) The sites from the Lüderitz profile with marked position on the continental shelf along latitude 26°S. The distance from the shore is 19 km, 56 km, 131 km and 171 km for the sites 26010 (12), 26030 (13), 26070 (14), 26090 (15), respectively. The exact sites locations are presented in the Table 1.

84 Additional terrigenous input comes from various rivers that flow into the ocean. There are only two  
 85 perennial rivers in Namibia, the Kunene in the north and the Orange in the south (Fig.1). The detrital  
 86 input to the continental shelf from the Kunene river is rich in the paramagnetic clay minerals smectite  
 87 and kaolinite with smaller amounts of illite (Bremner and Willis, 1993). The Orange river's sediment  
 88 consists mostly of the paramagnetic clay minerals smectite and illite (Setti et al., 2014). These sediments  
 89 are carried north of the Orange river delta by persistent longshore currents that can extend up to 1750 km  
 90 (Garzanti et al., 2014). The ephemeral rivers (Fig. 1) carry mostly paramagnetic clays, such as illite and  
 91 smectite, in varying concentrations (Setti et al, 2014).

92

93 **7.3. MATERIALS AND METHODS**

94 A series of sediment cores were collected at 15 sites during the Monthly Oceanic Monitoring (MOM)  
 95 cruise of the research vessel RV Mirabilis in April 2017 along the coast of Namibia (Fig.1). The cores  
 96 were collected using an MC-400 Hedrick/Marrs Multi-Corer. Information about the sampling core's  
 97 location, depth of the water column to the seafloor and number of samples for each site is listed in  
 98 Table 1.

No.	Core name	Latitude (°)	Longitude (°)	Distance from the shore (km)	Estimated Water Depth (m)	No. of samples	Core length (cm)
1	18010	-18.0	11.6	20	125	10	30
2	18030	-18.0	11.3	59	1000	8	20
3	GeoChe1-6	-18.4	11.3	22	90	11	35
4	20010	-20.0	12.9	18	95	11	35
5	20020	-20.0	12.7	36	123	11	35
6	Ugab ZZ7	21.3	13.5	26	100	9	25
7	GeoChe1-3	-22.1	13.8	45	110	10	30
8	GeoChe1-2	-22.2	14.2	5	20	9	25
9	23002	-23.0	14.4	3	40	10	30
10	23020	-23.0	14.0	37	128	10	30
11	GeoChe2-1	-24.1	14.3	21	100	13	45
12	26010	-26.0	14.8	19	116	11	35
13	26030	-26.0	14.4	56	198	7	15
14	26070	-26.0	13.7	131	509	9	25
15	26090	-26.0	13.3	171	1250	9	25
In total						148	

Table 1. Core locations from which samples were collected with position, distance from the coast, depth of the water column to the sediment, number of samples collected per core and the length of the core defined for each sample. Numbers are assigned to the cores, starting from the most northern core 18010 (1).

99 Top-layer samples with high water content were collected using a syringe and deposited into plastic  
 100 tubes. More solid samples were cut with stainless-steel sampling-utensils and packed into plastic bags.  
 101 The sample interval was 1 cm for the first 5 cm, and then every 5 cm for the remainder of the core. Each

102 sample was homogenised, frozen at -20°C, and freeze-dried prior to analysis. The number of sediment  
103 samples vary between different sites, due to different core lengths (Table 1). The four last samples  
104 (no. 12 - 15) are located along a latitude of 26 °S and differ in their distance to the coast and water  
105 depth; this is termed the Lüderitz profile.

106

107 The magnetic properties of the samples were obtained using a susceptibility bridge, vibrating sample  
108 magnetometer (VSM) and electron spin resonance (ESR) spectroscopy. A Kappabridge MFK-1 (Agico,  
109 Czech Republic) was used to measure bulk magnetic susceptibility of the samples with an applied AC  
110 field of 200 A/m with frequency 976 Hz. The Kappabridge is characterized by high sensitivity and a  
111 measurement accuracy of  $5 \times 10^{-8}$  (SI) (Pokorny et al., 2011). A Princeton Measurement Corporation  
112 (PCM), MicroMag VSM, model 3900, was used to measure magnetization as a function of field  
113 between  $\pm 1$  T with a variable sample interval with 0.5 mT steps between  $\pm 100$  mT with an averaging  
114 time of 300 ms, 2 mT steps from  $\pm 100$  to  $\pm 200$  mT with an averaging time of 200 ms, and 5 mT steps  
115 for fields between  $\pm 200$  and 1000 mT with an averaging time of 200 ms. Samples in which the  
116 ferrimagnetic minerals made a significant contribution showed a hysteresis. The magnetic susceptibility  
117 and VSM measurements were made at room temperature at the Laboratory of Natural Magnetism, ETH  
118 Zurich. The dynamic magnetic properties were measured by electron spin resonance (ESR)  
119 spectroscopy, which was used for a detailed analysis of the magnetic particles. ESR is a sensitive tool,  
120 which can be used to detect paramagnetic signals originating from uncoupled spins as electron  
121 paramagnetic resonance (EPR) or magnetic phases and their anisotropy properties as ferromagnetic  
122 resonance (FMR). In an ESR experiment, the sample is subjected to a DC magnetic field and an  
123 orthogonal microwave field. The application of the external magnetic field ( $B_{ext}$ ) causes a precessional  
124 motion of the magnetization ( $M$ ), the Larmor precession. As the field is swept, the Larmor frequency  
125 increases linearly with the field, and when the Larmor frequency matches the microwave frequency,  
126 resonance occurs and the sample absorbs the microwave radiation. The resonance equation is:  
127  $h\nu = g\mu_B B_{res}$  where  $h$  is Planck's constant,  $\nu$  is the microwave frequency,  $\mu_B$  is Bohr's magneton,  $g$   
128 is the spectroscopic splitting factor and  $B_{res}$  is the resonance field. The g-factor measures the energy

129 splitting of degenerate states in the magnetic field and  $B_{\text{res}}$  is the field at the maximum absorption. The  
130 measured net signal is the superposition of all resonance events, that is, the measured spectrum is the  
131 sum of the spectra originating from particles in all orientations. The absorption of the microwave  
132 radiation is generally plotted as the first derivative spectrum of intensity. The X-band Bruker ElexSys  
133 E500 spectrometer was used to record spectra with frequencies at around 9.39 GHz at Electron  
134 Paramagnetic Resonance research group, Laboratory of Physical Chemistry ETH Zurich. The  
135 spectrometer is equipped with temperature controllers and helium gas-flow cryostat from Oxford  
136 Instruments. The ESR spectra were recorded at variable temperatures. If it was possible, further  
137 processing using a simulation program by Charilaou et al. (2011) was performed, in order to model the  
138 contribution to a ESR spectra arising from a ferromagnetic (*s.l.*) phases with high uniaxial anisotropy  
139 or cubic anisotropy.

140 X-ray fluorescence was performed on most samples from the Lüderitz profile, to obtain major and  
141 minor elemental chemistry of the sediments. This type of analysis, when used together with magnetic  
142 measurements, allows one to determine the possible dependence between elements and the served  
143 magnetic signal. On some of the uppermost samples the XRF analysis was not performed, due to  
144 insufficient material. Firstly, samples were ball milled for 40 s in a Retsch RS1 with a speed of 1400  
145 revolutions per minute. Secondly, 4 g of each sample was mixed with 0.9 g of resin Cerox for 8 min  
146 and subsequently pressed to form a tablet under a 15-ton load. Finally, samples were measured with a  
147 SPECTROXEPOS spectrometer at the Soil Chemistry Laboratory ETH Zurich. The elements analysis  
148 was performed based on the elemental function as an environmental proxy obtained from Croudance  
149 and Rothwell (2015).

150

## 151 7.4. RESULTS

### 152 **Magnetic susceptibility**

153 The magnetic susceptibility varies strongly between the sampling cores (Fig.2); however, often it does  
154 not change significantly as a function of depth. The highest magnetic susceptibility is observed for the  
155 most northern sample, situated close to the border with Angola (18010 (1)). It has an average

156 susceptibility of  $42.3 \times 10^8 \text{ m}^3/\text{kg}$ . The lowest susceptibility is found at site UgabZZ7 (6) with an  
 157 average of  $3.03 \times 10^8 \text{ m}^3/\text{kg}$ ; it is located at the delta of the Ugab River.

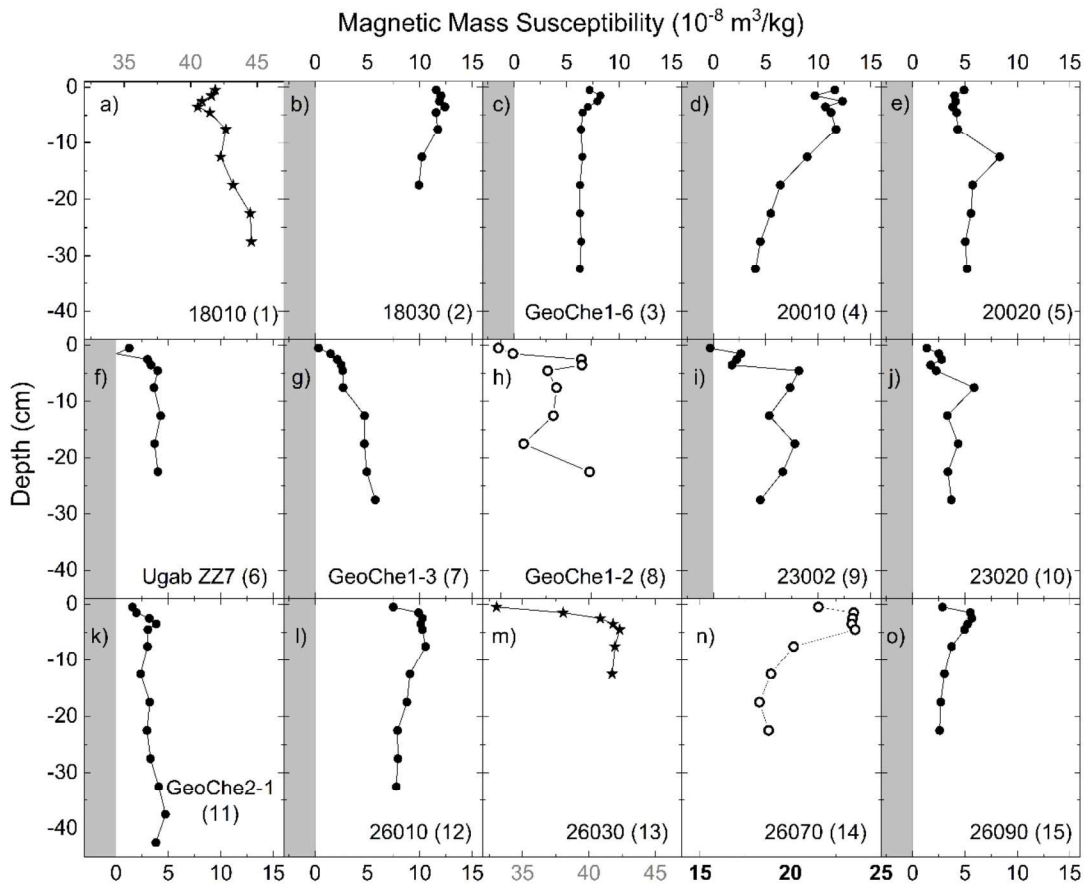


Fig.2 Magnetic susceptibility as a function of depth for each sample site. The grey colour indicates the negative part of a susceptibility, which indicates diamagnetic behaviour as observed for few samples from sites Ugab ZZ7 (6) and 23002 (9). The three ranges of the susceptibility are defined: cores a) 18010 (1) and m) 26030 (13) are indicated with ★ and their magnetic susceptibility range is  $32 - 47 \times 10^8 \text{ m}^3/\text{kg}$ , cores h) GeoChe1-2 (8) and n) 26070 (14) are indicated with ● and their magnetic susceptibility range is  $14 - 25 \times 10^8 \text{ m}^3/\text{kg}$ , the remaining cores are indicated with ● and are characterised by magnetic susceptibility  $-3 - 15 \times 10^8 \text{ m}^3/\text{kg}$ .

158 For samples within the Lüderitz profile (26010 (12), 26030 (13), 26070 (14), 26090 (15)), susceptibility  
 159 is the highest for the second site away from the coast (26030 (13),) and the lowest for site 26090 (15),  
 160 which is furthest from the coast.

161

162 **Magnetic hysteresis**



163 The magnetisation as a function of magnetic field was measured for selected samples from the  
164 uppermost sediments (0-1 cm) (Fig. A1, A2). Generally, the magnetization is very weak and strongly  
165 influenced by the paramagnetic contribution, although the presence of a weak hysteresis loop is  
166 observed for all measured samples. The surface sample from Site 18010 (1) with the highest magnetic  
167 susceptibility is dominated by a paramagnetic contribution, but has a small open loop (Fig. A1a),  
168 indicating a minor ferrimagnetic contribution that makes up 11% of the total magnetization (Table A1).  
169 The uppermost sample from the sites along the Lüderitz profile (Fig. A2) show a more pronounced  
170 hysteresis loop. Surprisingly, the samples from site 26030 (13) and 26070 (14) with the highest  
171 magnetic susceptibility reveal a weaker ferrimagnetic contribution to the saturation magnetization  
172 (Fig. A2b, c), compared to the samples from site 26010 (12) and 26090 (15), which have low  
173 susceptibility (Fig. A2a, d).

174

#### 175 **ESR at room temperature**

176 ESR spectra were measured on samples from the sediment-water interface at each site (Fig. 3). All  
177 samples display a broad magnetic signal, and many also show an additional contribution (sharp line(s)),  
178 which is due to a radical in a paramagnetic phase. The paramagnetic cation  $\text{Fe}^{3+}$  in octahedral  
179 coordination is clearly distinguishable around 150 mT (g value of 4.3) (Meads and Malden, 1975), as  
180 seen for example in Ugab ZZ7 and GeoChe1-3 (Fig. 3f,g). The paramagnetic cation  $\text{Mn}^{2+}$  is  
181 characterised by six narrow peaks at around  $g = 2$ , as observed for example in 23002 and 26090 (Fig. 3  
182 panels 9) and 15)). The very narrow peaks that are found in the middle of the spectra around 350 mT  
183 ( $g \approx 2.02$ ) represent a free electron radical in organic matter or clay minerals (e.g., Fig.5 panels 6), 7),  
184 10), 11)) (Perry, 1990).

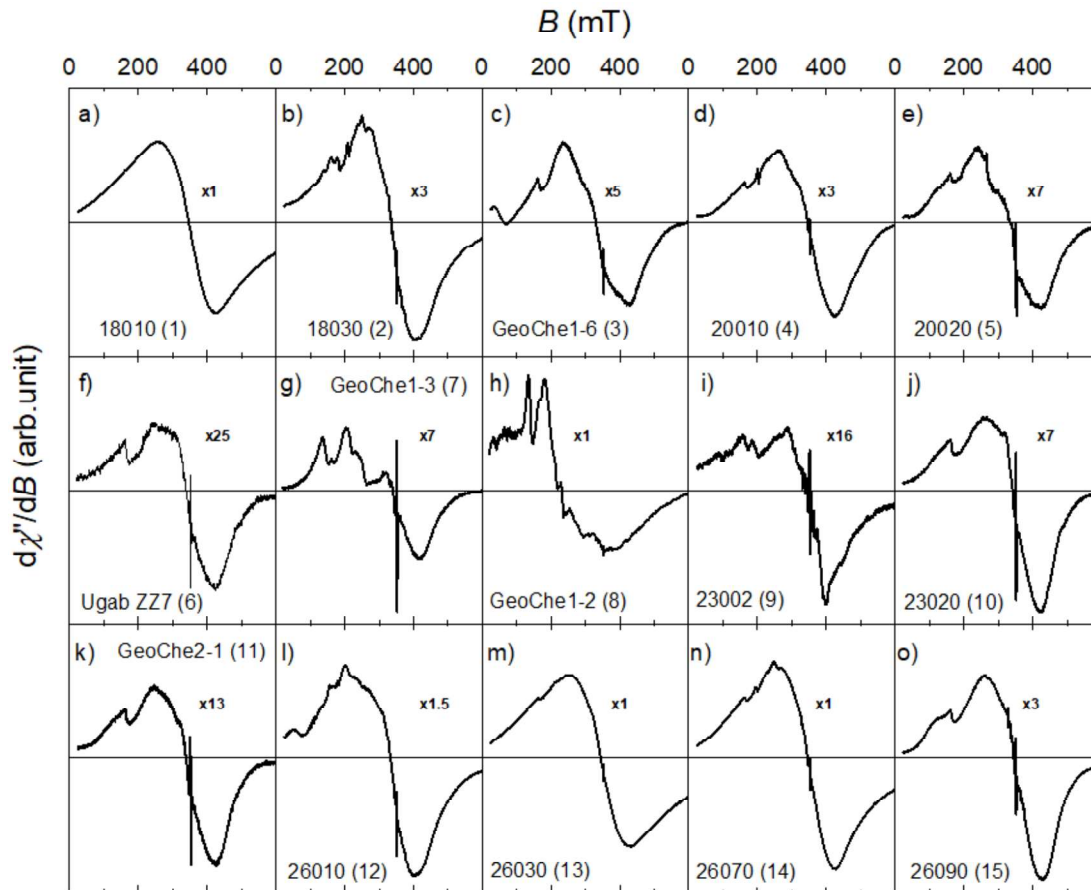


Fig. 3. ESR of selected samples at the sediment-water interface showing characteristically symmetric shapes. Note that all spectra have been normalized to the absorption of the strongest signal. The multiplication factor “x3” etc. indicates how much weaker the sample was compared to the strongest sample with factor 1. The samples were measured at room temperature.

185 Fig. 4 shows spectra signals from two sediment cores, 18010 (1) and 23020 (10), at different depths.  
 186 The samples from 18010 have the highest susceptibility and all show a strong resonance absorption  
 187 (Fig. 4a). The samples from 23020 (10) have low susceptibility and a resonance spectra 7x weaker than  
 188 18010 (1) (Fig. 4b). These two cores represent the most typical behaviour observed for all sediment  
 189 sites. The spectra from 18010 (1) do not change greatly with depth, and show a symmetric absorption  
 190 spectrum, i.e., the absorption is a Lorentzian distribution, thus the  $d\chi''/dB$  shows the characteristic  
 191 positive/negative curve. In contrast, the spectra for 23020 (10) change visibly with the depth. The  
 192 0-1 cm signal is complex and contains two low-field peaks with maxima at around 140 mT and 255 mT,  
 193 and one high-field peak at 420 mT. With increasing depth, the lower field peaks weaken until the

194 spectrum becomes nearly symmetric, except for a small  $\text{Fe}^{3+}$  contribution. These results suggest that  
 195 there is more than one contribution to the ESR signal.

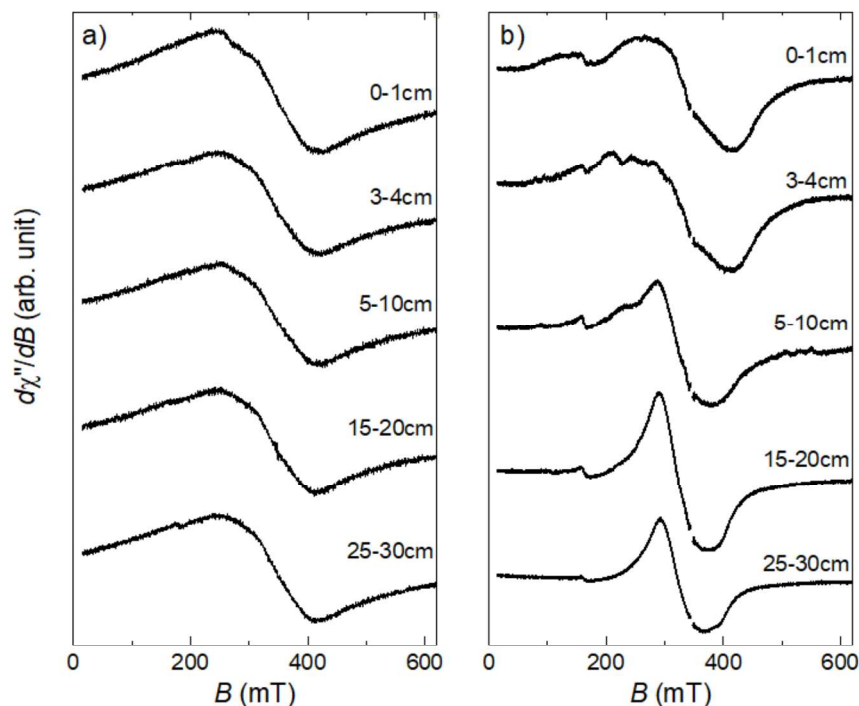


Fig. 4 ESR spectra of selected samples, measured at room temperature, for selected depths a) 18010 (1), and b) 23020 (10) illustrating the progressive change in mineralogy. N.B., the contribution from the radical has been removed from the ESR signal for easier comparison.

### 196 ESR at low temperature

197 To better understand the minerals that are responsible for the ESR signal, the uppermost sediment  
 198 samples from site 18010 (1) and 23020 (10) were measured as a function of temperature between 10 K  
 199 and 290 K (Fig. 5). The ESR signal from 18010 (1) increases by a factor of eight while cooling to 10 K  
 200 (Fig. 5a). The shape of the signal, however, remains relatively symmetric with decreasing temperature  
 201 down to 80 K, while cooling below 80 K results in a slight broadening of the signal. The  $g$  value is  
 202 around 2.14 at room temperature and with cooling it shifts to higher values, reaching 2.22 at 10 K. The  
 203 change of  $B_{\text{res}}$  with decreasing temperature is shown in Fig. 5b, where it decreases slightly from 329 mT  
 204 to 318 mT, with a slightly more pronounced decrease from 50 K to 10 K. The increase in the signal  
 205 with decreasing temperature and minor change of  $B_{\text{res}}$  is an indicative of paramagnetic resonance. The

206 slight drop in  $B_{\text{res}}$  at low temperatures may indicate the blocking of spins of the paramagnetic phase(s)  
 207 (Coey, 1988).  
 208 The ESR signal of 23020 (10) is characterised by the signal broadening with decreasing temperature.  
 209 The transition to a broader signal is visible around 100 K (Fig. 5c), where the  $B_{\text{res}}$  also undergoes a  
 210 sharp decrease (Fig. 5d). This behaviour is typical for magnetite found in chains that pass through the  
 211 Verwey transition (Gehring et al., 2011). Additionally, the sharp peak with g value around 4.3 from  
 212  $\text{Fe}^{3+}$  increases around 3 times, typical for this paramagnetic contribution (Perry, 1990). This peak is  
 213 superimposed with a broader shoulder extending in the direction of lower fields, which is clearly visible  
 214 at room temperature. That shoulder decreases at around 100 K, what indicates that it originates from  
 215 magnetite.

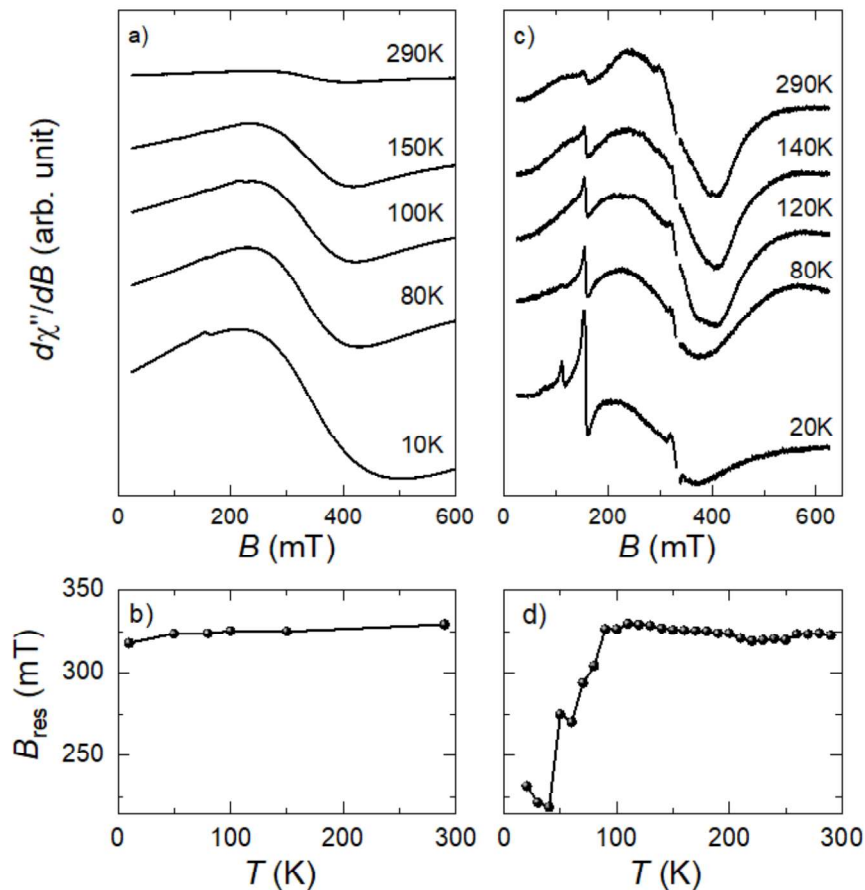


Fig. 5 ESR spectra for the sediment-water interface samples at various temperatures for the samples a) 18010 (1) with b) the change in  $B_{\text{res}}$  as a function of temperature, and the ESR spectra of c) 23020 (10) with d) the change in  $B_{\text{res}}$  as a function of temperature. The radical was removed from ESR spectra of the sample no.10.

---

**216 Simulation of the FMR signal**

217 To test whether the ESR signal complexity may originate from the presence of chains of nanoparticles,  
218 we compare the spectra with simulation results for MTB. Fig. 6 shows the experimental spectra for the  
219 surface sample at 23020 (10), which is the sample that shows ferromagnetic resonance that undergoes  
220 a Verwey transition. The simulated signal was obtained using model by Charilaou et al. (2011) (Fig.  
221 6a). It requires at least two contributions with different uniaxial fields to match the measured spectrum  
222 (Fig. 6b). One contribution of around 69 mT has low uniaxiality that would be associated with single  
223 randomly oriented particles, and the second contribution is characterised by high uniaxiality (175 mT)  
224 that would be typical for magnetosomes in a chain configuration. Such high signals are observed only  
225 for the biogenic nanoparticle assemblies. The signal with high uniaxiality is required to fit the low-field  
226 broad shoulder and the rather broad high-field minimum. In this case, the simulation predicts that the  
227 relative signal weight contributions to the total fit are: 64 % arising from dispersed particles and 36 %  
228 from chain fragments. The low-field broad shoulder overlaps with a sharp peak at 340 mT ( $g \approx 4.3$ ),  
229 which is a contribution from  $\text{Fe}^{3+}$ . This  $\text{Fe}^{3+}$  contribution and contribution from the radical (sharp  
230 maximum around 150 mT) are neglected.

231

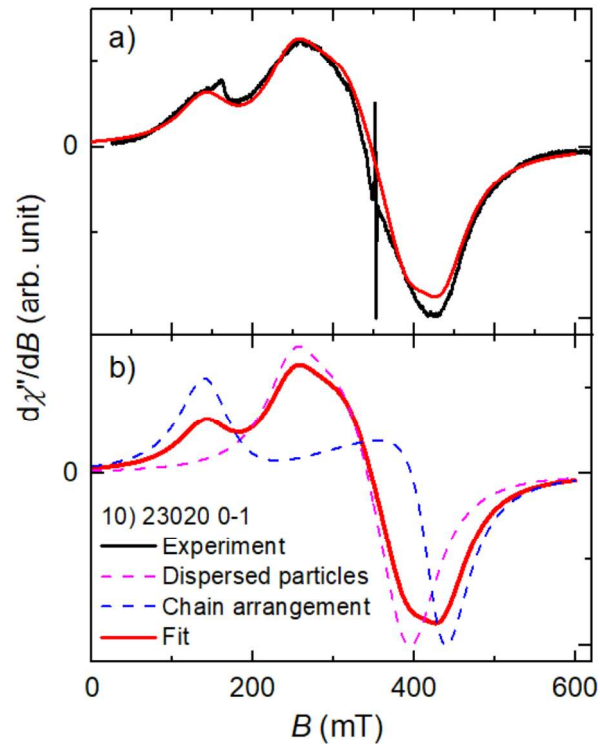


Fig. 6 a) Calculated FMR spectra for chains of magnetic nanoparticles for surface sample 23020 (10), at room temperature, such as those found in magnetotactic bacteria compared with experimental data b) Fit of the experimental FMR spectrum using the same model as in panel (a). For the simulation two different uniaxial field were used:  $B_{\text{uni}} = 69$  mT (64 %) and  $B_{\text{uni}} = 175$  mT (36 %), which are associated with dispersed particles and chain fragments, respectively.

### 232 The X-ray fluorescence of the Lüderitz profile

233 The samples from the Lüderitz profile (26010 (12), 26030 (13), 26070 (14), 26090 (15)) were collected  
 234 to analyse the magnetic response and geochemical parameters as a function of the distance from the  
 235 coast (Fig. 1b). All results are presented in Table A2 and selected data in Fig. A3. The different elements  
 236 and their ratios were analysed separately and Figure 10 displays the main elements together with  
 237 magnetic susceptibility, in which we focus on the elements and elemental ratios that reflect the  
 238 dependence on organic productivity (Br, Br/Ti) (Agnihotri et al., 2008; Caley et al., 2011; Mayer et al.,  
 239 2007; Ziegler et al., 2008), and terrigenous material and aeolian dust influx (Fe, Ti, Fe/Ca, Fe/Ti, Ti/Ca,  
 240 K, Si) (Adegbe et al., 2003; Blanchet et al., 2007; Calvert and Pedersen, 2007; Grutzner et al., 2003;  
 241 Itambi et al., 2010; Kuhlmann et al., 2004; Pierau et al., 2011; Vidal et al., 2002). Additionally, the  
 242 other elements were analyzed in order to reflect the presence of specific clay minerals, e.g., pyroxene

---

243 and illite (V, Cr, K) (Bourotte et al., 2009; Huang et al., 2015; Kuhlmann et al., 2004), carbonate content  
244 (Ca, Fe/Ca) (Adegbe et al., 2003; Röhl et al., 2004), and possible magnetite dissolution (Fe/Ti,  
245 comparison of Fe, Ti to susceptibility) (Funk et al., 2003; Hepp et al., 2009; Kuhlmann et al., 2004).

246

247 The magnetic susceptibility at Site 26010 is lowest at the water-sediment interface and is higher  
248 between 1 cm to 10 cm depth and then slowly decreases with depth (Fig, 10a). Fe, Ti, and V show a  
249 similar change with depth, but do not mirror the same trend as the susceptibility curve. Br shows the  
250 maximum at the top of the site and slightly decreases with the sediment depth. Site 26030 (13) is  
251 characterised by the highest magnetic susceptibility along the Lüderitz profile (Fig. 7b). There is a  
252 notable increase from the surface sediment to 5 cm depth, and with a negligible decrease to 15 cm. Fe,  
253 Ti and V follows the same trend as susceptibility with depth. Br shows the opposite trend of the other  
254 elements. Samples from site 26070 (14) have the second highest susceptibility in the Lüderitz profile  
255 (Fig. 7c). The magnetic susceptibility increases at 1-2 cm and is highest between 1 cm and 5 cm depth;  
256 it decreases abruptly at 10 cm and remains low to 22.5 cm. The trend in susceptibility is mirrored by  
257 Fe, while Ti and V also show a stronger increase at 1-2 cm depth and a marked decrease at 7.5 cm, but  
258 Ti increases from 7.5 cm to 22.5. Br shows the opposite behavior to Ti. The magnetic susceptibility of  
259 samples from the deepest water depth at site 26090 (15) shows low susceptibility at the surface and then  
260 a significant increase at 1 – 3 cm depth (Fig. 7d). Susceptibility decreases quickly to 7.5 cm depth and  
261 then more gradually to the bottom of the core. Although it was not possible to perform X-ray  
262 fluorescence measurements on the uppermost sediment samples, Fe displays the opposite trend to  
263 magnetic susceptibility, whereas Br follows the magnetic susceptibility. The variation of Ti and V does  
264 not mirror the other properties with depth.

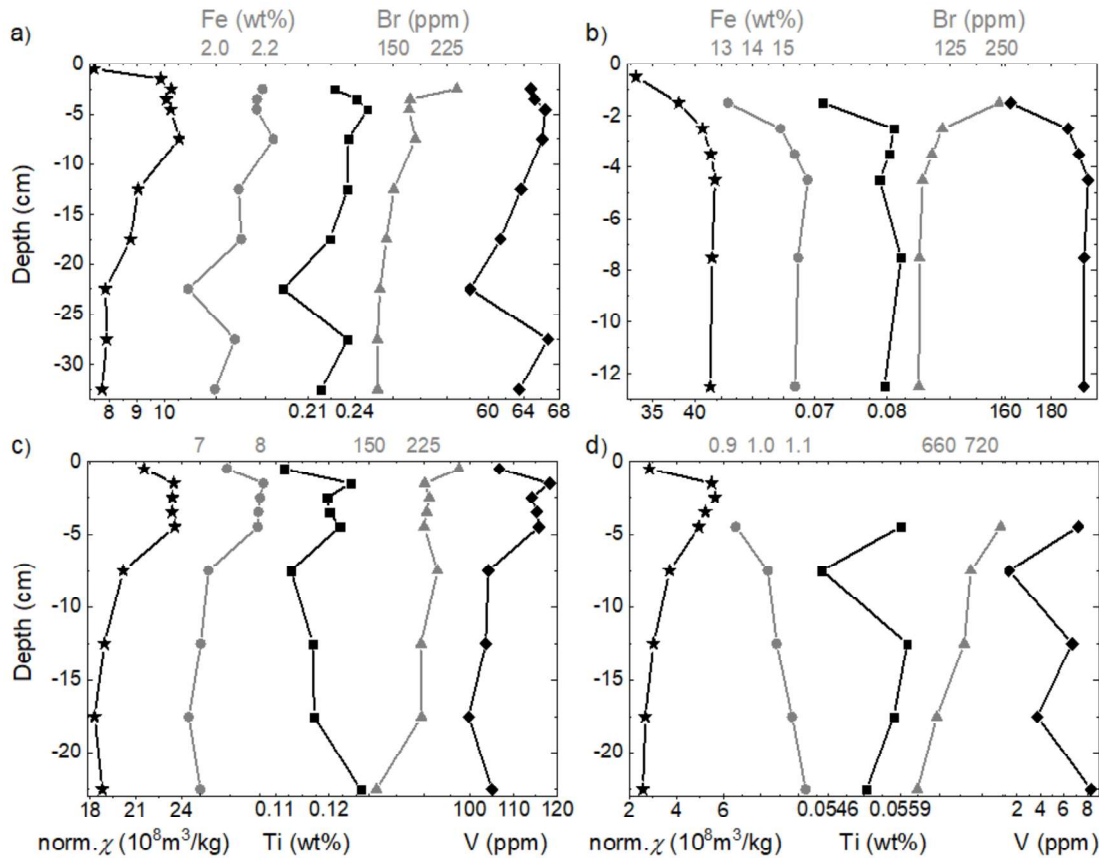


Fig. 7 The mass magnetic susceptibility compared to chosen geochemical properties for samples: a) 26010 (12), b) 26030 (13), c) 26070 (14), and d) 26090 (15). The curves show normalised magnetic susceptibility (★), Fe (●), Ti (■), Br (▲), V (◆) (left to right). For the samples with relatively high  $\chi$  (b,c), the  $\chi$  follows Fe content, similar behaviour is observed for Ti and V, whereas Br shows opposite behaviour. For samples with lower  $\chi$  the similarity becomes weaker (a) or fully disappears (d).

265 The Fe/Ti ratio is often used as an indicator for dissolution of magnetite (Appendix Fig. A3) (Croudace  
 266 and Rothwell, 2015). The ratio does not change coherently for the sites, except for Site 26030 (13),  
 267 which displays a small decrease with depth. The slight difference, however, precludes any  
 268 interpretation. Cd content, which is associated with diatomaceous mud, is the highest for the site closest  
 269 to the shore (Appendix Fig. A3) (Bremner, 1981).

270

271

272



---

**273 7.5. DISCUSSION**

274 The magnetic susceptibility at most sites is weak. The site with the strongest susceptibility, 18010 (1)  
275 has an induced magnetization that is predominantly paramagnetic (Fig. 2, A1a) and an ESR signal that  
276 increase in amplitude with decreasing temperature (Fig. 5a). This indicates that paramagnetic minerals  
277 dominate the samples' magnetization. As this site lies on the Kunene shelf, it is strongly influenced by  
278 a terrigenous input from the Kunene river. These detrital minerals carry a high concentration of  
279 paramagnetic clays, such as smectite and kaolinite (Bremner and Willis, 1993). The hysteresis loop that  
280 does not saturate by 150 mT indicates additional presence of hematite, as visible for site 18010 (1)  
281 (Fig. A1a) (Liu et al., 2019). The strong ESR signal with low uniaxial field is observed for detrital  
282 samples. It may originate from the total contribution of the paramagnetic signals overlapping one  
283 another (Fig. 3). Sites 18030 (2) and GeoChe1-6 (3) are most likely also influenced by input from the  
284 Kunene river, however, as they lie further from the source their contribution to the samples'  
285 magnetization signal is proportionally weaker (Fig. 8). For this reason, their ESR signals are narrower  
286 and uniaxial fields slightly higher, which may suggest a contribution from ferrimagnetic minerals, i.e.,  
287 MTB.

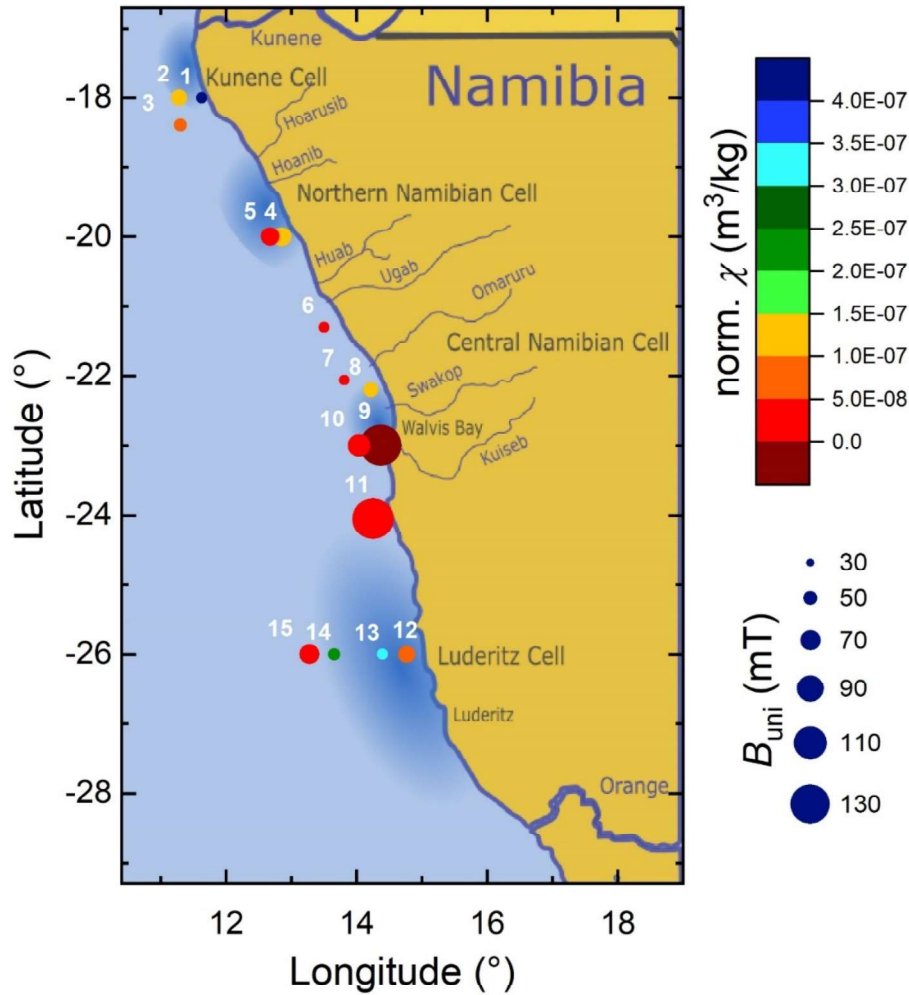


Fig. 8 Map of the Namibian coast summarising the spatial difference in magnetic susceptibility and uniaxial field from ESR measurements of the samples from the sediment-water interface. Note that the magnitude of susceptibility is reflected by the colour scale and the magnitude of  $B_{\text{uni}}$  by the size for the symbol. The numbers 1-15 refer to samples according to the Table 1.

288 The remaining sites are located on the Walvis shelf, and excluding the sites along the Lüderitz profile,  
 289 display low susceptibility and generally weak ESR signals (Fig. 2, 3). The ESR spectra from the surface  
 290 samples at sites 20010 (4) and 20020 (5) have a slightly higher  $B_{\text{uni}}$ , compared to other sites on the shelf,  
 291 and a narrower signal that may indicate a ferrimagnetic contribution originating from chain  
 292 arrangement. Sites GeoChe1-3 (7) and GeoChe1-2 (8) have relatively low  $B_{\text{uni}}$ , which together with the  
 293 shape of the signal suggests a strong dominance of the paramagnetic minerals (Fig. A1, 8). This may  
 294 account for the higher susceptibility at GeoChe1-2 (8), which is within 5 km of the coast. Therefore,

295 the source of the paramagnetic minerals may be the Omaruru river. The ESR signals from all sites  
296 between the Ugab and Omarur rivers (Sites Ugab ZZ7 (6), GeoChe1-3 (7), GeoChe1-2 (8), 23002 (9))  
297 have a strong contribution from the paramagnetic cation  $\text{Fe}^{3+}$  and  $\text{Mn}^{2+}$ , as seen from the hyperfine  
298 splitting around 345 mT (Fig. A1).

299

300 The three sites that are around Walvis Bay (23002 (9), 23020 (10) GeoChe2-1 (11)) are interesting in  
301 that they are characterised by very low or even diamagnetic susceptibility in the case of the top sediment  
302 at 23002 (Fig. 2i). The upper sediments at these sites are composed largely of diatomaceous mud, which  
303 has a negligible clay content and opal concentration. These samples also showed very weak hysteresis  
304 (Fig. A1b). ESR signals at these sites are narrower and have a higher  $B_{\text{uni}}$  (Fig. 3) than the other samples,  
305 which further indicates that the ferrimagnetic minerals aligned in chains make a significant contribution  
306 to the sample magnetization, similar to what was shown in Chapter 5. The ESR signal from the sediment  
307 from the site 23020 (10) decreases around 100 K, which is where the Verwey transition is usually found  
308 in chains of magnetite in MTB. The presence of MTB chains can be confirmed by the simulation for  
309 site 23020 (10) (Fig. 5). These sites indicate that when the sediments contain a low concentration of  
310 paramagnetic clays and mostly non-Fe phases, the ferrimagnetic component originating from  
311 magnetofossils become better expressed in ESR analysis.

312

313 The magnetic properties of the surface sediments from the Lüderitz upwelling cell (Sites 26010 (12),  
314 26030 (13), 26070 (14) and 26090 (15)) vary with respect to their distance from the coast (Fig. 8). The  
315 sites closest (19 km) and furthest (171 km) from the coast have low susceptibility, and 26030 (13) and  
316 26070 (14) that are 56 km and 131 km, respectively have significantly higher susceptibility. We first  
317 discuss these latter two sites that also show paramagnetic magnetization curves (Fig. A2), and broad  
318 ESR signals similar to what is seen at 18010 (1) (Fig. 3). This would suggest that the magnetization of  
319 sites 26030 and 26070 (14) are dominated by paramagnetic phases. This interpretation is supported  
320 further by XRF analysis, which reveals strong terrigenous influence as seen from Fe, K, and V content,  
321 which mirrors the variation of susceptibility with depth (Fig. 7). High V is often found in pyroxene,  
322 which is abundant in the Namib sand sea along the coast. Aeolian transport of sand could be responsible

---

323 for the higher V-content at these two locations on the shelf. K on the other hand is believed to originate  
324 from illite, which is common in the Orange river. Although the Orange River lies south of these sites,  
325 coastal currents lead to sediment transport to the north along the coast (Roger and Rau, 2006). At both  
326 sites Br shows the opposite trend with depth in comparison to the magnetic susceptibility. Br is related  
327 to productivity and has been used as an indicator of bacterial activity (Croudace and Rothwell, 2015).  
328 Therefore, it is unlikely that the dominant magnetic signal originates from microbial production.

329

330 Sites 26010 (12) and 26090 (15) are characterized by low magnetic susceptibility and slightly increased  
331  $B_{uni}$  in comparison to the samples at 26030 (13) and 26070 (14). At these sites Fe does not reflect the  
332 magnetic susceptibility, and both V and Ti also do not follow the variation in susceptibility (Fig. 7). Br,  
333 however, reflects the magnetic susceptibility, what suggests that the susceptibility may be related to  
334 bacterial activity. Such an interpretation is backed by the ESR spectra, which are characterized by  
335 increased  $B_{uni}$  arising from chain arrangement. Therefore, along the Lüderitz profile the presence of  
336 MTB is only seen where a paramagnetic contribution to the magnetization is not strong. The clear  
337 difference in the dominant magnetic signal between sites 26010 (12), 26090 (15) and sites 26030 (13),  
338 26070 (14) indicates that strong terrigenous influx may cover the signal originating from  
339 magnetofossils.

340

341 Our results indicate that magnetotactic bacteria can be identified in sediments along the Namibian coast  
342 in the Benguelan Upwelling ecosystem, an area with the highest productivity in the world. The strongest  
343 indication for the presence of MTB is at Walvis Bay and along the Lüderitz profile, thus at locations of  
344 upwelling cells. Our results, however highlight that other Fe minerals can contribute to the magnetic  
345 properties of these marine sediments, particularly paramagnetic Fe-bearing clay minerals, as supported  
346 by measurements of magnetization versus field, which indicates a strong paramagnetic contribution to  
347 all the surface sediments. These sites have ESR spectra that are compatible with a paramagnetic phase.  
348 In evaluating microbial systems, the predominant paramagnetic response does not necessarily exclude  
349 the presence of bacterial magnetite, but may only cover it, due to the strong terrigenous input. Therefore,  
350 we cannot rule out the presence of bacteria outside the upwelling cells, but their concentration would

351 be very low. When the paramagnetic contribution, however, is low and the sediment is mostly made up  
352 of organic and opal ooze, there is a much clearer indication for the MTB.

353

#### 354 **7.6. CONCLUSIONS**

355 Minerals that are responsible for the magnetic properties of marine sediments along the coast of  
356 Namibia within the Benguelan Ecosystem show two main sources. Many site locations north of Walvis  
357 Bay are dominated by a strong terrigenous input. The strong terrigenous influence of Fe-bearing clays  
358 originate from rivers, but also aeolian deposits from the Namib desert. Interestingly, the regions whose  
359 sediments are made up of organic and opal ooze, show not only a ferrimagnetic component to the  
360 magnetization but an increased uniaxial anisotropy that would only be found if the ferrimagnetic phase  
361 was arranged in chains. This feature implies the presence of chains of nanoparticles in the marine  
362 system, being a characteristic feature of the MTB. The magnetic signal originating from magnetofossils,  
363 however, may be covered by disproportionately high concentration of Fe-bearing paramagnetic clay  
364 minerals. Our results show the value of using ESR spectroscopy for identifying chains of magnetic from  
365 MTB, but also illustrate the complex nature of understanding which Fe-bearing minerals contribute to  
366 the magnetization of the samples. It is only by understanding the variation in iron-bearing minerals  
367 along the coast, that it will be possible to evaluate the balance terrigenous sediments and their transport  
368 and high productivity that leads to MTB in upwelling ecosystems.

369

#### 370 **7.7. AUTHOR CONTRIBUTIONS AND ACKNOWLEDGEMENTS**

371 The samples were collected under the Regional Research Graduate Network in Oceanography (RGNO)  
372 2017. Northern samples were collected by Anastasiia Ignatova from ETH Zurich (Zurich, Switzerland),  
373 and southern by Barbara Leśniak, under supervision of Daniel Montluçon.

374

375 I gratefully acknowledge the assistance of the instructors and students of the RGNO Discovery Camps  
376 [http://www.microeco.ethz.ch/Courses\\_overview/RGNO/announcement\\_rgno.pdf](http://www.microeco.ethz.ch/Courses_overview/RGNO/announcement_rgno.pdf), as well as the  
377 scientific staff and the crew on the R/V Mirabilis who made access to the Benguela Current Ecosystem  
378 possible for us. The samples were collected during the Mirabilis cruise Research and Training-

379 MOM/RGNO 0417. The Discovery Camps of the Regional Graduate Network for Oceanography  
380 (RGNO) are funded by the Agouron Institute, the Simons Foundation, the Scientific Committee for  
381 Oceanographic Research (SCOR), the Ministry of Fisheries and marine Resources (MFMR) through  
382 the National Marine Information and Research Center (Nat MIRC), the University of Namibia  
383 (UNAM), ETH Zurich and the Swiss i-research & training institute.

384

385 **7.8. REFERENCES**

- 386 Adegbe, A.T., Schneider, R.R., Röhl, U., Wefer, G., 2003. Glacial millennial-scale fluctuations in  
387 central African precipitation recorded in terrigenous sediment supply and freshwater signals  
388 offshore Cameroon. *Palaeogeography, palaeoclimatology, palaeoecology* 197, 323-333.
- 389 Agnihotri, R., Altabet, M.A., Herbert, T.D., Tierney, J.E., 2008. Subdecadally resolved  
390 paleoceanography of the Peru margin during the last two millennia. *Geochemistry, Geophysics,*  
391 *Geosystems* 9.
- 392 Bakun, A., Weeks, S.J., 2004. Greenhouse gas buildup, sardines, submarine eruptions and the  
393 possibility of abrupt degradation of intense marine upwelling ecosystems. *Ecology Letters* 7,  
394 1015-1023.
- 395 Blanchet, C.L., Thouveny, N., Vidal, L., 2009. Formation and preservation of greigite (Fe<sub>3</sub>S<sub>4</sub>) in  
396 sediments from the Santa Barbara Basin: Implications for paleoenvironmental changes during  
397 the past 35 ka. *Paleoceanography* 24.
- 398 Blanchet, C.L., Thouveny, N., Vidal, L., Leduc, G., Tachikawa, K., Bard, E., Beaufort, L., 2007.  
399 Terrigenous input response to glacial/interglacial climatic variations over southern Baja  
400 California: a rock magnetic approach. *Quaternary Science Reviews* 26, 3118-3133.
- 401 Bourotte, C., Bertolo, R., Almodovar, M., Hirata, R., 2009. Natural occurrence of hexavalent chromium  
402 in a sedimentary aquifer in Urânia, State of São Paulo, Brazil. *Anais da Academia Brasileira de*  
403 *Ciências* 81, 227-242.
- 404 Boyd, P.W., Ellwood, M.J., 2010. The biogeochemical cycle of iron in the ocean. *Nature Geoscience*  
405 3, 675-682.
- 406 Bremner, J.M., 1981. Shelf morphology and surficial sediment off central and northern South West  
407 Africa (Namibia). *Geo-Marine Letters* 1, 91.
- 408 Bremner, J.M., Willis, J.P., 1993. Mineralogy and geochemistry of the clay fraction of sediments from  
409 the Namibian continental-margin and the adjacent hinterland. *Marine Geology* 115, 85-116.
- 410 Caley, T., Malaizé, B., Zaragosi, S., Rossignol, L., Bourget, J., Eynaud, F., Martinez, P., Giraudeau, J.,  
411 Charlier, K., Ellouz-Zimmermann, N., 2011. New Arabian Sea records help decipher orbital  
412 timing of Indo-Asian monsoon. *Earth and Planetary Science Letters* 308, 433-444.
- 413 Calvert, S., Pedersen, T., 2007. Chapter fourteen elemental proxies for palaeoclimatic and  
414 palaeoceanographic variability in marine sediments: interpretation and application.  
415 *Developments in Marine Geology* 1, 567-644.
- 416 Calvert, S.E., Price, N.B., 1971. Upwelling and nutrient regeneration in the Benguela Current, October,  
417 1968. *Deep-Sea Research* 18, 505-523.
- 418 Capone, D.G., Hutchins, D.A., 2013. Microbial biogeochemistry of coastal upwelling regimes in a  
419 changing ocean. *Nature Geoscience* 6, 711-717.
- 420 Charilaou, M., Winklhofer, M., Gehring, A.U., 2011. Simulation of ferromagnetic resonance spectra of  
421 linear chains of magnetite nanocrystals. *Journal of Applied Physics* 109.
- 422 Coey, J., 1988. Magnetic properties of iron in soil iron oxides and clay minerals, *Iron in soils and clay*  
423 *minerals*. Springer, pp. 397-466.
- 424 Croudace, I.W., Rothwell, R.G., 2015. *Micro-XRF Studies of Sediment Cores: Applications of a non-*  
425 *destructive tool for the environmental sciences*. Springer.

- 426 Des Combes, H.J., Abelmann, A., 2007. A 350-ky radiolarian record off Luderitz, Namibia- evidence  
427 for changes in the upwelling regime. *Marine Micropaleontology* 62, 194-210.
- 428 Dunlop, D.J., Özdemir, Ö., 1997. *Rock Magnetism: Fundamentals and Frontiers*. Cambridge University  
429 Press, Cambridge.
- 430 Evans, M.E., Heller, F., 2003. *Environmental Magnetism: Principals and Applications of*  
431 *Enviromagnetics*. Academic Press, Amsterdam.
- 432 Fryberger, S.G., Dean, G., McKee, E.D., 1979. Dune forms and wind regime, in: McKee, E.D. (Ed.),  
433 *A Study of Global Sand Seas*. Geological Survey Professional Paper, Washington D.C., pp. 137-  
434 170.
- 435 Funk, J., Von Dobeneck, T., Reitz, A., 2003. Integrated rock magnetic and geochemical quantification  
436 of redoxomorphic iron mineral diagenesis in Late Quaternary sediments from the Equatorial  
437 Atlantic, The South Atlantic in the Late Quaternary. Springer, pp. 237-260.
- 438 Garzanti, E., Vermeesch, P., Ando, S., Lustrino, M., Padoan, M., Vezzoli, G., 2014. Ultra-long distance  
439 littoral transport of Orange sand and provenance of the Skeleton Coast Erg (Namibia). *Marine*  
440 *Geology* 357, 25-36.
- 441 Gehring, A.U., Fischer, H., Charilaou, M., Garcia-Rubio, I., 2011. Magnetic anisotropy and Verwey  
442 transition of magnetosome chains in *Magnetospirillum gryphiswaldense*. *Geophysical Journal*  
443 *International* 187, 1215-1221.
- 444 Grutzner, J., Rebesco, M., Cooper, A.K., Forsberg, C., Kryc, K., Wefer, G., 2003. Evidence for orbitally  
445 controlled size variations of the East Antarctic Ice Sheet during the late Miocene. *Geology* 31,  
446 777-780.
- 447 Hepp, D.A., Mörz, T., Hensen, C., Frederichs, T., Kasten, S., Riedinger, N., Hay, W.W., 2009. A late  
448 Miocene–early Pliocene Antarctic deepwater record of repeated iron reduction events. *Marine*  
449 *Geology* 266, 198-211.
- 450 Hilgenfeldt, K., 2000. Diagenetic dissolution of biogenic magnetite in surface sediments of the  
451 Benguela upwelling system. *International Journal of Earth Sciences* 88, 630-640.
- 452 Huang, J.-H., Huang, F., Evans, L., Glasauer, S., 2015. Vanadium: Global (bio) geochemistry.  
453 *Chemical Geology* 417, 68-89.
- 454 Huyer, A., 1983. Coastal upwelling in the california current system. *Progress in Oceanography* 12, 259-  
455 284.
- 456 Itambi, A.C., Von Dobeneck, T., Adegbe, A.T., 2010. Millennial-scale precipitation changes over  
457 Central Africa during the late Quaternary and Holocene: evidence in sediments from the Gulf of  
458 Guinea. *Journal of Quaternary Science: Published for the Quaternary Research Association* 25,  
459 267-279.
- 460 Karlin, R., 1990. Magnetite diagenesis in marine sediments from the Oregon continental margin.  
461 *Journal of Geophysical Research: Solid Earth* 95, 4405-4419.
- 462 Kuhlmann, H., Meggers, H., Freudenthal, T., Wefer, G., 2004. The transition of the monsoonal and the  
463 N Atlantic climate system off NW Africa during the Holocene. *Geophysical Research Letters* 31.
- 464 Larrasoana, J.C., Roberts, A.P., Liu, Q., Lyons, R., Oldfield, F., Rohling, E.J., Heslop, D., 2015.  
465 Source-to-sink magnetic properties of NE Saharan dust in Eastern Mediterranean marine  
466 sediments: review and paleoenvironmental implications. *Frontiers in Earth Science* 3.
- 467 Liu, P., Hirt, A.M., Schüler, D., Uebe, R., Zhu, P., Liu, T., Zhang, H., 2019. Numerical unmixing of  
468 weakly and strongly magnetic minerals: examples with synthetic mixtures of magnetite and  
469 hematite. *Geophysical Journal International* 217, 280-287.
- 470 Logan, R.F., 1960. *The Central Namib Desert, South West Africa* National Academy of  
471 Sciences/National Research Council, Washington D.C.
- 472 Lutjeharms, J.R.E., Meeuwis, J.M., 1987. The extent and variability of southeast atlantic upwelling.  
473 *South African Journal of Marine Science-Suid-Afrikaanse Tydskrif Vir Seewetenskap* 5, 51-62.
- 474 Lutjeharms, J.R.E., Stockton, P.L., 1987. Kinematics of the upwelling front off Southern-Africa. *South*  
475 *African Journal of Marine Science-Suid-Afrikaanse Tydskrif Vir Seewetenskap* 5, 35-49.
- 476 Marlow, J.R., Lange, C.B., Wefer, G., Rosell-Mele, A., 2000. Upwelling intensification as part of the  
477 Pliocene-Pleistocene climate transition. *Science* 290, 2288-+.
- 478 Mayer, L.M., Schick, L.L., Allison, M.A., Rutenberg, K.C., Bentley, S.J., 2007. Marine vs. terrigenous  
479 organic matter in Louisiana coastal sediments: The uses of bromine: organic carbon ratios.  
480 *Marine Chemistry* 107, 244-254.

- 481 Meads, R.E., Malden, P.J., 1975. Electron spin resonance in natural kaolinites containing Fe<sup>3+</sup> and  
482 other transitional metal ions. *Clay Miner.* 10, 313-345.
- 483 Mohamed, K.J., Rey, D., Rubio, B., Dekkers, M.J., Roberts, A.P., Vilas, F., 2011. Onshore-offshore  
484 gradient in reductive early diagenesis in coastal marine sediments of the Ria de Vigo, Northwest  
485 Iberian Peninsula. *Continental Shelf Research* 31, 433-447.
- 486 Pauly, D., Christensen, V., 1995. Primary production required to sustain global fisheries. *Nature* 374,  
487 255-257.
- 488 Perez-Cruz, L., Urrutia-Fucugauchi, J., 2009. Magnetic mineral study of Holocene marine sediments  
489 from the Alfonso Basin, Gulf of California - implications for depositional environment and  
490 sediment sources. *Geofisica Internacional* 48, 305-318.
- 491 Perry, D.L., 1990. Instrumental surface analysis of geologic materials. Wiley-VCH.
- 492 Petermann, H., Bleil, U., 1993. Detection of live magnetotactic bacteria in South Atlantic deep-sea  
493 sediments. *Earth and Planetary Science Letters* 117, 223-228.
- 494 Pierau, R., Henrich, R., Preiß-Daimler, I., Krastel, S., Geersen, J., 2011. Sediment transport and  
495 turbidite architecture in the submarine Dakar Canyon off Senegal, NW-Africa. *Journal of African*  
496 *Earth Sciences* 60, 196-208.
- 497 Pokorny, J., Pokorny, P., Suza, P., Hrouda, F., 2011. A multi-function kappabridge for high precision  
498 measurement of the ams and the variations of magnetic susceptibility with field, temperature and  
499 frequency. *Earth's Magnetic Interior* 1, 293-301.
- 500 Roberts, A.P., Florindo, F., Villa, G., Chang, L., Jovane, L., Bohaty, S.M., Larrasoña, J.C., Heslop,  
501 D., Fitz Gerald, J.D., 2011. Magnetotactic bacterial abundance in pelagic marine sediments is  
502 limited by organic carbon and availability of dissolved iron. *Earth and Planetary Sciences* 310,  
503 441-452.
- 504 Roberts, A.P., Turner, G.M., 1993. Diagenetic formation of ferrimagnetic iron sulphide minerals in  
505 rapidly deposited marine sediments, South Island, New Zealand. *Earth and Planetary Science*  
506 *Letters* 115, 257-273.
- 507 Roger, J., Rau, A.J., 2006. Surficial sediments the wave-dominated Orange River Delta and the adjacent  
508 continental margin off south-western Africa. *African Journal of Marine Science*, 511-524.
- 509 Röhl, U., Brinkhuis, H., Sluijs, A., Fuller, M., 2004. On the search for the Paleocene/Eocene boundary  
510 in the Southern Ocean: exploring ODP Leg 189 Holes 1171D and 1172D, Tasman Sea. *The*  
511 *Cenozoic Southern Ocean: Tectonics, Sedimentation, and Climate Change Between Australia*  
512 *and Antarctica. Geophysical Monograph Series* 151, 113-125.
- 513 Santana-Casiano, J.M., Gonzalez-Davila, M., Ucha, I.R., 2009. Carbon dioxide fluxes in the Benguela  
514 upwelling system during winter and spring: A comparison between 2005 and 2006. *Deep-Sea*  
515 *Research Part II-Topical Studies in Oceanography* 56, 533-541.
- 516 Scoullou, M., Oldfield, F., Thompson, R., 1979. Magnetic monitoring of marine particulate pollution in  
517 the Elefsis Gulf, Greece. *Marine Pollution Bulletin* 10, 287-291.
- 518 Setti, M., Lopez-Galindo, A., Padoan, M., Garzanti, E., 2014. Clay mineralogy in southern Africa river  
519 muds. *Clay Minerals* 49, 717-733.
- 520 Shi, M.N., Wu, H.C., Roberts, A.P., Zhang, S.H., Zhao, X.X., Li, H.Y., Su, X., Yang, T.S., Chang, L.,  
521 Hu, P.X., Zhao, X., Wang, H.Q., 2017. Tectonic, climatic, and diagenetic control of magnetic  
522 properties of sediments from Kumano Basin, Nankai margin, southwestern Japan. *Marine*  
523 *Geology* 391, 1-12.
- 524 Sowell, S.M., Abraham, P.E., Shah, M., Verberkmoes, N.C., Smith, D.P., Barofsky, D.F., Giovannoni,  
525 S.J., 2011. Environmental proteomics of microbial plankton in a highly productive coastal  
526 upwelling system. *Isme Journal* 5, 856-865.
- 527 Strohbach, B.J., 2008. Mapping the major catchments of Nambia. *Agricola* 18, 63-73.
- 528 Thompson, R., Oldfield, F., 1986. *Environmental Magnetism*. Allen & Unwin, London.
- 529 Vidal, L., Bickert, T., Wefer, G., Röhl, U., 2002. Late Miocene stable isotope stratigraphy of SE  
530 Atlantic ODP Site 1085: relation to Messinian events. *Marine Geology* 180, 71-85.
- 531 Wollin, G., Ericson, D.B., Ryan, W.B.F., Foster, J.H., 1971. Magnetism of the earth and climatic  
532 changes. *Earth and Planetary Science Letters* 12, 175-183.
- 533 Ziegler, M., Jilbert, T., de Lange, G.J., Lourens, L.J., Reichert, G.J., 2008. Bromine counts from XRF  
534 scanning as an estimate of the marine organic carbon content of sediment cores. *Geochemistry,*  
535 *Geophysics, Geosystems* 9.



## 536 7.9. APPENDIX

537

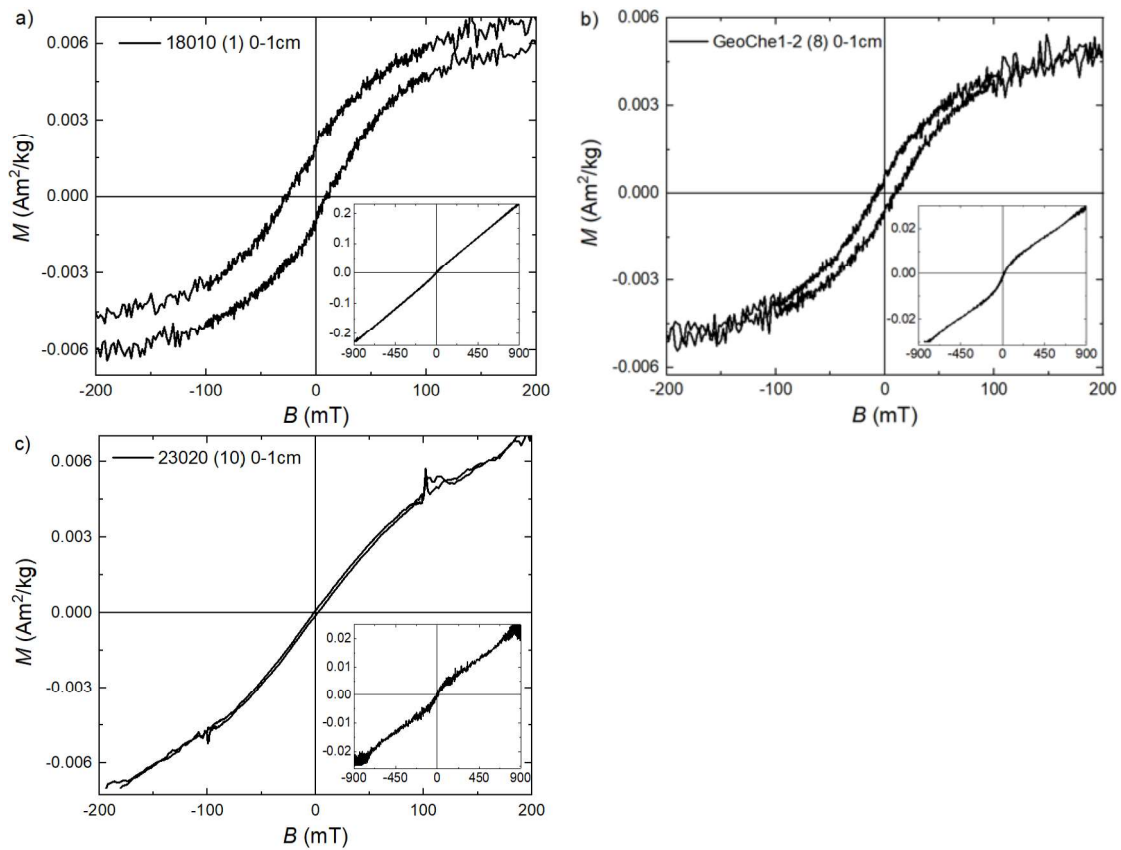


Fig. A1 Examples of the magnetisation as a function of applied field at room temperature for selected samples from the sediment-water interface: a) site 18010 (1), b) site GeoChe1-2 (8), c) site 23020 (10), showing small hysteresis loops, characteristic of a small ferrimagnetic contribution. The main figures show loops corrected for paramagnetic slope. The insets show the hysteresis without correction for high-field slope, which reveal the dominant contribution of a paramagnetic phase.

538

539

540

541

542

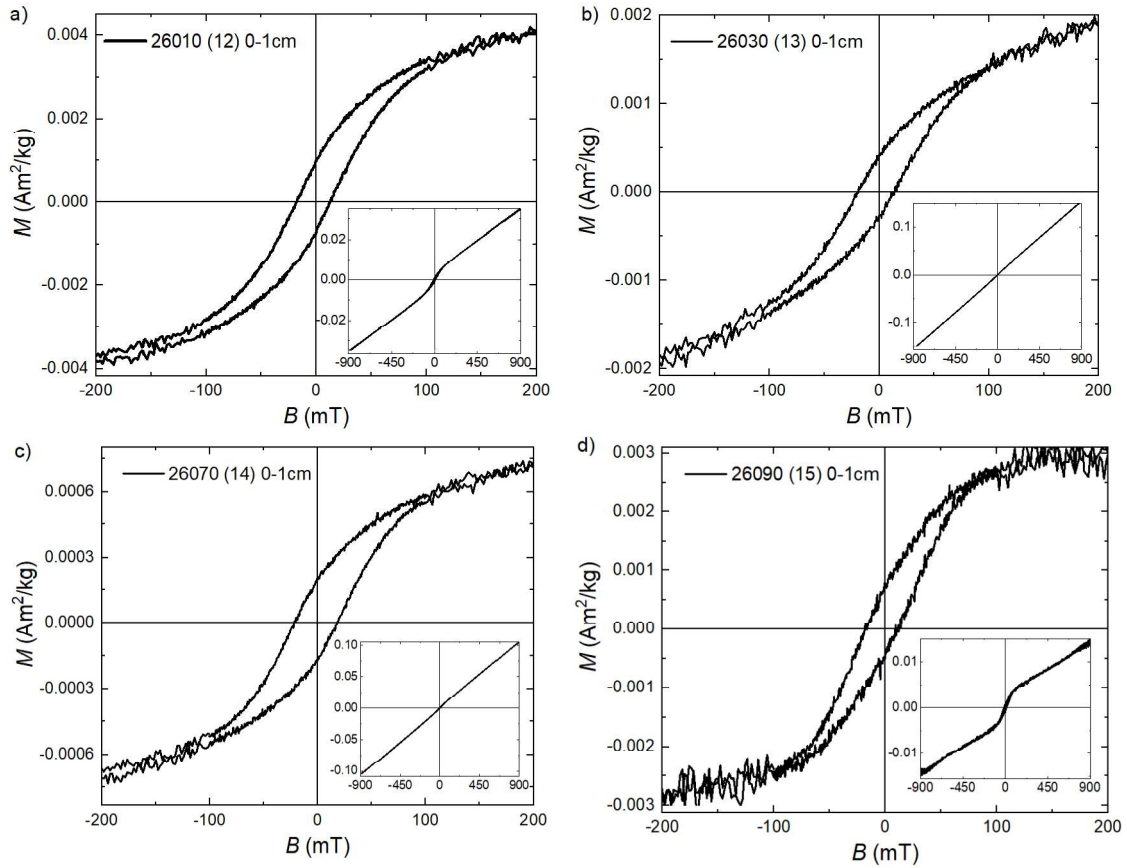


Fig. A2. Examples of the magnetisation as a function of applied field for the samples from the sediment-water interface of the Lüderitz profile: a) Site 26010 (12), b) Site 26030 (13), c) Site 26070 (14), d) Site 26090 (15). The main figures show loops corrected for paramagnetic slope. The insets show the hysteresis without correction for high-field slope, which reveal the dominant contribution of a paramagnetic phase.

543  
544  
545  
546  
547  
548

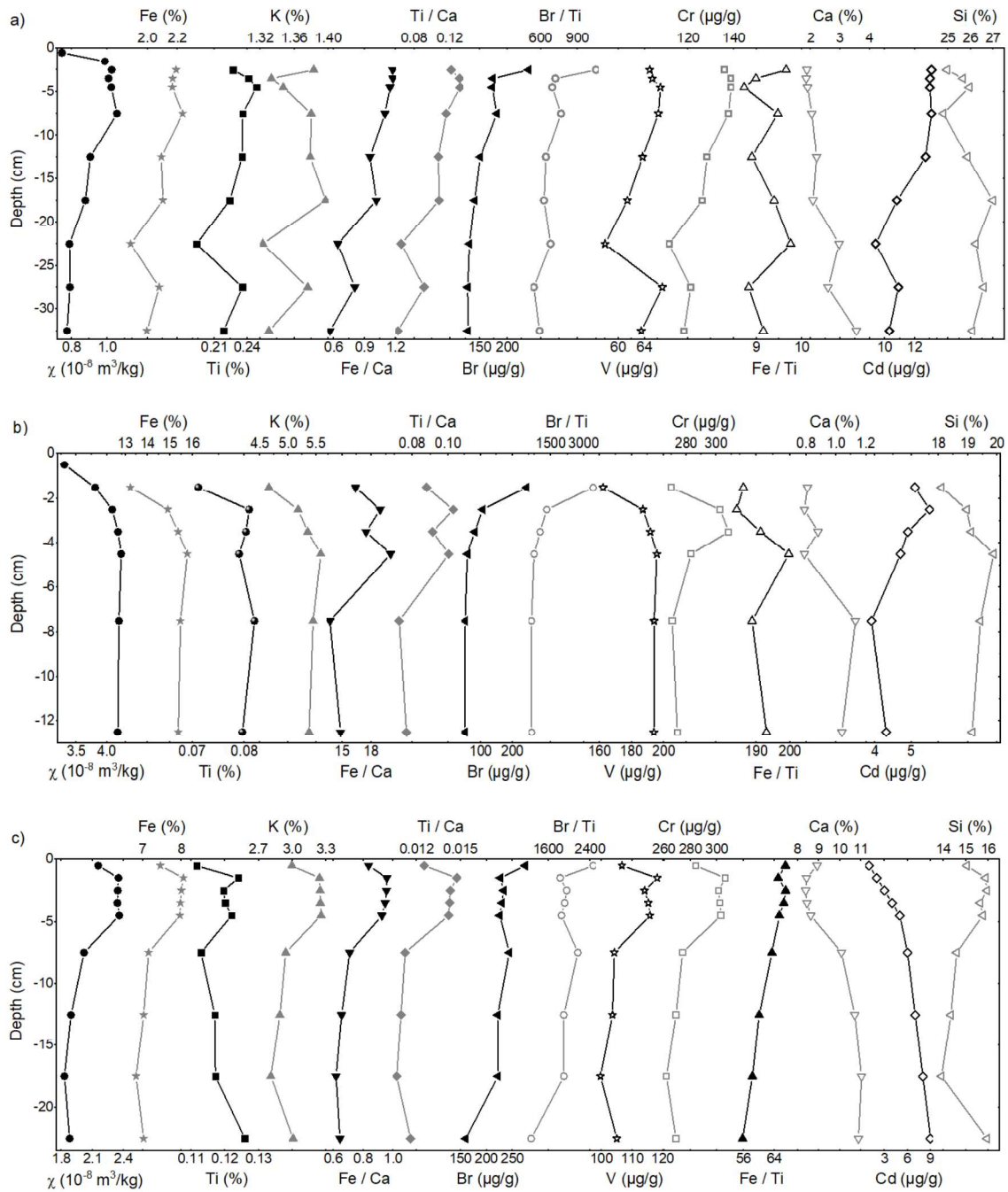


Fig. A3 Continued overleaf.

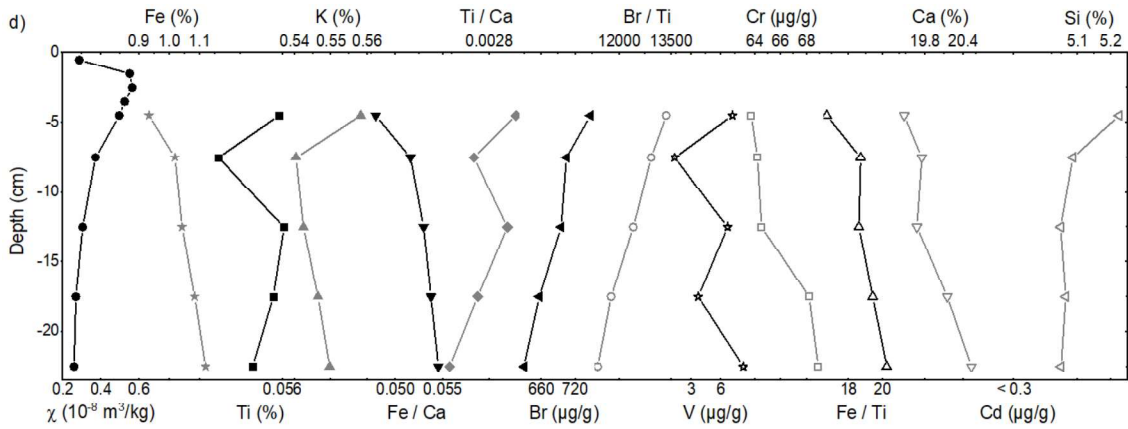


Fig. A3 The magnetic susceptibility comparison with extended geochemical data for each sample a) 26010 (12), b) 26030 (13), c) 26070 (14), d) 26090 (15). From the right hand site are presented: magnetic susceptibility, Fe, Ti, K, Fe/Ca-ratio, Ti/Ca-ratio, Br, Br/Ti-ratio, V, Cr, Fe/Ti-ratio, Ca, Cd, Si.

549

Site	Maximum magnetisation ( $\text{Am}^2/\text{kg}$ )	Relative ferrimagnetic contribution ( $\text{Am}^2/\text{kg}$ )	Percentage of ferrimagnetic phase (%)
1) 18010	0.25724	0.02917	11.3
8) GeoChe1_2	0.03326	0.00539	16.2
10) 23020	0.02638	0.00473	17.9
12) 26010	0.03856	0.00719	18.7
13) 26030	0.17094	0.01238	7.2
14) 26070	0.11677	0.01109	9.5
15) 26090	0.01583	0.00356	22.5

Table. A1 The contribution of the ferrimagnetic phase in paramagnetic medium for selected samples obtained from the magnetisation as a function of applied field for the samples from the sediment-water interface. Maximum magnetisation was obtained at the applied field of 1 T. Relative ferrimagnetic contribution is a magnetisation measured at the point where the hysteretic loop closes.

550

Element		Input Date	Eval Date	Na	Na	Na	Mg
Dimension				%	Abs. Error	Norm. Int.	%
26010_10-15		2/18/2019	2/18/2019	1.451	0.029	11.7825	0.843
26010_15-20		2/18/2019	2/18/2019	1.042	0.023	9.9845	0.805
26010_2-3		2/18/2019	2/18/2019	1.63	0.028	15.5728	1.035
26010_20-25		2/18/2019	2/18/2019	1.171	0.025	10.5341	0.768
26010_25-30		2/18/2019	2/18/2019	1.147	0.025	10.2026	0.815
26010_3-4		2/18/2019	2/18/2019	1.742	0.033	13.2194	0.936
26010_30-35		2/18/2019	2/18/2019	0.966	0.022	9.4787	0.776
26010_4-5		2/18/2019	2/18/2019	1.674	0.032	12.7588	0.926
26010_5-10		2/18/2019	2/18/2019	1.362	0.026	12.5609	0.946
26030_1-2		2/18/2019	2/18/2019	3.196	0.062	14.5217	2.446
26030_10-15		2/18/2019	2/18/2019	< 0.010	0	3.4523	2.307
26030_2-3		2/18/2019	2/18/2019	0.598	0.02	6.3446	2.363
26030_3-4		2/18/2019	2/18/2019	0.282	0.011	5.3716	2.299
26030_4-5		2/18/2019	2/18/2019	< 0.010	0	4.0585	2.358
26030_5-10		2/18/2019	2/18/2019	< 0.010	0	4.0097	2.307
26070_0-1		2/18/2019	2/18/2019	1.876	0.042	10.3472	1.827
26070_1-2		2/18/2019	2/18/2019	1.032	0.028	7.6866	1.824
26070_10-15		2/19/2019	2/19/2019	0.952	0.026	7.4411	1.642
26070_15-20		2/19/2019	2/19/2019	1.043	0.028	7.7921	1.601
26070_2-3		2/18/2019	2/18/2019	1.168	0.031	8.0683	1.847
26070_20-25		2/19/2019	2/19/2019	0.759	0.022	6.7169	1.727
26070_3-4		2/18/2019	2/18/2019	1.005	0.028	7.6645	1.776
26070_4-5		2/18/2019	2/18/2019	0.756	0.022	6.8217	1.8
26070_5-10		2/19/2019	2/19/2019	0.968	0.027	7.5369	1.668
26090_10-15		2/19/2019	2/19/2019	3.041	0.054	15.161	0.798
26090_15-20		2/19/2019	2/19/2019	2.709	0.051	13.959	0.796
26090_20-25		2/19/2019	2/19/2019	2.592	0.049	13.4673	0.74
26090_4-5		2/19/2019	2/19/2019	3.897	0.065	17.5699	0.897
26090_5-10		2/19/2019	2/19/2019	3.056	0.055	14.8357	0.811

Mg	Mg	Al	Al	Al	Si	Si	Si	P
Abs. Error	Norm. Int.	%	Abs. Error	Norm. Int.	%	Abs. Error	Norm. Int.	%
0.012	20.2518	3.298	0.014	184.5782	25.85	0.03	2832.407	0.2715
0.012	19.6413	3.636	0.015	202.0869	26.98	0.03	2940.41	0.2805
0.014	23.0582	3.085	0.014	167.4515	24.95	0.03	2629.038	0.2396
0.012	18.9863	3.71	0.015	206.1779	26.22	0.03	2865.735	0.4064
0.012	19.8931	3.58	0.014	200.5223	26.57	0.03	2922.798	0.3192
0.013	21.8635	3.081	0.014	173.0837	25.66	0.03	2811.735	0.2378
0.012	19.1218	3.445	0.014	192.3787	26.07	0.03	2856.773	0.2635
0.013	21.7642	3.202	0.014	180.0608	25.93	0.03	2849.701	0.244
0.013	21.7103	3.303	0.014	179.9453	24.79	0.03	2644.333	0.2573
0.024	41.9397	2.181	0.013	105.1877	18.1	0.03	1756.95	0.1584
0.022	41.1737	2.28	0.013	111.2605	19.14	0.03	1911.561	0.3116
0.022	41.5769	2.281	0.013	110.5034	18.95	0.03	1874.085	0.2016
0.022	40.3998	2.284	0.013	109.6889	19.11	0.03	1873.135	0.255
0.022	40.5319	2.309	0.013	108.7292	19.87	0.03	1907.812	0.2389
0.022	40.4164	2.326	0.013	111.1217	19.42	0.03	1899.047	0.3468
0.019	32.4264	2.338	0.012	113.8232	15.04	0.02	1494.562	0.3913
0.019	32.7704	2.405	0.013	117.7408	15.87	0.02	1592.005	0.3978
0.018	29.7487	2.431	0.012	118.0623	14.33	0.02	1432.236	0.3477
0.018	29.6569	2.451	0.012	121.1219	13.92	0.02	1421.189	0.3284
0.019	32.5688	2.421	0.013	116.4742	15.94	0.02	1569.348	0.3932
0.019	29.6476	2.728	0.014	125.0219	15.94	0.02	1508.272	0.3579
0.019	32.4033	2.389	0.012	118.2999	15.63	0.02	1587.828	0.3856
0.019	32.2427	2.388	0.012	116.4319	15.75	0.02	1573.631	0.4066
0.018	30.5427	2.376	0.012	117.3323	14.59	0.02	1479.994	0.353
0.013	18.0269	1.571	0.01	87.1651	5.048	0.012	574.1744	0.0858
0.013	17.9782	1.627	0.01	89.6863	5.064	0.012	575.0402	0.0829
0.012	17.0959	1.622	0.01	89.2811	5.05	0.012	573.1324	0.0786
0.014	18.764	1.596	0.01	84.3713	5.225	0.013	561.6217	0.0907
0.013	17.7678	1.576	0.01	84.8651	5.085	0.013	559.5266	0.0864

P	P	S	S	S	Cl	Cl	Cl	K
Abs. Error	Norm. Int.	µg/g	Abs. Error	Norm. Int.	µg/g	Abs. Error	Norm. Int.	%
0.0023	50.4338	6092	26	172.8793	17830	30	1129.06	1.379
0.0023	51.118	6137	26	171.8472	13190	30	822.2443	1.397
0.0022	43.4692	6354	28	175.0979	32140	40	1973.584	1.383
0.0027	74.3224	6071	26	171.8401	13570	30	854.5249	1.323
0.0024	58.8544	5739	25	163.4384	13640	30	861.1181	1.376
0.0022	44.2886	5600	26	158.7411	23490	30	1486.934	1.333
0.0022	49.5308	5676	25	162.3514	11880	20	752.9288	1.33
0.0022	45.4319	5622	26	159.1003	21930	30	1388.6	1.347
0.0023	47.3308	6580	28	183.7281	22630	30	1413.7	1.38
0.0022	28.6558	4190	26	115.2657	40530	50	2559.972	4.657
0.0026	56.1179	2060	17	58.0006	4516	15	293.8153	5.372
0.0022	36.3651	2444	19	68.2268	12780	30	822.8151	5.18
0.0024	45.409	2090	17	58.0301	10180	20	650.9073	5.348
0.0023	41.53	1885	17	51.0547	6210	18	388.8122	5.581
0.0027	61.1883	2074	17	57.2828	5500	17	350.5059	5.445
0.0027	78.7253	3736	22	111.8511	23000	30	1572.14	2.996
0.0026	79.6079	2968	19	88.8346	13330	30	914.6361	3.241
0.0024	72.7405	5174	24	157.9918	12540	20	875.0261	2.889
0.0023	70.7296	4933	23	154.5411	13210	20	941.7531	2.809
0.0026	77.5056	3136	20	92.2655	15770	30	1063.991	3.247
0.0025	70.305	4792	24	138.0484	11290	20	741.6002	3.006
0.0026	78.2661	3049	19	92.3328	14310	30	993.3823	3.249
0.0026	81.2408	2966	19	88.5948	11560	20	792.7401	3.255
0.0024	73.9812	4622	23	141.9881	13060	20	918.5556	2.94
0.0011	34.2421	8000	27	314.3813	35260	40	3058.696	0.5424
0.0011	33.9146	8071	27	317.4292	32510	40	2822.477	0.5464
0.0011	33.3333	7935	26	312.8065	29010	30	2525.966	0.5496
0.0012	32.9968	7844	28	290.2124	46960	50	3836.65	0.5582
0.0012	33.4114	7987	27	304.0552	36160	40	3044.931	0.5403

K	K	Ca	Ca	Ca	Sc	Sc	Sc	Ti
Abs. Error	Norm. Int.	%	Abs. Error	Norm. Int.	%	Abs. Error	Norm. Int.	%
0.001	2849.259	2.197	0.002	7383.611	0.00261	0.00032	15.674	0.2353
0.001	2857.252	2.075	0.001	6906.812	0.00231	0.00031	13.7882	0.224
0.001	2722.546	1.868	0.001	5997.649	0.00396	0.0003	22.9918	0.2269
0.001	2728.824	2.959	0.002	9910.808	0.0023	0.00038	13.5459	0.1937
0.001	2845.158	2.586	0.002	8687.627	0.00291	0.00035	17.3452	0.2355
0.001	2735.832	1.843	0.001	6173.868	0.00262	0.00029	15.8566	0.2412
0.001	2766.704	3.55	0.002	11944.91	0.00225	0.00043	13.0807	0.2183
0.001	2771.14	1.889	0.001	6335.798	0.00269	0.0003	16.2909	0.2483
0.001	2796.545	2.035	0.001	6714.995	0.00303	0.00031	17.9738	0.2359
0.003	9399.876	0.8085	0.001	2495.724	0.00256	0.0002	14.727	0.07109
0.003	11610.74	1.038	0.001	3354.875	0.00246	0.00023	14.7072	0.07961
0.003	11006.82	0.7879	0.001	2520.286	0.00252	0.0002	15.0283	0.08091
0.003	11309.82	0.8795	0.0011	2790.565	0.0025	0.00021	14.748	0.08028
0.003	11607.42	0.7877	0.001	2451.983	0.00245	0.0002	14.1967	0.07896
0.003	11524.14	1.128	0.001	3569.761	0.00218	0.00024	12.7587	0.08192
0.002	6675.84	8.913	0.005	30154.38	0.00897	0.00082	46.6273	0.1116
0.002	7331.625	8.411	0.004	28762.32	0.00844	0.00079	44.7843	0.124
0.002	6653.469	10.7	0.01	37093.76	0.00792	0.00096	40.4019	0.117
0.002	6597.278	11.02	0.01	38857.9	0.0071	0.00098	36.4897	0.1172
0.002	7209.723	8.371	0.004	28152.79	0.00809	0.00078	42.3503	0.1196
0.002	6541.523	10.87	0.01	35714.95	0.00581	0.00097	28.3477	0.1259
0.002	7422.082	8.428	0.004	29058.51	0.00853	0.00079	45.4942	0.1201
0.002	7381.632	8.607	0.005	29463.32	0.00733	0.0008	38.7417	0.122
0.002	6815.144	10.07	0.01	35174.7	0.00814	0.00091	42.3495	0.1129
0.0011	1488.032	19.67	0.01	80440.43	0.0348	0.0019	165.8921	0.05603
0.0011	1507.574	20.15	0.01	82557.65	0.0356	0.002	168.3885	0.05578
0.0011	1529.357	20.53	0.01	84591.81	0.0382	0.002	179.6287	0.05529
0.0011	1428.153	19.47	0.01	74726.58	0.0282	0.0019	129.429	0.05591
0.0011	1441.892	19.75	0.01	78835.81	0.0337	0.0019	158.1125	0.05448



Ti	Ti	V	V	V	Cr	Cr	Cr	Mn
Abs. Error	Norm. Int.	µg/g	Abs. Error	Norm. Int.	µg/g	Abs. Error	Norm. Int.	%
0.0003	1762.816	63.7	1.2	72.8969	128.2	0.5	226.8885	0.01985
0.0003	1669.22	61.4	1.1	70.4679	126.2	0.5	222.0698	0.01639
0.0003	1638.7	64.8	1.2	71.1062	135.9	0.5	231.6884	0.01635
0.0003	1421.978	58	1.1	65.447	111.7	0.5	193.6254	0.01511
0.0003	1744.642	66.7	1.2	74.7256	121.2	0.5	212.4566	0.01821
0.0003	1814.806	65.2	1.2	74.4242	138.6	0.5	246.3999	0.02225
0.0003	1582.086	63.5	1.2	69.7512	118.2	0.5	202.4534	0.01591
0.0003	1868.516	66.4	1.2	75.6852	138.7	0.5	246.4659	0.0173
0.0003	1742.064	66.1	1.2	73.9767	137.6	0.5	240.0137	0.01736
0.00017	506.6032	162.2	1	155.2813	269.9	0.7	458.6905	0.00312
0.00017	588.0545	193.8	1	191.7824	274	0.8	484.6827	0.00629
0.00017	596.6742	187	1	184.9266	302.7	0.7	533.6666	0.00671
0.00017	585.6882	191.7	1	187.482	308.3	0.7	537.9381	0.00673
0.00017	566.5949	195.7	1.1	188.1976	283.3	0.8	486.7792	0.00638
0.00017	591.946	194	1.1	187.817	270.7	0.8	468.6176	0.00634
0.0003	723.9156	106.7	1.2	95.9646	283.8	0.8	430.2974	0.00661
0.0003	817.8496	118.2	1.3	107.4852	306.2	0.8	473.75	0.00658
0.0003	746.714	103.6	1.3	92.5708	269	0.8	399.8328	0.00705
0.0003	751.461	99.7	1.3	89.6797	261.7	0.8	391.2187	0.0068
0.0003	780.2438	114.1	1.3	102.8924	301.2	0.8	460.5159	0.0066
0.0003	766.0196	105	1.3	89.2652	269	0.8	383.1547	0.00774
0.0003	798.3529	115.3	1.3	105.9159	302.2	0.8	470.4019	0.00567
0.0003	803.2096	115.8	1.3	105.3559	302.9	0.8	467.2163	0.00656
0.0003	733.728	104.2	1.3	94.5784	273.9	0.8	414.9445	0.00681
0.0003	406.7831	6.7	0.3	34.9918	64.5	0.7	89.2189	0.00546
0.0003	406.4403	3.7	0.1	34.0176	68.2	0.7	93.4798	0.00537
0.0003	401.3675	8.3	0.3	37.1369	68.9	0.7	94.0941	0.00541
0.0003	387.6381	7.2	0.3	32.7258	63.7	0.7	85.2731	0.00519
0.00029	389.4426	1.3	0.1	29.7659	64.2	0.7	87.5175	0.00536

Mn	Mn	Fe	Fe	Fe	Co	Co	Co	Ni
Abs. Error	Norm. Int.	%	Abs. Error	Norm. Int.	µg/g	Abs. Error	Norm. Int.	µg/g
0.00005	507.1736	2.093	0.002	10562.25	87.9	3.5	13.8039	25.7
0.00005	416.4216	2.103	0.002	10566.97	87.4	3.5	13.6524	25.5
0.00005	402.7254	2.19	0.002	10665.35	79.9	3.4	12.0947	23.1
0.00004	377.6763	1.889	0.002	9336.422	85.5	3.5	13.1583	22.9
0.00005	460.404	2.078	0.002	10378.05	79.2	3.4	12.3072	23.1
0.00005	571.6858	2.167	0.002	10994.58	84.4	3.4	13.3163	23.4
0.00005	392.871	1.997	0.002	9755.46	83.8	3.5	12.7272	25.6
0.00005	444.3484	2.166	0.002	10988.29	79.1	3.4	12.4833	23.3
0.00005	437.5115	2.234	0.002	11124.76	63.5	3.3	9.8468	25.8
0.00004	76.6678	13.23	0.01	54993.68	32.8	3.5	4.7329	19.2
0.00003	160.8709	15.36	0.01	65486.56	52.1	3.5	7.6973	< 0.5
0.00003	171.2946	14.9	0.01	63423.81	41.6	3.5	6.1473	20.9
0.00003	169.8627	15.35	0.01	64565.7	42.9	3.5	6.2743	18.5
0.00003	158.5348	15.76	0.01	65118.71	36.5	3.5	5.2493	18.3
0.00003	158.6394	15.46	0.01	64468.41	45.5	3.5	6.5792	< 0.5
0.00004	144.9974	7.454	0.004	28316.75	32.7	3.7	4.3256	19.3
0.00004	147.376	8.052	0.005	31094.46	36.3	3.6	4.8849	14.7
0.00004	151.4383	7.019	0.004	26161.45	37.2	3.7	4.8425	21.9
0.00004	146.9399	6.824	0.004	25650.82	34.1	3.7	4.4627	22.6
0.00004	146.0398	7.997	0.005	30492.66	36.9	3.6	4.9011	14.6
0.00005	159.4221	7.014	0.004	25032.56	34	3.7	4.2369	18.9
0.00004	127.7985	7.972	0.005	30997.38	35.7	3.6	4.8337	14.7
0.00004	146.5965	7.959	0.005	30602.91	35.7	3.6	4.7927	17.2
0.00004	149.2417	7.146	0.004	27146.07	34.1	3.6	4.5226	21.1
0.00005	107.1594	1.042	0.001	3686.166	24.1	4.1	3.0966	62.1
0.00005	104.5984	1.083	0.001	3801.756	32.9	4.2	4.1408	70.2
0.00005	105.0091	1.119	0.001	3912.392	12.4	3.9	1.6933	68.3
0.00005	98.5235	0.9333	0.0011	3189.89	9	3.7	1.2393	57.8
0.00005	103.6638	1.019	0.001	3543.663	22.2	4	2.8338	62.4

Ni	Ni	Cu	Cu	Cu	Zn	Zn	Zn	Ga
Abs. Error	Norm. Int.	µg/g	Abs. Error	Norm. Int.	µg/g	Abs. Error	Norm. Int.	µg/g
0.6	31.4517	13.5	0.3	23.8314	44.3	0.5	92.3203	9.3
0.6	31.1568	13.6	0.4	23.8317	44	0.5	91.3999	10.9
0.6	27.9071	12.3	0.3	21.5374	46.4	0.5	92.915	9.2
0.6	28.2288	13.2	0.3	23.2363	40.3	0.4	83.4178	10.9
0.6	28.5077	13.6	0.4	23.7846	42.1	0.5	86.856	10.2
0.6	29.1203	12.3	0.3	22.0963	44.4	0.5	92.4975	8.6
0.6	30.6518	13.4	0.3	23.2595	42.3	0.4	85.8131	10.6
0.6	28.9527	12.6	0.3	22.6041	44.5	0.5	92.6665	9.5
0.6	31.0662	12.1	0.3	21.4823	51.5	0.4	104.1009	7.7
0.6	19.4469	4.2	0.3	8.081	46.7	0.6	52.9371	10.2
0	7.1442	3.9	0.3	7.7382	45.5	0.7	48.99	12.5
0.7	20.756	4.9	0.3	8.512	51.2	0.6	55.918	11.9
0.6	19.2499	3.3	0.3	7.2657	49.7	0.7	53.1634	12.3
0.6	18.9148	< 1.2	-0.3	5.0872	49.1	0.7	51.495	9.9
0	6.7924	2.6	0.2	6.767	44.6	0.7	47.2728	10.9
0.7	18.8184	13.9	0.5	16.9401	41.9	0.5	53.5636	14.1
0.6	15.881	11.9	0.4	15.1294	43.3	0.5	54.9841	14
0.7	20.3425	17.3	0.5	19.9335	47.6	0.5	60.7999	13.5
0.7	20.9948	16.8	0.5	19.6645	47.3	0.5	61.1901	12
0.6	15.7291	11.4	0.4	14.6365	42.5	0.5	53.5113	13.9
0.7	17.8875	13.7	0.5	16.3574	46.9	0.5	58.1249	13
0.6	15.9614	11.8	0.4	15.1558	42.1	0.5	53.8926	13.6
0.7	17.5193	13.2	0.5	16.243	42.3	0.5	53.6483	15.2
0.7	20.0637	17.6	0.5	20.3284	44.1	0.5	56.9608	13.6
0.9	52.6244	55.8	0.6	62.5321	73.3	0.5	111.0632	2.5
0.9	58.4517	61.8	0.7	68.0782	79.1	0.5	118.688	1.3
0.9	56.7224	59.9	0.7	65.7754	81.1	0.5	121.0464	2.7
0.9	47.9697	51.4	0.6	56.4077	70.5	0.5	103.9678	1.2
0.9	52.109	55.5	0.6	61.3135	74.1	0.5	110.6287	2.4

Ga	Ga	Ge	Ge	Ge	As	As	As	Se
Abs. Error	Norm. Int.	µg/g	Abs. Error	Norm. Int.	µg/g	Abs. Error	Norm. Int.	µg/g
0.2	32.2717	< 0.5	0	0	29.4	0.2	123.6517	4.6
0.2	35.8076	< 0.5	0	0	20.9	0.2	87.893	5.1
0.2	31.211	< 0.5	0	0	34.8	0.2	141.0665	4.2
0.2	35.6729	< 0.5	0	0	20.9	0.2	87.4468	4.1
0.2	34.1582	< 0.5	0	0	16.7	0.2	69.5779	4.6
0.2	30.7112	< 0.5	0	0	33.9	0.2	142.5809	4.8
0.2	34.5061	< 0.5	0	0	15.4	0.2	63.2754	4.2
0.2	32.7775	< 0.5	0	0	34	0.2	143.2746	4.6
0.2	28.2666	< 0.5	0	0	35.4	0.2	146.5027	4
0.3	24.9913	0.8	0.3	1.657	23.9	0.3	56.2511	0.7
0.3	27.2554	4	0.3	7.2927	22.8	0.3	51.1922	1
0.3	26.6906	1.9	0.3	3.6458	24.2	0.3	55.042	0.2
0.3	26.9173	2.2	0.3	4.093	24	0.3	53.4939	0.1
0.3	23.5206	2.7	0.3	4.8896	24.1	0.3	52.6148	< 0.5
0.3	25.0274	3.7	0.3	6.6503	23.8	0.3	52.6437	0.3
0.3	33.015	< 0.5	0	0.1247	13.6	0.2	35.7351	2.2
0.3	32.6005	< 0.5	0	0	13.4	0.2	35.1477	2.1
0.3	32.0225	< 0.5	0	0	13.9	0.2	36.4792	2.9
0.3	29.9048	< 0.5	0	0	13.4	0.2	35.5431	3.1
0.3	32.3623	< 0.5	0	0	12.9	0.2	33.4588	1.9
0.3	30.6132	< 0.5	0	0	13.9	0.2	35.4629	2.2
0.3	32.1848	< 0.5	0	0.0476	12.5	0.2	33.0182	2.1
0.3	34.4854	0.4	0.3	0.9285	12.9	0.2	33.6359	1.9
0.3	32.3939	< 0.5	0	0	13.7	0.2	36.4183	2.7
0.1	15.5199	< 0.5	0	0	12.9	0.2	39.6678	6.8
0.1	13.2104	< 0.5	0	0	14.6	0.2	44.5414	7.6
0.1	15.7273	< 0.5	0	0	15.7	0.2	47.5008	8.1
0.1	12.9138	< 0.5	0	0	9	0.2	27.1136	6.6
0.1	15.2801	< 0.5	0	0	12	0.2	36.4537	7

Se	Se	Br	Br	Br	Rb	Rb	Rb	Sr
Abs. Error	Norm. Int.	µg/g	Abs. Error	Norm. Int.	µg/g	Abs. Error	Norm. Int.	µg/g
0.2	21.6085	151	0.4	919.9835	77.8	0.2	684.0317	159
0.2	23.5092	140.5	0.3	852.3458	79.5	0.2	696.7982	154.4
0.2	18.8636	238	0.4	1400.109	58.9	0.2	501.9358	143.1
0.2	18.8502	131.6	0.3	795.2949	62.6	0.2	547.0541	191.7
0.2	21.2728	128.1	0.3	773.3202	77.7	0.2	677.0517	173.8
0.2	22.115	173.5	0.4	1058.138	75	0.2	660.6072	141.5
0.2	18.8732	128.8	0.3	763.9102	62.1	0.2	533.8524	213.6
0.2	21.3217	172.2	0.4	1050.275	76	0.2	669.0496	142.7
0.2	18.5049	180.6	0.4	1082.259	78.6	0.2	681.1831	148.7
0.2	1.968	243.6	0.6	876.1155	219.2	0.5	1041.978	85.6
0.2	2.6426	49.4	0.3	168.4076	231.8	0.6	1051.375	106.2
0.2	0.5975	106.1	0.4	367.389	229.1	0.6	1051.855	77.5
0.1	0.2237	80.7	0.4	273.9419	232	0.6	1044.933	88.5
0	0	58.1	0.3	193.0544	233.4	0.6	1029.212	78.6
0.2	0.9493	50.5	0.3	170.0896	230.1	0.6	1028.365	114.4
0.1	6.8781	274.1	0.6	1121.652	152.1	0.4	806.1043	458.5
0.1	6.5778	226.5	0.5	919.2167	155	0.4	815.7196	432.4
0.1	9.2066	221.5	0.5	906.1108	142	0.4	751.4118	526.4
0.1	9.6447	222.3	0.5	919.3367	140	0.4	750.3494	542.1
0.1	5.8365	233.1	0.5	940.5924	155.2	0.4	810.1962	433.4
0.1	6.6918	159.9	0.4	635.3665	136.5	0.4	698.6832	523.4
0.1	6.5362	229.6	0.5	938.0171	154.8	0.4	820.5963	436.6
0.1	5.9583	225.7	0.5	917.0704	153.6	0.4	807.8338	446.1
0.1	8.6288	244.1	0.5	1008.088	146.5	0.4	783.2996	499.5
0.1	24.9386	694.9	0.8	3357.522	27.5	0.4	173.952	1034
0.1	27.4797	656	0.8	3133.609	28.6	0.3	179.0305	1033
0.1	29.3985	628.8	0.8	2990.264	29.2	0.3	181.5953	1042
0.1	23.5502	746.5	0.9	3518.641	26.9	0.4	165.5015	1016
0.1	25.5263	704	0.8	3360.134	27.5	0.4	171.1044	1032

Sr	Sr	Y	Y	Y	Zr	Zr	Zr	Nb
Abs. Error	Norm. Int.	µg/g	Abs. Error	Norm. Int.	µg/g	Abs. Error	Norm. Int.	µg/g
0.3	1641.301	22.7	0.2	235.1469	470.4	1	869.8131	7.9
0.3	1588.368	22.3	0.2	230.0057	444.3	0.9	820.0766	7.3
0.3	1427.137	21.7	0.2	216.5794	348.3	0.8	627.1423	7.2
0.3	1969.179	25.7	0.2	264.4758	400.6	0.9	737.6581	6.2
0.3	1780.112	23.8	0.2	244.007	505.1	1	926.281	7.3
0.2	1460.381	20.9	0.2	216.8017	451.8	0.9	836.4445	8.4
0.3	2157.468	25.3	0.2	255.4453	466.8	1	844.493	7
0.3	1473.424	21.6	0.2	223.1953	474.9	1	879.0432	8.3
0.3	1511.543	22.3	0.2	227.0326	447.5	0.9	816.6833	7.2
0.3	460.0485	18	0.3	98.838	79.1	0.6	87.7165	3.5
0.4	540.8464	46.4	0.4	241.1501	89.3	0.7	94.1331	2.9
0.3	400.5003	27.5	0.4	145.0486	74	0.6	80.8557	3.1
0.3	448.2838	30.5	0.4	157.5174	87.8	0.7	92.0915	2.7
0.3	389.5493	38.3	0.4	193.5256	72.8	0.6	77.1061	2.8
0.4	574.2027	50.2	0.4	257.1421	105.1	0.7	107.111	2.8
0.6	2804.626	56.5	0.3	348.2357	182.1	1	203.5584	4
0.6	2620.014	61.4	0.3	374.5968	197.1	1	218.1871	4.5
0.6	3223.816	55.6	0.3	342.5779	200.8	1	222.6465	3.7
0.6	3366.303	53.4	0.3	333.6201	178.3	1	201.5542	3.6
0.6	2606.651	61.7	0.3	373.8285	215	1	234.9558	5.4
0.6	3103.677	56.7	0.3	338.0914	186.3	1	200.5618	4.6
0.6	2666.125	63.6	0.3	390.9	207.2	1	230.5914	4.3
0.6	2701.763	65.2	0.3	397.3166	224.3	1	246.3508	3.4
0.6	3088.186	57.4	0.3	357.0997	208.1	1	232.8811	4.3
1	7588.577	17.8	0.2	137.5206	41.1	0.8	59.822	2.8
1	7504.836	18.1	0.2	138.2415	42	0.8	60.486	1.4
1	7541.535	18.6	0.2	141.3369	40.7	0.8	58.7128	0.7
1	7247.272	17.1	0.2	128.7932	38.7	0.8	55.5472	2.7
1	7445.715	17.8	0.2	135.0587	41.5	0.8	59.3999	1.9

Nb	Nb	Mo	Mo	Mo	Ru	Ru	Ru	Rh
Abs. Error	Norm. Int.	µg/g	Abs. Error	Norm. Int.	µg/g	Abs. Error	Norm. Int.	µg/g
0.2	20.3429	6.5	0.2	20.6287	< 0.5	0	2.6352	< 0.5
0.2	19.21	8.4	0.2	24.4219	< 0.5	0	2.8992	< 0.5
0.2	17.8441	4.7	0.2	16.4894	< 0.5	0	2.7458	< 0.5
0.2	17.6341	8.3	0.2	24.2713	< 0.5	0	3.3608	< 0.5
0.2	19.6984	10.3	0.2	28.3052	< 0.5	0	2.7692	< 0.5
0.2	20.3387	4.9	0.2	17.0961	< 0.5	0	3.2946	< 0.5
0.2	19.2238	10.1	0.2	27.6542	< 0.5	0	2.9011	< 0.5
0.2	20.3369	4.3	0.2	15.8503	< 0.5	0	2.7663	< 0.5
0.2	17.9069	4.5	0.2	16.1082	< 0.5	0	2.3934	< 0.5
0.2	8.7265	4.5	0.2	11.775	< 0.5	0	6.2631	< 0.5
0.1	9.4403	3.7	0.1	10.8805	< 0.5	0	7.0316	< 0.5
0.1	8.9428	3.7	0.1	10.8472	< 0.5	0	6.4227	< 0.5
0.1	9.3096	3.5	0.1	10.6483	< 0.5	0	6.399	< 0.5
0.1	9.0673	2.1	0.1	9.1139	< 0.5	0	6.5361	< 0.5
0.1	9.7272	3.5	0.1	10.7107	< 0.5	0	6.8271	< 0.5
0.2	9.8398	0.8	0.1	8.0039	< 0.5	0	4.5135	< 0.5
0.2	10.3712	0.4	0.1	7.5496	< 0.5	0	4.4412	< 0.5
0.2	9.8291	2.6	0.1	10.3101	< 0.5	0	4.7487	< 0.5
0.2	9.913	5.1	0.2	13.3274	< 0.5	0	4.7642	< 0.5
0.2	11.2926	< 0.5	0	6.857	< 0.5	0	4.1593	< 0.5
0.2	10.7723	4	0.2	11.7789	< 0.5	0	4.5438	< 0.5
0.2	10.2095	< 0.8	-0.3	7.4525	< 0.5	0	5.052	< 0.5
0.2	9.2593	< 0.5	0	6.8367	< 0.5	0	4.3707	< 0.5
0.2	10.3396	1.3	0.1	8.7124	< 0.5	0	4.6773	< 0.5
0.1	8.9208	3.8	0.1	12.4163	< 0.5	0	1.6151	< 0.5
0.1	8.3588	4.5	0.1	13.5632	< 0.5	0	0	< 0.5
0.1	8.3281	5.4	0.2	14.9442	< 0.5	0	0	< 0.5
0.1	8.1492	0.4	0.1	7.6352	< 0.5	0	1.2081	< 0.5
0.1	7.5767	2.3	0.1	10.2402	< 0.5	0	0.9789	< 0.5

Rh	Rh	Pd	Pd	Pd	Ag	Ag	Ag	Cd
Abs. Error	Norm. Int.	µg/g	Abs. Error	Norm. Int.	µg/g	Abs. Error	Norm. Int.	µg/g
0	0	< 0.5	0	0	< 0.5	0	29.9484	12.7
0	0	< 0.5	0	1.9291	< 0.5	0	29.1101	10.8
0	0	< 0.5	0	1.4094	< 0.5	0	29.0099	13.1
0	0	< 0.5	0	2.4646	< 0.5	0	29.5494	9.4
0	0	< 0.5	0	2.2708	< 0.5	0	30.3803	10.9
0	0	< 0.5	0	1.8142	< 0.5	0	30.215	13
0	0	< 0.5	0	2.4329	< 0.5	0	29.4199	10.3
0	0	< 0.5	0	2.3796	< 0.5	0	29.9473	13
0	0	< 0.5	0	1.6564	< 0.5	0	28.9911	13.1
0	5.2012	< 0.5	0	6.6424	< 0.5	0	33.4648	5.1
0	4.9326	< 0.5	0	5.8543	< 0.5	0	33.3111	4.3
0	5.285	< 0.5	0	5.9762	< 0.5	0	32.8369	5.5
0	5.2542	< 0.5	0	6.3129	< 0.5	0	33.2154	4.9
0	5.4891	< 0.5	0	6.1453	< 0.5	0	33.2647	4.7
0	4.6285	< 0.5	0	5.6193	< 0.5	0	33.3183	3.9
0	3.6609	< 0.5	0	3.7443	< 0.5	0	30.8726	< 0.3
0	2.8869	< 0.5	0	3.4244	< 0.5	0	30.558	< 0.3
0	2.562	< 0.5	0	3.28	< 0.5	0	30.7628	< 0.3
0	2.8302	< 0.5	0	3.3817	< 0.5	0	30.5735	< 0.3
0	2.6577	< 0.5	0	3.5048	< 0.5	0	30.8638	< 0.3
0	2.6342	< 0.5	0	3.9977	< 0.5	0	31.1676	< 0.3
0	3.368	< 0.5	0	4.0882	< 0.5	0	30.4938	< 0.3
0	3.0997	< 0.5	0	3.7081	< 0.5	0	30.4358	< 0.3
0	3.0647	< 0.5	0	3.7104	< 0.5	0	30.9311	< 0.3
0	0	< 0.5	0	0	< 0.5	0	29.4997	< 0.3
0	0	< 0.5	0	0	< 0.5	0	30.9967	< 0.3
0	0	< 0.5	0	0.5657	< 0.5	0	31.548	< 0.3
0	0	< 0.5	0	0	< 0.5	0	29.6664	< 0.3
0	0	< 0.5	0	1.051	< 0.5	0	31.4566	< 0.3



Cd	Cd	In	In	In	Sn	Sn	Sn	Sb
Abs. Error	Norm. Int.	µg/g	Abs. Error	Norm. Int.	µg/g	Abs. Error	Norm. Int.	µg/g
0.1	48.2834	< 0.5	0	1.2285	< 0.5	0	0	< 0.5
0.1	42.968	< 0.5	0	1.1029	< 0.5	0	1.7152	< 0.5
0.1	48.749	< 0.5	0	0.9092	< 0.5	0	1.6979	< 0.5
0.1	38.9927	< 0.5	0	1.4288	< 0.5	0	0.966	< 0.5
0.1	43.104	< 0.5	0	0	< 0.5	0	0	< 0.5
0.1	49.2404	< 0.5	0	0	< 0.5	0	0	< 0.5
0.1	41.2233	< 0.5	0	0	< 0.5	0	0.2507	< 0.5
0.1	49.2307	< 0.5	0	0	< 0.5	0	0	< 0.5
0.1	48.9302	< 0.5	0	0	< 0.5	0	2.8239	< 0.5
0.1	22.2244	0.7	0.1	4.3741	< 0.5	0	2.3044	0.7
0.1	20.4036	1.9	0.1	6.5852	< 0.7	-0.2	3.172	1.9
0.1	22.5621	1.5	0.1	5.8106	< 0.5	0	2.4553	1.1
0.1	21.3253	1.7	0.1	6.2626	< 0.5	0	2.5625	1.5
0.1	20.967	1.6	0.1	5.9015	< 0.5	0	2.8001	1.5
0.1	19.5701	1.2	0.1	5.218	< 0.5	0	2.1515	1.8
0	2.8337	0.4	0.1	3.933	< 0.5	0	2.9933	2.3
0	2.7635	< 0.5	0	2.9886	< 0.5	0	2.0662	1.2
0	2.7042	< 0.5	0	0	< 0.5	0	0	0.4
0	2.6089	< 0.5	-0.2	3.3527	< 0.5	0	1.4949	1
0	2.5705	< 0.5	0	2.9159	< 0.5	0	2.6505	1.7
0	2.9376	0.6	0.1	4.3689	< 0.5	0	2.6984	0.7
0	2.4805	< 0.5	-0.2	3.488	< 0.5	0	2.8115	< 0.5
0	2.4153	< 0.5	-0.3	3.7334	< 0.6	-0.3	3.5524	1.7
0	2.6341	< 0.5	0	2.9005	< 0.5	0	1.6126	0.7
0	2.0473	0.9	0.1	5.3002	2.3	0.2	8.3597	10.1
0	2.6719	1	0.1	5.6717	3.7	0.2	11.6827	12.1
0	1.7833	< 0.5	-0.2	3.5216	1.4	0.1	6.4175	8.6
0	1.2569	0.6	0.1	4.491	2.6	0.2	8.9896	11
0	0.9827	< 0.5	0	3.1832	1.6	0.1	6.8179	9.7

Sb	Sb	Te	Te	Te	I	I	I	Cs
Abs. Error	Norm. Int.	µg/g	Abs. Error	Norm. Int.	µg/g	Abs. Error	Norm. Int.	µg/g
0	0	< 0.5	0	0	136.6	0.6	381.7425	< 1.0
0	3.7144	< 0.5	0	5.625	136.2	0.6	380.0429	< 1.0
0	0	< 0.5	0	4.7686	176.7	0.6	483.8164	< 1.0
0	0	< 0.5	0	3.7061	105.9	0.6	297.0694	< 1.0
0	0	< 0.5	0	2.688	109.5	0.6	306.8046	< 1.0
0	0	< 0.5	0	3.7806	160.1	0.6	445.7642	< 1.0
0	1.9574	< 0.5	0	2.4772	104.5	0.6	291.206	< 1.0
0	2.8179	< 0.5	0	5.1275	162.2	0.6	452.042	< 1.0
0	0	< 0.5	0	6.1368	168.1	0.6	463.9486	< 1.0
0.1	5.1398	< 0.5	0	0	92.6	0.7	182.6353	< 1.0
0.1	7.2801	< 0.5	0	0	45	0.6	88.3256	< 1.0
0.1	5.861	< 0.5	0	2.6965	85.8	0.7	165.6067	< 1.0
0.1	6.5928	< 0.5	0	2.0959	66.6	0.6	127.6073	< 1.0
0.1	6.5325	< 0.5	0	0	60.3	0.6	114.0781	< 1.0
0.1	7.0296	< 0.5	0	0	49	0.6	94.4693	< 1.0
0.2	9.1178	< 0.5	0	6.6977	513.4	1.1	1057.245	< 1.0
0.1	6.6345	< 0.5	0	6.3186	465.4	1	955.1876	< 1.0
0.1	5.2407	< 0.5	0	3.1998	364.8	0.9	751.9839	< 1.0
0.1	6.524	< 0.5	0	0	347.5	0.9	724.6996	< 1.0
0.1	7.635	< 0.5	0	6.4971	458.6	1	934.3806	< 1.0
0.1	5.6967	< 0.5	0	4.8472	203.8	0.8	411.614	< 1.0
0	0	< 0.5	0	0	455.9	1	941.8573	< 1.0
0.1	7.8507	< 0.5	0	6.576	458.1	1	938.3679	< 1.0
0.1	5.8995	< 0.5	0	4.265	462.9	1	960.2154	< 1.0
0.2	30.9328	13.4	0.3	40.0507	1903	2	4334.958	5.8
0.2	35.6886	15.4	0.3	44.217	1604	2	3634.376	13.6
0.2	27.3671	9	0.2	30.057	1436	2	3246.639	4.7
0.3	32.199	15	0.3	42.9144	1989	2	4426.06	< 1.0
0.3	29.6961	12.3	0.3	37.2463	1922	2	4312.77	2.5

Cs	Cs	Ba	Ba	Ba	La	La	La	Ce
Abs. Error	Norm. Int.	µg/g	Abs. Error	Norm. Int.	µg/g	Abs. Error	Norm. Int.	µg/g
0	19.0587	321.9	1.3	622.3539	20.3	0.6	75.5594	47
0	25.0748	325.9	1.3	630.3114	25	0.7	83.7671	51.3
0	19.5127	302.1	1.3	580.8215	14.6	0.5	65.4465	31.7
0	22.2915	298.3	1.3	577.7903	23.1	0.7	80.0716	47
0	15.0351	305.4	1.3	591.0677	19	0.6	73.2073	45.7
0	20.3721	310.6	1.3	601.7551	19.6	0.6	74.2204	41.3
0	15.2094	288.6	1.3	558.6984	16.4	0.6	68.5273	43.3
0	21.7661	313.3	1.3	607.138	20.8	0.6	76.3159	47.3
0	23.4198	308	1.3	594.5764	20.6	0.6	75.7833	41.1
0	6.9928	54.5	1.1	91.0179	< 2.0	0	34.9132	27
0	11.9282	16.9	0.6	46.8415	26.2	0.8	65.4089	104.8
0	0	39	1	72.1757	3.9	0.2	41.7689	50.6
0	11.1113	30.4	0.9	61.8764	6.2	0.3	44.0216	56.7
0	10.9532	24	0.8	54.1672	18.8	0.6	56.9709	74.9
0	9.1595	15.5	0.6	45.0126	24	0.8	62.6951	107.4
0	0	236.6	1.7	311.1718	19.4	0.7	60.6895	35.3
0	12.9785	223.6	1.7	295.1721	19.1	0.7	60.2662	33.7
0	10.9042	290.3	1.8	373.8909	11.2	0.5	51.8495	23
0	13.3818	276.5	1.7	362.016	13.6	0.5	54.6447	22.5
0	17.0189	232	1.7	302.3115	24.6	0.8	66.1595	44
0	17.1472	253.5	1.7	320.1244	20.8	0.7	61.5784	34.1
0	12.57	241.9	1.7	319.1669	19.3	0.7	60.7949	35.5
0	15.2306	241.8	1.7	315.5655	23.6	0.8	65.246	42.7
0	13.1926	277.1	1.8	361.5201	13.2	0.5	54.2116	30.7
0.2	45.8627	1502	3	1981.509	5.5	0.2	55.8185	< 2.6
0.4	58.5904	1584	3	2076.848	42.9	1	101.0135	43.4
0.2	43.9934	1570	3	2052.127	6.2	0.3	57.1131	< 2.6
0	0	1405	3	1806.226	7.9	0.3	57.3256	< 5.6
0.1	40.5092	1469	3	1899.79	< 2.0	0	44.5044	< 2.6

Ce	Ce	Pr	Pr	Pr	Nd	Nd	Nd	Hf
Abs. Error	Norm. Int.	µg/g	Abs. Error	Norm. Int.	µg/g	Abs. Error	Norm. Int.	µg/g
1	124.2696	2.6	0.1	56.2335	25	1	77.1628	14.7
1	130.4753	7.4	0.3	65.612	30.2	1.1	83.2655	12.6
0.8	102.1278	< 3.0	-0.9	52.9042	20.3	0.9	71.3507	10.4
1	123.9825	3.1	0.2	57.2733	27.1	1.1	77.6364	13.6
1	122.3519	< 4.0	0	47.5458	18	0.8	68.6178	12.4
0.9	116.1853	4.3	0.2	59.4877	28	1.1	80.9802	13.4
0.9	118.5939	< 3.1	-1.3	53.6459	22.8	1	73.0098	13.7
1	124.7325	3.7	0.2	58.4101	24.8	1	77.2699	13.2
0.9	115.6615	3.9	0.2	58.7739	21.8	0.9	73.7839	10.7
0.8	82.0783	< 4.0	0	21.1553	< 5.1	0	42.195	4.2
1.5	155.92	< 4.0	0	30.3084	< 5.1	0	61.2648	< 2.0
1.1	104.217	< 4.0	0	27.2963	< 5.1	0	42.6617	6.8
1.2	109.4546	< 4.0	0	27.5951	< 5.1	0	47.7684	5.8
1.3	125.63	< 4.0	0	34.6092	< 5.1	0	55.9706	5.1
1.6	157.1318	< 4.0	0	25.6667	< 5.1	0	57.8532	< 2.0
0.9	91.8415	< 4.0	0	33.2092	< 5.1	0	55.7151	< 2.0
0.9	90.156	< 4.0	0	29.9334	< 5.1	0	51.6707	< 2.0
0.7	79.7077	< 4.0	0	27.6504	< 5.1	0	52.2723	< 2.0
0.7	79.4816	< 4.0	0	30.7585	< 5.1	0	51.9089	< 2.0
1	100.1427	< 4.0	0	41.7782	< 5.1	0	65.8468	< 2.0
0.9	89.6799	< 4.0	0	37.289	< 5.1	0	55.5248	< 2.0
0.9	92.2817	< 4.0	0	29.6427	< 5.1	0	53.9316	< 2.0
1	99.1436	< 4.0	0	39.8508	< 5.1	0	64.8657	< 2.0
0.8	87.6601	< 4.0	0	29.8658	< 5.1	0	55.8461	< 2.0
0	62.2105	< 4.0	0	50.0899	13.8	0.6	67.1391	< 2.0
0.9	109.4476	35.7	0.9	109.6662	70.5	1.8	117.8742	< 1.6
0	62.9724	< 3.5	0	51.8345	12.9	0.6	67.3444	< 2.0
0	63.4224	< 3.5	-1.3	53.3373	10.9	0.5	61.9104	< 2.0
0	51.2616	< 4.0	0	48.8979	7.2	0.4	60.2194	< 2.0

Hf	Hf	Ta	Ta	Ta	W	W	W	Au
Abs. Error	Norm. Int.	µg/g	Abs. Error	Norm. Int.	µg/g	Abs. Error	Norm. Int.	µg/g
0.7	10.8625	< 1.6	0	0	660	1.9	571.7541	2
0.7	9.6955	< 1.6	0	0.7351	713.1	2	614.4599	2.2
0.6	8.278	< 1.6	0	0	584.7	1.8	488.6398	3.3
0.7	10.1673	< 1.6	0	0	621.8	1.9	533.5349	4.4
0.7	9.5326	< 1.6	0	0.3041	639.2	1.9	548.8214	2.4
0.6	10.172	< 1.6	0	0	670.6	1.9	581.8275	2.2
0.7	10.1193	< 1.6	0	0	603.1	1.9	508.6881	3.5
0.6	10.0346	< 1.6	0	0	650.9	1.9	564.7811	1.8
0.6	8.5544	< 1.6	0	3.7995	426.7	1.5	364.4439	2.3
0.4	5.3695	< 1.6	0	3.0079	4	0.1	22.2701	0.9
0	3.1086	< 1.6	0	3.1854	< 1.2	0	14.0476	< 0.6
0.5	6.4359	< 1.6	0	2.7597	< 1.2	0	22.7409	< 0.6
0.5	6.076	< 1.6	0	3.1931	< 1.2	0	20.4295	< 0.6
0.4	5.8421	< 1.6	0	3.4404	< 1.2	0	19.0516	< 0.6
0	2.9139	< 1.6	0	4.1577	< 1.2	0	5.2288	< 0.6
0	2.1589	< 1.6	0	2.0693	21.2	0.6	22.9647	1.6
0	1.9579	< 1.6	0	3.4254	17	0.5	21.4739	0.6
0	2.7666	< 1.6	0	2.7705	16.8	0.5	19.6017	0.7
0	2.3435	< 1.6	0	3.4766	18.4	0.6	20.4844	0.5
0	1.8473	< 1.6	0	3.4901	18.4	0.5	22.0059	1.2
0	1.688	< 1.6	0	1.97	29.2	0.7	26.0192	< 0.5
0	2.8057	< 1.6	0	3.7542	15.7	0.5	20.7475	< 0.5
0	2.5327	< 1.6	0	2.4892	20.7	0.6	23.4538	1.3
0	1.9499	< 1.6	0	1.5452	19.8	0.6	21.8113	1.2
0	1.7506	< 1.6	0	1.8609	15.7	0.7	12.2872	6.6
-0.8	2.9352	< 1.6	0	6.0354	19.2	0.7	14.6835	6.8
0	2.2688	< 1.6	0	3.1447	15.7	0.7	12.2381	6.9
0	2.5037	< 1.6	0	3.118	16.6	0.7	12.4325	6.8
0	2.4259	< 1.6	0	2.2037	16.7	0.7	12.7923	6.5

Au	Au	Hg	Hg	Hg	Tl	Tl	Tl	Pb
Abs. Error	Norm. Int.	µg/g	Abs. Error	Norm. Int.	µg/g	Abs. Error	Norm. Int.	µg/g
0.3	5.3673	< 0.7	0	0	1.6	0.2	4.4195	6.8
0.3	5.8248	< 0.7	0	0	1.7	0.2	4.512	7.3
0.3	8.2157	< 0.7	0	0	1.7	0.2	4.3514	6.4
0.3	11.1494	< 0.7	0	0	1.8	0.2	4.6093	7.1
0.3	6.1498	< 0.7	0	0	1.6	0.2	4.2238	7
0.3	5.7182	< 0.7	0	0	1.5	0.2	4.1724	6.1
0.3	8.8804	< 0.7	0	0	1.4	0.2	3.7129	6.6
0.3	4.7436	< 0.7	0	0	1.4	0.2	3.8099	6.3
0.3	5.9696	6.4	0.7	9.4987	1.7	0.2	4.3994	6.4
0.3	1.346	4.2	0.6	3.8437	< 0.7	0	0	6.7
0	0	4.8	0.7	4.1738	< 0.7	0	0	7.1
-0.2	0.3291	2.7	0.6	2.4204	< 0.7	0	0	8.3
0	0	2.1	0.6	1.8558	< 0.7	0	0	9
0	0	1.2	0.6	1.0489	< 0.7	0	0	4.9
0	0	4.2	0.6	3.5688	< 0.7	0	0	6.5
0.3	2.7123	6.7	0.5	6.8664	< 0.7	0	0	3.4
0.3	1.0403	4.1	0.6	4.1848	< 0.7	0	0	3.1
0.3	1.227	5.3	0.6	5.4059	< 0.7	0	0	3.5
0.3	0.8972	5.8	0.5	5.9438	< 0.7	0	0	3.7
0.3	1.977	5.2	0.6	5.2313	< 0.7	0	0	3.6
0	0	7.5	0.6	7.3836	< 0.7	0	0	3
0	0	6.4	0.6	6.5163	< 0.7	0	0	3.8
0.3	2.1968	5.9	0.6	5.982	< 0.7	0	0	3.1
0.3	2.0433	6.1	0.5	6.3247	< 0.7	0	0	3.6
0.3	13.2434	< 0.7	0	0	< 0.7	0	0	4.9
0.3	13.4522	< 0.7	0	0	< 0.7	0	0	5.2
0.3	13.5575	< 0.7	0	0	< 0.7	0	0	4.7
0.3	13.3018	< 0.7	0	0	< 0.7	0	0	5.4
0.3	12.7777	< 0.7	0	0	< 0.7	0	0	5

Pb	Pb	Bi	Bi	Bi	Th	Th	Th	U
Abs. Error	Norm. Int.	µg/g	Abs. Error	Norm. Int.	µg/g	Abs. Error	Norm. Int.	µg/g
0.4	17.2078	< 0.5	0	0	8.1	0.2	32.4522	4.1
0.4	17.9844	< 0.5	0	0	7.9	0.2	31.5543	4.5
0.5	15.7135	< 0.5	0	0	7.3	0.2	28.647	2.1
0.4	17.4328	< 0.5	0	0	7.6	0.2	30.5762	8.1
0.4	16.959	< 0.5	0	0	8.2	0.2	32.6076	7.2
0.5	15.5151	< 0.5	0	0	6.8	0.2	28.2348	< 0.4
0.4	15.7816	< 0.5	0	0	8.1	0.2	31.6637	8.5
0.5	16.1506	< 0.5	0	0	7.8	0.2	31.3038	0.9
0.5	16.1016	< 0.5	0	0	7	0.2	28.6702	1
0.7	8.7613	< 0.5	0	0	0.6	0.1	8.8585	< 0.4
0.7	8.9008	< 0.5	0	0	0.7	0.1	9.1517	6.1
0.7	10.3957	< 0.5	0	0	< 0.4	0	7.3879	1.2
0.7	10.9316	< 0.5	0	0	< 0.4	0	4.7743	7.3
0.7	6.212	< 0.5	0	0	5.4	0.4	17.2224	4.9
0.7	8.092	< 0.5	0	0	1.9	0.2	11.2192	9.6
0.5	5.2765	< 0.5	0	0	4.1	0.2	16.5582	3.7
0.5	4.8375	< 0.5	0	0	3.6	0.2	15.5012	2.6
0.5	5.375	< 0.5	0	0	4.1	0.2	16.5804	6.3
0.5	5.677	< 0.5	0	0	3.1	0.1	14.5715	6.7
0.5	5.3334	< 0.5	0	0	4	0.2	16.1418	2.8
0.5	4.5602	< 0.5	0	0	3.3	0.2	14.6468	7.5
0.5	5.7663	< 0.5	0	0	3.6	0.2	15.5527	3.1
0.5	4.7334	< 0.5	0	0	4.6	0.2	17.4521	4.7
0.5	5.5307	< 0.5	0	0	4.2	0.2	16.9189	4.5
0.4	8.3116	< 0.5	0	0	5.4	0.1	21.9339	1.8
0.4	8.835	< 0.5	0	0	5.2	0.1	21.2648	9.5
0.4	7.9608	< 0.5	0	0	5.1	0.1	21.0895	14.9
0.4	8.7469	< 0.5	0	0	5.6	0.1	21.9732	< 0.4
0.4	8.3339	< 0.5	0	0	5.3	0.1	21.5597	1.7

U	U
Abs. Error	Norm. Int.
0.2	28.1117
0.2	29.3977
0.1	18.468
0.2	43.5262
0.2	39.8275
0	10.0144
0.2	44.8821
0.1	15.1232
0.1	15.746
0	5.9526
0.4	23.7883
0.1	13.1402
0.4	26.1241
0.4	20.4247
0.5	30.9669
0.2	25.8797
0.1	22.5181
0.2	33.4463
0.2	34.9978
0.2	22.8234
0.3	35.2486
0.2	24.0136
0.2	27.8435
0.2	28.747
0.1	32.7721
0.2	55.4358
0.2	71.2439
0	24.3333
0.1	32.2321

Table A2 XRF data obtained for selected samples from the Luderitz profile.



## 1 8. Conclusions and Outlook

### 2 8.1 CONCLUSIONS

3 The intrinsic properties of greigite and magnetite nanoparticles were studied in detail using an  
4 experimental approach, with special focus on their presence in natural systems. Synthetic greigite nano-  
5 flakes, and magnetite that was cultured from magnetotactic bacteria were studied by means of electron  
6 spin resonance spectroscopy, rock magnetic methods and supporting, non-magnetic experiments. The  
7 analysis of the synthetic and lab-cultured samples was used as a comparison during the analysis of  
8 naturally-occurring samples with similar morphology.

9

10 Both, the synthetic and the natural samples of **greigite** reveal similar, flake-like morphology. The  
11 synthetic sample reveals a mark change in spectra properties below 50 K, which indicates strong  
12 magnetostatic interaction and plausible variations in anisotropy energies (Chapter 3). This is a new  
13 feature that has been shown for greigite, and it may be an intrinsic feature of greigite or may arise from  
14 the flake-like morphology. A similar change in spectroscopic properties is observed for the natural  
15 sample (Chapter 4). It is, however, found at slightly elevated temperatures, which can be a result of the  
16 presence of other magnetic minerals in the sediments. Moreover, magnetic signals from the sediment  
17 profile imply the replacement of greigite with pyrite framboids under the change of redox conditions.  
18 This, in turn, indicates an evolution of environmental conditions in a former tailing's pond related to  
19 rehabilitating processes.

20

21 **Magnetite** that is associated with MTB is an important indicator for environmental conditions.  
22 Magnetite particles are often arranged in chains within MTB, which results in unique anisotropy  
23 properties. This chain arrangement, however, can be destroyed after the bacteria die due to the  
24 decomposition of organic matter under reducing conditions. The lab-cultured MTB were analysed under  
25 heat treatment that serves as a proxy for this decomposition process, and define how it influences spectra  
26 form ferromagnetic resonance (FMR) measurements (Chapter 5). This experimental study reveals that

27 chains of magnetosomes undergo two stages: 1) the decomposition of the organic matter, leading to the  
28 breakdown of the chain arrangement; and 2) the possible oxidation of the magnetite particles through  
29 maghemitization. The  $B_{uni}$  values, which is obtained from the FMR spectra, were defined for all the  
30 stages of deterioration that can be assigned to chains, chain-fragments, and clustered particles. These  
31 feature can be used as a reference for assessing the stage of decomposition of chains of magnetosomes  
32 in nature. The decomposition processes of organic matter were taken into account, while analysing the  
33 sediment profiles from Lake Constance (Chapter 6) and offshore Namibia (Chapter 7), where an  
34 indication of the magnetosomes were found. The analysis of the sediments from the Lake Constance  
35 reveals the variations in the abundance of magnetosomes, which is influenced by environmental  
36 changes, specifically eutrophication. The results, from the marine ecosystem, which was claimed  
37 formerly to be rich in MTB, does not reveal their widespread presence. The experimental properties,  
38 expected for magnetosomes, are only clearly present in sediments from marine sediments, consisting of  
39 organic and opal ooze, which is characterised by very weak magnetic properties. The regions with other  
40 sediments reveal strong magnetic signal, originating most-likely from Fe-bearing clays from rivers and  
41 aeolian deposits from the desert. In these sediments it does not disprove the presence of magnetosomes,  
42 but only shows that the magnetic properties of the sediments are characterised by a high concentration  
43 of Fe-bearing paramagnetic clay minerals.

44

## 45 8.2. OUTLOOK

46 The results, which were obtained in the five studies comprising this thesis, have answered questions  
47 that were posed for this research. On the other hand, the results have also raised new questions. Further  
48 work that could be carried out is discussed below.

49

50 The studies on **greigite**, characterized by a flake-like morphology and nanotexture, could be broaden  
51 by seeking answers to the following questions. Firstly, what is the exact structure of a single flake?  
52 How are the nanocrystallites positioned relative to each other? The additional crystallographic analysis

53 could help to define the crystallographic axis of each crystallite. Secondly, why both the synthetic and  
54 the natural samples show similar morphology? Were there similar chemical conditions during they  
55 formation in the laboratory and in the natural environment? If yes, what are they and how does the  
56 manipulation of those conditions influence greigite's morphology? What are the specific conditions  
57 required for formation of flakes of greigite? Is this related to the morphology of mackinawite, which  
58 serves as a precursor? Thirdly, could additional low temperature spectroscopic analysis of greigite  
59 samples define if the low-temperature anomaly originates from the morphology or greigite itself? Does  
60 crystalline greigite with cubic morphology show a similar temperature dependence in FMR spectra? If  
61 the change in magnetic properties below 50 K is an intrinsic feature of greigite, what is its origin and  
62 could it be used to unambiguously define the greigite presence in the sedimentary records? Finally, the  
63 transition from greigite to pyrite is already well-documented in the sedimentary records. However,  
64 could the flake-like structure of greigite be exclusively responsible for the framboidal shape of pyrite?  
65 If not, what are the other forms and what factors control the morphology?

66

67 The studies on **magnetite** from MTB, could be extended by including TEM heating analysis of lab-  
68 cultured samples. This was planned, but due to the shutdown during the COVID 19 outbreak, it could  
69 not be carried out. This information, however, would allow to direct observation on how the chain  
70 behaves during the decomposition of organic matter. Additionally, different methods lead to  
71 decomposition of organic matter, such as employing UV-radiation, could be used to verify the data  
72 accuracy and exclude potential thermal influence on the magnetite particles. Moreover, the analysis of  
73 the magnetic records, with special focus on MTB could be performed in sedimentary records at other  
74 lakes with specific, well-known geochemical conditions, in order to define their potential application  
75 in the analysis of the decomposition phenomena. Furthermore, the magnetic and spectroscopic analysis  
76 of the marine sediments could be extended to other upwelling systems. It could help to define  
77 differences and similarities in the presence and preservation of MTB and magnetosomes in the most  
78 biologically productive regions of the worlds' ocean, and simplify detection of MTB and their fossils  
79 in the marine sediments.

80 It is only through a good understanding of magnetic properties of ferromagnetic (*s.l.*) minerals, as  
81 shown in Chapters 3 and 5, that it is possible to fully exploit their applicability, and can be applied when  
82 analyzing natural systems as seen in Chapters 4, 6, 7. As our understanding of the factors that affect  
83 magnetic mineralogy improve, we will also have a better understanding of geological and  
84 environmental processes. There is, however, plenty work to be done in the future, if we wish to better  
85 understand nature.

## 9. Acknowledgments

During those four years I have met many people who were willing to support me both scientifically and personally.

Firstly, I would like to thank Prof. Dr. Andrew Jackson for supporting me in the hard times, but with the valuable criticism, which has allowed me not to lose my head. A very special thanks to Prof. Ann Hirt, who was always there for me. Without her strong scientific guidance and warm heart, I would never finalize this thesis.

I am also grateful to PD. Dr. Andreas Gehring for his readiness to offer unlimited amount of time to discuss troubling scientific issues and therefore, being a persistent and talented mentor. Due to the good relations of PD. Dr. Andreas Gehring with other scientists worldwide, we were able to extend our research to broader scope. I would also like to thank Prof. Dr. Michalis Charilaou for his openness, criticism and friendship, which he offered me multiple times.

Many thanks to Prof. Dr. Timothy Eglinton and Prof. Dr. Michael Winklhofer for reviewing my thesis, giving feedback on my research, and being part of my committee. Additionally, I would like to thank Prof. Dr. Derek Vance for acting as the chairperson of my defense.

For diverse collaborations I would like to give thanks to:

- Prof. Dr. Gunnar Jeschke for providing EPR lab facilities, and Rene Tschaggelar for introduction, support with EPR, and long-hours conversations, which made me not to feel alone.
- Stefan Beetschen for friendship, advices and for support in work at Laboratory of Natural Magnetism, ETH.
- Dr. Luiz Grafulha Morales and Dr. Karsten Kunze from Scientific Centre for Optical and Electron Microscopy (ScopeM) of ETH Zürich for the SEM pictures of natural greigite (Chapter 4).

- Dr. Severian Gvasaliya for assistance operating MPMS and Prof. Dr. Andrey Zheludev for providing the access to facilities of Neutron Scattering and Magnetism Group, ETH Zurich.
- Prof. Dr. Jörg F. Löffler for allowing me to use PPMS facilities, and Alexander Firlus for PPMS assistance at Laboratory of Metal Physics and Technology, ETH.
- Prof. Dr. Ruben Kretzschmar for enabling Soil Chemistry lab facilities, and Kurt Barmettler for introduction to XRF.
- All RGNO organizers and team for an unforgettable field work.

I would have never survived that PhD without the amazing and understanding people, who I was lucky to meet on my way. I would like to thank all my friends and colleagues from ETH, who made me so many times to feel like home. In particular, I would like to thank Fede, Antonio, Johannes, Leo, Adrian, Melissa and the whole EPM group. I would also love to mention here all of the other amazing people who I had a chance to meet in Zurich. You definitely made my time! Special thanks to Henner and Monika for the long conversations, thousands of messages and all those nice words!

During those four years nobody supported me as much as Dimitrios Lazaris, who was next to me in my best and worst moments, and who was always ready to face all my struggles with me. For all of that he deserves a PhD too (or maybe even two?).

And last but not least, I thank my family and long-time friends from Poland. Especially I would like to thank to my parents Elżbieta and Tomasz, and my siblings Agnieszka and Stanisław for their constant love and support.